Dirac and Weyl semimetals with holographic interactions

V. P. J. Jacobs

Dirac and Weyl semimetals with holographic interactions
Vivian Petronella Jacoba Jacobs
PhD thesis Utrecht University, August 2015
Cover: Illustration of the semiholographic model for
Dirac and Weyl semimetals, discussed in this thesis.
ISBN: 978-90-393-6378-2
Gedrukt door Ipskamp Drukkers, Enschede

Dirac and Weyl semimetals with holographic interactions

Dirac- en Weyl-halfmetalen met holografische wisselwerkingen

(met een samenvatting in het Nederlands)

Proefschrift

ter verkrijging van de graad van doctor aan de Universiteit Utrecht op gezag van de rector magnificus, prof.dr. G.J. van der Zwaan, ingevolge het besluit van het college voor promoties in het openbaar te verdedigen op maandag 24 augustus 2015 des ochtends te 10.30 uur

door

Vivian Petronella Jacoba Jacobs

geboren op 21 juni 1988 te Enschede

Promotoren: Prof.dr.ir. H. T. C. Stoof
Prof.dr. S. J. G. Vandoren

*****

Contents

*****

Publications

The content of the following chapters is based on published work,

- **Chapter 3**
  U. Gürsoy, V. Jacobs, E. Plauschinn, H. Stoof and S. Vandoren, *Holographic models for undoped Weyl semimetals*, J. High Energy Phys. **04** (2013) 127.

- **Chapter 4**
  V. P. J. Jacobs, S. J. G. Vandoren, and H. T. C. Stoof, *Holographic interaction effects on transport in Dirac semimetals*, Phys. Rev. B **90**, 045108 (2014).

- **Chapter 5**
  V. P. J. Jacobs, S. Grubinskas, and H. T. C. Stoof, *Towards a field-theory interpretation of bottom-up holography*, J. High Energy Phys. **04** (2015) 033.

and various elements of this thesis are based on joint work that lead to three Master's theses [1–3].

Other publications to which the author has contributed:

- M. P. Mink, V. P. J. Jacobs, H. T. C. Stoof, R. A. Duine, M. Polini, and G. Vignale, *Spin transport in a unitary Fermi gas close to the BCS transition*, Phys. Rev. A **86**, 063631 (2012).

Chapter 1

Introduction

Experiments on quantum mechanical systems with many constituents such as atoms and electrons have shown the richness of physical phenomena that can emerge from the interplay between the constituents. The theory of a single electron or atom is well established and confirmed by experiment, and many accurate theories exist for interacting systems of many particles as well. However, experimentalists have found classes of many-particle systems exhibiting various behaviour that cannot be explained by the current theoretical models, e.g., the high-temperature superconductors [4]. The difficulty here is that these systems are so strongly correlated, that the usual theoretical approach of performing a power expansion in a small parameter, such as the coupling between one electron and its neighbour, does not make sense simply because no suitable parameter exists. Advanced numerical methods have proven to be insufficient as well [5].

Remarkably, there is a tantalizing similarity between some of these strongly correlated electron systems and other systems that naively appear to be unrelated. Namely, strongly correlated electrons turned out to have much in common with the primordial soup created in ultra-high-energy collider experiments, atomic gases cooled to the incredibly low temperature of a few nanokelvins, and even the physics of black-hole horizons [6]. The attempt to uncover the underlying mechanisms governing all of these examples has brought together researchers from many fields of physics, not only condensed-matter physics but also particle physics, astrophysics, atomic physics, mathematical physics, and string theory.

Recently, this led to progress in theoretical physics under the heading of the holographic duality, which has made it possible to apply ideas from string theory to strongly correlated quantum systems. The duality is ideally suited for a qualitative description of strongly coupled systems that behave in a universal way. Despite many new and general insights, a more precise understanding still lacks and the more practical question remains how precisely the duality can be of quantitative use for specific condensed-matter systems.

The research in this thesis is aimed at further bridging the gap between holographic computations and realistic quantum liquids. We investigate the semiholographic prescription especially intended for the computation of correlators of single-particle creation- and annihilation operators. These are relevant for condensed-matter experiments because they can be directly measured in the laboratory. The theoretical model is applied to Dirac and Weyl semimetals. These condensed-matter systems have been discovered very recently, and are interesting already by themselves because of their relativistic dispersion and topological properties. Another measurable quantity is the electrical conductivity of these systems, and we find how it is affected by holographic interactions. Finally, we present ongoing work focused on extending the model to a more general setting, including a nonrelativistic scaling and nonzero density. The recent experimental progress on these condensed-matter systems, is a step closer towards the ultimate goal of this line of research, to make quantitative predictions from holography that are testable in solid-state systems in the laboratory.

In this introduction we first recapitulate some of the basic ingredients found in this thesis. Section 1.5 summarizes the content of each chapter. An outlook can be found in section 1.6.

1.1 Dirac and Weyl semimetals

In 1928, the theoretical physicist Paul Dirac formulated an equation that describes relativistic fermions, reconciling Einstein's theory of special relativity with quantum mechanics in an elegant way [7]. Originally intended for electrons, the Dirac equation accurately describes all relativistic spin-1/2 fermions, such as the elementary fermions found in the standard model of particle physics. Remarkably, also nonrelativistic systems can have low-energy excitations that are described by the Dirac equation of relativistic quantum mechanics. An example is the class of condensed-matter systems known as Dirac semimetals. Dirac semimetals are gapless semiconductors whose low-energy quasiparticles behave as massless Dirac fermions, resulting in a linear dispersion close to the band-touching point, called the Dirac point. One of the most prominent examples is graphene, a (2+1)-dimensional Dirac semimetal which was successfully realized and detected in 2004 [8, 9]. Graphene consists of a 2-dimensional sheet of carbon atoms arranged in a hexagonal lattice structure having two inequivalent sublattices. As a result, the effective low-energy excitations of graphene are massless two-component Dirac spinors. The two components are associated to the "which-sublattice" degree of freedom, referred to as a pseudospin. The Dirac fermions of graphene are pseudorelativistic, meaning that their energy is

proportional to their momentum with a proportionality factor v_F, the Fermi velocity, of the order of 10^6 m/s [10], and not the speed of light, $c \simeq 3 \times 10^8$ m/s.

The discovery of (2+1)-dimensional Dirac physics in graphene, caused an eruption of work on Dirac physics in condensed-matter systems. In particular, the search was out for other systems exhibiting relativistic Dirac fermions as effective degrees of freedom. This thesis deals with the three-dimensional generalization of graphene, Dirac and Weyl semimetals in three spatial dimensions, having, respectively, Dirac or Weyl points in the bulk of the material. To appreciate the difference that the extra dimension makes, we take some time for a detailed look at the Dirac physics in the (2+1)-dimensional case. The minimal model for a single Dirac point in two spatial dimensions is the two-component Hamiltonian

$$\mathcal{H}(\vec{k}) = \hbar v_F \left(\sigma^1 k_x + \sigma^2 k_y\right), \tag{1.1}$$

where k_x, k_y, and v_F are respectively the wavevector components in the x and y directions, and the Fermi velocity. Furthermore, σ^i with $i = 1, 2$ are the usual Pauli matrices that are associated with the pseudospin in graphene. The second-quantized Hamiltonian is $\hat{H} = \sum_{\vec{k}} \psi^\dagger_{\vec{k}} \mathcal{H}(\vec{k}) \psi_{\vec{k}}$ with $\psi^\dagger_{\vec{k}}$ and $\psi_{\vec{k}}$ two-component fermionic creation and annihilation operators. In real systems this Hamiltonian is the result of an expansion of the momentum around the Dirac point, ignoring $\mathcal{O}(k_i^2)$ corrections. Graphene has two distinct Dirac points, referred to as valleys and located at different points in the Brillouin zone. In two spatial dimensions, it is possible to destroy a Dirac point by adding a perturbation proportional to σ^3 to the Hamiltonian that leads to a band gap. This is a consequence of the von Neumann-Wigner theorem [11] which says that a stable twofold degeneracy in eigenvalues of a hermitian Hamiltonian requires three changeable parameters. In two spatial dimensions, we have the two tunable parameters k_x and k_y which can freely reach the value zero, but an accidental band touching requires the manual finetuning of a third parameter. The coefficient of σ^3 has to be put to zero either by an additional symmetry or an experimental condition. In graphene, ignoring the spin degree of freedom, this is achieved by the presence of both time-reversal and spatial inversion symmetry [10, 12].

1.1.1 Weyl semimetals

Going up one dimension, the minimal model in Eq. (1.1) generalizes to

$$\mathcal{H}(\vec{k}) = \hbar v_F \left(\sigma^1 k_x + \sigma^2 k_y + \sigma^3 k_z\right). \tag{1.2}$$

This is the Weyl Hamiltonian [13], and the band-touching point is called the Weyl point. The corresponding excitations are (3+1)-dimensional massless Weyl fermions

with a linear dispersion and a definite chirality. A (3+1)-dimensional condensed-matter system that is at low energies described by this Hamiltonian is called a Weyl semimetal.

Chiral fermions transform according to a left or right-handed irreducible representation of the Lorentz group. This means they are eigenstates of the chirality operator, a 4×4 matrix γ^5 defined below, with eigenvalues ± 1. A mass gap would mix a right and a left-handed representation so it does not exist for chiral fermions. Therefore, this time the band-touching point is stable without additional symmetry requirements, as opposed to the (2+1)-dimensional case. In other words, in three spatial dimensions there are no more independent 2×2 matrices available to make a perturbation with.[1] Indeed, a perturbation proportional to the 2×2 unit matrix results in a shift of the total energy without gapping the band-touching point. Adding a perturbation proportional to one of the Pauli matrices in three dimensions merely leads to a renormalization of the momentum vector, moving the Weyl point around in momentum space but not destroying it. Therefore, the band touching is said to be topologically stable. However, two Weyl points of opposite chirality that coincide in momentum space can annihilate each other.

This topological stability of noninteracting Weyl semimetals at zero temperature is captured by the fact that Weyl points give rise to a nontrivial Berry curvature [14] whose field strength has the form of a magnetic monopole or antimonopole in momentum space, depending on the chirality. The integral of this Berry curvature over a surface surrounding the monopole is a topological (Chern) number representing the number of (anti)monopoles. Due to its topological nature represented by the nontrivial Chern number of the Weyl points, a Weyl semimetal has gapless surface states. The surface states of a Weyl semimetal do not have a closed Fermi surface as do those of a topological insulator, but instead their Fermi surface consists of open line segments called Fermi arcs. Each Fermi arc connects the projection onto the surface Brillouin zone of two Weyl points of opposite chirality, as sketched in Fig. 1.1. Moreover, Weyl semimetals exhibit nondissipative transport that is a manifestation of the underlying chiral anomaly [15–24]. This nondissipative transport may be of interest for technological applications [25]. We will see some of these consequences of the topological nature of the Weyl semimetal in more detail in chapter 2. For example, a free Weyl semimetal without time-reversal symmetry has at zero temperature a nonzero anomalous Hall conductivity $\sigma^{xy} = e^2 \Delta k_z / \pi h$, where Δk_z is the momentum-space separation between the two Weyl points, which is chosen to be along the z-direction in this case [17]. This result is rederived in section 2.2.1. Of course, besides this we can also consider dissipative transport in Weyl semimetals. In section 2.1.1

[1] This agrees with the von Neumann-Wigner theorem. Namely, the Weyl point is determined by equating three tunable parameters to zero, the three wavevector components k_x, k_y and k_z.

we show that the diagonal components of the electrical conductivity are at zero temperature given by

$$\sigma^{xx}(\omega) = \frac{e^2|\omega|}{12hv_F} \tag{1.3}$$

per Weyl point [26]. The conductivity scales linearly with frequency in accordance with what is expected for quantum critical transport in 3+1 dimensions [27].

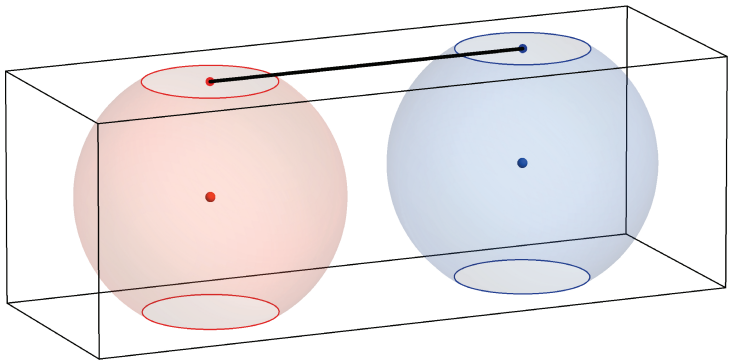

Figure 1.1: Schematic representation of a Weyl semimetal in momentum space with a Fermi arc. The cuboid surface denotes the surface Brillouin zone whereas the inside of the cuboid denotes the bulk Brillouin zone. There are two Weyl points, and to their Berry curvature a magnetic field strength in momentum space is associated, that has the form of an (anti)monopole. The locations of the corresponding magnetic (anti)monopole are shown as red and blue points. The location of the top surface Fermi arc is shown as a solid black line segment. It terminates at the projection of the bulk Weyl points to the surface. In principle there are also Fermi arcs on the front, back and bottom of the cuboid, which are not shown, but there are no Fermi arcs on the left- and right facing surfaces. The red and blue spheres are surfaces enclosing the (anti)monopole, integration of the Berry curvature over these surfaces yields the corresponding Chern number.

1.1.2 Three-dimensional Dirac semimetals

Under spatial inversion (I), momentum changes sign, so I symmetry requires $E(\vec{k}) = E(-\vec{k})$ for a single energy eigenvalue $E(\vec{k})$ at momentum $\vec{k}$. Under time reversal (TR), the signs of both momentum and spin are changed, so TR symmetry requires $E_\sigma(\vec{k}) = E_{-\sigma}(-\vec{k})$ where σ denotes the spin projection. When both TR symmetry and I symmetry are present, we have the requirement $E_\sigma(\vec{k}) = E_{-\sigma}(\vec{k})$. Thus, the

bands must be twofold degenerate everywhere in momentum space, and the band-touching point becomes fourfold degenerate [28, 29].[2] In this case, two Weyl points of opposite chirality coincide in momentum space, and the low-energy Hamiltonian is that of a massless (3+1)-dimensional Dirac fermion, i.e.,

$$\mathcal{H}(\vec{k}) = \hbar v_F \begin{pmatrix} \vec{\sigma}\cdot\vec{k} & 0 \\ 0 & -\vec{\sigma}\cdot\vec{k} \end{pmatrix} = -\hbar v_F \gamma^0 \vec{\gamma}\cdot\vec{k}. \tag{1.4}$$

In the second equality we have used a specific representation of the 4×4 Dirac matrices that is also used in the rest of this thesis, namely, $\gamma^0 = -i\sigma^2 \otimes \mathbb{1}_2$, and $\gamma^j = \sigma^1 \otimes \sigma^j$ with $j = 1, 2, 3$. The chirality matrix is $\gamma^5 = i\gamma^0\gamma^1\gamma^2\gamma^3 = \sigma^3 \otimes \mathbb{1}_2$ and $\mathbb{1}_n$ is the $n \times n$ unit matrix. In this product notation, the first and second 2×2 matrices describe respectively the chirality and the spin degree of freedom. The Dirac matrices satisfy the anticommutation relations $\{\gamma^\mu, \gamma^\nu\} = 2\eta^{\mu\nu}\mathbb{1}_4$, where $\eta^{\mu\nu}$ is the Minkowski metric with signature $(-1, 1, 1, 1)$. This convention is used everywhere in the following chapters.

A system described by the effective Hamiltonian in Eq. (1.4) is a (3+1)-dimensional Dirac semimetal.[3] We already mentioned that the two coinciding Weyl points of opposite chirality can couple, annihilating each other and giving rise to a gapped phase. Therefore, the Dirac point described by Eq. (1.4) is in general not stable in the presence of TR and I symmetries. However, the appearance of off-diagonal terms in the Hamiltonian of Eq. (1.4) can be prevented in various ways by additional symmetries or finetuning, e.g., to a topological phase transition. It was proposed that a three-dimensional Dirac semimetal exists at the critical (gap-closing) point between a topological and a trivial insulator [30, 31]. As the phase transition depends on multiple parameters, experiments require a lot of fine-tuning which impedes a detailed study of this Dirac semimetal [32]. More recent theoretical [28, 33–35] and experimental [36] work resulted in the identification of various compounds as promising candidates for a (3+1)-dimensional Dirac semimetal phase. Three-dimensional Dirac semimetals were ultimately realized experimentally in the crystals Na_3Bi [37] and Cd_3As_2 [38–40]. In these materials, the stability of the Dirac point against the formation of a gap is ensured by the crystal symmetry. To see how this works we take a closer look at the band structure calculations of Cd_3As_2 presented in Ref. [28]. The crystal structure of Cd_3As_2 has a particular tetragonal symmetry. If TR and I symmetry are present, the Fermi surface of Cd_3As_2 consists of two fourfold degenerate Dirac points located at different positions in the Brillouin zone. Each of the Dirac points is a crossing of two twofold degenerate bands. The crossing cannot be avoided

[2] Thus the von Neumann-Wigner theorem for twofold degeneracies does not apply anymore.

[3] Although graphene is technically a (2+1)-dimensional Dirac semimetal, in this thesis the term Dirac semimetal is used predominantly for (3+1)-dimensional systems.

because the excitations of each band are 2-component fermions that transform according to a distinct irreducible representation of the tetragonal symmetry group. So at leading order in momentum, the Hamiltonian close to a Dirac point takes the form of the massless Dirac Hamiltonian. Because of the tetragonal symmetry, all its matrix elements have the form of a certain polynomial of k_x, k_y and k_z, and it turns out that a mass term appears only at $\mathcal{O}(k_i^2)$. If this symmetry is broken, e.g. by compressing the crystal, a mass term is allowed at leading order and makes the system gapped. The situation is very similar in Na_3Bi [35]. However, in BiO_2 it is slightly different [33] as there is only a single Dirac point. For more details we refer to the classification comprehensibly presented in Ref. [29].

Following the discovery of stable (3+1)-dimensional Dirac semimetals, very recently also a (3+1)-dimensional Weyl semimetal was experimentally realized in the compound TaAs [41, 42]. Interestingly, also other types of Dirac and Weyl semimetals in which the dispersion in one or more spatial direction is quadratic instead of linear, have been proposed [29, 34, 43] and found experimentally [44]. Besides solid-state systems, the prospect is that Dirac and Weyl semimetals can soon be realized in cold atomic systems in an optical lattice as well [45]. This environment provides good control over almost all external parameters, which makes it possible to analyse the semimetals thoroughly under all sorts of circumstances.

1.2 Interactions and effective selfenergy

So far, we have discussed the properties of noninteracting Dirac and Weyl semimetals, but in general it is desirable to have a full account of the role of interactions in these materials. A very interesting and relevant question is how the topological properties of Weyl semimetals, which are derived in the free case, are affected by interactions.

Theoretical calculations indicate that a three-dimensional semimetal phase can exist in the case of Coulomb interactions [26, 46]. The interactions affect the spectral-weight function and the conductivity. A power-counting argument shows that Coulomb interactions are marginally irrelevant in 3+1 dimensions [47, 48], just like in 2+1 dimensions [49, 50]. This leads to logarithmic corrections to the free results of physical quantities in undoped Dirac and Weyl semimetals. In the spectral-weight function, the effect of interactions can be captured by an effective selfenergy of the form $\omega \log(\omega + i0)$, leading to a finite lifetime proportional to $1/|\omega|$ at the Dirac point [51]. For the conductivity, a typical result is the dc conductivity of a Dirac semimetal with Coulomb interactions [26],

$$\sigma_{\mathrm{dc}} \simeq \frac{e^2 k_B T}{\hbar^2 v_F(T)} \frac{0.9}{\pi \alpha^2(T) \ln\left(\alpha^{-1}(T)\right)}. \tag{1.5}$$

Here $v_F(T)$ and $\alpha(T)$ are respectively the renormalized Fermi velocity and fine structure constant that run logarithmically with temperature. The linear dependence on energy scale is similar to the free result from Eq. (1.3), but here it has additional logarithmic corrections. A calculation including Coulomb interactions at nonzero chemical potential can be found in Ref. [52].

1.2.1 Quantum critical sector and holography

Instead of the marginally irrelevant Coulomb interactions, in this thesis we set out to investigate an even more strongly-interacting case where the interactions between the fermions are dominant at long distances and time scales.[4] So the low-energy behaviour is in general very different from the noninteracting behaviour, and we do not expect any indication of linear scaling of the conductivity with energy scale as in Eq. (1.5). We are after the interacting single-particle Green's function and the electrical conductivity in this case. The motivation for the former is that the imaginary part of the single-particle Green's function is proportional to the spectral-weight function. This quantity is directly measurable in experiment, using angle-resolved photoemission spectroscopy (ARPES) for solid-state systems or radio-frequency spectroscopy in the case of ultracold atoms [53–55]. The electrical conductivity is also observable and contains generally additional information not present in the spectral-weight function.

The spectral-weight function of elementary fermions satisfies a sum rule that is a consequence of the fermionic canonical anticommutation relations (for a derivation see chapter 7 of [56] or chapter 8 of [57]),

$$\int_{-\infty}^{\infty} \mathrm{d}\omega\, \rho(\vec{k},\omega) = 1. \tag{1.6}$$

Here, $\rho(\vec{k},\omega)$ is the spectral-weight function at wavevector $\vec{k}$ and frequency ω. The sum rule is valid in the free and interacting case at zero and nonzero temperature. It is important for experiments, for instance because it helps identifying missing spectral weight indicating that a measurement has overlooked certain excitations. In our case the effective selfenergy dominates at low frequency, destroying the quasiparticle picture. However, at high enough frequency the free kinetic term ultimately takes over, ensuring convergence of the frequency integral in Eq. (1.6).

As will be explained in more detail in chapter 5, such a situation can occur when the interactions between the fermions are caused by a critical degree of freedom. The quantum critical system has universal scaling behaviour determined by the critical exponents of the corresponding universality class. A field-theoretic description then

[4] This is sometimes referred to as relevant interactions in the renormalization group sense, but we refrain from using the word relevant as it may be misleading in the holographic setup discussed shortly: we are not talking about a relevant perturbation of the bulk theory.

involves coupling of the fermionic theory to the quantum critical system. In the simplest case where the quantum critical system is described by the action S_{QC} that is a functional of a single scalar field Φ, the total action is for instance

$$S = S_{\mathrm{fermion}}[\bar{\psi}, \psi] + ig \int \mathrm{d}^3\vec{x} \int \mathrm{d}t\, \bar{\psi}\,(\Phi + \Phi^*)\,\psi + S_{\mathrm{QC}}[\Phi^*, \Phi], \tag{1.7}$$

where g is a dimensionful coupling constant. Integrating out the Φ-field we obtain an effective interaction potential for the fermions proportional to the two-point function of Φ. For certain values of the critical exponents the interaction potential dominates over the free term at low energy. An example of a recent calculation in this spirit for fermions in the vicinity of a magnetic quantum critical point in two spatial dimensions is Ref. [58]. In this thesis we consider a very similar setup for which the effect of the interactions can be captured by an effective selfenergy for the fermions instead of an effective interaction potential.

When the quantum critical system is itself strongly interacting, integrating it out exactly is not possible and we have to treat the critical fluctuations in some kind of approximation. Our first simplification is describing the quantum critical point by a strongly coupled conformal field theory. This is reasonable because a quantum critical point is scale invariant, and often also invariant under special conformal transformations.[5] Every conformal field theory is characterized by its operators having certain conformal dimensions, and the task is to compute correlation functions of these operators. For a strongly coupled conformal field theory, this is still not an easy task with conventional techniques because the generating functional of the conformal field theory is usually unknown. The microscopic composition of the operators is usually also unknown, we only know their conformal dimension and symmetry properties.

The direction taken in this thesis is the treatment of the conformal field theory provided by the holographic duality or Anti-de Sitter/conformal field theory (AdS/CFT) correspondence. This field has a long and interesting history of itself. Since the original works in the '90s [60–62], it has become a rapidly developing and interdisciplinary field, with applications in many other branches of physics. Of particular interest for this thesis are the applications to condensed-matter physics in the Anti-de Sitter/condensed-matter theory (AdS/CMT) correspondence. This programme was originally developed to understand the experimental observations in certain fermionic systems, such as the high-temperature superconductivity mentioned in the beginning of this text [63, 64].

The original conjecture in Refs. [60–62] tells us that the partition function of a certain supersymmetric conformal field theory is equal to the partition function of a certain string theory. The canonical example is the duality between type-IIB string

[5] But not always! See e.g. Ref. [59].

theory on $AdS_5 \times S_5$ and $\mathcal{N} = 4$ supersymmetric Yang-Mills theory in 3+1 spacetime dimensions. Taking the low-energy and classical limit on the string-theory side of the duality reduces it to a more tractable classical supergravity theory. On the field-theory side, this limit is equivalent to the strong-coupling and large-N_c limit, where N_c^2 denotes the number of degrees of freedom of the quantum field theory.

The AdS/CMT framework provides a broader interpretation of holography where it is assumed that more general strongly-coupled quantum liquids without gravity have a so-called gravity dual. It then offers a recipe for the computation of correlators in the strongly-coupled field theory by solving equations of motion in a classical gravity theory in one higher dimension. With this recipe comes a dictionary that translates properties of one of the theories into the corresponding properties of the dual theory. A few useful entries of the dictionary are summarized in table 1.1.

Strongly coupled quantum field theory in d spacetime dimensions (boundary)	General relativity in $d+1$ spacetime dimensions (bulk)
Scalar composite operator O	Scalar field φ
Chiral composite operator	Dirac field
Source of operator	(Chiral component of) boundary value of dual field
Conformal dimension of operator	Mass M of the field
Global U(1) current	U(1) gauge field
Thermal equilibrium at temperature T	Black hole with Hawking temperature T

Table 1.1: A selection of the dictionary rules used in later chapters provided by the AdS/CMT correspondence. The classical gravitational theory is also called the bulk theory, and the dual field theory is said to live on the boundary of the bulk spacetime. The bulk field φ is the dual of O, and similarly the bulk dual of a chiral fermionic operator is dual to a Dirac field in one extra dimension. The conformal dimension of the operators is a function of the mass M of the bulk fields. For example, the conformal dimension of a chiral operator O is $M+2$ in our conventions. We must solve the equation of motion of the dual field, and put the bulk action on shell. The boundary value of the bulk fields is proportional to the source of the operators in the field theory. Furthermore, gauge symmetries in the bulk become global symmetries on the boundary. Lastly, if the gravity theory has a black hole with Hawking temperature T, the boundary is in a thermal state at the same temperature.

To give a flavour of the procedure we show one of the key expressions of the AdS/CMT correspondence for the case of a scalar operator O in the quantum field theory having conformal dimension d,

$$\left\langle e^{\int \mathrm{d}^d x\, O\phi} \right\rangle_{\mathrm{cft}} = \exp\left(\frac{i}{\hbar} S_{\mathrm{bulk}}[\varphi \to \phi]\right). \tag{1.8}$$

On the left-hand side, we have the generating functional for correlation functions of O in a strongly coupled field theory without gravity in d spacetime dimensions. Here ϕ is the source of O. On the right-hand side, S_{bulk} is the action of a $(d+1)$-dimensional gravitational theory coupled to a massless scalar φ that is the field dual to O. This field lives in a spacetime with negative curvature that has a boundary looking like Minkowski space at some value of the extra dimension. This is often an Anti-de Sitter spacetime or a related spacetime. The notation $\varphi \to \phi$ indicates that the bulk action must be put on-shell, subject to the boundary condition that the solution to the classical equation of motion for φ asymptotes to the source ϕ on the boundary. Then, the right-hand side is a functional of the boundary value ϕ of the dual field of O. Taking functional derivatives with respect to ϕ on both sides of the equation, we find an expression for the correlators of O in the quantum field theory. For higher-order correlation functions of O, we thus need an interacting bulk theory for φ. For massive fields and fermionic operators, the prescription is a bit more involved but its essence is still expressed by Eq. (1.8).

Solving equations of motion, albeit in a curved background, is usually easier than calculating correlators in a strongly coupled quantum field theory, and this makes the AdS/CMT framework potentially very powerful. The challenge lies in determination of an appropriate dual gravity theory. At present, this is a matter of making an educated guess for the bulk action according to the class of field theories we want to treat. The action is specified prior to the calculations in chapters 3, 4, and 6. The phenomenological nature of this approach is elaborated on in section 5.1 of chapter 5. The introductions of these chapters should provide sufficient prior knowledge for the computations done in these chapters. For a thorough introduction to the AdS/CMT correspondence, we advice to turn to one of the many excellent overviews to be found in the literature [65–67].

1.3 Semiholography

So the strongly coupled quantum critical system can be dealt with using holography, and the correlation functions of its operators are obtainable. However, these are the correlators of composite operators, whereas we require the correlator of an elementary fermion satisfying Eq. (1.6). In fact, the goal is to incorporate the correlator of the composite operators as a selfenergy for the elementary fermions.

This is achieved by a modified approach to holography that is known as semiholography. The semiholographic approach was first written down in Ref. [68]. Later a semiholographic model was constructed for non-Fermi liquids in Ref. [69], and a similar approach was proposed for heavy-ion collisions in Ref. [70]. It amounts to coupling the conformal field theory with a gravity dual to another quantum field

theory that is treated with conventional field-theory methods. This makes the semiholographic approach a flexible option for phenomenological model-building.

In our case the other field theory is just the theory of Dirac or Weyl fermions that are free except for the coupling to the strongly coupled quantum field theory, for which we write down an appropriate gravity dual. Instead of the action in Eq. (1.7), the boundary action has now the following form,

$$S = -i\hbar c \int \mathrm{d}^d x\, \bar{\psi}\gamma^\mu \partial_\mu \psi + ig \int \mathrm{d}^d x\, \left(\bar{\psi} O + \bar{O}\psi\right) + S_{\mathrm{cft}}[\bar{O}, O], \tag{1.9}$$

where O is a fermionic composite operator in the conformal field theory. The first term corresponds to the low-energy effective theory of a Dirac semimetal, the second term is the coupling to the quantum critical system and the third term is the action of the conformal field theory describing the quantum critical system and treated in the holographic approach. The bulk theory for the dual of O is quadratic, which makes it possible to integrate out the conformal field theory. The goal is the Green's function of ψ, which contains a selfenergy proportional to the two-point function of the operator O, i.e.,

$$\Sigma(\vec{k}, \omega, T) \propto g^2 \left\langle \bar{O} O \right\rangle_{\mathrm{cft}} . \tag{1.10}$$

The selfenergy depends in general on two parameters, the coupling constant g and a parameter M, the mass of the bulk fields, that is related to the scaling dimension of the operator O.

In chapters 3, 4 and 6 of this thesis we use the specific semiholographic model that is introduced in Ref. [71]. This model goes a step further by deriving the form of the total action in Eq. (1.9) completely from the bulk theory, and leads to the same end result as in Ref. [68]. In Ref. [71], the field ψ in Eq. (1.9) plays the role of the source in Eq. (1.8). It is possible to add elementary degrees of freedom on the boundary, as long as they do not interfere with the variational principle leading to the bulk equations of motion [72]. Based on this realization, a kinetic term for the source is added to the bulk action as an irrelevant perturbation, confined to a spacetime slice close to the boundary at fixed value of the extra holographic dimension. This slice is later taken to the boundary in a double-scaling limiting procedure. We compute the two-point correlator of the source of O, and it turns out that the correlator $\langle \bar{O} O \rangle$ appears as an effective selfenergy in it. Since it is the field which was originally the source which is made dynamical on the boundary, this model is called the dynamical-source model in this thesis. A more detailed study of the dynamical-source model and its interpretations can be found in chapter 5. In the low-energy limit the semiholographic approach coincides with the holographic result in the alternative quantization.

At this point we wish to stress that the bulk fermions are probe fermions, meaning that their average density in the bulk theory is zero and their backreaction on the

geometry can be ignored. In other words, the background metric is the solution of a pure gravity theory, on top of which we have fermionic fluctuations. Furthermore, the effect of the elementary dynamical-source fermion is small compared to the large conformal field theory, in the following sense. If the conformal field theory has a number of degrees of freedom of $\mathcal{O}(N_c^2)$, where $N_c \gg 1$, the number of degrees of freedom of the dynamical source fermion is of $\mathcal{O}(1)$. The double-scaling limit is done in such a way that the product $g^2\langle\bar{O}O\rangle$ is also of $\mathcal{O}(1)$. The whole bulk action S_{bulk} in Eq. (1.8) is of $\mathcal{O}(N_c^2)$ as well which justifies the saddle-point approximation, but the effective action of the dynamical-source fermion is of $\mathcal{O}(1)$. Quantum corrections of the bulk theory are of $\mathcal{O}(1)$ too, however, these are not taken into account. This N_c dependence is addressed in chapter 5 in more detail. To clarify this further, we present here a result from chapter 5. It tells us that the total electrical conductivity which is a sum of various terms, scales in the following way with N_c and temperature,

$$\sigma_{\text{dc}} \sim \underbrace{\Big(\mathcal{O}\left(N_c^2\right) + \mathcal{O}\left(1\right)\Big)T}_{\text{conformal field theory}} + \underbrace{\mathcal{O}\left(1\right)T^{2-2M}}_{\text{interference}} + \underbrace{\mathcal{O}\left(1\right)T^{3-4M}}_{\text{dynamical source}} + \mathcal{O}\left(\frac{1}{N_c^2}\right). \tag{1.11}$$

In Eq. (1.11), the symbol N_c^2 is equivalent to what is called N in chapter 5, and the dynamical-source fermion contribution is equivalent to the contribution of the probe fermion of chapter 5. Although the result in chapter 5 is derived for a specific field-theory model, there are strong indications that exactly the same happens in general in the semiholographic dynamical-source model [73].

1.4 Preview of results

With this setup we can compute the spectral-weight functions of strongly-interacting many-body systems that behave as Weyl or Dirac semimetals. This is done in chapter 3 for a single Weyl point, and in chapter 4 for a single Dirac point. To anticipate the outcomes in later chapters, we discuss a selection of some typical results already here.

A free or weakly coupled semimetal has well-defined quasiparticles, signaled by a delta function or a Lorentzian peak in the spectral-weight function, caused by a single pole close to the real axis in the complex-frequency plane. However, the holographic semimetals do not have long-lived quasiparticles. Instead, as can be seen in Fig. 1.2, the spectral-weight function has a branch-cut behaviour. This is because the selfenergy falls off in a nonanalytic manner as $(\omega + i0)^{2M}$ at $\vec{k} = 0$, i.e., with a fractional power determined by M.[6] More precisely, at zero temperature we find for

[6] A similar behaviour is sometimes referred to as unparticle physics (see Refs. [74, 75] and references therein).

the selfenergy

$$\Sigma(k) = -\frac{\hbar g^2}{2^{2M}} \frac{\Gamma\left(\frac{1}{2} - M\right)}{\Gamma\left(\frac{1}{2} + M\right)} \not{k} k^{2M-1}. \tag{1.12}$$

Therefore, the retarded single-particle Green's function at $\vec{k} = 0$ roughly has the form

$$G_R(\vec{0}, \omega) \sim \frac{1}{\omega - g_M \omega^{2M}}\,, \tag{1.13}$$

where g_M is a dimensionful function of M and g. In our case, the parameter M, originally the mass of the dual bulk fields which is related to the universality class of the quantum critical point, ultimately determines the falloff of the effective selfenergy.

For reasons that are made clear in Ref. [71] and in chapter 3, the parameter M lies in the range $-1/2 < M < 1/2$. As $M \to 1/2$ the selfenergy obtains a linear scaling with frequency. The point $M = 1/2$ can be treated too with some extra effort. It turns out that for $M = 1/2$, the selfenergy scales as $\omega \log \omega$. So at this point the semiholographic calculation makes contact with the Coulomb case mentioned just above Eq. (1.5), at least at the level of scaling behaviour. Furthermore, in chapter 3 we consider a generalization of the dynamical-source model to a system with Lifshitz scaling on the boundary. Here, time and space scale in an anisotropic way under a scale transformation, i.e.,

$$\vec{x} \to \lambda \vec{x}, \qquad t \to \lambda^z t, \tag{1.14}$$

with $z > 1$ the dynamical critical exponent of the quantum critical point. Among other things, this influences the scaling exponents in Eqs. (1.12) and (1.13).

Note that the dynamical-source model describes the properties of Dirac and Weyl semimetals at low energies around the degeneracy point at strong coupling. This is a prediction from holography for the behaviour of real Dirac and Weyl semimetals close to a quantum critical point. However, it does not describe the emergence of Dirac and Weyl fermions from a microscopic theory.

1.4.1 Ultracold atoms

Not only in Dirac and Weyl semimetals, but also in a system of ultracold fermionic atoms we encounter situations in which the AdS/CMT correspondence is possibly applicable. An example of such an ultracold atom system is a collection of fermionic Lithium-6 atoms in a harmonic trap. Remarkably, his system can be cooled to extremely low temperatures of the order of 10^{-7} K [76, 77].[7] On account of these low temperatures, the system is highly quantum degenerate and the fermionic statistics dominate its behaviour. Furthermore, with magnetic fields the interactions between

[7] Compare this to the already very low temperature of 2.7 K of the cosmic background radiation.

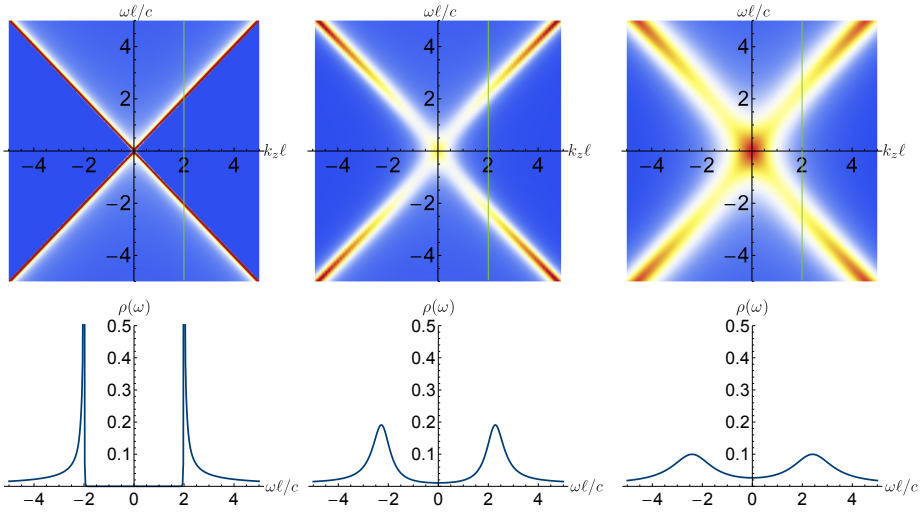

Figure 1.2: Spectral-weight function $\rho(\vec{k},\omega)$ of a semiholographic Dirac semimetal for various values of the dimensionless temperature $T' = k_B T\ell/\hbar c$, where ℓ is the AdS radius. From left to right: $T' = 1/30$, $T' = 1$, $T' = 2$. Upper panel: density plots of the spectral-weight function as a function of dimensionless frequency $\omega\ell/c$ and wavevector component $k_z\ell$. Lower panel: spectral-weight function as a function of frequency for $k_z\ell = 2$, i.e., at the location of the light-coloured vertical lines in the upper figures. These plots are for the parameter values $M = 1/4$, $g^2 = c\ell^{2M-1}$ and $z = 1$. Because of the relativistic nature of the gravity dual, we have a Fermi velocity c.

the atoms can be tuned experimentally. When the quantity parameterizing the interaction strength, the scattering length, becomes infinite, the system is strongly interacting. It then exhibits universal behaviour and the system is said to be at unitarity [78, 79]. A manifestation of this universality is the behaviour of the chemical potential, the energy needed to add a single particle to the system. In the free case, this quantity is equal to the Fermi energy. At unitarity it is still proportional to the Fermi energy, but the numerical prefactor is strongly renormalized. As is also pointed out in section 5.1, this universal behaviour occurs close to the end point of the superfluid phase transition, which is a quantum critical point at zero temperature and chemical potential. Ultracold trapped atoms are nonrelativistic systems with a quadratic dispersion, so at this point a nonrelativistic conformal field theory description may be applicable [80], and possibly also a holographic description. An example of a purely holographic model exhibiting certain features also seen in ultracold gases is the one proposed in Ref. [81].

Measurable quantities in ultracold atom systems include various single- and two-particle correlation functions [53, 82, 83]. This is an additional motivation to investigate the possibilities of a semiholographic approach for ultracold atoms systems. One of the questions is whether the renormalization of the chemical potential can be quantitatively reproduced by semiholography. Motivated by this, we set out to extend the dynamical-source model in the direction of ultracold atoms. In chapter 6 we describe how to turn on a chemical potential on the boundary in a situation with the anisotropic Lifshitz scaling from Eq. (1.14). These are the first steps towards a more realistic semiholographic model for ultracold atoms.

1.4.2 Transport without quasiparticles

When the fermions on the boundary are charged, a charge current can be created by turning on an electric field. In this way the electrical transport properties of the system can be addressed. In semiholography, a theoretical description involves coupling the fermions to a U(1) gauge field on the boundary, and the conductivity is calculated purely in field theory. In chapter 4 the fermionic contribution to the dissipative part of the electrical conductivity is computed. We saw already in Fig. 1.2 that the boundary excitations are not quasiparticle-like anymore when the holographic interaction effects are incorporated. Therefore we speak of charge transport without quasiparticles.

One of the main results of chapter 4 is the conductivity in the dc limit at zero chemical potential, which scales as

$$\sigma_{\mathrm{dc}} \propto T^{3-4M}, \tag{1.15}$$

with $-1/2 < M < 1/2$ as before. For nonzero frequency and temperature we find a peak shown in Fig. 1.3. The result in Eq. (1.15) is the $\mathcal{O}(1)$ contribution to the conductivity labeled "dynamical source" in Eq. (1.11), where the elementary fermions are charged while the conformal field theory is kept neutral. The total conductivity includes the contribution of the conformal field theory that can also be charged. This issue is addressed at length in chapter 5.

The field of quantum transport without quasiparticles has an incoherent nomenclature that might sometimes be confusing, so it is important to take a little time to clarify the mechanism behind the current relaxation and our use of certain words. In our model the conductivity is finite in the absence of translational symmetry breaking. That is because an external electric field creates a pair of excitations and couples with a different sign to the excitations above and below the Fermi level, so the charge current is carried by the momentum difference between them. Because the chemical potential is zero, the system is neutral and the net centre-of-mass momentum is always zero. However, relative momentum is not conserved and the charge current

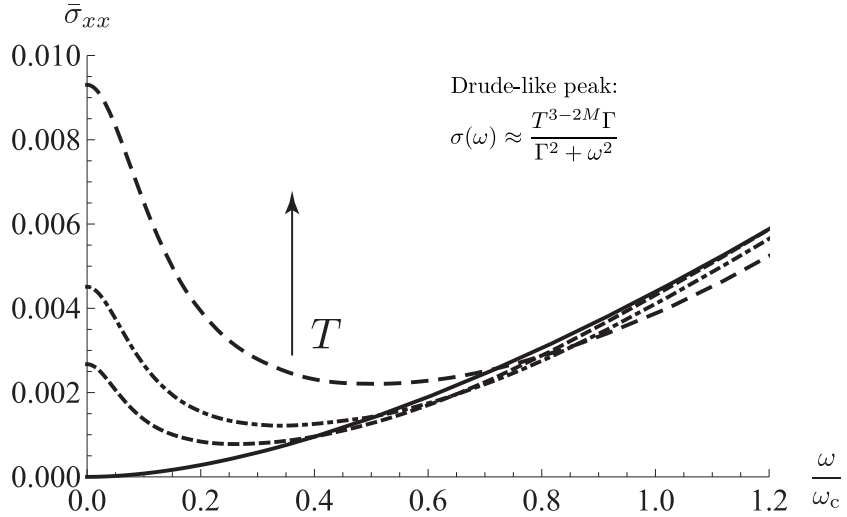

Figure 1.3: Optical conductivity of a semiholographic Dirac semimetal at $M = 1/4$ and various temperatures. This figure is identical to Fig. 4.1 up to the insets. The vertical axis corresponds to the fermionic conductivity, and on the horizontal axis we find the frequency of the boundary electric field. Both are made dimensionless with the frequency scale ω_c defined in chapter 4. For $\omega/\omega_c \gg 1$, we find the free zero-temperature result that $\sigma \propto |\omega|$ (not visible here). For $T = 0$ (solid curve) and below $\omega/\omega_c = 1$, the conductivity scales as $\sigma \propto |\omega|^{3-4M}$. However, for $T > 0$, we have the additional contribution of thermally excited pairs in the same band, leading to the Drude-like peak discussed in the main text. The height of this peak scales as $\sigma_{dc} \propto T^{3-4M}$, and the width scales for very low frequencies $\omega \ll k_B T/\hbar \ll \omega_c$ as T^{2M}, resulting in the functional form discussed in the main text.

relaxes solely due to the interactions, a mechanism that is very similar to spin drag [84, 85]. This type of transport is thus direct a consequence of the absence of an energy scale (chemical potential) other than temperature, as is discussed in detail in Ref. [86]. However, note that in the semiholographic case there is an inherent energy scale corresponding to the coupling between the dynamical-source fermion and the conformal field theory. This scale is $\hbar\omega_c$ in chapter 4 and it allows for the M-dependent scaling in Eq. (1.15), without breaking particle-hole symmetry.

In the case of nonzero chemical potential the system has a Fermi surface which also contributes to transport. Our translation-invariant system would obtain a nonzero centre-of-mass momentum leading to ballistic transport, i.e., an unlimited acceleration of the charge-carrying excitations. Conservation of momentum thus leads to an infinite dc conductivity. In principle, this Fermi surface contribution is added up to the finite dc contribution due to relative momentum relaxation of pair-created excitations at zero chemical potential [87], which is the contribution of the Fermi sea to

transport. To make the Fermi-surface contribution finite at nonzero chemical potential and zero frequency, we should incorporate momentum-relaxing effects. There are various holographic models where (weak or strong) momentum relaxation is realized by impurities or other means, see e.g. Refs. [88–96]. It is also possible to compute the conductivity of small $\mathcal{O}(1)$ excitations, e.g., around a holographic Fermi surface such as in Refs. [97, 98]. The conductivity is then finite due to momentum dissipation into the $\mathcal{O}(N_c^2)$ background. Note that this is similar to the $\mathcal{O}(1)$ contribution to the conformal field theory in Eq. (1.11), but at nonzero chemical potential. The semiholographic framework has the additional advantage that a momentum-relaxing term such as a lattice can be easily incorporated also in the free fermionic theory.

Finally, we refer to the peak in Fig. 1.3 and in chapter 4 as a Drude-like peak because of its functional form. So it is not a Drude peak in the sense that our peak does not describes relaxation of the centre-of-mass momentum which is directly coupled to the charge current. In transport without quasiparticles, the functional form of a Drude-like peak comes from a single singularity close to the real frequency axis [99]

$$\sigma \propto \frac{1}{1 - i\omega/\Gamma(T)}, \tag{1.16}$$

This corresponds to a charge-carrying excitation with a long lifetime $\sim 1/\Gamma$. In our case without momentum relaxation, $\Gamma \propto (k_B T/\hbar)^{2M}$ comes from the friction due to interactions between counterpropagating excitations. In the context where $\Gamma \ll k_B T/\hbar$ is related to a relatively small relaxation rate of the total momentum, some authors refer to this mechanism as "coherent transport" [91, 100], using the word coherent in a different context than the usual quantum mechanical one that is used in Ref. [86]. This is opposed to "incoherent transport" where momentum relaxation is so strong that charge transport is controlled by a different mechanism, diffusion. Then the conductivity may have a peak with width $\Gamma \gtrsim k_B T/\hbar$ [100].

1.5 This thesis

The discussion up to now should have clarified the motivation for and context of the research presented in the rest of this thesis. Various elements of this introduction will be emphasized multiple times in the coming chapters. The main content and purport of each of the chapters is the following.

Chapter 2 is a warming-up comprising of a derivation of the optical conductivity of free Dirac fermions, and providing more computational details that supplement the results in chapter 4. We also compute the anomalous Hall conductivity of a free Weyl semimetal with broken time-reversal symmetry at zero temperature, as well as the wavefunction of its surface states.

In chapter 3 we first turn to (semi)holography. The dynamical-source model is presented in more detail and results for the spectral-weight function of an interacting Weyl semimetal are shown. We consider both the relativistic case and the Lifshitz case where the dynamical exponent in Eq. (1.14) is unequal to 1. In the case $z = 2$ the model contains an extra dimensionful parameter related to the strength of the spin-orbit coupling, denoted by λ in chapter 3. This new scale governs a quantum phase transition between a phase with and one without a Fermi surface. By means of a WKB approximation around the Fermi surface we show that there are quasiparticles that are extremely long-lived.

So far the semiholographic model describes only a single Weyl point. However, to address the topological properties of the Weyl semimetal we need two Weyl points. In chapter 4 we generalize the semiholographic model to an interacting Dirac semimetal, by considering two species of bulk fermions that each contribute the opposite chiral component of a Dirac fermion on the boundary. The interacting optical conductivity is computed and we find the Drude-like peak discussed in section 1.4.2.

The boundary interpretation of the dynamical-source model is investigated in chapter 5. This chapter clarifies the interpretation of a free fermion coupled to a quantum critical sector discussed above. By constructing two toy field-theory models and showing which choices reproduce the semiholographic result for the fermionic selfenergy, we get more insight into the microscopics underlying the semiholographic framework. The conductivity of these field-theory models is also computed and this illustrates how the various contributions from the conformal field theory and dynamical-source fermion split up.

Finally, in chapter 6 we extend the dynamical-source model by turning on a chemical potential. The bulk is now described by a Reissner-Nordström background for $z = 1$ and a related background for arbitrary z. We also investigate the effect on the spectral-weight function of additional parameters, including a boundary mass term. For nonzero chemical potential the spectral-weight function has multiple Fermi surfaces which are further analysed.

1.6 Outlook

All in all, semiholography provides a feasible and highly adaptable setup for phenomenological model-building. However, the phenomenological character of this approach may also be seen as a disadvantage, and although several experimental predictions have been made in this thesis, the validity of this framework has at this point not been convincingly affirmed nor negated.

The recent realization of Weyl semimetals is very encouraging in this context, making it likely that these systems can in the near future also be investigated when

coupled to a critical system. In the semiholographic model, this corresponds to a fixed value of M. One of the more immediate questions for theory is how the topological nature and nondissipative transport properties of semiholographic Weyl semimetals are affected in this case. This requires lifting the degeneracy between the Weyl points on the boundary, corresponding to lifting the degeneracy between the two species of Dirac fermions in the dual theory in a specific way. When both the longitudinal and Hall conductivity are known, the behaviour of their ratio, the Hall angle, could shed more light on the microscopic mechanisms at work in the system [87]. A semiholographic treatment of Weyl semimetals is ongoing work. Clearly, before predictions can be made for ultracold atoms the semiholographic model presented here should be further improved as discussed in chapter 6.

An important future direction is considering $1/N_c^2$ corrections to the conformal field theory. This makes the semiholographic setup more consistent since the dynamical-source fermion is also subdominant compared to the $\mathcal{O}(N_c^2)$ dual field theory. The parameter N_c characterizes the number of species in the quantum critical system, which is usually not very large in a realistic setting. In general, we expect that $1/N_c$ corrections may for instance change the numerical prefactors of the conformal field theory contribution in Eq. (1.11). However, sometimes $1/N_c$ corrections lead to qualitative differences in some features of holographic models. Examples are the exponentially large quasiparticle lifetime found in chapter 3, and possibly the multiple Fermi surfaces found in chapter 6, which are thought to be a remnant of the large-N_c approximation.

In the dual bulk theory, $1/N_c$ corrections correspond to quantum or loop corrections. In the case of bulk fermions, this means going beyond the probe limit where the average fermion density is zero, to a case where there is a macroscopic density of fermions, which backreacts on the geometry. Describing the backreacted situation exactly amounts to performing the fermionic path integral, which is much more complex than just solving equations of motion. A consistent approximation then also means that we should take into account fluctuations of the other fields present in the bulk. However, this may be circumvented by approximating the density of fermions by a charged perfect fluid. In a procedure very similar to solving the Tolman-Oppenheimer-Volkoff equation for neutron stars, solving simultaneously the equations of motion for the metric, a U(1) bulk gauge field and the thermodynamic state variables of the fluid leads to the so-called electron star background [101]. The fluid can carry all or part of the charge if there is a charged black hole present [102, 103]. Backreaction is thus particularly of interest for boundary theories with nonzero chemical potential such as the models for ultracold atoms, whereas in chapter 6 we have so far treated the bulk fermions in the probe limit. Fermionic correlation functions in the electron star background have also been considered [104], as well as

various related quantum corrections [105, 106].

By the nature of the AdS/CMT correspondence, our predictions for single-particle properties are rather universal and general. Predictions for higher-order correlation functions are less universal, which could support verification of the semiholographic approach for specific systems. In principle, there is no objection to adding higher-order terms of the probe fermion to the free field-theory action in Eq. (1.9). This approach is also taken by the authors of Ref. [69]. They also consider nonzero chemical potential, more precisely, non-Fermi liquids in which the additional fermion plays the role of the excitation at the Fermi surface. In particular they study collective modes of the non-Fermi liquid. A realization of this in the dynamical-source model where the probe-fermion theory originates from the bulk requires a more careful analysis.

Everywhere in this thesis the boundary field theory is at infinitely strong coupling. It would be interesting to analyse finite-coupling effects in the semiholographic model. A particular direction could be to examine the idea put forward in chapter 5 that finite-coupling effects lead to a kinetic term on the boundary. Going beyond the strong coupling limit leads to $1/\lambda$ corrections, where $\lambda = g_{\mathrm{YM}} N_c$ is the 't Hooft coupling and g_{YM} is the coupling of the underlying microscopic gauge theory. Corrections of this order in λ arise when higher-derivative corrections to Einstein gravity are considered in the bulk theory. There are many ways to do this, one of which is including a Gauss-Bonnett term in the gravitational action, which contains fourth-order derivatives of the metric. In this way an extra parameter is introduced which is the coefficient of this term, and the boundary theory can be investigated as a function of it. This was for instance done in the condensed-matter context for 2+1 boundary dimensions in Ref. [99].

As a final remark, we conclude that semiholography has certain appealing features. However, applications of semiholography to condensed matter are still in their infancy. So far no direct quantitative contact with experiment has been made. This is one of the future aims of this line of research. Achieving a direct correspondence with experiments will lead to a more complete understanding of critical quantum liquids. In a more general setting, it can be surprising and amusing to learn that certain phenomena are being described in a very distinct way in high- or low-energy physics. So, there is much to gain from a discussion between the fields of experimental and theoretical condensed-matter physics and string theory. Holographic methods have already played a prime role in encouraging this discussion. Who knows what discoveries and surprises are to be found.

Chapter 2

Free three-dimensional semimetals

In this chapter we present a minimal field-theory toy model of a Dirac "semimetal" that just consists of free Dirac fermions. In section 2.1, the electrical conductivity of a single Dirac point is calculated. Next, in section 2.2 we split up the Dirac point into two Weyl points in a phenomenological way. This allows us to explore some topological properties of the Weyl semimetal, the anomalous Hall effect and the Fermi arc surface states. The purpose of this chapter is twofold. Firstly the simplicity of this chapter allows the reader to get acquainted with the type of calculations done later on. Secondly, it allows us to communicate some of the fascinating properties of Weyl semimetals in the free case, since a treatment of the anomalous Hall effect in the interacting case is beyond the scope of this thesis.

2.1 Electrical conductivity

In this section we compute the electrical conductivity of free three-dimensional semimetals. Employing a relativistic field-theory approach, the free Dirac semimetal with Fermi velocity c is described by the Lagrangian density for a free Dirac field ψ and its conjugate $\bar{\psi} = \psi^\dagger \gamma^0$. We minimally couple it to a nondynamical U(1) gauge field A_μ,

$$\mathcal{L} = -i\hbar\bar{\psi}\left(\not{\partial} - \frac{ie}{\hbar}\not{A}\right)\psi. \tag{2.1}$$

It can be written as $\mathcal{L} = -i\hbar\bar{\psi}\not{\partial}\psi + J^\mu A_\mu/c$, where the fermion charge current is given by

$$J^\mu = -ec\bar{\psi}\gamma^\mu\psi. \tag{2.2}$$

We first compute the current-current correlation function $\langle J^\mu(x)J^\nu(y)\rangle$. In the free case, the expectation value is taken with respect to the free Dirac theory in the absence of the gauge field. Therefore, the current-current correlation function

factorizes into the product of two time-ordered Green's functions of the Dirac field. Explicitly writing the spinor indices, the time-ordered Green's function is given by

$$G_{\beta\alpha}(y-x) = i\Big\langle \psi^\dagger_\alpha(x)\psi_\beta(y)\Big\rangle. \tag{2.3}$$

The sum over all possible contractions of ψ with its conjugate leads to two terms, the first of which is a disconnected contribution that vanishes due to the charge neutrality of the Dirac semimetal. Going to momentum space, the current-current correlation function is given in terms of the second, connected contribution as

$$\begin{aligned}\hbar\Pi^{\mu\nu}(q) &= \frac{1}{c}\int \mathrm{d}^4(x-y)\Big\langle J^\mu(x)J^\nu(y)\Big\rangle e^{-iq\cdot(x-y)} \\ &= e^2 c\int \frac{\mathrm{d}^4k}{(2\pi)^4}\mathrm{Tr}\Big[G(k)\gamma^0\gamma^\mu G(k+q)\gamma^0\gamma^\nu\Big].\end{aligned} \tag{2.4}$$

Here, the trace is over spinor indices, and $G(k)$ denotes the Fourier transform of the time-ordered Green's function from Eq. (2.3), which is a matrix in spinor space. It has SI units of Meter in our conventions, which explains the extra factor of $1/c$. It is convenient to separate the matrix part from the rest of the Green's function, so we define the notation

$$G(k) \equiv \gamma^\lambda\gamma^0\mathcal{G}_\lambda(k). \tag{2.5}$$

In the free case, $\mathcal{G}_\lambda(k) = -k_\lambda/k^2$ where $k^2 = k_\mu k^\mu$, but we keep the Green's function general for now. The expression in Eq. (2.4) can be represented diagrammatically by the bubble diagram in Fig. 2.1.

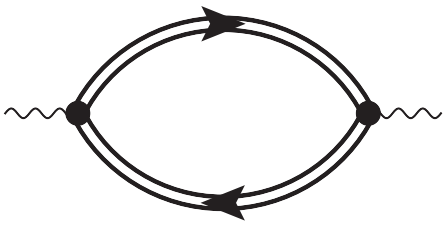

Figure 2.1: Feynman diagram corresponding to Eq. (2.4). The wavy lines denote the external electric field, the double lines denote the fermion Green's function and the circles denote the vertices proportional to $e\gamma^0\gamma^\mu$.

Next, we go to the Matsubara formalism by Wick rotating the frequency ck^0 to $i\omega_n$ and the external frequency cq^0 to $i\omega_b$, where ω_n and ω_b denote fermionic and bosonic Matsubara frequencies, respectively. The Matsubara current-current

correlation function is given by

$$\hbar\Pi^{\mu\nu}(\vec{q}, i\omega_b) = \frac{e^2}{\hbar\beta}\int\frac{\mathrm{d}^3\vec{k}}{(2\pi)^3}\sum_{n=-\infty}^{\infty}\mathrm{Tr}\Big[G(\vec{k}, i\omega_n)\gamma^0\gamma^\mu G(\vec{k}+\vec{q}, i\omega_n + i\omega_b)\gamma^0\gamma^\nu\Big]. \tag{2.6}$$

Here, $\beta = 1/k_BT$ with T the temperature, and $G(\vec{k}, i\omega_n)$ denotes the Matsubara Green's function, that is, the Fourier transform of the imaginary-time-ordered Green's function. From the Matsubara Green's function, the retarded Green's function is obtained by performing a Wick rotation of $i\omega_n$ to $\omega^+ = \omega + i0$. The separation of the Dirac matrix from the rest of the Green's function in Eq. (2.5) does not affect the analytical properties. So we can define a componentwise spectral-weight function that is proportional to the imaginary part of the components of the retarded Green's function $\mathcal{G}_\lambda$, i.e., $\mathcal{A}_\lambda(\vec{k}, \omega) = -\operatorname{Im}\mathcal{G}_\lambda(\vec{k}, \omega^+)/\pi$. Vice versa, the components of the Matsubara Green's function can be conveniently expressed as frequency integrals over the componentwise spectral-weight function, namely,

$$\mathcal{G}_\lambda(\vec{k}, i\omega_n) = \int_{-\infty}^{\infty}\mathrm{d}\omega\frac{\mathcal{A}_\lambda(\vec{k}, \omega)}{i\omega_n - \omega}. \tag{2.7}$$

This can be checked by Wick rotating and taking the imaginary part of Eq. (2.7). Plugging the definition from Eq. (2.7) into the Matsubara current-current correlation function, we obtain

$$\begin{aligned}&\hbar\Pi^{\mu\nu}(\vec{q}, i\omega_b)\\ &= \frac{e^2}{\hbar\beta}\int\frac{\mathrm{d}^3\vec{k}}{(2\pi)^3}\sum_{n=-\infty}^{\infty}\int_{-\infty}^{\infty}\mathrm{d}\omega'\int_{-\infty}^{\infty}\mathrm{d}\omega''\frac{\mathcal{A}_\lambda(\vec{k}, \omega')\mathcal{A}_\rho(\vec{k}+\vec{q}, \omega'')}{(i\omega_n - \omega')\,(i\omega_n + i\omega_b - \omega'')}\mathrm{Tr}\Big[\gamma^\lambda\gamma^\mu\gamma^\rho\gamma^\nu\Big].\end{aligned} \tag{2.8}$$

The frequency integrals commute with the Matsubara sum, so the latter can be performed directly, which yields

$$\frac{1}{\hbar\beta}\sum_{n=-\infty}^{\infty}\frac{1}{(i\omega_n - \omega')\,(i\omega_n + i\omega_b - \omega'')} = \frac{N_f(\omega') - N_f(\omega'')}{i\omega_b + \omega' - \omega''}, \tag{2.9}$$

where $N_f(x) = (1 + e^{\hbar\beta x})^{-1}$ is the Fermi distribution. The conductivity tensor is obtained from the Kubo formula,

$$\sigma^{\mu\nu}(\omega) = -\frac{\Pi^{\mu\nu}(\vec{0}, \omega^+)}{i\omega}, \tag{2.10}$$

where $\Pi^{\mu\nu}(\vec{q}, \omega^+)$ is the retarded current-current correlation function obtained by Wick rotating the external frequency from $i\omega_b$ to $\omega^+ = \omega + i0$. We are primarily interested in the real, dissipative part of the conductivity tensor. This amounts to taking

minus the imaginary part of the integrand, resulting in a factor $-\pi\delta(\omega+\omega'-\omega'')$ from the energy denominator. After integrating over ω'' we consider the spatial components of the conductivity tensor. We also need the standard expression for the trace over four Dirac matrices in 3+1 dimensions,

$$\mathrm{Tr}[\gamma^\lambda\,\gamma^\mu\,\gamma^\rho\,\gamma^\nu] = 4\left(\eta^{\mu\lambda}\eta^{\nu\rho}+\eta^{\nu\lambda}\eta^{\mu\rho}-\eta^{\mu\nu}\eta^{\rho\sigma}\right). \tag{2.11}$$

These steps lead to the following expression for the ii-component of the conductivity tensor

$$\begin{aligned}\mathrm{Re}\,\sigma^{ii}(\omega) = \frac{4\pi e^2}{\hbar\omega}\int\frac{\mathrm{d}^3\vec{k}}{(2\pi)^3}\int_{-\infty}^{\infty}\mathrm{d}\omega'\Big(N_f(\omega')-N_f(\omega'+\omega)\Big)\Big(2\mathcal{A}^i(\vec{k},\omega')\mathcal{A}^i(\vec{k},\omega'+\omega)\\ +\mathcal{A}^0(\vec{k},\omega')\mathcal{A}^0(\vec{k},\omega'+\omega)-\sum_{j=1}^{3}\mathcal{A}^j(\vec{k},\omega')\mathcal{A}^j(\vec{k},\omega'+\omega)\Big),\end{aligned} \tag{2.12}$$

where no sum over the index i is implied. The system is rotationally invariant, so $\sigma^{11}=\sigma^{22}=\sigma^{33}$, i.e., $\sigma^{ii}=\sum_j\sigma^{jj}/3$, and the latter expression is what we consider from now on. Inside the integral, the sum over spatial components just leads to the replacement of $(\mathcal{A}^i)^2$ by $\vec{\mathcal{A}}^2/3$. Thus, the linear combination of components of the spectral-weight function in the integrand of Eq. (2.12) reduces to

$$\mathcal{A}^0(\vec{k},\omega')\mathcal{A}^0(\vec{k},\omega'+\omega)-\frac{1}{3}\vec{\mathcal{A}}(\vec{k},\omega')\cdot\vec{\mathcal{A}}(\vec{k},\omega'+\omega). \tag{2.13}$$

We can rearrange this expression in a more insightful way, separating it into so-called interband and intraband contributions. For this we need the fact that $\vec{\mathcal{A}}$ always points in the direction of $\vec{k}$. This is true in general: both in the free case and the interacting, semiholographic case that is the topic of this thesis. Indeed, as will be derived in chapter 4, the Green's function of an interacting semiholographic Dirac semimetal is in the conventions of this chapter a 4×4 block-diagonal matrix

$$G(k) = -c\frac{ck_\mu+\Sigma_\mu(k)}{\big(ck+\Sigma(k)\big)^2}\gamma^\mu\gamma^0, \tag{2.14}$$

The components of the selfenergy four-vector are specified in Eq. (4.6). What is important at this stage, is that the selfenergy three-vector $\vec{\Sigma}$ points along the direction of $\vec{k}$ due to rotational invariance of the bulk Dirac equation. Thus, the vector $\vec{\mathcal{A}}$ also points in this direction. Combining this with Eqs. (2.5), (2.7) and (2.14), we can define linear combinations of the components of the spectral-weight functions,

$$\mathcal{A}_\pm = \mathcal{A}^0 \pm |\vec{\mathcal{A}}|, \tag{2.15}$$

where the $+(-)$ component corresponds to the conduction (valence) band. Up to the conventional factor $-c$, this coincides with Eq. (4.7) in chapter 4. Suppressing

the momentum dependence for a moment, the integrand Eq. (2.13) can, with the definition in Eq. (2.15), be decomposed as

$$\mathcal{A}^0(\omega')\mathcal{A}^0(\omega'+\omega)-\frac{1}{3}\vec{\mathcal{A}}(\omega')\cdot\vec{\mathcal{A}}(\omega'+\omega)=\frac{1}{3}\Big(\underbrace{\mathcal{A}_+(\omega')\mathcal{A}_-(\omega'+\omega)+\mathcal{A}_-(\omega')\mathcal{A}_+(\omega'+\omega)}_{\text{interband}}$$
$$+\frac{1}{2}\underbrace{\big(\mathcal{A}_+(\omega')\mathcal{A}_+(\omega'+\omega)+\mathcal{A}_-(\omega')\mathcal{A}_-(\omega'+\omega)\big)}_{\text{intraband}}\Big). \tag{2.16}$$

So both interband and intraband transitions contribute to the conductivity, which is finally given by

$$\operatorname{Re}\sigma^{ii}(\omega)=\sigma^{\text{inter}}(\omega)+\sigma^{\text{intra}}(\omega), \tag{2.17}$$

where

$$\begin{aligned}\sigma^{\text{inter}}(\omega)=\frac{4\pi e^2}{3\hbar\omega}\int\frac{\mathrm{d}^3\vec{k}}{(2\pi)^3}\int_{-\infty}^{\infty}\mathrm{d}\omega'\Big(N_f(\omega')-N_f(\omega'+\omega)\Big)\\ \times\Big(\mathcal{A}_+(\omega')\mathcal{A}_-(\omega'+\omega)+\mathcal{A}_-(\omega')\mathcal{A}_+(\omega'+\omega)\Big),\end{aligned} \tag{2.18}$$

and

$$\begin{aligned}\sigma^{\text{intra}}(\omega)=\frac{2\pi e^2}{3\hbar\omega}\int\frac{\mathrm{d}^3\vec{k}}{(2\pi)^3}\int_{-\infty}^{\infty}\mathrm{d}\omega'\Big(N_f(\omega')-N_f(\omega'+\omega)\Big)\\ \times\Big(\mathcal{A}_+(\omega')\mathcal{A}_+(\omega'+\omega)+\mathcal{A}_-(\omega')\mathcal{A}_-(\omega'+\omega)\Big).\end{aligned} \tag{2.19}$$

Note the factor two difference in their prefactors. We have now reproduced the two expressions in Eqs. (4.9) and (4.10) of chapter 4. This is as far as we can go without specifying the spectral-weight functions.

2.1.1 Free case

In this section, the electrical conductivity of the free Dirac semimetal is computed. The Green's function and spectral-weight function are given by

$$G(k)=-\frac{1}{\not{k}}\gamma^0,\qquad \mathcal{A}_\pm(\vec{k},\omega)=c\delta(\omega\mp c|\vec{k}|). \tag{2.20}$$

To get the ii-component of the conductivity in the free case, we plug this into Eq. (2.17). We also go to spherical coordinates and carry out the angular integrals, leading to a factor $1/(2\pi^2)$. Integrating over ω' and writing $r=|\vec{k}|$, we obtain for the intraband contribution

$$\sigma^{\text{intra}}(\omega)=\frac{e^2c^2}{3\pi\hbar\omega}\delta(\omega)\int_0^\infty\mathrm{d}r\,r^2\Big(N_f(cr)-N_f(cr+\omega)+N_f(-cr)-N_f(-cr+\omega)\Big). \tag{2.21}$$

The only nonzero contribution is at zero frequency. Considering the Fermi distributions in the limit $\omega \to 0$ together with the prefactor $1/\omega$, we obtain

$$-\lim_{\omega\to 0}\frac{N_f(cr+\omega)-N_f(cr)}{\omega} = -N_f'(cr) = \frac{\hbar}{4k_BT\cosh^2(y/2)}, \tag{2.22}$$

and the same happens for the other pair of Fermi distributions, because $\cosh^2$ is even under sign changes of its argument. In Eq. (2.22), we have defined the dimensionless variable $y = \hbar cr/(k_BT)$. Then we finally obtain for the intraband contribution

$$\sigma^{\text{intra}}(\omega) = \frac{e^2}{6\pi\hbar c}\left(\frac{k_BT}{\hbar c}\right)^2\delta(\omega)\underbrace{\int_0^\infty \mathrm{d}y\,\frac{y^2}{\cosh^2(y/2)}}_{=2\pi^2/3} = \frac{e^2\pi}{9\hbar c}\left(\frac{k_BT}{\hbar}\right)^2\delta(\omega). \tag{2.23}$$

The intraband contribution is a Drude-like peak with weight T^2. Next, the interband contribution is

$$\begin{aligned}\sigma^{\text{inter}}(\omega) = \frac{e^2c}{3\pi\hbar\omega}\int_0^\infty \mathrm{d}r\,r^2\Big\{&\Big(N_f(cr)-N_f(cr+\omega)\Big)\delta\left(r+\frac{\omega}{2c}\right)\\ &+\Big(N_f(-cr)-N_f(-cr+\omega)\Big)\delta\left(r-\frac{\omega}{2c}\right)\Big\}.\end{aligned} \tag{2.24}$$

Because r is positive, the first term only contributes for $\omega < 0$ and the second term only for $\omega > 0$. It turns out that when ω changes sign the two Fermi distributions are interchanged which gives a minus sign, but the $1/\omega$ in front also changes sign. So in both cases we get the same result, being

$$\begin{aligned}\sigma^{\text{inter}}(\omega) &= \frac{e^2\omega^2}{12\pi\hbar c\omega}\Big[N_f\big(-\frac{\omega}{2}\big)-N_f\big(\frac{\omega}{2}\big)\Big]\\ &= \frac{e^2\omega}{12\pi\hbar c}\tanh\left(\frac{\hbar\omega}{4k_BT}\right).\end{aligned} \tag{2.25}$$

So the total contribution to the ii-components of the free conductivity is given by the sum of the expressions in Eqs. (2.23) and (2.25). Now we have reproduced the result in Eq. (4.8) of chapter 4.

2.1.2 Complex conductivity

So far we have only considered the real part of the conductivity. The imaginary part may be of interest as well in optics, e.g. for light scattering problems and impedance measurements. The experimental relevance of knowing the complete complex conductivity of a Weyl semimetal was pointed out recently [107]. Here we present a calculation of the full complex conductivity of a Dirac semimetal in the free case

at zero temperature. The final result, in Eq. (2.31) below, is given in section 4.3 without a derivation. The real part of the conductivity is finite as we have seen above. Notably, the imaginary part of the conductivity has a quadratic divergence that has to be subtracted, and a logarithmic divergence containing a nonuniversal cutoff parameter. During the renormalization we impose the condition that the current-current correlation tensor is transversal with respect to the four-momentum q^μ.

We go back to Eq. (2.6), and plug in the free Green's function given below Eq. (2.5). At zero temperature, k is a Euclidean four-vector, i.e., $k^2 = k_\mu k^\mu = -(i\omega/c)^2 + \vec{k}^2$, where ω is real. Then, we introduce a Feynman parameter u in the following way,

$$\frac{1}{k^2(k+q)^2} = \int_0^1 \mathrm{d}u \frac{1}{\left((1-u)k^2 + u(k+q)^2\right)^2}, \tag{2.26}$$

and perform a shift $k \to k - uq$ in the integrand, which is allowed as long as the diverging parts are subtracted. This takes care of the angular integrations, and in particular the integral over $k^\mu k^\nu$ is equal to the integral over $k^2\eta^{\mu\nu}/4$, because the odd parts of the integrand drop out. As a consequence, we only have to consider the integral over the length r of the four-vector k in Euclidean spherical coordinates, i.e.,

$$\hbar\Pi^{\mu\nu}(q) = \\ \frac{e^2 c}{2\pi^2} \int_0^1 \mathrm{d}u \int_0^\infty \mathrm{d}r \frac{r^3}{\left(r^2 + u(1-u)q^2\right)^2} \left(-\frac{1}{2} r^2 \eta^{\mu\nu} - u(1-u)\left(2q^\mu q^\nu - q^2\eta^{\mu\nu}\right) \right). \tag{2.27}$$

All terms have a logarithmic divergence. The term with r^2 in the numerator gives rise to an additional quadratic UV divergence. These divergencies can be dealt with using dimensional regularization [108]. However, it is instructive to "manually" regularize the integral with minimal subtraction, which leads to the same result, so we proceed in this way. The quadratic divergence is regulated by subtracting from the term in the integrand with this divergence, its large-momentum behaviour (at $q^2 = 0$), which has the form of $\int_0^\infty \mathrm{d}r\, r$ with an appropriate prefactor. This leads to a factor $q^2\eta^{\mu\nu}$ in front of this term, namely,

$$\begin{aligned} &-\frac{1}{2}\eta^{\mu\nu} \int_0^\infty \mathrm{d}r\, r \left[\frac{r^4}{\left(r^2 + u(1-u)q^2\right)^2} - 1 \right] \\ &= \eta^{\mu\nu} u(1-u)q^2 \int_0^\infty \mathrm{d}r \frac{r^3}{\left(r^2 + u(1-u)q^2\right)^2} + \frac{1}{4}\eta^{\mu\nu} u(1-u)q^2. \end{aligned} \tag{2.28}$$

Plugging this back into Eq. (2.27), we obtain an expression which still has a logarithmic divergence. The upshot is that we have extracted a factor q^2 from the part

with the quadratic divergence. Now we can write the tensor structure of $\Pi^{\mu\nu}$ in the form

$$\Pi^{\mu\nu}(q) = \left(q^2\eta^{\mu\nu} - q^\mu q^\nu\right)\Pi_1(q^2) + q^2\eta^{\mu\nu}\Pi_2. \tag{2.29}$$

Here, Π_2 is a q^2-independent, regular constant and the scalar function $\Pi_1(q^2)$ contains the logarithmic divergence. The latter is dealt with by regulating not $\Pi^{\mu\nu}$ but the scalar functions Π_1 and Π_2, i.e., without the prefactor q^2 and the tensor structure. This time, we regulate by subtracting from Π_1 and Π_2 their value at a fixed, nonzero value of q^2. The Π_2 term is independent of q^2 so it drops out in this subtraction. Of course, when we subtracted the quadratic divergence, we should have added an additional integration constant. The renormalization condition of transversality tells us it is precisely zero. Now, the current-current correlation function is transversal with respect to the four-momentum q^μ, which is required by gauge invariance.

In the function $\Pi_1(q^2)$, the subtraction at a fixed value of q^2 results in a $\log(q^2)$ term as expected. The left-over integral over u gives a factor $1/6$. Ultimately, this yields the following for the renormalized current-current correlation function

$$\hbar\Pi^{\mu\nu}(q) = \frac{e^2 c}{12\pi^2}\left(q^2\eta^{\mu\nu} - q^\mu q^\nu\right)\log\left(\frac{\omega_{\text{exp}}^2}{c^2 q^2}\right), \tag{2.30}$$

where $\omega_{\text{exp}}^2 > 0$ is a subtraction point to be determined by experiment. To obtain the complex conductivity we Wick rotate back to real frequency as $i\omega \to \omega^+ = \omega + i\epsilon$. The complex conductivity then follows from the Kubo formula as

$$\sigma^{xx}(\omega) = \frac{ie^2\omega}{12\pi^2\hbar c}\log\left[-\left(\frac{\omega^+}{\omega_{\text{exp}}}\right)^2\right]. \tag{2.31}$$

Indeed, using $\operatorname{Im}\log(-\omega^2 - i\epsilon\,\operatorname{sign}(\omega)) = -\pi\,\operatorname{sign}(\omega)$, we see that the real part of the above expression is the zero-temperature limit of Eq. (2.25), or equivalently, twice Eq. (1.3), since we are dealing with two coincident Weyl points. The imaginary part of the conductivity is

$$\operatorname{Im}\sigma^{xx}(\omega) = \frac{e^2\omega}{12\pi^2\hbar c}\log\left(\frac{\omega^2}{\omega_{\text{exp}}^2}\right). \tag{2.32}$$

2.2 Nontrivial topology of Weyl semimetal band structure

In this section, instead of the fourfold degenerate Dirac point of a Dirac semimetal, we consider a Weyl semimetal consisting of two twofold degenerate Weyl points with

opposite chirality separated in momentum space. This particular system has a nontrivial topology that is manifest in the nonzero Berry phase of the Weyl points. This has fascinating consequences, such as a nonzero anomalous Hall conductivity and gapless surface states, that are absent in the case of a Dirac semimetal. In this section we first compute the anomalous Hall conductivity, and next we present a simple model exhibiting gapless modes on the surface of a Weyl semimetal.

To obtain a Weyl semimetal from a Dirac semimetal, we have to break either time-reversal symmetry or spatial inversion symmetry, or both. A simple, phenomenological way is to add a term of the form $\psi^\dagger\gamma^0\gamma^\mu\gamma^5\psi$ to the Lagrangian density of Eq. (2.1) i.e.,

$$\mathcal{L} = \bar{\psi}\left(-i\hbar\partial\!\!\!/ - eA\!\!\!/ + \hbar b\!\!\!/\gamma^5\right)\psi, \tag{2.33}$$

where b^μ is a constant and real four-vector having the dimensions of a wavenumber, and γ^5 anticommutes with all other Dirac matrices. A nonzero four-vector b^μ lifts the fourfold degeneracy at the Dirac point, resulting into two Weyl points that are separated in energy-momentum space by an amount $2b^\mu$. The γ^5 makes sure that each Weyl point is shifted in the opposite direction in energy-momentum space. A nonzero b^0 breaks spatial inversion (parity) symmetry, which yields a shift in energy of the two Weyl points, i.e., b^0 acts as a chiral chemical potential. A nonzero spatial vector $\vec{b}$ breaks time-reversal symmetry and separates the Weyl cones in momentum space in the spatial direction, while keeping the energy degenerate. These two cases are shown in Fig. 2.2. Both situations can in principle occur in Weyl semimetals in nature. The Weyl semimetal realized in TaAs has broken inversion symmetry [109].

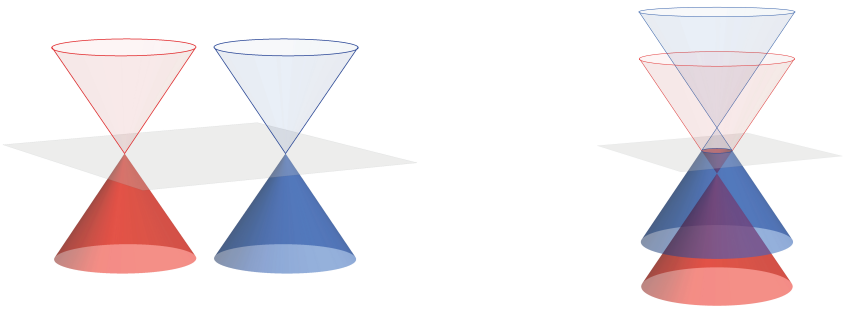

(a) broken TR (b) broken I

Figure 2.2: Weyl semimetal consisting of two Weyl points in the case of broken TR symmetry (left) and broken I symmetry (right). Shown is the dispersion in each case, the red and blue colours denote the two chiralities, and zero energy is denoted by the grey plane. Occupied bands are indicated by a dark colour, whereas the light colour indicates the band is empty.

2.2.1 Anomalous Hall conductivity

In this section we show that a time-reversal symmetry-breaking term in the Lagrangian results in a nonzero anomalous Hall conductivity for the free Weyl semimetal, that is proportional to $\vec{b}$. Indeed, in the case $\vec{b} = 0$ where we retrieve the Dirac semimetal, the Hall conductivity is zero. The calculation is very similar to the 4×4 calculation in section 2.1, up to the point where the Green's functions are specified. The difference in the Green's functions is the matrix structure which now comprises of two distinct 2×2 subsectors. The noninteracting inverse Matsubara Green's function of the Weyl semimetal is

$$G^{-1}(k) = \gamma^0 \left(\not{k} + \not{b}\gamma^5 \right) = \begin{pmatrix} -k_0 \mathbb{1}_2 - \vec{\sigma} \cdot \left(\vec{k} + \vec{b} \right) & 0 \\ 0 & -k_0 \mathbb{1}_2 + \vec{\sigma} \cdot \left(\vec{k} - \vec{b} \right) \end{pmatrix}, \quad (2.34)$$

where $k^0 = i\omega_n / c$. Inverting the matrix structure leads to

$$G(k) = \begin{pmatrix} G^+(k) & 0 \\ 0 & G^-(k) \end{pmatrix}, \quad (2.35)$$

where we defined the 2×2 nodal Green's functions G^α as

$$G^\alpha(k) = \frac{-k_0 \mathbb{1}_2 + \alpha \vec{\sigma} \cdot \left(\vec{k} + \alpha \vec{b} \right)}{\left(-k_0 - |\vec{k} + \alpha \vec{b}| \right) \left(-k_0 + |\vec{k} + \alpha \vec{b}| \right)}, \quad (2.36)$$

with $\alpha = \pm 1$. Now, starting from Eq. (2.6) we find the following expression for the off-diagonal spatial components of the current-current correlation tensor

$$\hbar \Pi^{ij}(\vec{0}, i\omega_b) = \frac{e^2}{\hbar \beta} \int \frac{\mathrm{d}^3 \vec{k}}{(2\pi)^3} \sum_{n=-\infty}^{\infty} \sum_{\alpha} \mathrm{tr} \Big[G^\alpha(\vec{k}, i\omega_n) \sigma^i G^\alpha(\vec{k}, i\omega_n + i\omega_b) \sigma^j \Big]. \quad (2.37)$$

Analogous to the 4×4 calculation in section 2.1, it is possible to separate the 2×2 Pauli matrix structure from the rest of the Green's function, just like in Eq. (2.5). Now, the trace over Pauli matrices can be performed. This results in terms similar to the ones in Eq. (2.11) that are symmetric in the external indices i and j and contribute to the diagonal part of the conductivity. We also get an additional term that is antisymmetric in i and j and is responsible for the Hall conductivity. Focusing on this term from now on, we take the antisymmetric part of the current-current correlation tensor. An intermediate result is

$$\begin{aligned} \hbar \Pi^{[ij]}(\vec{0}, \omega^+) = 2ie^2 \int \frac{\mathrm{d}^3 \vec{k}}{(2\pi)^3} \int_{-\infty}^{\infty} \mathrm{d}\omega' \int_{-\infty}^{\infty} \mathrm{d}\omega'' \frac{N_f(\omega') - N_f(\omega'')}{\omega^+ + \omega' - \omega''} \\ \times \sum_{\alpha = \pm 1} \sum_{\ell = 1}^{3} \alpha \epsilon^{ij\ell} \left(\delta_0^\mu \delta_\ell^\nu - \delta_0^\nu \delta_\ell^\mu \right) A_\mu^\alpha(\vec{k}, \omega') A_\nu^\alpha(\vec{k}, \omega''), \end{aligned} \quad (2.38)$$

where the componentwise spectral-weight functions are given by

$$A_0^\alpha(\vec{k},\omega) = \frac{c}{2}\left(\delta(\omega - c|\vec{k}+\alpha\vec{b}|) + \delta(\omega + c|\vec{k}+\alpha\vec{b}|)\right), \tag{2.39}$$

and

$$A_i^\alpha(\vec{k},\omega) = \frac{c(k_i+\alpha b_i)}{2|\vec{k}+\alpha\vec{b}|}\left(\delta(\omega - c|\vec{k}+\alpha\vec{b}|) - \delta(\omega + c|\vec{k}+\alpha\vec{b}|)\right). \tag{2.40}$$

The Hall conductivity is given by

$$\begin{aligned}\mathrm{Re}\,\sigma^{[ij]}(\omega) = &-\sum_{\ell=1}^{3}\frac{(ec)^2\,\epsilon^{ij\ell}}{2\hbar}\int\frac{\mathrm{d}^3\vec{k}}{(2\pi)^3}\sum_{\alpha=\pm1}\frac{\alpha\left(\vec{k}+\alpha\vec{b}\right)_\ell}{c(\vec{k}+\alpha\vec{b})^2}\\ &\times\left(N_f(-c|\vec{k}+\alpha\vec{b}|) - N_f(c|\vec{k}+\alpha\vec{b}|)\right)\left(\mathcal{P}\frac{1}{\omega-2c|\vec{k}+\alpha\vec{b}|} - \mathcal{P}\frac{1}{\omega+2c|\vec{k}+\alpha\vec{b}|}\right).\end{aligned} \tag{2.41}$$

For $\omega = 0$ and $T = 0$, in which case Eq. (2.41) reduces to

$$\mathrm{Re}\,\sigma_{\mathrm{dc}}^{[ij]} = \sum_{\ell=1}^{3}\frac{(ec)^2}{2\hbar}\epsilon^{ij\ell}\int\frac{\mathrm{d}^3\vec{k}}{(2\pi)^3}\sum_{\alpha=\pm1}\frac{\alpha c\left(\vec{k}+\alpha\vec{b}\right)_\ell}{c^3|\vec{k}+\alpha\vec{b}|^3}, \tag{2.42}$$

the momentum integral can be performed analytically. However, the issue arises that the momentum integral is not absolute convergent [1]. It goes over two singularities, a monopole and antimonopole of Berry field strength, that cancel each other in a subtle way, resulting in a finite end result. Choosing coordinates such that $\vec{b} = b_\ell\hat{\ell}$ lies along the ℓ-direction, we only get a correct result if a subsequent variable substitution does not mix up the ℓ-direction with the i- and j-directions in $\mathrm{d}^3\vec{k} = \mathrm{d}k_\ell\mathrm{d}k_j\mathrm{d}k_i$. For instance, we can use cylindrical coordinates,

$$k_i = r\cos(\phi), \qquad k_j = r\sin(\phi), k_\ell = h, \tag{2.43}$$

so that $\mathrm{d}^3\vec{k} = \mathrm{d}h\mathrm{d}\phi\mathrm{d}r\,r$, and $|\vec{k}+\alpha\vec{b}| = \sqrt{r^2+(h+\alpha b_\ell)^2}$. Thus, the integral can be rewritten as

$$\begin{aligned}\mathrm{Re}\,\sigma_{\mathrm{dc}}^{[ij]} = &\sum_{\ell=1}^{3}\frac{e^2\epsilon^{ij\ell}}{2\hbar(2\pi)^3}\\ &\times\int_{-\infty}^{\infty}\mathrm{d}h\int_0^{2\pi}\mathrm{d}\phi\int_0^{\infty}\mathrm{d}r\,r\left(\frac{h+b_\ell}{(r^2+(h+b_\ell)^2)^{3/2}} - \frac{h-b_\ell}{(r^2+(h-b_\ell)^2)^{3/2}}\right).\end{aligned} \tag{2.44}$$

The angular integration is trivial and gives 2π. The integral over r can also be done. Finally, we obtain

$$\begin{aligned}\operatorname{Re}\sigma_{\mathrm{dc}}^{[ij]} &= \sum_{\ell=1}^{3}\frac{e^2}{2\hbar(2\pi)^2}\epsilon^{ij\ell}\int_{-\infty}^{\infty}\mathrm{d}h\left(\frac{h+b_\ell}{|h+b_\ell|}-\frac{h-b_\ell}{|h-b_\ell|}\right)\\ &= \sum_{\ell=1}^{3}\frac{e^2}{2\hbar(2\pi)^2}\epsilon^{ij\ell}\int_{-\infty}^{\infty}\mathrm{d}h\left(\operatorname{sign}\left(h+b_\ell\right)-\operatorname{sign}\left(h-b_\ell\right)\right)\\ &= \sum_{\ell=1}^{3}\frac{e^2}{\hbar(2\pi)^2}\epsilon^{ij\ell}\int_{-b_\ell}^{b_\ell}\mathrm{d}h.\end{aligned} \tag{2.45}$$

Thus, the anomalous Hall conductivity of a Weyl semimetal with two Weyl cones is

$$\operatorname{Re}\sigma_{\mathrm{dc}}^{[ij]} = \frac{e^2}{2\pi^2\hbar}\sum_{\ell=1}^{3}\epsilon^{ij\ell}b_\ell. \tag{2.46}$$

It coincides with the result in the literature [17]. The anomalous Hall conductivity is linearly proportional to the time-reversal symmetry breaking perturbation, the momentum-space separation between the Weyl nodes. It vanishes for the time-reversal-invariant Dirac semimetal which has $\vec{b}=0$. The three-dimensional result is very reminiscent of the universal, frequency-independent value found one dimension lower in graphene, $\operatorname{Re}\sigma^{xy}=e^2/h$ per valley [110, 111]. However, in three spatial dimensions the anomalous Hall conductivity is quasi-universal, i.e., it is independent of the Fermi velocity (c in this model), but the vector $\vec{b}$ may vary in different Weyl semimetals. This quasi-universality is a consequence of ignoring internode scattering by taking $\omega=T=0$, which is the extreme limit of $\omega \ll c|\vec{b}|$ and $k_BT \ll \hbar c|\vec{b}|$. In a more realistic setting, the Weyl cones will be coupled at high enough energy, leading to nonuniversal corrections. In general, we expect the result in Eq. (2.46) to be valid at low energies, i.e., as long as $\hbar c|\vec{b}|/\Lambda \gg 1$, where Λ denotes the lowest energy scale associated to scattering between the Weyl nodes.

In the absence of scattering between the Weyl nodes, the diagonal conductivity of the total system is just the sum of the conductivity per node, so it is independent of $\vec{b}$.

2.2.2 Chiral surface states and Fermi arc

One of the fascinating properties of a Weyl semimetal, that reflects the topological nature of these systems, is the existence of gapless modes on its boundary. In Weyl semimetals with broken time-reversal symmetry, this phenomenon is manifest in the so-called Fermi arcs, that is, line segments in momentum space where gapless bound states exist at the surface of a Weyl semimetal [112, 113]. It is insightful to look a

little closer at these surface states. In this section, we compute the bound states on the boundary of a Weyl semimetal, which is a topological state of matter, to a Dirac semimetal, which is trivial. The setup in this section is one of the simplest in which Fermi arcs can be theoretically realized. The calculations presented here are fully based on Ref. [22] and follow this paper closely. See e.g. Ref. [114] for a calculation of the Fermi arcs in the case of broken I symmetry.

The idea is to find solutions of the Dirac equation with boundary conditions that simulate the surface of the Weyl semimetal, and look for bound states. We start by solving the eigenvalue equation

$$\hat{H}\Psi(\vec{x}) = E\Psi(\vec{x}), \tag{2.47}$$

with the Hamiltonian corresponding to the Lagrangian density in Eq. (2.33) at zero gauge field, but taking into account a nonzero Dirac mass m,

$$\hat{H} = \hbar c\gamma^0\vec{\gamma}\cdot\left(i\vec{\nabla} - \gamma^5\vec{b}\right) - i\gamma^0 mc^2, \tag{2.48}$$

Again, there are two Weyl nodes in momentum space, and the time-reversal symmetry breaking vector $\vec{b}$ represents the shift in momentum space between the two Weyl nodes. The Dirac mass m makes the Hamiltonian off-diagonal, coupling the two chiral components and creating a gap for zero time-reversal-symmetry breaking. However, for nonzero $\vec{b}$, certain values of m do not spoil the fact that there are two nondegenerate gapless points. In order to understand this, we diagonalize the Hamiltonian at $m \neq 0$. Setting $\vec{b} = (0, 0, b)$ with $b > 0$, the four eigenvalues are

$$E = \pm\hbar c\sqrt{k_x^2 + k_y^2 + \left(b \pm \sqrt{k_z^2 + \hat{m}^2}\right)^2}, \tag{2.49}$$

with $\hat{m} = mc/\hbar$. Each unique choice of two signs corresponds to a single eigenvalue. The two eigenvalues with the upper sign under the square root are fully gapped. Those two eigenvalues with the lower sign under the square root are gapped for $b^2 < \hat{m}^2$. However, they are gapless for $b^2 > \hat{m}^2$, at the points $k_z = \pm\sqrt{b^2 - \hat{m}^2}$. This is shown in Fig. 2.3. Thus, a nonzero value of m causes a renormalization of the shift in momentum space $\vec{b} \to \hat{b}\sqrt{b^2 - \hat{m}^2}$, where $\hat{b} = \vec{b}/b$. Linearizing the Hamiltonian close to these effective Weyl points, we obtain the low-energy Weyl Hamiltonian

$$\hat{H} = \begin{pmatrix} \hbar c\vec{\sigma}\cdot\left(\vec{k} + \hat{b}\sqrt{b^2 - \hat{m}^2}\right) & 0 \\ 0 & -\hbar c\vec{\sigma}\cdot\left(\vec{k} - \hat{b}\sqrt{b^2 - \hat{m}^2}\right) \end{pmatrix}. \tag{2.50}$$

The states corresponding to the gapless bands are not anymore eigenstates of γ^5, but of an effective chirality matrix, whose form is not important for us.

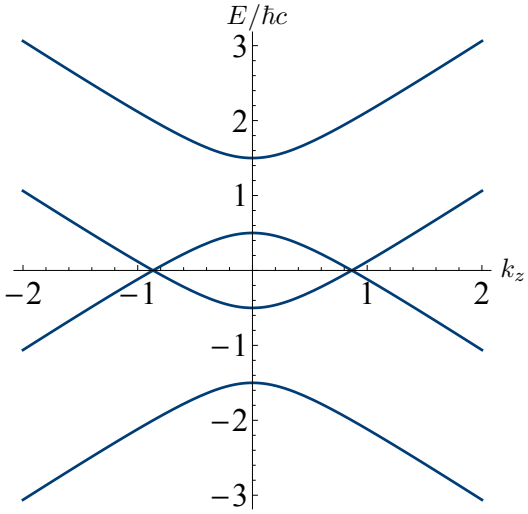

Figure 2.3: Energy bands of the Weyl Hamiltonian from Eq. (2.49) with $b = 1$ and $\hat{m} = 1/2$ in arbitrary units, plotted at $k_x = k_y = 0$. There are two Weyl points at $k_z = \pm\sqrt{3}/2$.

Now that the effect of m is understood, we continue solving Eq. (2.47) by specifying boundary conditions. To simulate the edge of the Weyl semimetal, we take $\vec{b} = (0, 0, b\theta(x))$. So there is a breaking of time-reversal symmetry in the z-direction for $x > 0$, and none for $x < 0$, i.e., there we have the degenerate cones of a Dirac semimetal. We take $0 < \hat{m}^2 < b^2$ in both regions so that the Dirac bulk is gapped, and the Weyl bulk contains two gapless Weyl nodes with a renormalized momentum-space separation $2\sqrt{b^2 - \hat{m}^2}$ in the z-direction. The boundary between the Dirac and Weyl semimetal regions lies in the yz-plane. The solution is separable, so the solution parallel to the boundary, in the y- and z-direction, is given by a plane wave. Writing the full wavefunction as

$$\Psi(\vec{x}) = e^{ik_y y + ik_z z}\psi(x), \tag{2.51}$$

the problem is reduced to finding the 4-component wavefunction $\psi(x)$ in the direction orthogonal to the boundary. It is a solution to the differential equation

$$\partial_x \psi(x) = \tilde{H}\psi(x), \tag{2.52}$$

where $\tilde{H} = -i\gamma^0\gamma^1[E + \hbar c\gamma^0(\gamma^2 k_y + \gamma^3 k_z + \gamma^3\gamma^5 b) + i\gamma^0 mc^2]/\hbar c$. The system can be solved by diagonalizing $\tilde{H}$, and using an exponential Ansatz for every component of ψ. Then the solution is given by a linear combination of the four eigenvectors $\vec{u}_i$

of $\tilde{H}$, multiplied by the exponent of the corresponding eigenvalues λ_i times x, i.e.,

$$\psi(x) = \sum_{i=1}^{4} A_i e^{\lambda_i x} \vec{u}_i. \tag{2.53}$$

From now on, we use a notation where the subscript $>$ denotes the Weyl region in position space, i.e. $x > 0$, and where the subscript $<$ denotes the Dirac region, $x < 0$. For $x > 0$, there are four distinct eigenvalues of $\tilde{H}$, namely,

$$\pm\sqrt{-\hat{E}^2 + k_y^2 + \left(\pm b + \sqrt{k_z^2 + \hat{m}^2}\right)^2} \equiv \pm\lambda_>^{\pm}, \tag{2.54}$$

with $\hat{E} = E/\hbar c$. For $x < 0$ there are only two unique eigenvalues,

$$\pm\sqrt{-\hat{E}^2 + k_y^2 + k_z^2 + \hat{m}^2} \equiv \pm\lambda_<. \tag{2.55}$$

Next to the eigenvalues of $\tilde{H}$, we also need the corresponding eigenvectors $\vec{u}_{>,i}$ and $\vec{u}_{<,i}$, and normalize them according to the normalization condition $\vec{u}_i^{\dagger} \cdot \vec{u}_i = 1$, so that the wave-function is a probability density normalized to 1.

Surface states are bound states localized at $x = 0$, so we look for real and negative combinations of $\lambda_i x$. Discarding the solutions that blow up at $|x| \to \infty$ amounts to setting the coefficients of the eigenvectors corrsponding to eigenvalues $-\lambda_<$ and $+\lambda_>^{\pm}$ to zero. Then, the solution $\psi(x)$ from Eq. (2.53) in both regions becomes

$$\begin{aligned} \psi_>(x) &= A_1 e^{-\lambda_>^{-} x}\ \vec{u}_{>,1} + A_3 e^{-\lambda_>^{+} x}\ \vec{u}_{>,3}, \\ \psi_<(x) &= e^{\lambda_< x}\Big(B_3\ \vec{u}_{<,3} + B_4\ \vec{u}_{<,4}\Big). \end{aligned} \tag{2.56}$$

There are four unknown coefficients, A_1, A_3, B_3 and B_4, and the energy $\hat{E}$ is also unknown. We also have four equations, namely the matching equations corresponding to continuity of the wavefunction at $x = 0$, i.e., $\psi_<(0) = \psi_>(0)$. These four matching equations will give us three of the four coefficients, and the energy. The fourth coefficient can then be determined by normalizing the wave-function, i.e.,

$$\int_{-\infty}^{\infty} \mathrm{d}x\ \psi^{\dagger}(x)\psi(x) = 1, \tag{2.57}$$

assuming that the plane waves in the y- and z-directions are properly normalized. Writing the matching equations in matrix form as

$$M \cdot (A_1, A_3, B_3, B_4)^T = 0, \tag{2.58}$$

it is clear that we just have to find those values of $\hat{E}$ that make $\det(M) = 0$. This has to be done numerically, as $\det(M)$ does not only contain fourth powers but also

square roots of $\hat{E}$. It turns out that there is a solution with dispersion $\hat{E} = k_y$ for the region in parameter space $b > \sqrt{k_z^2 + \hat{m}^2}$, where $\lambda_>^- = b - \sqrt{k_z^2 + \hat{m}^2}$ is real, and where $\lambda_>^+$ and $\lambda_<$ are also real. Therefore, the corresponding wavefunction given by Eq. (2.56) decays exponentially on both sides of the surface at $x = 0$, and is thus localized at the surface. This is what we interpret as a surface state. Furthermore, it is chiral because its dispersion comes only with one sign, i.e., $\hat{E} = -k_y$ is not a solution. For completeness, we write down the surface-state wavefunction,

$$\psi(x) = A_1 \frac{\exp\left[\left(-b\theta(x) + \sqrt{k_z^2 + \hat{m}^2}\right) x\right]}{2\sqrt{1 + \frac{k_z}{\hat{m}^2}\left(k_z - \sqrt{k_z^2 + \hat{m}^2}\right)}} \begin{pmatrix} \frac{1}{\hat{m}}\left(\sqrt{k_z^2 + \hat{m}^2} - k_z\right) \\ \frac{i}{\hat{m}}\left(\sqrt{k_z^2 + \hat{m}^2} - k_z\right) \\ i \\ 1 \end{pmatrix}. \tag{2.59}$$

So the spinor structure is the same in both regions, the only difference is the factor multiplying x in the exponent. Finally, normalization of the total wavefunction results in

$$|A_1| = \sqrt{-\frac{2}{b}\sqrt{k_z^2 + \hat{m}^2}\left(-b + \sqrt{k_z^2 + \hat{m}^2}\right)}. \tag{2.60}$$

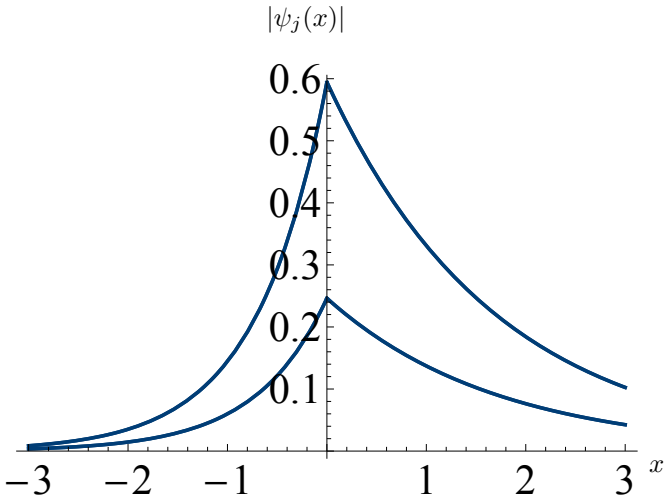

Figure 2.4: Absolute value of the components ψ_j with $j = 1, \cdots, 4$ of the wavefunction in Eq. (2.59) as a function of x, for $b = 2$, $\hat{m} = 1$ and $k_z = 1$ in arbitrary units.

The wavefunction is plotted in Fig. 2.4. The fact that its derivative is discontinuous at the boundary is due to usage of the low-energy approximation for the Hamiltonian in this calculation.

Let us comment on what happened. After solving the eigenvalue problem Eq. (2.47) with the boundary conditions discussed above, we found one surface state, i.e., a localized state around $x = 0$ that propagates in the yz-plane. This surface state is gapless and chiral, having dispersion $E = \hbar c k_y$. Furthermore, it exists only in a certain region in momentum space, where $|k_z| < \sqrt{b^2 - \hat{m}^2}$. The locus $\{\vec{k} | k_y = 0, |k_z| < \sqrt{b^2 - \hat{m}^2}\}$ is the so-called "Fermi-arc" region of momentum space. This Fermi arc lies precisely in between the two bulk Weyl cones. Outside the Fermi-arc region, the parameters λ in the exponents of the surface state become purely imaginary, which means that there is scattering with the bulk states. Indeed, for those values the dispersion relation of the would-be surface state lies inside the bulk Weyl cones and there are no well-defined surface states. The dispersion relation of the total system including the surface state is shown in Fig. 2.5.

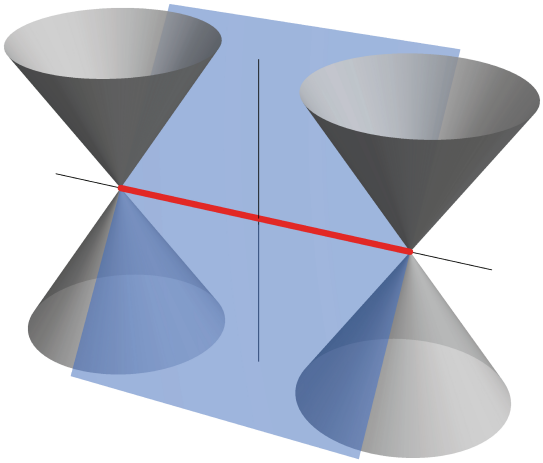

Figure 2.5: Dispersion relation of the bulk (gray) and the surface state (blue). The red line is the Fermi arc at zero energy.

To conclude, in this chapter we discussed a toy model for a three-dimensional semimetal. It served to illustrate in a simple case the conductivity calculation that is done in chapter 4. Furthermore, it is an opportunity to show some of the interesting properties of Weyl and Dirac semimetals. The anomalous Hall effect and surface states will not be discussed further in this thesis. Semiholographic results for these quantities are expected in future work.

Chapter 3

Holographic models for undoped Weyl semimetals

Abstract — We continue our recently proposed holographic description of single-particle correlation functions for four-dimensional chiral fermions with Lifshitz scaling at zero chemical potential, paying particular attention to the dynamical exponent $z = 2$. We present new results for the spectral densities and dispersion relations at nonzero momenta and temperature. In contrast to the relativistic case with $z = 1$, we find the existence of a quantum phase transition from a non-Fermi liquid into a Fermi liquid in which two Fermi surfaces spontaneously form, even at zero chemical potential. Our findings show that the boundary system behaves like an undoped Weyl semimetal.

3.1 Introduction

Over the past years, the AdS/CFT correspondence has become a more and more popular and widespread tool which offers the opportunity to apply ideas from string theory to realistic materials studied in condensed-matter physics, see e.g. [65, 66, 116–118] and references therein. More specifically, it is potentially very useful when considering strongly coupled or critical condensed matter, which is generically not possible to describe within perturbation theory. However, in the context of the AdS/CFT correspondence these systems can be understood and investigated more conveniently using a dual theory in a higher-dimensional curved spacetime, i.e., in the framework of general relativity. Most commonly, the duality exists between a weakly coupled, classical gravity theory in a curved anti-de Sitter (AdS) spacetime

This chapter is published as *Holographic models for undoped Weyl semimetals*, U. Gursoy, V. Jacobs, E. Plauschinn, H. Stoof, and S. Vandoren, J. High Energy Phys. **04** (2013) 217 [115].

on the one hand, and a strongly coupled, conformal field theory (CFT) living on the flat boundary of the AdS spacetime on the other hand. Such a conformal field theory describes for example a quantum critical point of the condensed-matter system under consideration, and the observables that are most readily available from the AdS/CFT correspondence are usually correlation functions of the *composite* operators that classify the conformal field theory. For our purposes, most relevant are correlators of fermionic operators, since they may show Fermi or non-Fermi liquid-like behaviour most easily [64, 105, 119–121].

However, in condensed-matter physics it is more natural to think in terms of fermionic *single-particle* operators, i.e., creation and annihilation operators in a Fock space, that satisfy the following (equal-time) anticommutation relations

$$\left[\psi_\alpha(\vec{x},t),\psi^\dagger_{\alpha'}(\vec{x}',t)\right]_+ = \delta(\vec{x}-\vec{x}')\delta_{\alpha,\alpha'} \ , \tag{3.1}$$

where α labels the spin of the electron. Furthermore, in experiments on condensed-matter systems, the quantity that is measured is essentially always related to *single-particle* or *two-particle* correlation functions and not to the above-mentioned composite operators. For example, the retarded single-particle correlation or Green's function G_R is measurable in electronic systems using angle-resolved photoemission spectroscopy (ARPES). For this reason, we are interested in finding G_R of a strongly interacting condensed-matter system using holographic methods. Inspired by previous work on this topic, such as [72] and [68, 122], we have shown recently how the usual holographic prescription can be modified in such a manner that it allows for the construction of the retarded *single-particle* Green's function [71]. In a sense, our method can be seen as a bulk derivation of the semiholographic description advocated in [68].

A crucial consequence of the anticommutation relations in equation (3.1) is the existence of a sum rule for the corresponding single-particle two-point correlation function, given by

$$\frac{1}{\pi}\int_{-\infty}^{+\infty} \mathrm{d}\omega \ \mathrm{Im}\left[G_{R;\alpha,\alpha'}(\vec{k},\omega)\right] = \delta_{\alpha,\alpha'} \ . \tag{3.2}$$

This sum rule is essential in determining whether the quantity under consideration is the correlator of a single-particle or a composite operator, and therefore plays a central role in our construction.

The quantum critical points described by the AdS/CFT correspondence are characterized by their dynamical scaling exponent z. In the usual correspondence, an anti-de Sitter background leads to a quantum critical point with relativistic scaling, i.e., $z = 1$. But from a condensed-matter perspective we are also interested in quantum critical points that have a dynamical scaling exponent different from

one. To achieve this, the usual anti-de Sitter background is generalized into a so-called Lifshitz background, which leads to a nonrelativistic, i.e., $z \neq 1$ scaling on the boundary [123]. Nonzero-temperature effects can then be studied by placing a black brane in the Lifshitz spacetime [124], see also [125] for a more recent discussion. The pure Lifshitz geometry without a black brane develops singularities due to diverging tidal forces [126]; as a result the zero-temperature limit might become ill-defined[9]. While this could be of possible concern for our analysis, our findings show that the fermionic Green's function is well defined at zero temperature and the limit $T \to 0$ is smooth, so at least the spectral-weight function for fermions does not suffer from any singularities.

In [71] we have described how to construct the retarded Green's function of a strongly interacting, but particle-hole symmetric system of chiral fermions with an arbitrary dynamical exponent z using a Lifshitz black-brane background. The aim of the present paper is to analyse the physics that follows from our prescription. In particular, we calculate the retarded single-particle Green's function in various cases, at zero and nonzero temperatures, and present the corresponding spectral-weight function and dispersion relations. Although we give some results for $z = 1$, we mostly focus on the case $z = 2$ and four boundary spacetime dimensions. With this number of dimensions, the boundary fermions are Weyl fermions and the boundary system behaves like an interacting Weyl semimetal. A semimetal is a gapless semiconductor. In addition, a Weyl semimetal [112, 129] is a semimetal with touching valence and conduction bands based on chiral two-component fermions that in the noninteracting limit and at low energies, satisfy the Weyl equation $\pm\vec{\sigma} \cdot \vec{k}\,\psi = E\,\psi$. Here, the $\pm$ denotes the chirality of the fermion. Because the total system has to be chirality invariant, the most simple realizations of such a Weyl semimetal considered in the literature usually contain two of such linear-dispersion cones with opposite chirality, separated in momentum space [129]. The single-particle propagator presented here represents the physics of one of these chiral cones. Since the holographic boundary theory is that of Weyl fermions, and one cannot write down mass terms for Weyl fermions, the system will automatically be gapless at zero chemical potential. Due to the Weyl character of the holographic boundary fermions, the topology of the band structure is therefore protected, just like in Weyl semimetals.

We would like to stress that holography is employed in a bottom-up manner in this paper. That is, the holographic model is an effective low-energy theory, satisfying the above definition of a Weyl semimetal, whereas the microscopic structure of the actual condensed-matter system remains hidden. Of course, all holographic AdS/CMT models have this latter feature in common. We just assume that the Weyl semimetal under consideration leads to a low-energy theory that is strongly coupled, chiral and

[9] See however [127, 128] for possible resolutions within string theory.

scale invariant. The advantage of a bottom-up approach is that we can explore a range of possible situations.

In this paper, we are studying the properties of the ground state of such a holographic model for a semimetal at zero doping, so there is a zero total charge density. But as will be discussed, this ground state has in fact very interesting properties. In particular, zero chemical potential corresponds to particle-hole symmetric systems, and there are many-body correlations due to the possibility of creating particle-hole pairs. This indicates that we are not describing a single fermionic excitation, but a fermionic many-body problem. By computing the momentum distribution of the particles and holes, we find for $z \neq 1$ that our holographic model for a Weyl semimetal contains a quantum phase transition between a non-Fermi-liquid phase and a Fermi-liquid phase with two Fermi surfaces, one for the particles and one for the holes, even at zero doping. In this phase, there is a nonzero density of both particles and holes, and conduction can take place.

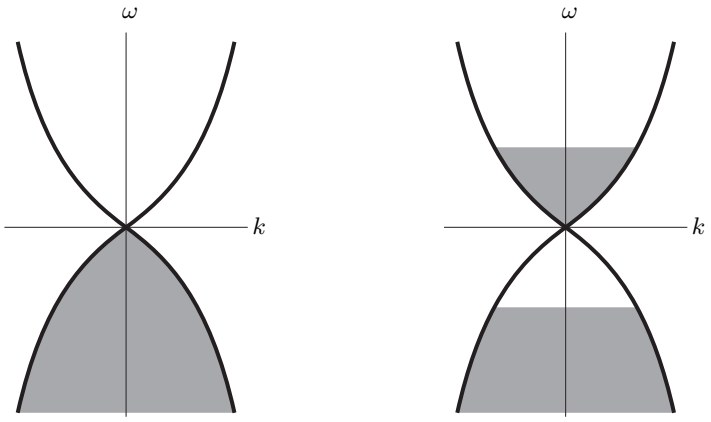

(a) $\lambda > 0$ **(b)** $\lambda < 0$

Figure 3.1: An idealized picture of the ground state that we find for $\lambda > 0$ and $\lambda < 0$. Grey areas refer to filled energy levels. In this picture, we only show the effect of the interactions on the occupation numbers and not on the dispersion relations.

The scale set by the Fermi surface is determined by an appropriate combination of dimensionless parameters λ and g that enter in our prescription for the Green's function on the holographic boundary [71], and the quantum critical point is at $\lambda = 0$. One can think of $1/\lambda$ as a spin-orbit coupling constant and of g as an effective interaction parameter coupling the elementary fermion to the conformal field theory. These parameters are not present in the standard formulation of holography, but enter our holographic prescription for the fermionic single-particle Green's function.

We discuss the nature of these parameters in more detail in the next section.

The phase transition that takes place is schematically illustrated in Fig. 3.1, where we show the noninteracting band structure and how it is populated in the ground state of each phase. In particular, for $\lambda > 0$ the conduction band is empty and the valence band is completely filled, whereas for $\lambda < 0$ the conduction band contains a Fermi sea of particles and the valence band a Fermi sea of holes. Note that we present here an idealized picture that neglects the renormalization of the Fermi surfaces involved, which is discussed at length in this paper.

The layout of the paper is as follows. In section 3.2, we briefly summarize some basic formulas from [71] that are needed here. In section 3.3, we present analytic and numerical results for the single-particle spectral function for the cases $z = 1$ and $z = 2$. In section 3.4 we consider the single-particle momentum distribution, and describe properties of the quantum phase transition and the Fermi liquid involved, that does allow for well-defined but strongly renormalized quasiparticles and quasiholes near the two Fermi surfaces. The main part of the paper ends with conclusions in section 3.5. Finally, there are a number of appendices which contain our conventions and give more details about the calculations.

3.2 Single-particle Green's function for Lifshitz fermions

In this section, we determine solutions to the Dirac equation in a Lifshitz spacetime, from which we construct the retarded fermionic single-particle Green's function. To keep the paper self-contained, we start by defining our notation and conventions. Readers who are only interested in the result of the calculation may skip directly to equation (3.13). Further details on the derivation can be found in the appendices, in particular, for remarks on how to switch from natural to SI units we would like to refer to appendix 3.A.1. Some of the results in this section have already appeared in more detail in our previous work [71], other related work on fermions in Lifshitz backgrounds can be found in [130–132].

We begin by specifying the gravitational background metric of a Lifshitz black brane [124], i.e.,

$$\mathrm{d}s^2 = -V^2(r)\, r^{2z}\mathrm{d}t^2 + \frac{\mathrm{d}r^2}{r^2\, V^2(r)} + r^2\mathrm{d}\vec{x}^2 \ , \qquad V^2(r) = 1 - \left(\frac{r_h}{r}\right)^{d+z-1}, \tag{3.3}$$

where d denotes the number of spatial dimensions. The extra spatial coordinate r runs from the horizon at $r = r_h$ to the boundary at $r = \infty$, and the temperature of the black brane is obtained by demanding the absence of a conical singularity at r_h,

leading to [124]

$$T = \frac{d+z-1}{4\pi}(r_h)^z. \tag{3.4}$$

The metric (3.3) enjoys the Lifshitz isometry, which will be inherited by the boundary theory as we will show shortly, and which reads

$$r \to \lambda r\,, \qquad t \to \lambda^{-z} t\,, \qquad x \to \lambda^{-1} x\,, \qquad T \to \lambda^z T\,. \tag{3.5}$$

Next, we introduce a Dirac fermion Ψ into the above gravitational background. Following [71, 72], we include a boundary action on an ultraviolet (UV) cutoff surface at $r = r_0$. While many of the results can be phrased for arbitrary dimensions, for later purposes we specify to $d = 4$ spatial dimensions already here. In the conventions of [71], the total action for the bulk fermion that we consider is

$$\begin{aligned} S_{\text{total}}[\Psi] = i\, g_f \int \mathrm{d}^5x \sqrt{-g}\, \left(\frac{1}{2}\overline{\Psi}\overrightarrow{\not{D}}\Psi - \frac{1}{2}\overline{\Psi}\overleftarrow{\not{D}}\Psi - M\,\overline{\Psi}\Psi \right) \\ - \int_{r=r_0} \mathrm{d}^4x \sqrt{-g}\, \left(\Psi_+^\dagger Z \not{D}_z(r,x)\Psi_+ + i\, g_f \sqrt{g^{rr}}\, \Psi_+^\dagger \Psi_- \right), \end{aligned} \tag{3.6}$$

where the first term on the right-hand side is the Dirac action in the bulk and the second term is the boundary action. Our notation is such that $\overline{\Psi} = \Psi^\dagger \Gamma^{\underline{0}}$ with $\Gamma^{\underline{0}}$ being antihermitian, and a natural choice for the Dirac matrices employed in this paper is given in appendix 3.A.2. Furthermore, we have decomposed Ψ into chiral components according to its eigenvalue under $\Gamma^{\underline{r}}$ [64, 121] in the following way

$$\Psi \equiv \begin{pmatrix} \Psi_+ \\ \Psi_- \end{pmatrix}, \qquad \Gamma^{\underline{r}}\Psi = \begin{pmatrix} +\Psi_+ \\ -\Psi_- \end{pmatrix}. \tag{3.7}$$

The normalization constants g_f and Z appearing in (3.6) are left unspecified for the moment. The coupling of the fermions to the gravitational field is through the vielbeins $e_{\underline{a}}{}^{\mu}$ and the spin connection $(\Omega_\mu)_{\underline{ab}}$, which are determined from the geometry and whose explicit form can be found in appendix 3.A.2. The symbol $\not{D}_z$ appearing in the boundary action is the usual Dirac operator for a fermion in a Lifshitz background with arbitrary dynamical exponent z.

Following [133], we also define Fourier-transformed spinors on each constant r slice as

$$\Psi_\pm(r,x) = \int \frac{\mathrm{d}^4p}{(2\pi)^4}\, \psi_\pm(r,p)\, e^{ip_\mu x^\mu}\,, \qquad p_\mu = (-\omega, \vec{k})\,, \tag{3.8}$$

where ω and $\vec{k}$ denote the frequency and momenta of the plane wave. The Dirac equation $\big(\not{D} - M\big)\Psi = 0$ resulting from (3.6) (see [71] for more details) and infalling boundary conditions that we shall employ at the horizon imply a relation between ψ_+ and ψ_-. It can be expressed as

$$\psi_-(r,p) = -i\xi(r,p)\,\psi_+(r,p)\,, \tag{3.9}$$

and can be used to integrate out ψ_- from the action. Together with (3.6) and (3.8) this results in a holographic effective action for the field ψ_+ on the cutoff surface as

$$S_{\text{eff}}[\Psi_+] = -\int_{r=r_0} \frac{\mathrm{d}^4 p}{(2\pi)^4}\, \sqrt{-g}\, \psi_+^\dagger \left[Z \not{D}_z(p) + g_f \sqrt{g^{rr}} \xi(r_0, p) \right] \psi_+ \,. \tag{3.10}$$

The Green's function of ψ_+ that follows from (3.10) for our geometry (3.3) reads

$$G_R(r_0, p) = -\left(r_0^z V(r_0) \not{D}_z(p) + \frac{g_f}{Z} r_0^{1+z} V^2(r_0)\, \xi(r_0, p) \right)^{-1} \,, \tag{3.11}$$

where we have rescaled ψ_+ so that it acquires a canonically normalized kinetic term. The final step is now to take a double-scaling limit

$$r_0 \to \infty \,, \qquad g_f \to 0 \,, \qquad g_f r_0^{1+z-2M} = \text{const.} \tag{3.12}$$

As we take this limit, we make sure that the resulting effective action has a kinetic term expected from a theory with dynamical scaling z. In the case $z \neq 1$, this can be achieved by renormalizing away a relativistic kinetic term and adding appropriate counterterms to the action [71]. The result for $z \neq 1$ then is

$$G_R(\vec{k}, \omega) = -\left(\omega - \frac{1}{\lambda} \vec{\sigma} \cdot \vec{k}\, |\vec{k}|^{z-1} - \Sigma(p) \right)^{-1} \,, \tag{3.13}$$

where λ is an arbitrary real number in our approach and where in the following we denote $k = |\vec{k}|$. Before we discuss the selfenergy $\Sigma(p)$, we would like to spend some words on the nature and interpretation of the parameter λ, both from a holographic point of view, and from a condensed-matter point of view of the boundary.

The parameter λ appeared first in [71], where it was denoted $\lambda = -1/\eta$ (see the discussion between (3.18) and (3.19) in that reference). It is a coefficient that is determined by the holographic renormalization procedure for Lifshitz geometries in the presence of bulk fermions that has not been not carried out. In our set-up, it is the parameter that multiplies the counterterm for the fermions on the UV brane involving spatial derivatives, after sending the UV cutoff to infinity. Given a particular bulk model, λ is a fixed number. For instance, for a dynamical exponent $z = 1$, and relativistic symmetry, $\lambda = \pm 1$ (or $\pm 1/c$ in natural units, c being the speed of light). For other values of the dynamical exponent, we do not know the magnitude of λ, neither do we know its sign. It is fixed and not tunable for a given bulk action. Nevertheless, we treat it here as a variable, and allow it to vary in the phase diagram of the boundary system, in much the same way as the bulk fermion mass M. In this manner we can explore all the possible physical properties of the system, even though at present we do not precisely know its value for the background that we are using. Moreover, as explained in section 3.4.4, the same phase diagram

can be obtained from a fixed value of λ, but by varying the bulk mass M over a broader range, see also (3.16). From this point of view, treating λ as a variable is perfectly viable, as long as one has enough bulk models (or string compactifications) with sufficiently many different choices for λ. This is completely consistent within our approach, as we have not specified the bulk action. We only used the metric that couples to the bulk fermions.

Forgetting about holography, and looking at the boundary system from a condensed-matter point of view, the parameter λ is the strength of the spin-orbit coupling $\vec{\sigma} \cdot \vec{k}\, k^{z-1}$. What the value of the spin-orbit coupling is depends on the underlying microscopic model for the fermions, and we cannot compute it without specifying the model. In fact, it may depend on the properties of the material. Hence we treat it as a parameter that encodes this ignorance, and we allow to vary it. In other words, we study how the physics changes as a function of λ, and the result of this analysis is the main content of our paper. In particular, we found that the sign of λ appears to be crucial in determining whether the system displays Fermi-liquid behaviour or not. In a certain sense, we are doing model building, and thus we checked that for all values of λ, important physical consistency conditions such as sum rules and Kramers-Kronig relations are satisfied.

After having discussed the significance of the parameter λ, we return to the selfenergy appearing in the Green's function (3.13). In our set-up, the holographic selfenergy $\Sigma(p)$ is by construction an effective description of the interactions between the elementary chiral fermions. This interaction term arises from coupling the elementary field ψ_+ to the conformal field theory encoded in the Lifshitz background. As can be seen by comparing with (3.11), it is related to the quantity $\xi(r,p)$ introduced in (3.9) by

$$\Sigma(p) = -g \lim_{r_0 \to \infty} r_0^{2M} \xi(r_0, p) \,, \qquad\qquad -\tfrac{1}{2} < M < \tfrac{1}{2} \,, \tag{3.14}$$

where g is the coupling constant which stays finite in the limit (3.12) and reads

$$g = \frac{g_f}{Z}\, r_0^{1+z-2M}. \tag{3.15}$$

The definition of the selfenergy $\Sigma(p)$ in (3.14) is valid for all values of the momentum $\vec{k}$, however, for $\vec{k} = 0$ the allowed range of M is extended to $-z/2 < M < z/2$. This can be derived from the asymptotic behaviour of $\xi(r,p)$ near the boundary, and for more details we refer the reader to appendix 3.B. Furthermore, it is possible to extend the relation between $\xi(r,p)$ and $\Sigma(p)$ even to $|M| > 1/2$ for nonzero momentum, which requires introducing certain counterterms on the cutoff surface at r_0 before taking the limit $r_0 \to \infty$. Since we will also be interested in the range $1/2 < M < z/2$, using the results in appendix 3.B, we can show that the relation

(3.14) in this case should be modified to

$$\Sigma(p) = -g \lim_{r_0\to\infty} \left(r_0^{2M}\xi(r_0,p) - \frac{\vec{\sigma}\cdot\vec{k}}{2M-1}\, r_0^{2M-1} \right) , \qquad \tfrac{1}{2} < M < \tfrac{z}{2} . \quad (3.16)$$

Note that the second term in this expression, which is divergent for $M > 1/2$, removes the divergence in $\xi(r,p)$ and yields a finite result for $\Sigma(p)$.

The transfer matrix $\xi(r,p)$ defined in equation (3.9) is a complex two-by-two matrix. In the case we are interested in, that is, $d = 4$, it can be diagonalized by choosing the Weyl basis of gamma matrices (3.87). A first-order differential equation for the eigenvalues $\xi_\pm(r,p)$ of $\xi(r,p)$ can be derived, which was achieved in the anti-de Sitter case ($z = 1$) in [133] and generalized to arbitrary z in [71]. The resulting differential equations read

$$r^2 V \partial_r \xi_\pm + 2Mr\xi_\pm = \frac{\omega}{r^{z-1}V} \mp k_3 + \left(\frac{\omega}{r^{z-1}V} \pm k_3 \right) \xi_\pm^2 , \quad (3.17)$$

where we used rotational invariance to set $\vec{k} = (0,0,k_3)$. Imposing infalling boundary conditions at the black-brane horizon, which corresponds to considering the retarded Green's function, leads to the boundary condition

$$\xi_\pm(r_h) = i . \quad (3.18)$$

The functions $\xi_\pm(r,p)$ as well as the resulting selfenergy $\Sigma(p)$ have various symmetries, which are discussed in more detail in appendix 3.C.

From the imaginary part of the retarded Green's function G_R, the total spectral weight, or spectral function, can be obtained, which is of great importance in condensed-matter physics and is also directly observable in experiments. It is defined as the trace of the two-by-two matrix G_R, i.e.,

$$\rho(\vec{k},\omega) = \frac{1}{2\pi} \operatorname{Im} \operatorname{Tr} \left[G_R(\vec{k},\omega) \right] . \quad (3.19)$$

It was shown in [71] that the spectral-weight function corresponding to (3.13) satisfies the sum rule

$$\int_{-\infty}^{\infty} \mathrm{d}\omega\, \rho(\vec{k},\omega) = 1 \quad (3.20)$$

in the physically allowed range for the scale dimensions of the CFT operator coupled to ψ. In [71], this range was found to be $-z/2 < M < z/2$, where the lower bound is due to unitarity in the field theory, and the upper bound is a consequence of the requirement that the coupling of the elementary fermion to the CFT is irrelevant in the ultraviolet. Within this allowed physical range for M, we have checked numerically that the Kramers-Kronig relations are satisfied and the sum rule (3.20) is

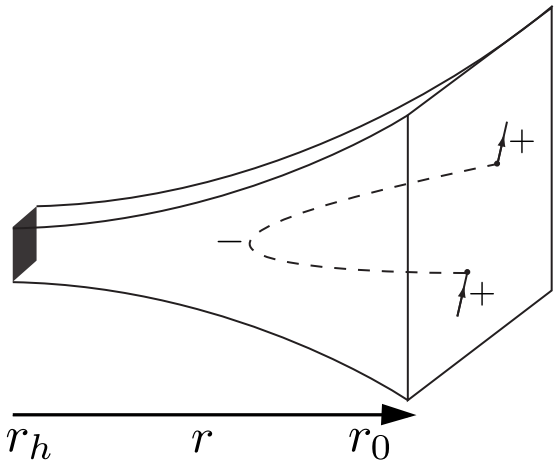

Figure 3.2: Illustration of our holographic construction of the selfenergy.

obeyed. The latter is a consequence of the fact that G_R is the Green's function for an elementary field ψ and its hermitian conjugate $\psi^\dagger$, that satisfy anticommutation relations. In conclusion, the prescription (3.13) thus allows us to holographically compute *single-particle* Green's functions, which are important from a condensed-matter perspective.

To close this section, we summarize and illustrate our holographic construction in Fig. 3.2. In particular, equation (3.13) describes chiral single-particle propagators on the boundary of the spacetime. These single-fermion excitations are modeled as dynamical sources coupled to the fermionic composite operators in the conformal field theory. These chiral single-fermions interact with each other, which is described via the coupling with the conformal field theory due to a fermionic excitation of opposite chirality that travels into the bulk spacetime, feels the bulk gravitational effects classically, and comes back to the boundary, forming the selfenergy of the single fermions. In the ultraviolet (UV), the points where the chiral dynamical source emits and reabsorbs the fermion of opposite chirality are very close together and the latter fermion cannot travel far into the bulk. Hence, it only notices the flat background on the cutoff surface in the bulk spacetime, which leads to a free fermionic propagator in the UV. For the infrared (IR) case, however, the fermion of opposite chirality can indeed travel far into the curved part of the bulk spacetime, and as a result the IR dynamics will be dominated by interactions and will generally not be free. This corresponds physically to the usual "energy-scale" interpretation of the extra spatial direction. For clarity, we recite the three different couplings that one should distinguish here.

1. The first coupling is the analog of the 't Hooft coupling λ_H that describes the effective coupling in the conformal field theory. This is assumed to be large in our model, hence the corresponding string states in the bulk are assumed to decouple.

2. The second coupling is the inverse of Newton's constant, G_5^{-1}, that is proportional to N^2, where N is the degree of the gauge group governing the conformal field theory. This is assumed to be large, allowing us to treat the fermion bulk action as a perturbation on the action of general relativity. In particular, we may ignore the back-reaction of the bulk fermions on the spacetime in the large-N limit. This corresponds to the fact that the connected parts of four-point functions of composite operators in the conformal field theory vanish.

3. Finally there is what we call g, the coupling between the dynamical source and the dominant channel in the conformal field theory.

The first two coupling constants are implicit in our model, as the gravitational action is not specified. A strongly interacting conformal field theory is characterized by nontrivial scaling dimensions, different than the engineering dimensions. This is indeed the case modeled here. In order to produce a nontrivial selfenergy for the single fermion, the first and last coupling constants should be large, at least of order 1. As a consequence, there is always a momentum-space region in the IR where the selfenergy is dominant over the kinetic term in the single-fermion propagator (3.13). This is what we mean when saying that the single fermions are "strongly interacting". In the context of the Weyl semimetal, the single-particle propagator from (3.13) models the excitations of one of the chiral cones.

3.3 Single-particle spectra

In the previous section, we have outlined the construction of the retarded single-particle Green's function. In the present section, we now study this Green's function for both the relativistic $z = 1$ and nonrelativistic $z = 2$ case in more detail, and work out its physical properties. The zero-temperature results were first obtained in [71], and here we consider nonzero temperatures as well. However, let us stress that the systems we describe are always at zero chemical potential.

3.3.1 Relativistic case $z = 1$

In the case that the elementary fermion ψ_+ interacts with a relativistic CFT, the background is given by an AdS black brane and is described by the metric shown in

equation (3.3) for $z = 1$. The mass range for the bulk Dirac fermion is then restricted to lie within the interval $-1/2 < M < 1/2$.

3.3.1.1 Zero temperature

For vanishing temperature and $z = 1$, the selfenergy $\Sigma(p)$ can be computed analytically for arbitrary frequencies ø and momenta $\vec{k}$. The result for the full retarded Green's function has been worked out in [71] and reads

$$G_R(\vec{k},\omega) = -\frac{1}{p^2\left(1 - g\,c_1\,e^{-i\pi(M+\frac{1}{2})}p^{2M-1}\right)}\left(\omega + \vec{\sigma}\cdot\vec{k}\right) , \tag{3.21}$$

where we defined $p \equiv \sqrt{\omega^2 - \vec{k}\cdot\vec{k}}$ as well as the constant (for arbitrary values of z)

$$c_z = (2z)^{-\frac{2M}{z}}\frac{\Gamma\left(\frac{1}{2} - \frac{M}{z}\right)}{\Gamma\left(\frac{1}{2} + \frac{M}{z}\right)} . \tag{3.22}$$

Note that (3.21) can be extended into the complex plane by allowing for complex momenta p, which is important when determining the pole structure of the Green's function. Because of the branch point at $p = 0$, we need to introduce a branch cut which is taken to run from $p = 0$ to $p = -i\infty$ for later convenience. Furthermore, we find that in order for (3.21) to be free of singularities in the upper half ω plane, i.e., to satisfy the Kramers-Kronig relations, we have to demand

$$g > 0 , \tag{3.23}$$

which is derived in detail in appendix 3.D.1. It is then straightforward to show that the Green's function (3.21) also satisfies the sum rule (3.20), as it was done in [71] and summarized in appendices 3.D.2 and 3.D.3. Furthermore, as mentioned above, (3.21) is valid on the complex p plane, with the prescription that on the real ω line the selfenergy is found by using

$$p^{2M-1}e^{-i\pi(M+\frac{1}{2})} = \begin{cases} +p^{2M-1}e^{-i\pi(M+\frac{1}{2})} , & p \equiv \sqrt{\omega^2 - \vec{k}\cdot\vec{k}} , & \omega > +|\vec{k}| , \\ +p^{2M-1}e^{+i\pi(M+\frac{1}{2})} , & p \equiv \sqrt{\omega^2 - \vec{k}\cdot\vec{k}} , & \omega < -|\vec{k}| , \\ -p^{2M-1} , & p \equiv \sqrt{\vec{k}\cdot\vec{k} - \omega^2} , & -|\vec{k}| < \omega < +|\vec{k}| . \end{cases} \tag{3.24}$$

This directly follows from (3.21) by noting that the region $\omega < -|\vec{k}|$ for real frequencies is obtained from the region $\omega > |\vec{k}|$ by $p \to e^{i\pi}p$, that is, $\omega \to e^{i\pi}\omega$ and $\vec{k} \to e^{i\pi}\vec{k}$, while the region $|\omega| < |\vec{k}|$ is obtained via $p \to e^{i\pi/2}p$. Note also that the Green's function for $-|\vec{k}| < \omega < +|\vec{k}|$ has no imaginary part.

3.3.1.2 Nonzero temperature

We have studied the effects of nonzero temperature on the structure and form of the Green's function by numerical integration of the Dirac equation. To illustrate our results, we have included figures 3.3 and 3.4 which show the total spectral-weight function (3.19) for $T = 1/30$ and $T = 2$, respectively. Furthermore, we made a distinction between positive and negative masses M, and we employed the rotational symmetry to set $\vec{k} = (0, 0, k_3)$. Let us discuss these figures in some more detail:

- First, we note that a nonvanishing temperature results in a smearing out of the features of the Green's function, as can be seen by comparing Figs. 3.3 and 3.4.
- For $M > 0$ we observe a large spectral weight approximately at $\omega = \pm k_3$, which is due to the "light cone" of relativistic physics. In the zero-temperature case (3.24), the imaginary part of the Green's function is strictly zero outside of the light cone in the region $-|\vec{k}| < \omega < +|\vec{k}|$. For nonzero temperatures, there is a small contribution in this region, which increases with temperature.

  Note that the peak in the spectral weight is not caused by a pole in the Green's function, but by the aforementioned branch cut. Therefore, it has no interpretation as a well-defined quasiparticle excitation, but it is still possible to approximately determine the dispersion relation, as it is shown in the next subsection.
- For negative masses $M < 0$, the spectrum has a similar form. Indeed, there is again a large peak at $\omega = \pm k_3$. However, for low T, the imaginary part of the Green's function goes to zero at $k_3 = 0$ as $\omega \to 0$. It has a maximum in between, which leads to a broad maximum in the spectrum. Its approximate location is determined analytically in section 3.3.1.3.

  We have also investigated the ratio $\mathcal{R}$ of the location of the maximum and its width as a function of g. This ratio is approximately constant, which means that its shape becomes broader as we increase its position, and vice versa. The spectral function at $k_3 = 0$ looks very similar to what is plotted in Fig. 3.7 for the nonrelativistic case with $z = 2$. It is not possible to tune the parameters such that the peak is located sufficiently far away from the origin at $\omega = 0$ while its maximum remains sharp. Therefore, we cannot interpret this feature in the spectral function as a massive particle. Again, we give some further analytic arguments of this statement at zero temperature in section 3.3.1.3.

3.3.1.3 Dispersion relation

In the last subsection 3.3.1.2, we have illustrated that the spectral weight is peaked at particular functions $\omega(\vec{k})$. In this section, we now investigate the correspond-

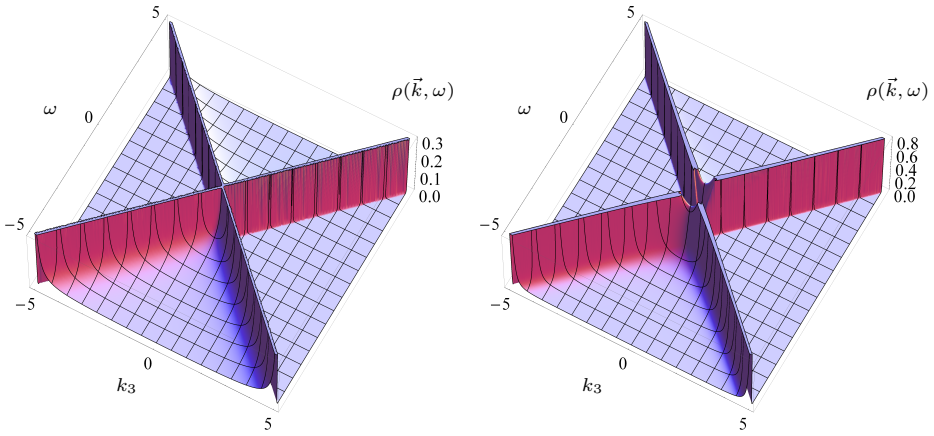

(a) $M = +1/4$ **(b)** $M = -1/4$

Figure 3.3: Total spectral function for $T = 1/30$, $g = 1$ and $M = \pm 1/4$.

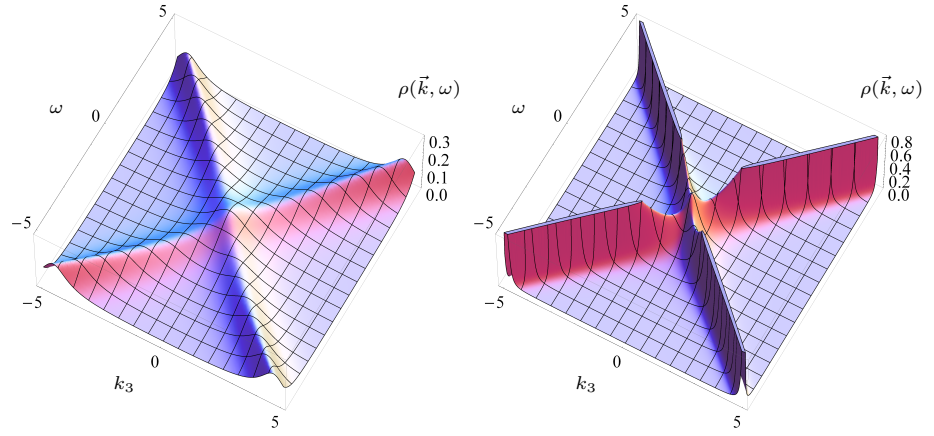

(a) $M = +1/4$ **(b)** $M = -1/4$

Figure 3.4: Total spectral function for $T = 2$, $g = 1$ and $M = \pm 1/4$.

ing dispersion relation of the theory. For vanishing temperature this can be done analytically via the single-particle Green's function by solving

$$\mathrm{Re}\, G_R^{-1}(\vec{k},\omega) = 0\ . \tag{3.25}$$

By definition, the solutions to this equation determine the dispersion relation of the would-be (quasi)particle. The interpretation as a particle only becomes justified if the width is small compared to the energy of the particle. Indeed, a large peak in the spectral density function is only obtained when both $\mathrm{Re}\,(G_R^{-1})$ and $(\,\mathrm{Im}\,\Sigma)^2$ are minimal, as follows from the identity

$$\mathrm{Im}\, G_R = -\frac{\mathrm{Im}\,\Sigma}{(\,\mathrm{Re}\, G_R^{-1})^2 + (\,\mathrm{Im}\,\Sigma)^2}\ . \tag{3.26}$$

Let us first solve (3.25). Using the explicit expression (3.21), equation (3.25) generically gives two possible dispersion relations, namely

$$\omega = \pm|\vec{k}| \qquad \text{and} \qquad g\, c_1\, \mathrm{Re}\left[e^{-i\pi(M+\frac{1}{2})} p^{2M-1}\right] = 1\ . \tag{3.27}$$

The first solution describes a free, massless relativistic excitation which is always present. The second equation in (3.27) should be studied separately in the two regions $|\omega| < |\vec{k}|$ and $|\omega| > |\vec{k}|$. In the first case, using (3.24) we obtain the solution

$$p^2 = \left(-\frac{1}{g\, c_1}\right)^{\frac{2}{2M-1}}\ . \tag{3.28}$$

Since $g\, c_1 > 0$ and the left-hand side of (3.28) should be real, we conclude that there is no solution for $|\omega| < |\vec{k}|$. In the second case, $|\omega| > |\vec{k}|$, the solution reads

$$p^2 = \left(g\, c_1 \cos\left[\pi(M+\tfrac{1}{2})\right]\right)^{\frac{2}{1-2M}}\ . \tag{3.29}$$

For $0 < M < 1/2$, we do not find a solution since $g\, c_1 > 0$. On the other hand, for $-1/2 < M < 0$, we obtain

$$\omega = \pm\sqrt{\vec{k}\cdot\vec{k} + m^2}\ , \qquad m^2 = \left(g\, c_1 \cos\left[\pi(M+\tfrac{1}{2})\right]\right)^{\frac{2}{1-2M}}\ , \tag{3.30}$$

which is indeed close to the locations of the maxima in the spectral-weight function that were found for nonzero temperature. For zero temperature, equation (3.30) yields the exact result.

Now we can look at the width, by computing the imaginary part of the selfenergy at the values (3.30). A straightforward calculation shows that, at zero temperature, we have

$$\mathrm{Im}\,\Sigma = -(\omega - \vec{\sigma}\cdot\vec{k}) \tan\left[\pi\left(M+\frac{1}{2}\right)\right]\ , \tag{3.31}$$

with ω given by (3.30). However, for momenta small compared to the gap m (in the rest frame of the would-be particle), we can approximate

$$\mathrm{Im}\,\Sigma \approx m \tan\left[\pi\left(M+\frac{1}{2}\right)\right] \ . \tag{3.32}$$

The width is then comparable to the gap, and therefore the peak in the spectral density does not have a quasiparticle interpretation. One might try to make the width smaller by taking the value of M close to the unitarity bound, $M = -1/2$. However, notice that then the gap also narrows down. We conclude therefore that no true quasiparticles exist.

3.3.2 Non-relativistic case $z \neq 1$

In principle, every value of the dynamical exponent z can be considered using the prescription shown in (3.13). However, for our purposes we are mostly interested in $z = 2$ where the elementary fermion interacts with a CFT exhibiting $z = 2$ Lifshitz scale invariance.

3.3.2.1 Zero temperature

Unlike the relativistic case studied above, for an arbitrary dynamical exponent z we were not able to obtain $G_R(\omega, \vec{k})$ analytically for the both ω and $\vec{k}$ nonvanishing. But it is possible to determine the zero-temperature result for $\vec{k} = 0$ and $\omega = 0$ separately, and then restrict the general expression to a great extent.

Let us therefore start with the case $\vec{k} = 0$ and $T = 0$. From [71] we recall the expression for the Green's function as

$$G_R(\vec{0}, \omega) = -\frac{1}{\omega - g\, c_z\, \omega^{\frac{2M}{z}} e^{-i\pi\left(\frac{M}{z}+\frac{1}{2}\right)}} \ , \tag{3.33}$$

where we employed the definition (3.22). In the case with $\omega = 0$ and $T = 0$ we instead find [71]

$$G_R(\vec{k}, 0) = \frac{1}{\frac{1}{\lambda}\,\vec{\sigma}\cdot\vec{k}\,k^{z-1} + g\, c_1\, k^{2M-1}\vec{\sigma}\cdot\vec{k}} \ , \tag{3.34}$$

where again k denotes $|\vec{k}|$. The generic case at vanishing temperature when both $\vec{k}$ and ω are nonzero can then be restricted as follows. Using the scaling and rotational symmetries of the selfenergy (see appendix 3.C.1), and defining $u = \omega/k^z$ for notational simplicity, we have

$$G_R(\vec{k}, \omega) = -\frac{1}{\omega - \frac{1}{\lambda}\,\vec{\sigma}\cdot\vec{k}\,k^{z-1} - g\left(k^{2M} s_{1,M}(u) + k^{2M-1} s_{2,M}(u)\,\vec{\sigma}\cdot\vec{k}\right)} \ , \tag{3.35}$$

where $s_{1,M}$ and $s_{2,M}$ are complex functions of u and M only. Furthermore, we can derive conditions on the functions $s_{1,2}$ using the symmetry of $\Sigma(p)$ under the change $M \to -M$, as discussed in appendix 3.C.4. The asymptotic behaviour of the functions $s_{1,M}(u)$ and $s_{2,M}(u)$ in the limits $u \to 0$ and $u \to \infty$ is fixed by the expressions (3.33) and (3.34) given above. We therefore have

$$\begin{aligned} s_{1,M}(u) &\xrightarrow{u\to\infty} u^{\frac{2M}{z}} e^{-i\pi\left(\frac{M}{z}+\frac{1}{2}\right)} c_z \ , & s_{2,M}(u) &\xrightarrow{u\to\infty} 0 \ , \\ s_{1,M}(u) &\xrightarrow{u\to 0} 0 \ , & s_{2,M}(u) &\xrightarrow{u\to 0} c_1 \ . \end{aligned} \tag{3.36}$$

Unfortunately, these conditions do not seem to be sufficient to determine the analytic form of (3.35). Therefore we have to study the Green's function numerically. Yet, we can determine the qualitative form of the dispersion relation by analytic arguments as we describe below in section 3.3.2.3.

3.3.2.2 Nonzero temperature

We have studied the retarded Green's function and the corresponding spectral-weight function for $z = 2$ numerically as a function of ω, $\vec{k}$, T and λ. Using the symmetries summarized in appendix 3.C, that is chirality and particle-hole symmetry, we observe that the components of the spectral-weight function obey the following relations

$$\rho^{\pm}(\vec{k},\omega) = \rho^{\mp}(-\vec{k},\omega) = \rho^{\pm}(-\vec{k},-\omega) \ . \tag{3.37}$$

Consequently, it suffices to consider separate components instead of the trace over chiral components.

Next, we recall that for $z \neq 1$ the Green's function (3.13) contains the parameter λ, which we have not determined analytically. Treating λ as a free parameter, we observe that under a change of sign of λ, the far UV behaviour of one component of the spectral weight function asymptotes the UV behaviour of the other component with the original sign, that is,

$$\rho^{\pm}_{-\lambda}(\vec{k},\omega) \xrightarrow{|\omega|\to\infty,\ |k|\to\infty} \rho^{\mp}_{+\lambda}(\vec{k},\omega) = \rho^{\pm}_{+\lambda}(-\vec{k},\omega) \ . \tag{3.38}$$

Since λ can be interpreted as a spin-orbit coupling constant, we use the following convention for plotting components of the spectral-weight function: when λ is positive (negative), the plus(minus) component of the spectral-weight function is shown. In this manner we make sure that we always compare spectra with equal group velocity in the UV, also when λ changes sign. We make this choice because qualitatively the UV physics is then, apart from the topology of the band structure, independent of the sign of λ. This allows us to compare more clearly the physics for positive and negative values of λ as we will see shortly.

In figures 3.5 and 3.6 we show numerical results for separate components of the corresponding spectral-weight function. The parameters are chosen as $M = \pm 1/4$, $g = 1$ and $T = 1/30$, for a number of different values for λ. We discuss some of the features in turn:

- In Fig. 3.5, showing the results for positive M, we see that the spectral-weight function is very sharply peaked in the UV and behaves as a free chiral fermion with a quadratic dispersion. In the IR, the selfenergy becomes dominant which changes and smears out the form of the free-fermion dispersion due to strong interactions. When λ switches sign, the spectral-weight function changes in the IR, with the convention such that the far UV behaviour stays the same. For $\lambda > 0$, the band structure is similar to that of a Weyl semimetal, as can be seen by combining it with the density plot of $\rho^-(\vec{k}, \omega)$ for $\lambda > 0$ (not shown) and comparing it with Fig. 3.1. Indeed, the observed $\vec{\sigma} \cdot \vec{k}$ dependence and the absence of a gap are defining properties of the Weyl semimetal. For $\lambda < 0$, the system is gapless too, and similar to a Weyl semimetal in the presence of Fermi surfaces.

- In Fig. 3.6, where M is negative, we observe a phenomenon similar to the relativistic case with $M < 0$. In particular, the spectral weight has to vanish for $k = 0$ as $\omega \to 0$, so there is a maximum in the spectral-weight function at nonzero ω. However, the ratio of the location and the width of the peak, $\mathcal{R}$, again remains constant as we change g, so there is no gap generation with a quasiparticle interpretation. This is further illustrated in Fig. 3.7.

To close our discussion about nonzero-temperature effects in the case of $z = 2$, let us consider the strict IR (or hydrodynamic) limit $\omega \to 0$, $k \to 0$. As explained in appendix 3.B.3, in this limit the contribution from the free propagator vanishes and the Green's function reduces to the inverse of the selfenergy $\Sigma(p)$. An analytical result for all values of the dynamical exponent z and dimension d and for nonzero temperature has been obtained for this case in equation (3.110), which we recall here for convenience

$$G_R(\vec{0}, 0) = \frac{i}{g}\, 2^{\frac{4M}{d+z-1}} \left(\frac{d+z-1}{4\pi}\right)^{\frac{2M}{z}} T^{-\frac{2M}{z}} \,. \tag{3.39}$$

3.3.2.3 Dispersion relation

We now consider the dispersion relation for $z \neq 1$ at zero temperature, which can be derived from the general form of the Green's function given in (3.35). In particular,

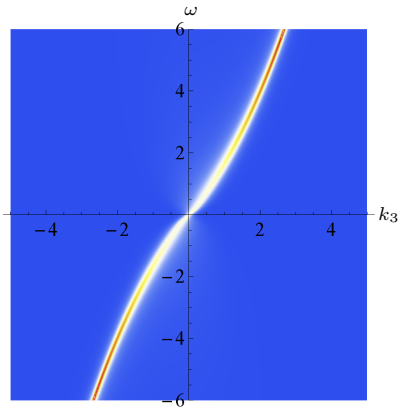

(a) Density plot of $\rho^+(\vec{k},\omega)$ at $\lambda = 2$

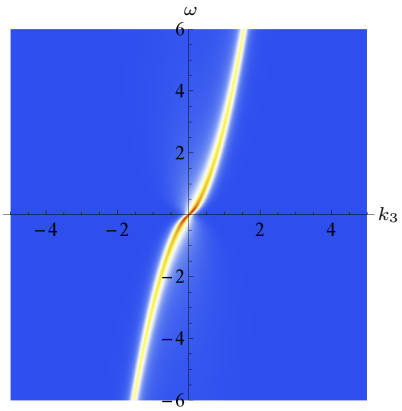

(b) Density plot of $\rho^+(\vec{k},\omega)$ at $\lambda = 0.5$

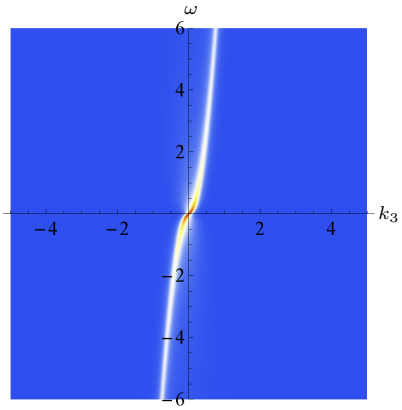

(c) Density plot of $\rho^+(\vec{k},\omega)$ at $\lambda = 0.1$

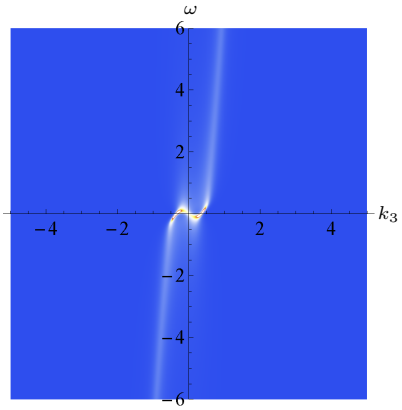

(d) Density plot of $\rho^-(\vec{k},\omega)$ at $\lambda = -0.1$

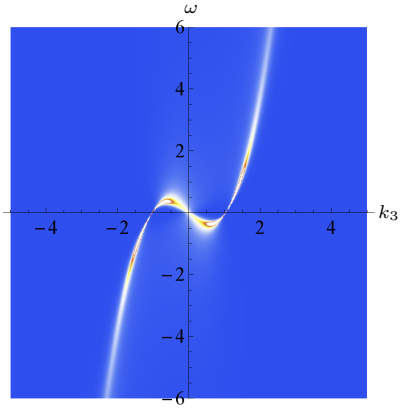

(e) Density plot of $\rho^-(\vec{k},\omega)$ at $\lambda = -0.5$

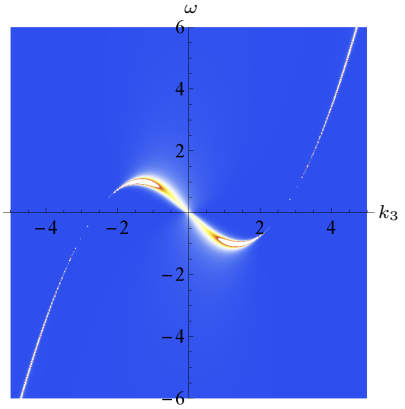

(f) Density plot of $\rho^-(\vec{k},\omega)$ at $\lambda = -2$

Figure 3.5: Density plot of $\rho^{\pm}(\vec{k},\omega)$ for $z = 2$, $M = +1/4$, $T = 1/30$, $g = 1$.

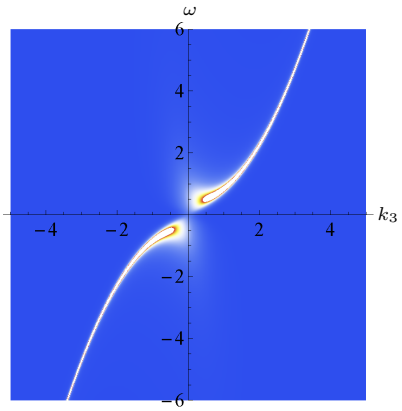

(a) Density plot of $\rho^+(\vec{k},\omega)$ at $\lambda = 2$

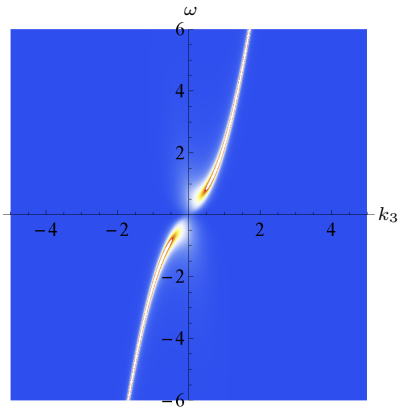

(b) Density plot of $\rho^+(\vec{k},\omega)$ at $\lambda = 0.5$

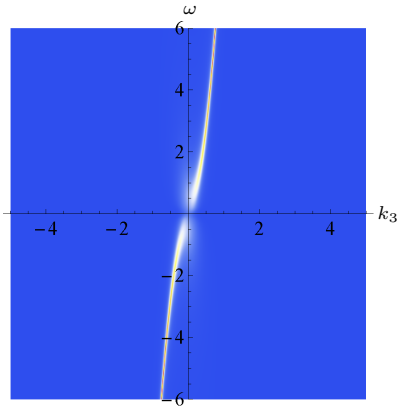

(c) Density plot of $\rho^+(\vec{k},\omega)$ at $\lambda = 0.1$

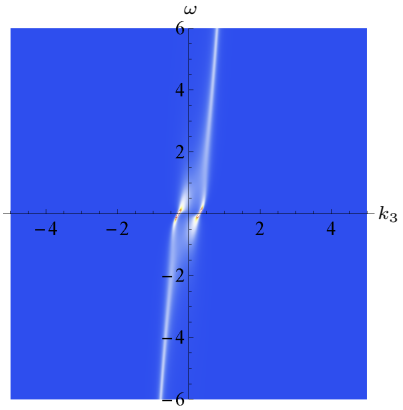

(d) Density plot of $\rho^-(\vec{k},\omega)$ at $\lambda = -0.1$

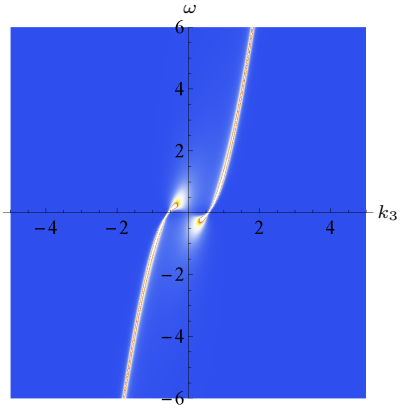

(e) Density plot of $\rho^-(\vec{k},\omega)$ at $\lambda = -0.5$

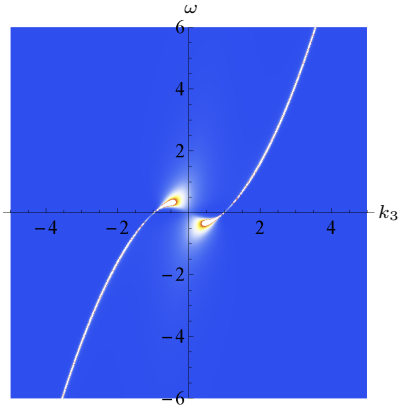

(f) Density plot of $\rho^-(\vec{k},\omega)$ at $\lambda = -2$

Figure 3.6: Density plot of $\rho^{\pm}(\vec{k},\omega)$ for $z = 2$, $M = -1/4$, $T = 1/30$, $g = 1$.

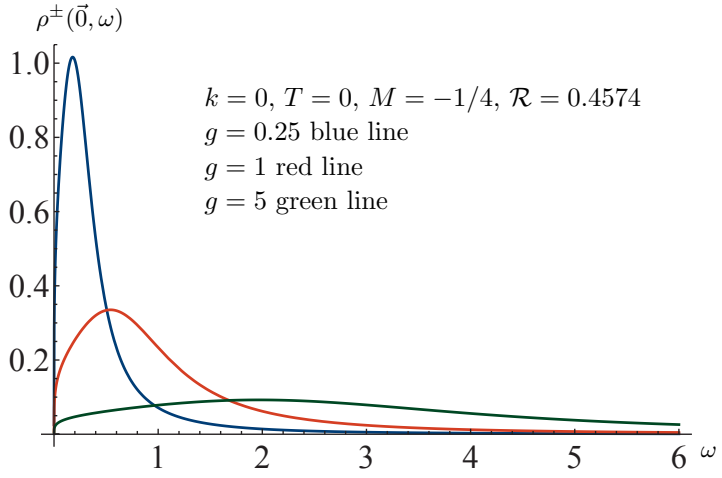

Figure 3.7: Spectral-weight function for vanishing momentum determined from (3.33). Since the ratio of the location and the width of the peak remains constant ($\mathcal{R} = 0.4574$ in the figure), there is no quasiparticle interpretation.

the dispersion relation is obtained by solving (3.25), which in the present case reads

$$\omega - \frac{1}{\lambda}\,\vec{\sigma}\cdot\vec{k}\,k^{z-1} - g\,k^{2M}\,\mathrm{Re}\left(s_{1,M}\,(u) + \frac{\vec{\sigma}\cdot\vec{k}}{k}\,s_{2,M}\,(u)\right) = 0\,. \tag{3.40}$$

In the following we consider the upper-spin component for definiteness. The latter means that $\vec{\sigma}\cdot\vec{k}/k$ is replaced by $\mathrm{sign}(k_3)$, where we again employed the rotational symmetry to align the momenta in the z-direction. For positive (negative) momentum k_3 the dispersion relation then becomes

$$\omega \mp \frac{1}{\lambda}\,k^z - g\,k^{2M}\,\mathrm{Re}\left(s_{1,M}\,(u) \pm s_{2,M}\,(u)\right) = 0\,. \tag{3.41}$$

In order to determine the qualitative form of the dispersion relation, we study various limits of the equation above.

- We first consider the UV limit $\omega \to \infty$, $k \to \infty$ for which there are the three distinct possibilities: $\omega/k^z \to \infty$, $k^z/\omega \to \infty$ and $\omega/k^z \to$ const. The first two do not allow for a solution of (3.41), but the third possibility leads to

  $$\omega \approx \pm\frac{1}{\lambda}\,k^z \qquad\qquad \text{for } k \gg 1 \tag{3.42}$$

  in the allowed mass range $-z/2 < M < z/2$. This result confirms our general picture that the interaction of the elementary fermion with the CFT is irrelevant in the UV, hence the dispersion becomes that of a free fermion.

- Next, we consider the limit $k_3 \to 0^+, \omega > 0$. In the mass range $-z/2 < M < z/2$ we determine the dispersion curve from (3.33) as

$$\omega + g\, c_z \left|\cos\Big[\pi\big(\tfrac{M}{z} + \tfrac{1}{2}\big)\Big]\right| \operatorname{sign}(M)\, \omega^{\frac{2M}{z}} = 0\ . \tag{3.43}$$

  Noting that $g > 0$ and $c_z > 0$, we find that the only solution to this equation is $\omega = 0^+$ for $M > 0$. On the other hand, for $M < 0$ we obtain the only solution as

$$\omega = \left(g\, c_z \left|\cos\Big[\pi\big(\tfrac{M}{z} + \tfrac{1}{2}\big)\Big]\right|\right)^{\frac{z}{z-2M}} \equiv m_z\ , \qquad M < 0\ . \tag{3.44}$$

  These solutions correspond to the points where the dispersion curve touches the axis at $k = 0$.

  Studying the dispersion relation for the case of $k_3 \to 0^+$ and $\omega < 0$, we find another solution at $\omega = -m_z$, consistent with the particle-hole symmetry. This is the nonrelativistic analog of the result we obtained in equation (3.30). As mentioned above, and similar to the case with $z = 1$, the corresponding peaks in the spectral-weight function cannot be interpreted as a true gapped quasiparticle excitation. This is further illustrated by a plot of the analytic result in Fig. 3.7.

- The most interesting case is when $0 < M < 1/2$ and $\lambda < 0$. As one can see from Fig. 3.5, this situation is quite different from $0 < M < 1/2$ and $\lambda > 0$. The dispersion curve $\omega(\vec{k})$ for $\lambda < 0$ crosses the $\omega = 0$ axis three times, instead of only once at $\omega = k = 0$. It therefore seems that two Fermi surfaces appear at the momenta for which $\omega(\pm k_F) = 0$. This signals a phase transition as one crosses from positive to negative λ. The remainder of this paper is devoted to a detailed study of this phase transition.

3.4 Quantum phase transition

In figures 3.5 and 3.6 we have already seen that for $z = 2$ the parameter λ controls features of the spectral density significantly. In particular, when switching the sign of λ the number of zeros of the dispersion relation $\omega(\vec{k})$ changes, as becomes clear when comparing for instance figures 3.5(a) and 3.5(f). In the present section, we study this phenomenon in more detail. For simplicity we focus on the case $0 < M < 1/2$ since the quantum phase transition discussed here is also present for $-1/2 < M < 0$. However, we also briefly consider the case $|M| > 1/2$ in section 3.4.5.

3.4.1 Momentum distribution

Let us start by defining the momentum distribution function. We choose again a convention such that the group velocity of a particle with one of the spin components always has the same sign at large momenta, irrespectively of the sign of λ. More concretely, with $n_F(\omega)$ the Fermi distribution we write

$$N^{\pm}_{\vec{k}} = \begin{cases} \dfrac{1}{\pi}\displaystyle\int_{-\infty}^{\infty} \mathrm{d}\omega \ \mathrm{Im}\, G^{\pm}_R(\omega, \vec{k})\ n_F(\omega) & \text{for} \quad \lambda > 0\ , \\ \dfrac{1}{\pi}\displaystyle\int_{-\infty}^{\infty} \mathrm{d}\omega \ \mathrm{Im}\, G^{\mp}_R(\omega, \vec{k})\ n_F(\omega) & \text{for} \quad \lambda < 0\ . \end{cases} \tag{3.45}$$

The behaviour of $N^{\pm}_{\vec{k}}$ when λ changes sign is illustrated in Fig. 3.8 for nonzero temperatures, where we again employed the rotational symmetry to set $\vec{k} = (0, 0, k_3)$. In particular, for $\lambda < 0$ the momentum distribution indicates a Fermi surface with a certain width, on which we comment later. When λ switches sign, two extrema appear that develop into sharp discontinuities as λ increases. This is a clear signature of a Fermi surface. The locations of the jumps are determined analytically in the next section.

3.4.2 Fermi momentum

We now study analytically how the number of putative Fermi surfaces changes as we vary the parameter λ. To do so, we recall that Fermi surfaces are determined by the poles of the Green's function at vanishing frequencies $\omega = 0$. The latter can be computed by setting to zero the denominator in (3.13). Note also that the selfenergy is given by (3.14) which satisfies the particle-hole symmetry derived from (3.126). Employing the general form of the selfenergy implied by (3.35), we see that in the limit $\omega \to 0$ the imaginary part of $\Sigma(p)$ vanishes and the condition for the presence of a Fermi surface coincides with the presence of zeros of the dispersion relation (3.25). Thus, the loci of the Fermi surfaces are given precisely by the points where the dispersion curve $\omega(\vec{k})$ crosses the $\omega = 0$ axis.

We therefore consider equation (3.41) in the limit $\omega \to 0$. Using (3.36) and the expression (3.22) for c_1, we obtain the following formula for the loci of the Fermi surfaces

$$\frac{1}{\lambda}\, k^z + g\, k^{2M} c_1 = 0\ . \tag{3.46}$$

Then, as we have mentioned in equation (3.23), to avoid violation of causality we have to require $g > 0$. Equation (3.46) can thus have nontrivial solutions in the range $-1/2 < M < 1/2$ only when $\lambda < 0$, that is

$$k = k_F = \left(-g\lambda c_1\right)^{\frac{1}{z-2M}}\ . \tag{3.47}$$

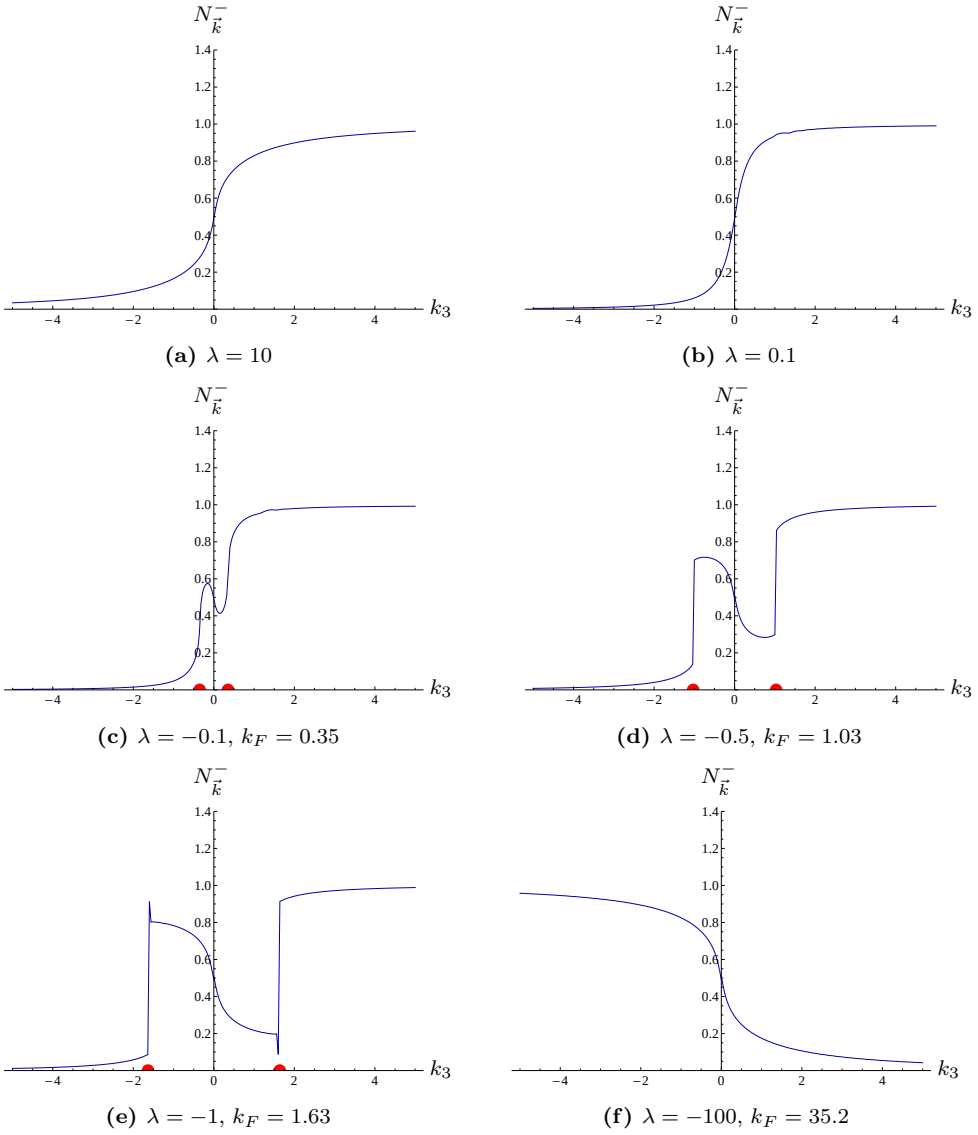

(a) $\lambda = 10$ **(b)** $\lambda = 0.1$

(c) $\lambda = -0.1$, $k_F = 0.35$ **(d)** $\lambda = -0.5$, $k_F = 1.03$

(e) $\lambda = -1$, $k_F = 1.63$ **(f)** $\lambda = -100$, $k_F = 35.2$

Figure 3.8: Momentum distribution of the minus component for $M = +1/4$, $T = 1/30$, $g = 1$. For $\lambda > 0$ it has a smooth kink-like behaviour whereas for $\lambda < 0$ two Fermi surfaces develop. The red dots give the analytic value (3.47) of k_F. For small and negative λ, the Fermi surfaces are smeared out because of the nonzero value of the temperature.

Next, let us consider again the numerical results for the imaginary part of the Green's function shown in Fig. 3.5. For $\lambda < 0$, there are zero-energy modes at nonvanishing momentum, suggesting that the system indeed has two Fermi surfaces at zero temperature. However, due to the small but nonzero temperature which we have to employ in our numerics, the spectrum shown in the plots has a finite width and the locations of the zero modes are approximately at the Fermi momentum (3.47). To investigate this point further and to confirm that we are indeed dealing with a genuine Fermi surface, in the following we compute the quasiparticle weight Z as a function of λ and g, as well as the effective mass and the lifetime at the Fermi surface as a function of ω, T, g and λ.

3.4.2.1 Quasi-particle residue

In order to scrutinize the Fermi surfaces, in this subsection we determine the quasiparticle residue by linearizing the dispersion relation around the Fermi surface at $\omega \approx 0$, $k \approx k_F$. For convenience, we choose the lower component of the Green's function which results in the spectral-weight function shown in figures 3.5(d)-(f). Furthermore, we employ the rotational symmetry to set $\vec{k} = (0, 0, k_3)$ with $k_3 > 0$, and thus $k_3 = k$ in the following. We then compute up to first order in derivatives

$$\begin{aligned} &- \operatorname{Re}\left(G_R^-\right)^{-1}\Big|_{k\approx k_F,\,\omega\approx 0} \\ &\qquad \approx \omega\left(1 - \partial_\omega \operatorname{Re}\Sigma^-(k_F,\omega)\Big|_{\omega=0}\right) - (k-k_F)\,\partial_k\left(\operatorname{Re}\Sigma^-(k,0) - \frac{1}{\lambda}k^z\right)\Big|_{k=k_F} . \end{aligned} \tag{3.48}$$

Using (3.48) in the retarded Green's function, close to the Fermi surface we obtain the expression

$$G_R^-(k,\omega) = \frac{-Z}{\omega - Z(k-k_F)\,\partial_k\left(\operatorname{Re}\Sigma^-(k,0) - \frac{1}{\lambda}k^z\right)\big|_{k=k_F} - i\,Z\operatorname{Im}\Sigma^-(k,\omega)} , \tag{3.49}$$

where the wavefunction renormalization factor, or quasiparticle residue Z, is given by

$$Z = \frac{1}{1 - \partial_\omega \operatorname{Re}\Sigma^{\pm}(k_F,\omega)\big|_{\omega=0}} . \tag{3.50}$$

The residue is equal for both spin components because the ω derivatives of $\operatorname{Re}\Sigma^{\pm}$ are equal at $\omega = 0$. Furthermore, note that Z depends on the coupling g explicitly due to the factor g in $\Sigma(p)$, but also implicitly via the dependence of k_F on g shown in (3.47). The dependence on λ is only through k_F. To be able to determine the quasiparticle residue, the real part of the selfenergy has to be linear in $\omega = 0$, which is indeed the case, as shown in Fig. 3.9. The first derivative of the real part of the selfenergy is shown for $T = 1/100$ in Fig. 3.10(a).

Let us illustrate the calculation of Z for a particular value of λ and g, namely $\lambda = -0.5$ and $g = 1$. For $T = 1/30$, the first derivative of the real part of the selfenergy has the nonzero value $\partial_\omega \operatorname{Re}\Sigma^+(k_F, 0) \approx -0.8$ at $\omega = 0$. This leads to a finite quasiparticle residue of about $Z \approx 0.56$, which is precisely the height of the step in the momentum distribution at $k_3 = \pm k_F$, as shown in Fig. 3.11. Repeating this calculation for different values of λ, we have determined $Z(\lambda)$, which is shown in Fig. 3.12. Note that $0 \leq Z \leq 1$ as is required. Furthermore, the large deviation from 1 of the quasiparticle residue for small and negative λ, demonstrates that we are indeed describing a strongly interacting system.

3.4.2.2 Effective mass

In the last subsection we have seen that at the Fermi surfaces there are quasiparticles which are strongly renormalized. Now, to further characterize the Fermi liquid we should also compute their effective mass. The latter is defined as the inverse of the slope of the quasiparticle dispersion around the Fermi surface, that is,

$$\omega(k) = \frac{1}{m_{\text{eff}}} (k - k_F) k_F \qquad \text{near the Fermi surface,} \tag{3.51}$$

where we are again employing $k_3 > 0$ and thus $k_3 = k$. Therefore, in our present situation the retarded Green's function near the Fermi momentum can be written as

$$G_R^-(k, \omega) = \frac{-Z}{\omega - \frac{1}{m_{\text{eff}}}(k - k_F)k_F - iZ \operatorname{Im}\Sigma^-(k, \omega)} , \tag{3.52}$$

and by comparing with the explicit form given in (3.49) we conclude that

$$\frac{1}{m_{\text{eff}}} = \frac{Z}{k_F} \partial_k \left(\operatorname{Re}\Sigma^-(k, 0) - \frac{1}{\lambda} k^z \right) \Big|_{k=k_F} . \tag{3.53}$$

At zero temperature, we can calculate the effective mass analytically. In particular, for $z = 2$ we obtain from the exact result given in equation (3.34) that

$$\operatorname{Re}\Sigma^-(k, 0) = g c_1 k^{2M} , \qquad \partial_k \operatorname{Re}\Sigma^-(k, 0)\big|_{k=k_F} = -\frac{2M}{\lambda} k_F , \tag{3.54}$$

where we eliminated $g c_1$ in favor of k_F. Therefore, the effective mass for $z = 2$ at zero temperature reads

$$m_{\text{eff}} = -\frac{\lambda}{2Z(\lambda)(M + 1)} . \tag{3.55}$$

The effective mass is shown in the inset in Fig. 3.12.

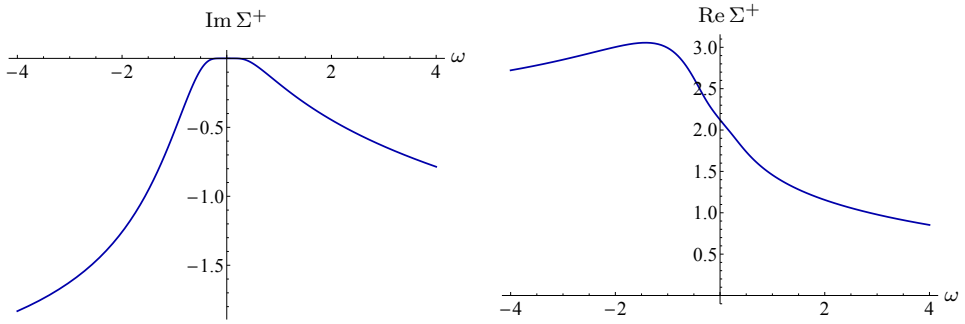

(a) $\mathrm{Im}\,\Sigma^+(k_F,\omega)$ **(b)** $\mathrm{Re}\,\Sigma^+(k_F,\omega)$

Figure 3.9: Imaginary and real part of the selfenergy $\Sigma^+(p)$ evaluated at the Fermi momentum for $T = 1/100$, $g = 1$, $\lambda = -0.5$ and $M = 1/4$. The imaginary part is zero around $\omega = 0$ and the real part is linear around $\omega = 0$, which are both defining properties of a Fermi liquid.

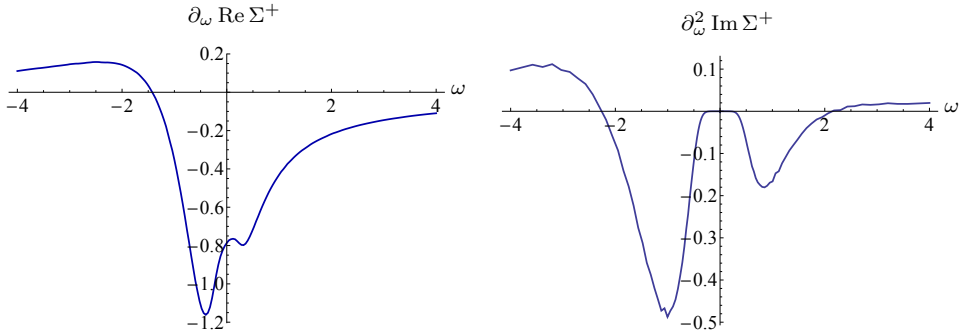

(a) $\partial_\omega\,\mathrm{Re}\,\Sigma^+$ **(b)** $\partial_\omega^2\,\mathrm{Im}\,\Sigma^+$

Figure 3.10: This figure shows the first derivative of $\mathrm{Re}\,\Sigma^+(p)$ and the second derivative of $\mathrm{Im}\,\Sigma^+(p)$, both at $\lambda = -0.5$, $T = 1/100$, $M = 1/4$ and $g = 1$, evaluated at the Fermi momentum.

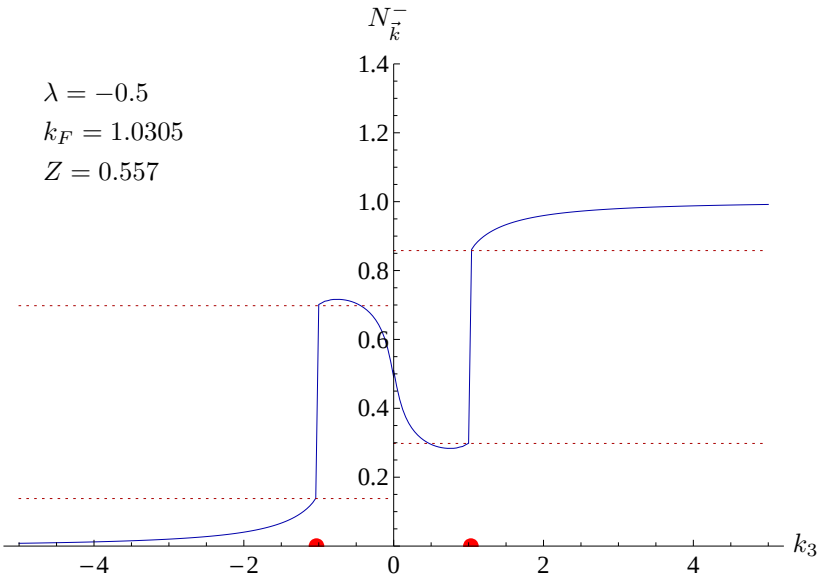

Figure 3.11: The momentum distribution for $M = 1/4$, $T = 1/30$ and $g = 1$. The quasiparticle residue is given by the distance between the dotted lines: the difference in height is the numerical value of Z, which is 0.56 for $\lambda = -0.5$. The red dots give the analytic value of $\pm k_F$.

3.4.2.3 Quasi-particle decay rate

We now turn to the lifetime of the quasiparticles. At zero temperature, from the analytic result (3.34) we infer that the imaginary part of the selfenergy vanishes at $\omega = 0$, $k = k_F$. In Fig. 3.9, which shows the imaginary part of the selfenergy, we see that this behaviour is confirmed numerically. This implies that the spectral function at the Fermi surface is a δ-function at $T = 0$, which is a well-known and defining property of a Fermi liquid. As a consequence, the momentum distribution shows a discontinuity at the Fermi surfaces. Now, the inverse of the imaginary part of the selfenergy $\operatorname{Im}\Sigma^{\pm}$ has SI units of time, and at $\omega = 0$, we associate it to a lifetime for the quasiparticles[10]

$$\tau_{\vec{k}} = \frac{1}{-2Z \operatorname{Im}\Sigma^{\pm}(\vec{k}, 0)} \,. \tag{3.56}$$

The lifetime τ_{k_F} is infinite precisely at the Fermi momentum. We can also define a frequency-dependent decay rate at the Fermi momentum as

$$\Gamma(\omega) = -2Z \operatorname{Im}\Sigma^{\pm}(k_F, \omega) \,. \tag{3.57}$$

[10]Here, we ignore ω-dependent corrections to the lifetime, as the dominant contribution comes from the behaviour at $\omega = 0$.

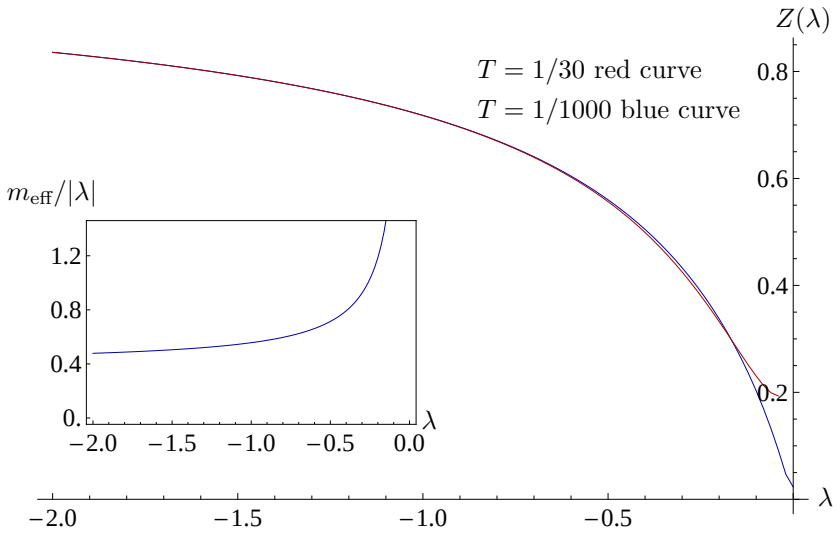

Figure 3.12: Wavefunction renormalization factor Z as a function of λ for $g = 1$, $M = 1/4$ and for different temperatures. Z is only defined for negative λ. The quasiparticle weight lies between one and zero, as expected. It approaches unity for very large and negative values of λ, i.e., very far away from the phase transition. For $\lambda \to 0^-$ it vanishes only strictly at $T = 0$. Due to nonzero-temperature effects, the quasiparticle residue has a nonzero minimum at $\lambda = 0$, which is smaller for the lower temperature curve. The inset shows a plot of $m_{\rm eff}/|\lambda|$ as a function of λ for $M = 1/4$.

At the Fermi surface $\omega = 0$, the decay rate Γ is the inverse of the quasiparticle lifetime, therefore it vanishes for $\omega \to 0$. This behaviour can also be observed in the spectra above. In particular, when T and ω are small but nonzero, the δ-function is broadened, which is indeed visible numerically, as shown in Fig. 3.13. For completeness, we note that the retarded Green's function given in (3.49) can now be written as

$$G_R^-(k,\omega) = \frac{-Z}{\omega - \frac{1}{m_{\rm eff}}(k - k_F)k_F + \frac{i}{2\tau_k}} \,. \tag{3.58}$$

A broadening of the δ-function implies a nonzero decay rate for the quasiparticles. For a normal Fermi liquid, the imaginary part of the selfenergy at the Fermi momentum vanishes at zero temperature and small frequency as ω^2, which stems from Pauli blocking for scattering near the Fermi surface. For small nonzero temperatures, thermal averaging over ω^2 yields a T^2 dependence of the decay rate.

Let us compare this with our numerical results. We observe that the decay rate vanishes much faster than in a conventional Fermi liquid. In Fig. 3.10, we show the first derivative of $\mathrm{Re}\,\Sigma^+(p)$ and the second derivative of $\mathrm{Im}\,\Sigma^+(p)$ as a function of ω

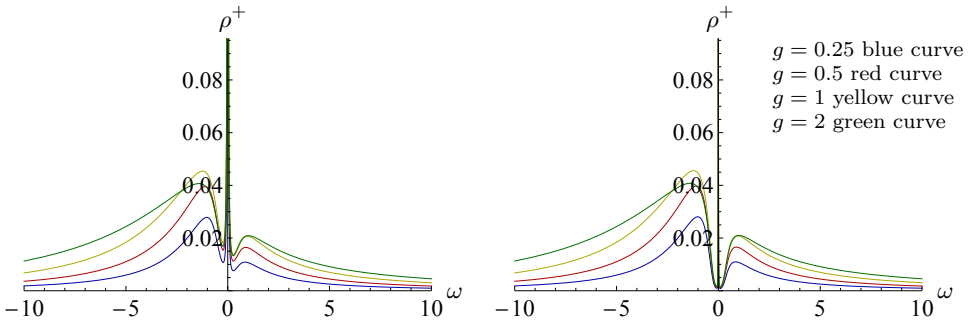

(a) $T = 1/20$ **(b)** $T = 1/50$

Figure 3.13: The spectral function for the spin-up component at the Fermi momentum as a function of ω. In both plots parameters are chosen as $g\lambda = -0.5$. This figure confirms numerically two important points that were made in the text. Firstly, for the higher temperature (a), a sharp peak is just visible at $\omega = 0$. For the lower temperature (b), this sharp peak is still there but is so narrow that it can barely be discerned. This indeed indicates that, at $T = 0$, there is a δ-function behaviour at the Fermi surface, and that this δ-function peak becomes broader as temperature increases. Secondly, close to the Fermi surface, that is, for small ω, the form of the spectrum depends only on the product $g\lambda$. Indeed, all four curves for different g but equal $g\lambda$ overlap for small ω. This overlap is better for lower T. This shows that the scale of the Fermi momentum is indeed set by the combination $g\lambda$ and that the spectra are close to the Fermi surface indeed governed by k_F from (3.47) as we expect.

at $k = k_F$. The former is nonzero at $\omega = 0$, which indicates a nonzero value of Z as explained above. The latter is zero at $\omega = 0$, which shows that the quasiparticle decay rate vanishes faster than ω^2. The behaviour shown in Fig. 3.10 is in agreement with the existence of Fermi surfaces at $k = k_F$, however the decay rate is more suppressed than the typical ω^2 behaviour of a conventional Fermi liquid. This indicates that, next to Pauli blocking, there is another mechanism at hand which strongly suppresses interactions around the Fermi surface for low temperatures T and small frequencies ω. This appears to be a general feature of holographic Fermi liquids and can be understood better by performing a WKB analysis of the bulk Dirac equation.

3.4.3 Second-order WKB analysis around the Fermi surface

In section 3.4.2.3 we have seen that the fermionic quasiparticles are rather stable since their lifetime at the Fermi surface diverges faster than the power law expected from Fermi-liquid theory. To gain more insight into this property, we would like to obtain an analytic expression for the selfenergy at the Fermi surface, that is, we want to know the form of the selfenergy for both $\omega \neq 0$ and $k = k_F \neq 0$. As stated

before, it is not possible to solve the differential equation for ξ exactly for generic nonzero values of ω and k, however, we can deploy the WKB approximation to study the fermionic excitations around the Fermi surfaces analytically, as was done for instance in [104, 134].

In principle, the WKB calculation gives the exact result for the retarded Green's function in the limit $k \to k_F$ and $\omega \ll 1$. Indeed, as we will see, it yields very elegantly the functional form of the selfenergy at the Fermi surface, from which we can derive the behaviour of the quasiparticle lifetime at $k = k_F$. The behaviour turns out to be exponential, i.e.,

$$\mathrm{Im}\,\Sigma \sim e^{-\alpha \frac{k^2}{\omega}} , \tag{3.59}$$

with α a constant to be determined. This result is consistent with the exponential behaviour found in [104, 134]. Furthermore, we also find, to first approximation, an analytical result for the wavefunction renormalization Z, which is consistent with the strong quasiparticle renormalization found numerically. Notably, to obtain the latter result, we have to use the second-order WKB approximation.

However, before presenting the explicit result for the selfenergy of our second-order WKB calculation, we have to mention the following. Obtaining the exact prefactors of the various terms in the final result, e.g. the constant α in (3.59), turns out to be nontrivial. The reason is that several integrals in the computation cannot be performed analytically (see appendix 3.E for details) but have to be evaluated numerically. Alternatively, we could make an approximation to the integrals which, however, turns out to be similarly difficult. Our approach here is to deploy the WKB approximation to gain an understanding of the functional form of the quasiparticle lifetime at the Fermi surfaces. Therefore, the result that we present in equation (3.65) is obtained using the latter method, and so the prefactors, including α, are not exact. At the end of appendix 3.E, we show some numerical evidence for the conjectured value of the constant α.

Let us outline the basic steps of our WKB calculation and refer to appendix 3.E for further details. We determine the Green's function at *zero temperature*. The expansion parameter that plays the role of $1/\hbar$ in the conventional WKB approximation, and that we take to be large in order to satisfy the WKB conditions, is the rescaled momentum (see appendix 3.C.1)[11]

$$\bar{k} = \frac{k}{\sqrt{\omega}} \gg 1 . \tag{3.60}$$

To simplify the calculation we also assume that both ω and $\bar{k}$ are positive, and we introduce the rescaled variable $x = r/\sqrt{\omega}$. Choosing the up and down components

[11] We will specialize to the case of interest $z = 2$ in this section, although the calculation can easily be generalized to arbitrary $z > 1$.

$u_\pm$ and $d_\pm$, respectively, of $\psi_\pm$ introduced in (3.8) as

$$\psi_\pm = \frac{1}{\sqrt{r^5 V(r)}} \begin{pmatrix} u_\pm \\ d_\pm \end{pmatrix} , \tag{3.61}$$

we define new fluctuation fields $y_\pm$ in terms of the original fields $u_\pm$ as

$$y_\pm = \frac{\sqrt{x\bar{k} \pm 1}}{x^{3/2}}\, u_\pm \, . \tag{3.62}$$

Then, the once-iterated Dirac equation can be written as a Schrödinger-like equation

$$\frac{1}{\bar{k}^2} \frac{\mathrm{d}^2}{\mathrm{d}x^2}\, y_\pm(x) - V_\pm(x)\, y_\pm(x) = 0 \, , \tag{3.63}$$

with the effective Schrödinger potential at $T = 0$ of the form

$$V_\pm(x) = \frac{1}{x^4} - \frac{1}{\bar{k}^2 x^6} + \frac{\left(\frac{1}{2} \pm M\right)\left(\frac{3}{2} \pm M\right)}{\bar{k}^2 x^2} + \frac{3}{4} \frac{1}{\left(x\bar{k} \pm 1\right)^2} - \frac{\frac{3}{2} \pm M}{x\bar{k}\left(x\bar{k} \pm 1\right)} \, . \tag{3.64}$$

The characteristic behaviour of the Schrödinger potentials for the chiral components is illustrated in Fig. 3.14. In particular, V_+ has a single classical turning point at x_{tp} and V_- has a pole and a turning point. For $\bar{k} \gg 1$, both effective potentials have a very high potential barrier close to $x \to 0$. For simplicity we present here the calculation only for the plus-component, the result for the minus-component is easily obtained using the symmetry explained in appendix 3.C. Also, we only perform the calculation for the case $M > 0$ so that the single turning point of V_+ at x_{tp} divides the entire range into two regions, a classically allowed region where $V < 0$ and a classically disallowed region where $V > 0$.

The strategy to determine the WKB solution is as follows. We first incorporate the infalling near-horizon boundary condition into the WKB wavefunction in the classically allowed region $x < x_{\mathrm{tp}}$. Then, we apply the usual linearized connection formulae at $x = x_{\mathrm{tp}}$ to continue the solution into the classically disallowed region $x > x_{\mathrm{tp}}$. Next, we match this solution onto the exact near-boundary solution to fix the remaining integration constants. Finally, from the asymptotic expansion of the solution we read off the coefficients $A_\pm$ (see appendix 3.B.2) that determine G_R via $\xi = iA_-/A_+$. The details of this calculation are explained in appendix 3.E, and the final result for the WKB selfenergy reads

$$\Sigma^+(\vec{k}, \omega) = g\, c_1\, k^{2M}\, \frac{\gamma_+}{\epsilon_+}\, \frac{1 - \frac{i}{2}\frac{\gamma_-}{\gamma_+} e^{-i\pi M} e^{-2\frac{k^2}{\omega}}}{1 + \frac{i}{2}\frac{\epsilon_-}{\epsilon_+} e^{i\pi M} e^{-2\frac{k^2}{\omega}}} \, , \tag{3.65}$$

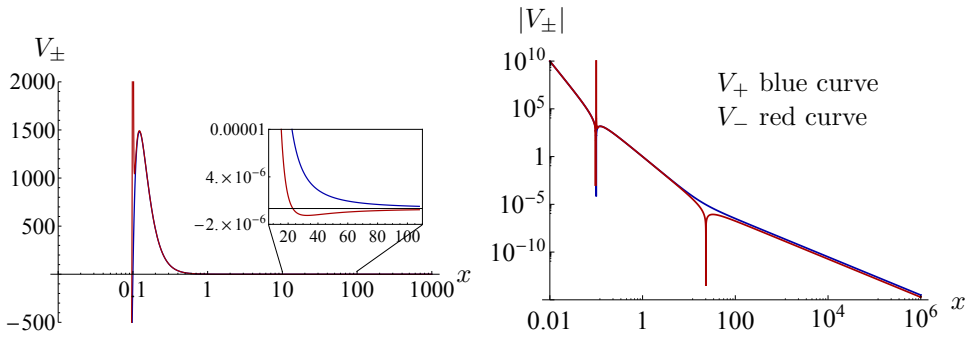

(a) Linear plot of the effective potential $V_\pm$ **(b)** Double-logarithmic plot of $|V_\pm|$

Figure 3.14: Plots of the effective potentials V_+ and V_- (blue and red line) as function of $x = r/\sqrt{\omega}$ at $T = 0$ for $\bar{k} = 10$ and $M = 1/4$. In the near-horizon region $0 < x < x_{\rm tp}$, both effective potentials are negative. The potential V_+ has a turning point at $x_{\rm tp}$, which can be seen as the first dip from the left in (b). V_- has a pole located approximately at the position of the classical turning point of V_+. V_+ is always positive for $x > x_{\rm tp}$, while V_- has a different turning point at an intermediate value of x. This point can be seen in the inset in (a) and as the second dip from the left in (b).

where we employed again $\vec{k} = (0, 0, k_3)$ with $k_3 > 0$, so that the corresponding Green's function in the limit $\bar{k} \gg 1$ reads

$$G_R^+(\vec{k},\omega) = -\left(\omega - \frac{1}{\lambda}k^z - g\,c_1\,k^{2M}\,\frac{\gamma_+}{\epsilon_+}\,\frac{1 - \frac{i}{2}\frac{\gamma_-}{\gamma_+}e^{-i\pi M}e^{-2\frac{k^2}{\omega}}}{1 + \frac{i}{2}\frac{\epsilon_-}{\epsilon_+}e^{i\pi M}e^{-2\frac{k^2}{\omega}}}\right)^{-1} . \tag{3.66}$$

The constant c_1 was given in (3.22), and we defined

$$\epsilon_\pm = 1 \pm \frac{M}{2\bar{k}^2}\log\bar{k} \mp \frac{1}{4\bar{k}^2} , \qquad \gamma_\pm = 1 \pm \frac{M}{2\bar{k}^2}\log\bar{k} \mp \frac{3}{4\bar{k}^2} . \tag{3.67}$$

As mentioned before, the result (3.65) comes from performing an expansion *within* the framework of the WKB calculation. In this case, we find $\alpha = 2$ for the aforementioned coefficient in (3.59), which we can improve by taking into account more terms in the expansion. In particular, as explained in more detail in appendix 3.E, the correct prefactor in the exponent seems to be approximately $\alpha \approx \pi/2$.

After having obtained our result, let us now study the Green's function (3.66) in more detail. As a first consistency check, we see that in the limit $\omega \to 0$, which corresponds to $\bar{k} \equiv k/\sqrt{\omega} \to \infty$, we find the same locus for the Fermi surface at $k = k_F$ as in equation (3.47). Furthermore, the decay rate of the quasiparticle excitations around the Fermi surface is calculated using (3.56) and employing the

imaginary part of the selfenergy at $k = k_F$, which reads

$$\mathrm{Im}\,\Sigma^+(\vec{k}_F,\omega) = \frac{1}{2}\, g\, c_1\, k_F^{2M} \sin\left(\pi\left(M-\tfrac{1}{2}\right)\right) \frac{\gamma_+}{\epsilon_+}\left(\frac{\gamma_-}{\gamma_+}+\frac{\epsilon_-}{\epsilon_+}\right) e^{-2\frac{k_F^2}{\omega}}\ , \tag{3.68}$$

where k_F is given by (3.47). We note that $\gamma_\pm$ and $\epsilon_\pm$ become unity in the strict Fermi-surface limit, and the result thus shows an exponentially suppressed decay rate with additional ω/k_F^2 corrections. This result demonstrates the extremely stable nature of the quasiparticle excitations on the Fermi surface and is consistent with previous WKB calculations that similarly find exponentially narrow decay rates [104, 134]. A comparison with the numerical results is made in Fig. 3.15.

Another analytic result that we extract from (3.65) is the wavefunction renormalization (3.50) on the Fermi surface. This follows from the real part of the selfenergy which reads

$$\mathrm{Re}\,\Sigma^+(\vec{k},\omega) = g\, c_1\, k^{2M}\, \frac{\gamma_+}{\epsilon_+}\ , \tag{3.69}$$

up to exponentially small terms multiplied by $\exp(-\alpha k^2/\omega)$ that will drop out in the limit $\omega \to 0$ after differentiation. Combining (3.69) with (3.47) and (3.50), we arrive at an analytic result for the wavefunction renormalization factor of the form

$$Z = \frac{2\lambda}{2\lambda - 1}\ , \tag{3.70}$$

which for $\lambda < 0$ satisfies $0 \leq Z \leq 1$ as required. We note that, to obtain this nontrivial result different from one, we have to go beyond the leading order in the WKB approximation, since otherwise the derivative of the selfenergy in (3.65) would vanish due to the exponential suppression. Interestingly, because all factors M in (3.67) are multiplied by ω, these drop out in the limit $\omega \to 0$ so that the analytic result (3.70) is independent of M. This is in contrast to the numerical results which do depend on the value of M. The analytic result (3.70) is therefore expected to be the $M = 0$ part of a larger expression, that one may obtain using a more sophisticated WKB calculation. This presumption is supported by Fig. 3.16, which shows that both results are consistent in the case $M = 0$. However, the aim of the WKB calculation was merely to support our numerical results, and finding perfect agreement is beyond the scope of this work.

3.4.4 Phase diagram

The results obtained in the sections above, in particular the plots in Fig. 3.8, can be explained by the existence of a quantum phase transition at $\lambda = 0$ and $g \geq 0$. Firstly, we can understand why there must be different phases. Consider again the Green's function (3.13) and recall that λ can change sign whereas g is required to

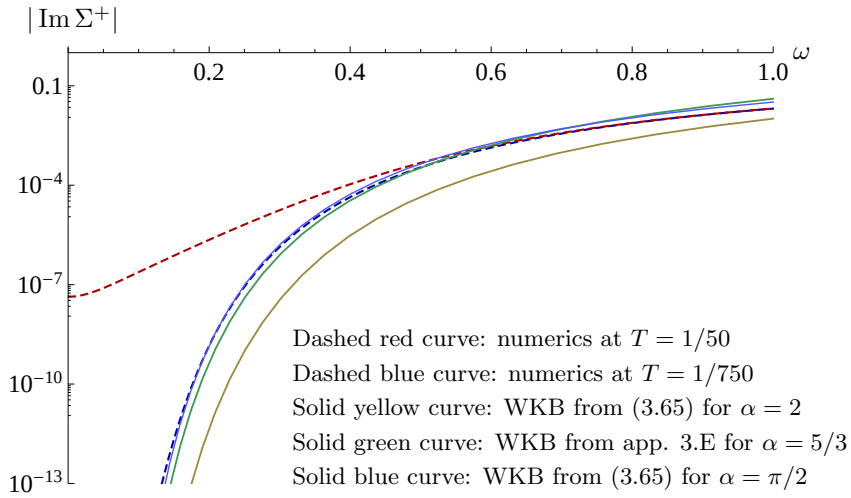

Figure 3.15: Comparison of WKB and numerical results for $|\operatorname{Im}\Sigma^{+}|$ at $k = k_F$ with $\lambda = -1$ yielding $k_F \approx 1.64$, and $M = 1/4$ as a function of ω. The dashed curves are numerical results, the solid curves are second-order WKB results at $T = 0$. Note that the WKB result (3.65) for $\alpha = \pi/2$ agrees very well with the low temperature numerical result.

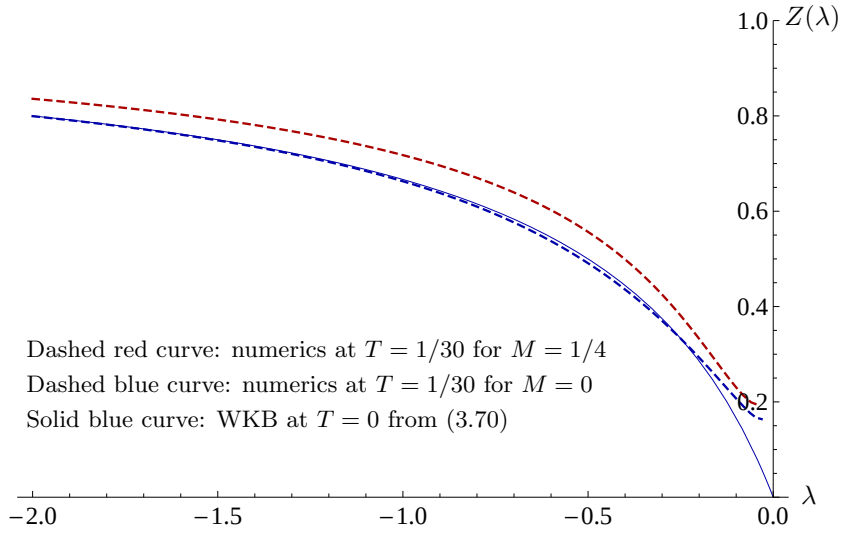

Figure 3.16: Comparison of WKB and numerical results for the quasiparticle residue Z from (3.50) as a function of λ. The dashed curves are numerical results, the solid curve is the second-order WKB result at $T = 0$. This figure shows that the WKB result for Z resembles the $M = 0$ result, indicating that the analytic expression may be the $M = 0$ part of a more general result.

be positive (in the range $-1/2 < M < 1/2$) in order to satisfy the Kramers-Kronig relation. Furthermore, the kinetic term scales as k^z, but the selfenergy is proportional to k^{2M} which is a lower power of k. As a consequence, there will always be a small but nonzero $\vec{k}$ interval at low values of the momentum in which the selfenergy term dominates. When there is a difference in the relative sign, there can be a cancellation between the kinetic and the interaction term in the Green's function at low momenta. This is what brings the Fermi surfaces into existence. When there is no relative sign difference, the selfenergy contribution adds up to the kinetic term, which results in a different behaviour of $N^{\pm}_{\vec{k}}$ and therefore in a different phase. Thus, the crucial property is the possibility of a relative sign change between the kinetic and interaction term which is dominant at low momenta.

We sketch the phase diagram of our system in Fig. 3.17, and relate it to our results for the momentum distribution at various values of λ and T.

- For $\lambda < 0$ and temperatures T small compared to the Fermi energy $\epsilon_F = k_F^z/|\lambda|$, we have a phase with two Fermi surfaces: one for the particles and one for the holes, which can be seen as two sharp discontinuities in the momentum distribution at $k_3 = \pm|k_F|$. The system is formally only a Fermi liquid at exactly zero temperature. Numerically we can obtain only nonzero-temperature results, and the effect of temperature is to smear out the discontinuities over an interval around $\pm|k_F|$. However, when T/ϵ_F is small (outside the critical region) we still see the Fermi-liquid-like or degenerate behaviour. Indeed in Fig. 3.8 for small $\lambda < 0$ the jumps are not infinitely sharp but still very much located around a single value of $\vec{k}$.

- When increasing temperature, in the region $T \sim \epsilon_F$ there is a crossover between the Fermi-liquid phase and the quantum critical phase, indicated by the dashed lines in Fig. 3.17. To calculate the crossover temperature as a function of λ we realize that the crossover occurs when $T \approx \epsilon_F$, thus at

$$T \approx \epsilon_F = \frac{1}{|\lambda|}\, k_F^z = |\lambda|^{\frac{2M}{z-2M}} = g\, c_1 k_F^{2M} \ . \tag{3.71}$$

  In the case $M = 1/4$, $z = 2$, the crossover is at $T \sim |\lambda|^{1/3}$.

- When $T \gg \epsilon_F$ the Fermi surfaces will be smeared out to an extend that they are difficult to identify, as can be seen in Fig. 3.18(a). Then the system is in the quantum critical phase. As $\lambda \to 0^-$, ϵ_F decreases, and as a consequence the Fermi surfaces develop into smooth bumps for very small λ. Numerically, we will always observe temperature effects for small values of $|\lambda|$.

- At $\lambda = 0$ and $T = 0$, there is a quantum phase transition from a phase with two Fermi surfaces to a phase with no Fermi surfaces. At $\lambda = 0$ and $T > 0$,

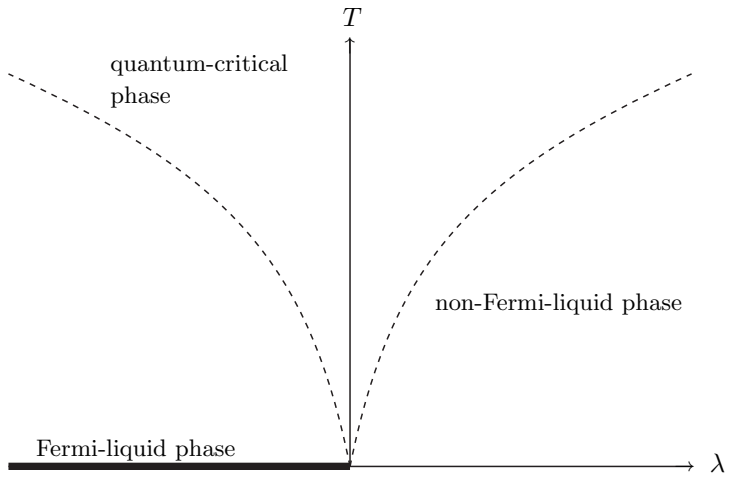

Figure 3.17: Sketch of the phase diagram in the case $-1/2 < M < 1/2$ and $g = 1$, showing the non-Fermi-liquid phase for low T and positive λ, the Fermi-liquid phase for low T and negative λ, and two qualitatively different quantum-critical phases for high temperatures and λ positive and negative. The system is strictly only a Fermi liquid at $T = 0$ (thick line), but has Fermi-liquid-like behaviour for low temperatures. The dashed curves correspond to the crossovers to the quantum-critical regimes. There is a quantum phase transition at $\lambda = 0$, $T = 0$.

the system is in the quantum critical phase. Interestingly, there is a qualitative difference between the quantum critical $\lambda < 0$ and $\lambda > 0$ phases, see Fig. 3.18(b) for an impression of the behaviour of $N_{\vec{k}}^{\pm}$ for very small λ.

- In the case $\lambda > 0$, the momentum distribution has a kink-like behaviour and is centered around $k = 0$. For $T \ll \epsilon_F$, the width of the kink is determined by $k_F \equiv (g\lambda c_1)^{1/(z-2M)}$, whereas for $T \gg \epsilon_F$ it is determined by T, see Fig. 3.18(c).

3.4.5 Fermi surfaces and the quantum phase transition for $\frac{1}{2} < |M| < \frac{z}{2}$

In the previous sections, we have studied the system in the particular range $0 < M < 1/2$ and we have demonstrated the appearance of Fermi surfaces for $\lambda < 0$. However, we obtain a similar behaviour also for positive values of λ if we consider $1/2 < M < z/2$ and $-z/2 < M < -1/2$.

Let us demonstrate this for $1/2 < M < z/2$. In this case, the relation between the selfenergy $\Sigma(p)$ and the bulk quantity $\xi(r, p)$ is given by equation (3.16). However, the expression (3.134) for the Green's function is unchanged because this form is

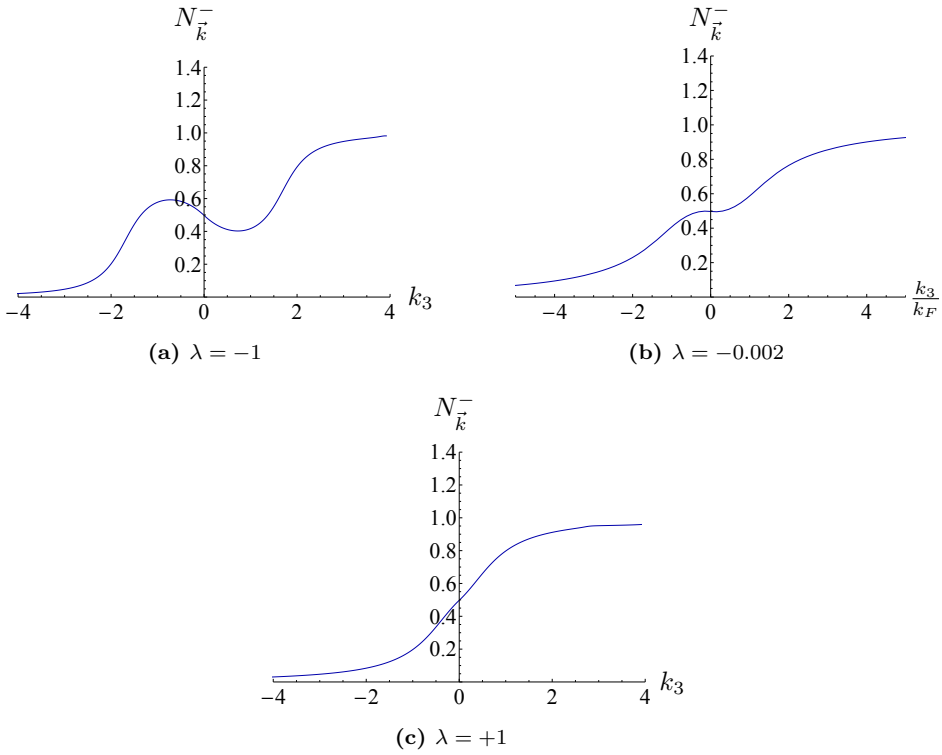

(a) $\lambda = -1$ **(b)** $\lambda = -0.002$

(c) $\lambda = +1$

Figure 3.18: Momentum distribution in the quantum critical region for $T = 5$, $g = 1$, $M = 1/4$ and various values of λ. For $\lambda < 0$, the momentum distribution always shows two extrema at nonzero k_3, which develop into Fermi surfaces when the temperature is lowered. This is shown in (a). The behaviour for small negative λ is illustrated in figure (b) with $k_F \approx 0.026$. Note that because k_F is relatively small, we plotted $N^-_{\vec{k}}$ here as a function of k_3/k_F for clarity. For $\lambda > 0$ the momentum distribution is very broad as can be seen in (c).

determined solely by the symmetry properties of $\xi(r, p)$, which are also satisfied by the counterterm in (3.16). In particular, the $\omega \to 0$ limit of the dispersion relation is again given by equation (3.46) which we recall for convenience,

$$\frac{1}{\lambda}\, k^z + g\, k^{2M} c_1 = 0\,. \tag{3.72}$$

Now, we can find a nontrivial, real solution to this equation in the range $1/2 > M > z/2$ *for positive* λ because the constant c_1 given by (3.22) is negative in this range. Note that the same conclusion applies for $-z/2 < M < -1/2$. Thus, we now obtain Fermi surfaces for positive λ in these ranges for M. Furthermore, we

also find a quantum phase transition at $\lambda = 0$ below which the aforementioned Fermi surfaces disappear.

3.5 Conclusion and discussion

In our recent work [71] we proposed the construction of a holographic fermionic retarded Green's function modified to describe single-particle correlations, using the AdS/CMT correspondence. Two aspects of this prescription that make it particularly interesting for condensed-matter applications, are the following. Firstly, the retarded Green's function satisfies the zeroth frequency sum rule and the Kramers-Kronig relation both at zero and also at nonzero temperatures. We have checked that this is the case analytically where possible, see appendix 3.D, and otherwise numerically. This shows that the correlation function is a genuine single-particle correlation function that can be compared to experimental ARPES data. Secondly, it can describe quantum critical points with relativistic as well as nonrelativistic dynamical exponent $z > 1$, as a consequence of the (approximate) Lifshitz isometry of the used bulk spacetime.

In this paper, we have investigated the physics arising from this modified holographic prescription. The resulting spectral-weight function and dispersion relations that we presented in section 3.3, show that we are describing a particle-hole symmetric, gapless, chiral boundary system that behaves as a strongly interacting Weyl semimetal in the sense that it satisfies the Weyl equations in the noninteracting and low-energy limit. To be more precise, our results show that the system has strong interactions in the infrared, where the selfenergy is dominant over the kinetic energy, while in the far ultraviolet the system becomes free.

An important point mentioned in the introduction is repeated here. We use holography here in a bottom-up approach. This means that the model is an effective low-energy theory which has the properties of a Weyl semimetal as described above. As with all holographic AdS/CMT models, the microscopic structure of the actual boundary system is unknown. We do not claim to describe the emergence of a Weyl fermion from a chirality-invariant microscopic structure. What we present is a specific model that may or may not be able to capture the IR physics of generic realistic Weyl semimetals. Our working assumption is that the Weyl semimetal under consideration gives rise to a strongly-coupled, chiral, scale-invariant theory in the IR. The main problem here is that in principle, we cannot be sure that our holographically obtained selfenergy corresponds sufficiently accurately to a selfenergy that stems from Coulomb interactions between the (chiral) electrons. This should be scrutinized for instance using feedback from future experiments on realistic materials.

On the other hand, bottom-up model building has the advantage of being able to capture a wide range of possible situations, and it provides an exploratory study of possible strongly-coupled dynamics. The model that we consider is specified by the following features:

1. The IR theory is Lifshitz invariant with dynamical scaling exponent z.
2. Single-particle excitations are coupled to the CFT only through a single channel, specified by the scaling dimension of the chiral CFT operator that is determined by the corresponding bulk fermion mass M.
3. The chemical potential, corresponding to the number of particles, vanishes. In condensed-matter language this means that there is particle-hole symmetry.
4. Considering the single-particle dispersion relation, the single-particle cones of definite chirality are separated in momentum space in the IR and we are considering only the physics of one of these cones.

Assumption 1. is fairly general and covers a wide range of interesting IR physics. Assumption 2. is merely a simplifying working assumption. The single fermion in this model is described by a dynamical source field that is coupled to gauge-invariant composite operators in the dual CFT, and we do not claim that this generally happens in nature. However, many CFTs exhibit a discrete spectrum of scaling dimensions, making it plausible that one particular channel will contribute dominantly to the selfenergy of a single fermion in the IR. Assumptions 3. and 4. are merely a convenient restriction of this paper. What is presented in this work corresponds to a subspace in the phase diagrams of these types of models specified by zero chemical potential and neglecting (large-momentum) Umklapp processes that couple the two cones. However, this subspace is not unrealistic. The chemical potential couples to the number of particles minus the number of holes in the spectrum of the theory. In the case of zero chemical potential there is still nontrivial IR dynamics in the form of particle-hole excitations. Indeed, at zero doping the various phases and the corresponding quantum phase transition described in section 3.4 are realized. The scale that governs the quantum phase transition is an appropriate combination of the parameters g and λ appearing in our prescription. As a generalization of our holographic model for a Weyl semimetal we will extend the prescription to nonzero doping in future work. This is interesting for condensed-matter purposes as it corresponds for instance to turning on a gate voltage in the material. Holographically this can be done by adding another U(1) gauge field to the bulk spacetime under which the fermions are charged, and by considering charged Lifshitz black branes [135]. It will be interesting to investigate the consequences for the phase diagram described in section 3.4. Finally, the simplified description obtained by focusing on a single

chiral sector is reasonable, as we are interested in energy scales lower than the scale separating the two chiral cones in momentum space. Indeed we are currently working on generalizing this picture to two (opposite) chiral cones.

Weyl semimetals have recently received considerable interest in the condensed-matter community because of their fascinating and unusual properties that result from the topological nature of the band structure [17, 24, 112, 129, 136–139]. In order to investigate the band structure, the Weyl semimetals are usually treated as free or weakly interacting systems. Using our holographic prescription for models of Weyl semimetals, we are now also able to explore these systems when they are strongly interacting or critical. In particular, the inclusion of a holographic selfenergy leads to the existence of several different phases including a Fermi-liquid phase and a non-Fermi-liquid phase, separated by a quantum phase transition, as we have shown in section 3.4.

There are various interesting directions in which our prescription can be extended. Firstly, our current prescription is intended to describe single-particle correlation functions, which appear often in condensed matter. However, in experiments one also encounters two-particle correlation functions. Important examples include the current-current correlation function that determines the electrical conductivity, σ, and the heat current-heat current correlation function which is related to the thermal conductivity κ. The electrical conductivity has been investigated in a holographic context before, starting with [63], but it would be interesting to also consider this particular function using our holographic prescription. In particular, since our present discussion is at zero doping, that is, it contains an equal amount of particles and holes, we expect the corresponding conductivity in the boundary system to remain finite in the $\omega \to 0$ limit even without impurities. Additionally, in Fermi-liquid theory the thermal conductivity κ scales as $1/T$, whereas the electrical conductivity σ scales as $1/T^2$. Their ratio is therefore proportional to temperature, i.e., $\kappa/\sigma \sim T$, which is the famous Wiedemann-Franz law. It would be interesting to investigate whether this law also holds here using the holographic results for electrical and thermal conductivity.

A topic often discussed in the AdS/CMT literature is the well-known Luttinger theorem from Fermi-liquid theory, which states that the total particle density in a system is proportional to the total volume in momentum space enclosed by its Fermi surfaces. In our case, this can be checked as follows. The system we describe is at zero doping, so the total number density of the particles and holes together is zero. The Fermi surfaces for particles and holes separately enclose a nonzero volume, but the difference in volume enclosed by the Fermi surfaces is zero. Therefore, the Luttinger theorem is trivially satisfied in our case.

Finally, whereas our current prescription takes into account only the leading-order contributions in the $1/N$ expansion, it would be interesting to also consider quantum

or $\mathcal{O}(1/N)$ corrections. In particular, it is sometimes proposed [140] that the typical feature of holographic Fermi liquids, an exponentially suppressed quasiparticle decay rate at the Fermi surface, may be a large N remnant, i.e., a consequence of the fact that the leading order does not take into account all possible quasiparticle decay processes. Therefore, considering also $1/N$ contributions may resolve this problem and restore the conventional ω^2 power-law behaviour, which is rather robust in Fermi liquids. An example of $1/N$ corrections that are ignored here, are the back-reaction of the massive fermions on the gravitational background in the bulk, but one may also think of other $1/N$ corrections.

3.A Conventions

3.A.1 A note on dimensions and units

In this paper, we work with natural units in which $\hbar = c = k_B = 1$, where k_B is Boltzmann's constant, and we use dimensionless coordinates $r, t, \vec{x}$. As a consequence, Newton's constant G_{d+1} as well as the metric are dimensionless. However, to convert the Lifshitz metric (3.3) to standard SI units, we introduce a length scale l and define the dimensionful expression

$$\mathrm{d}\tilde{s}^2 \equiv l^2 \mathrm{d}s^2 = \frac{l^2}{\tilde{r}^2}\frac{\mathrm{d}\tilde{r}^2}{V^2(\tilde{r})} - V^2(\tilde{r})\,\frac{\tilde{r}^{\,2z}}{l^{2z}} c^2 \mathrm{d}\tilde{t}^{\,2} + \frac{\tilde{r}^{\,2}}{l^2}\mathrm{d}\vec{\tilde{x}}^{\,2}\ , \tag{3.73}$$

where

$$\tilde{r} = l\, r\ , \qquad \vec{\tilde{x}} = l\,\vec{x}\ , \qquad \tilde{t} = \frac{l}{c}\, t\ , \tag{3.74}$$

which has the correct units of meter and second, respectively. Note that l can be interpreted as the scale characterizing the size of the Lifshitz spacetime. The temperature of the black brane, obtained in (3.4), can be converted to have dimension of Kelvin by the rescaling

$$\tilde{T} = \frac{\hbar c}{k_B}\frac{T}{l}\ , \tag{3.75}$$

and the mass of the fermions in SI units takes the form

$$\tilde{M} = \frac{\hbar M}{cl}\ . \tag{3.76}$$

Next, $\tilde{G}_{d+1}$ is Newton's constant which has dimension $\mathrm{m}^d \cdot \mathrm{s}^{-2} \cdot \mathrm{kg}^{-1}$. To convert the dimensionless frequencies ω and momenta $\vec{k}$ to SI units, one should rescale

$$\tilde{\omega} = \frac{c}{l}\,\omega\ , \qquad \vec{\tilde{k}} = \frac{\vec{k}}{l}\ . \tag{3.77}$$

Employing the results of this section, the reader can at any time convert to physical units. However, for ease of notation, we present our analysis and results in dimensionless coordinates.

3.A.2 Vielbeins and Dirac matrices

Here, we collect some formulae related to the spin connection and vielbeins, and state our choice of Dirac matrices. The vielbeins are denoted by $e^{\underline{a}}{}_{\mu}$ with $\mu = 0, \ldots, d$ and $\underline{a} = 0, \ldots, d$, and satisfy

$$g_{\mu\nu} = e^{\underline{a}}{}_{\mu}\, \eta_{\underline{ab}}\, e^{\underline{b}}{}_{\nu} \,, \qquad \eta_{\underline{ab}} = \mathrm{diag}\,(-1, +1, \ldots, +1) \,. \tag{3.78}$$

We will furthermore employ the following notation and relations

$$e^{\underline{a}} = e^{\underline{a}}{}_{\mu} \mathrm{d}x^{\mu} \,, \qquad \Omega^{\underline{a}}{}_{\underline{b}} = (\Omega_{\mu})^{\underline{a}}{}_{\underline{b}}\, \mathrm{d}x^{\mu} \,, \qquad 0 = \mathrm{d}e^{\underline{a}} + \Omega^{\underline{a}}{}_{\underline{b}} \wedge e^{\underline{b}} \,, \tag{3.79}$$

where Ω is the torsion-free spin connection. Given the metric (3.3), we can read off

$$e^{\underline{r}} = \frac{\mathrm{d}r}{rV} \,, \qquad e^{\underline{t}} = r^z V \, \mathrm{d}t \,, \qquad e^{\underline{i}} = r \, \mathrm{d}x^i \,, \tag{3.80}$$

where $\underline{a} = \{\underline{t}, \underline{r}, \underline{i}\}$ with $i = 2, \ldots, d$ labeling the spatial directions. Using the relation in (3.79) as well as the antisymmetry of Ω, we determine its nonvanishing components as

$$\Omega^{\underline{t}}{}_{\underline{r}} = rV\, \partial_r \big(r^z V\big)\, \mathrm{d}t \,, \qquad \Omega^{\underline{i}}{}_{\underline{r}} = rV \mathrm{d}x^i \,. \tag{3.81}$$

For the spinors, we use the following notation

$$\overline{\Psi} = \Psi^{\dagger}\Gamma^{\underline{t}} \,, \qquad \mathcal{D}_{\mu} = \partial_{\mu} + \frac{1}{4}\,(\Omega_{\mu})_{\underline{ab}}\Gamma^{\underline{ab}} \,, \qquad \not{\mathcal{D}} = \Gamma^{\underline{a}} e_{\underline{a}}{}^{\mu} \mathcal{D}_{\mu} \,. \tag{3.82}$$

Here, $e_{\underline{a}}{}^{\mu}$ is the inverse transpose of $e^{\underline{a}}{}_{\mu}$ and the symbol $\Gamma^{\underline{ab}}$ is defined in terms of the Gamma matrices $\Gamma^{\underline{a}}$ as

$$\Gamma^{\underline{ab}} = \frac{1}{2}\,\big[\Gamma^{\underline{a}}, \Gamma^{\underline{b}}\big] \,. \tag{3.83}$$

We also perform chiral projections using

$$\Psi_{\pm} \equiv \frac{1}{2}\,\big(1 \pm \Gamma^{\underline{r}}\big)\,\Psi \,, \qquad \Gamma^{\underline{r}}\,\Psi_{\pm} = \pm\,\Psi_{\pm} \,. \tag{3.84}$$

A convenient choice of Gamma matrices reads as follows [141]:

- For odd dimensions d, we can choose

$$\Gamma^{\underline{r}} = \begin{pmatrix} \mathbb{1} & 0 \\ 0 & -\mathbb{1} \end{pmatrix} \,, \qquad \Gamma^{\underline{t}} = \begin{pmatrix} 0 & \gamma^{\underline{0}} \\ \gamma^{\underline{0}} & 0 \end{pmatrix} \,, \qquad \Gamma^{\underline{i}} = \begin{pmatrix} 0 & \gamma^{\underline{i}} \\ \gamma^{\underline{i}} & 0 \end{pmatrix} \,, \tag{3.85}$$

where the γ-matrices are the d-dimensional Dirac matrices of the boundary theory. We then decompose Ψ into chiral components of the bulk spinor,

$$\Psi = \begin{pmatrix} \psi_+ \\ \psi_- \end{pmatrix} , \tag{3.86}$$

where the components $\psi_\pm$ are chiral in the bulk, but they are Dirac spinors on the boundary.

- In the case when d is even, a natural choice is given by

$$\Gamma^{\underline{r}} = \gamma^{d+1} , \qquad \Gamma^{\underline{t}} = \gamma^0 , \qquad \Gamma^{\underline{i}} = \gamma^{\underline{i}} , \tag{3.87}$$

where γ^{d+1} is the analog of γ^5 in four dimensions and γ are the gamma matrices of the boundary theory. In this case $\Psi_\pm$ correspond to operators with *definite chirality* on the boundary.

- Most of our interest lies in the case $d = 4$. Using (3.84), and with a slight abuse of notation, we write the four-component Dirac bulk spinor Ψ in terms of two-component spinors Ψ_+ and Ψ_- as

$$\Psi = \begin{pmatrix} \Psi_+ \\ \Psi_- \end{pmatrix} . \tag{3.88}$$

The four-dimensional gamma matrices can be expressed in terms of $\sigma^{\underline{a}} = (1, \vec{\sigma})$ and $\overline{\sigma}^{\underline{a}} = (-1, \vec{\sigma})$ with $\sigma^{\underline{i}}$ being the Pauli matrices in the following way

$$\Gamma^{\underline{a}} = \begin{pmatrix} 0 & \overline{\sigma}^{\underline{a}} \\ \sigma^{\underline{a}} & 0 \end{pmatrix} , \qquad \underline{a} = \{\underline{t}, \underline{i}\} . \tag{3.89}$$

3.B Details on the near-boundary asymptotics

3.B.1 Dirac equation

The Dirac equation for the fermion field Ψ can be obtained from varying the action (3.6) with respect to $\overline{\Psi}$, and imposing $\delta\Psi_+ = 0$ at $r = r_0$ (see [71] for more details). We find the usual expression $(\not{\mathcal{D}} - M)\Psi = 0$, which can be written as follows

$$\left[rV\,\Gamma^{\underline{r}}\partial_r + \frac{i}{r}\,\Gamma\cdot\tilde{k} + \frac{1}{2}\,\Gamma^{\underline{r}}\,p_z(r) - M \right]\psi(r) = 0 . \tag{3.90}$$

Here we defined the function $p_z(r) = r^{1-z}\partial_r[r^z V] + (d-1)V$, and used the notation $\Gamma\cdot\tilde{k} = \Gamma^{\underline{t}}\tilde{\omega} + \Gamma^{\underline{i}}k_i$ together with the *generalized momenta*

$$\tilde{k} = \big(\tilde{\omega}, k_i\big) , \qquad \tilde{\omega} = -\frac{\omega}{r^{z-1}V} . \tag{3.91}$$

Next, we can simplify equation (3.90) by introducing

$$\psi(r) = \frac{1}{\sqrt{r^{d-1+z}V}}\,\phi(r)\,, \tag{3.92}$$

which leads to

$$\left[\, rV\,\Gamma^r\partial_r + \frac{i}{r}\,\Gamma\cdot\tilde{k} - M\,\right]\phi(r) = 0\,. \tag{3.93}$$

In terms of the chiral components $\phi_\pm(r)$, the Dirac equation (3.93), both in even and odd dimensions d, then reads

$$\phi_\pm(r) = \mp\frac{i}{\tilde{k}^2}\,(\gamma\cdot\tilde{k})\,\mathcal{A}(\mp M)\,\phi_\mp(r)\,, \qquad \mathcal{A}(M) \equiv r\big(rV\partial_r - M\big)\,, \tag{3.94}$$

where we employed the notation for the Γ matrices given in appendix 3.A.2. Finally, we can also derive a *second-order* equation by applying $\mathcal{A}(\pm M)(\gamma\cdot\tilde{k})$ to both sides of the Dirac equation in (3.94), which leads to

$$\tilde{k}^2\phi_\pm(r) = \mathcal{A}(\mp M)\mathcal{A}(\pm M)\phi_\pm(r) - r^2V\,\frac{\partial_r\tilde{\omega}}{\tilde{k}^2}\,\gamma^0(\gamma\cdot\tilde{k})\mathcal{A}(\pm M)\phi_\pm(r)\,. \tag{3.95}$$

Note that for the case of interest in this paper, that is $d = 4$, half of the components in equations (3.94) and (3.95) are trivial, because we can use the Weyl representation of the gamma matrices so that $\phi_\pm$ correspond to the upper and lower two components of ϕ.

3.B.2 Asymptotic solutions near the boundary

We now determine the form of the asymptotic solutions near the boundary at $r = \infty$. In contrast to the AdS case with $z = 1$, for $z \neq 1$, the asymptotics are different for vanishing and nonvanishing spatial momentum $\vec{k}$. We therefore consider both cases in turn.

Asymptotics for $\vec{k} = 0$

In the case of vanishing spatial momentum, we make a power-law ansatz for the second-order differential equation of the chiral components. The asymptotic expansion near the boundary then comprises two independent solutions and is given by

$$\phi_\pm = r^{\pm M}\left(1 + r^{-2z}c_\pm + \ldots\right)A_\pm + r^{\mp M - z}\left(1 + r^{-2z}d_\pm + \ldots\right)B_\pm\,, \tag{3.96}$$

where we included subleading corrections in the two separate branches. Here, $A_\pm$ and $B_\pm$ are spinors in the Clifford algebra, and the coefficients $c_\pm$ and $d_\pm$ are matrices therein. We also observe that (3.96) agrees with the AdS case [141] for $z = 1$, and we

note that a subleading term in the A (or B) branch can be more dominant over the leading term in the B (or A) branch for certain ranges of M and z. Employing the expansion (3.96) in the first order Dirac equation (3.94), we derive a local relation between $B_\mp$ and $A_\pm$ of the form

$$B_\pm = -i\frac{\omega\gamma^0}{2M \pm z}A_\mp \ , \tag{3.97}$$

which fixes half of the integration constants. The coefficients of the subleading terms are found as

$$c_\pm = \frac{\omega^2}{2z(\pm 2M - z)} \ , \qquad d_\pm = \frac{\omega^2}{2z(\mp 2M - 3z)} \ . \tag{3.98}$$

However, here we need to assume that the subleading terms in the expansion (3.96) are still leading over the subleading terms in the Dirac equation (3.94) which appear in the function V. A careful analysis translates this assumption into the condition

$$z < d - 1 \ . \tag{3.99}$$

As we can see from (3.97) and (3.98), the above analysis breaks down for $M = \pm z/2$. Moreover, in that case the powers in the asymptotic expansion (3.96) can become equal and so the spinor coefficients cannot be disentangled. The way to treat the case $M = \pm z/2$ is to allow for logarithmic terms in the asymptotic expansion, which lift the degeneracy in the two branches A and B. In particular, for $M = -z/2$ we have

$$\begin{aligned} \phi_+ &= r^{-\frac{z}{2}}A_+ + r^{-\frac{z}{2}}\log(r)B_+ + \dots \ , \\ \phi_- &= r^{+\frac{z}{2}}\Big(1 + c_- r^{-2z}\log(r) + \dots\Big)A_- + r^{-3\frac{z}{2}}\Big(1 + \dots\Big)B_- \ , \end{aligned} \tag{3.100}$$

with the coefficients of the form

$$B_+ = i\omega\gamma^0 A_- \ , \qquad B_- = \frac{i\omega\gamma^0}{2z}A_+ \ , \qquad c_- = \frac{\omega^2}{2z} \ . \tag{3.101}$$

For $M = +z/2$, we find

$$\begin{aligned} \phi_+ &= r^{+\frac{z}{2}}A_+ + r^{-3\frac{z}{2}}B_+ + \dots \ , \\ \phi_- &= r^{-\frac{z}{2}}A_- + r^{-\frac{z}{2}}\log(r)B_- + \dots \ , \end{aligned} \tag{3.102}$$

together with

$$B_- = -i\omega\gamma^0 A_+ \ , \qquad B_+ = -\frac{i\omega\gamma^0}{2z}A_- \ . \tag{3.103}$$

Asymptotics for $\vec{k} \neq 0$

For nonzero spatial momenta $\vec{k}$ and generic values of the Dirac mass M, the asymptotic solution to the second-order differential equation (3.95) reads

$$\phi_\pm = r^{\pm M}\left(1 + r^{-2}c_\pm + \ldots\right) A_\pm + r^{\mp M-1}\left(1 + r^{-\delta_\pm} d_\pm + \ldots\right) B_\pm \,. \tag{3.104}$$

Note the important difference compared to (3.96), namely that the exponent of the leading order term does not depend on z. The relation between $A_\pm$ and $B_\mp$ can again be derived via the first-order Dirac equation (3.94). Together with the subleading coefficient $c_\pm$, their form reads

$$B_\pm = i\frac{\vec{k}\cdot\vec{\gamma}}{2M \pm 1} A_\mp \,, \qquad\qquad c_\pm = -\frac{\vec{k}^2}{2(\pm 2M - 1)} \,. \tag{3.105}$$

The subleading behaviour in the B branch turns out to be more complicated. Both the exponent $\delta_\pm$ and the coefficient $d_\pm$ depend on the value of z. We have to distinguish between three separate cases

$$\begin{aligned}
1 < z < 3 \,: \qquad & \delta_\pm = z - 1 \,, \qquad && d_\pm = \frac{\omega}{\vec{k}^2}\left(\frac{\pm 2M + 1}{\pm 2M + z}\right)\vec{\gamma}\cdot\vec{k} \,, \\
z = 3 \,: \qquad & \delta_\pm = 2 \,, && d_\pm = \frac{1}{3 \pm 2M}\left(\frac{\vec{k}^2}{2} + \frac{\omega}{\vec{k}^2}(2M \pm 1)\,\vec{\gamma}\cdot\vec{k}\right) \,, \\
3 < z \,: \qquad & \delta_\pm = 2 \,, && d_\pm = \frac{\vec{k}^2}{2(3 \pm 2M)} \,.
\end{aligned} \tag{3.106}$$

As is clear from (3.105), the case of $M = \pm 1/2$ is again special and needs to be treated separately. Along similar lines as for vanishing momenta, logarithmic terms will appear in the expansion.

3.B.3 Hydrodynamic limit

We can determine the Green's function analytically in the strict hydrodynamic limit $\omega \to 0$, $\vec{k} \to 0$ for arbitrary temperatures T in the region $|M| < z/2$. However, one has to be careful in defining this limit because the $r \to r_h$ and $\omega \to 0$ limits do not commute in the differential equation (3.17). Here, we define the limiting procedure as first setting $\vec{k} = 0$, and then taking $\omega \to 0$ while keeping T finite. Thus, we should use the same boundary condition $\xi(r_h) = i$ as before. The differential equation (3.17) for $\xi(r)$ then becomes

$$r^2 V \partial_r \xi_\pm + 2Mr\xi_\pm = 0 \,, \tag{3.107}$$

whose solution with the boundary condition $\xi_+(r_h) = i$ reads

$$\xi_\pm(r) = i\, e^{-2M\int_{r_h}^{r} \frac{\mathrm{d}t}{t\,V(t)}} \,. \tag{3.108}$$

Substituting then the expression for $V(r)$ given in (3.3) and performing the integral, we find

$$\xi_{\pm}(r) = i \left(\frac{r}{r_h}\right)^{-2M} \left[1 + V(r)\right]^{-\frac{4M}{d+z-1}} , \tag{3.109}$$

where we have left the dimension d and the dynamical exponent z unspecified. The selfenergy appearing in the Green's function is given by (3.14), and so we obtain

$$G_R(\vec{0}, 0) = \frac{i}{g}\, 2^{\frac{4M}{d+z-1}} \left(\frac{d+z-1}{4\pi}\right)^{\frac{2M}{z}} T^{-\frac{2M}{z}} , \tag{3.110}$$

where we employed (3.4) to related r_h to the temperature T. Note that this expression is valid for $d + z - 1 \neq 0$, which includes the case of interest in this paper, namely $d = 4$ and $z = 2$.

3.C Symmetry properties of the Green's function

In this appendix, we discuss symmetries of the selfenergy $\Sigma(p)$ defined in (3.14) and of the full Green's function (3.13). This analysis utilizes the properties of the differential equation (3.17) and boundary condition (3.18), which we recall for convenience

$$r^2 V \partial_r \xi_{\pm} + 2Mr\xi_{\pm} = \frac{\omega}{r^{z-1}V} \mp k_3 + \left(\frac{\omega}{r^{z-1}V} \pm k_3\right) \xi_{\pm}^2 , \qquad \xi_{\pm}(r_h) = i . \tag{3.111}$$

3.C.1 Scale-invariant variables

We start our discussion with the scaling properties of (3.111). To simplify our notation, we define the constant $\kappa = \frac{d+z-1}{4\pi}$, and we can distinguish three cases which will be considered in turn.

- We define new variables in the following way

$$\overline{\omega} = \frac{\omega}{k_3^z} , \qquad \overline{T} = \frac{T}{k_3^z} , \qquad x = \frac{r}{k_3} , \tag{3.112}$$

  which leads to

$$V = \sqrt{1 - \left(\frac{x_h}{x}\right)^{d+z-1}} , \qquad x_h = \left(\frac{\overline{T}}{\kappa}\right)^{\frac{1}{z}} . \tag{3.113}$$

  The differential equations (3.111) then takes the form

$$x^2 V \partial_x \xi_{\pm} + 2Mx\xi_{\pm} = \frac{\overline{\omega}}{x^{z-1}V} \mp 1 + \left(\frac{\overline{\omega}}{x^{z-1}V} \pm 1\right) \xi_{\pm}^2 , \qquad \xi_{\pm}(x_h) = i , \tag{3.114}$$

  and we obtain

$$\xi_{\pm}\big(\overline{x}_0, \overline{\omega}, \overline{T}\big) = k_3^{-2M}\, \xi_{\pm}\big(r_0, \omega, k_3, T\big) . \tag{3.115}$$

- Along similar lines, we can define another set of variables as follows

$$\overline{k} = \frac{k_3}{\omega^{\frac{1}{z}}} , \qquad \overline{T} = \frac{T}{\omega} , \qquad y = \frac{r}{\omega^{\frac{1}{z}}} , \tag{3.116}$$

leading to

$$V = \sqrt{1 - \left(\frac{y_h}{y}\right)^{d+z-1}} , \qquad y_h = \left(\frac{\overline{T}}{\kappa}\right)^{\frac{1}{z}} , \tag{3.117}$$

as well as

$$y^2 V \partial_y \xi_\pm + 2My\xi_\pm = \frac{1}{y^{z-1}V} \mp \overline{k} + \left(\frac{1}{y^{z-1}V} \pm \overline{k}\right) \xi_\pm^2 , \qquad \xi_\pm(y_h) = i . \tag{3.118}$$

We then find

$$\xi_\pm\big(\overline{y}_0, \overline{k}, \overline{T}\big) = \omega^{-\frac{2M}{z}} \, \xi_\pm\big(r_0, \omega, k_3, T\big) . \tag{3.119}$$

- Finally, we can define variables as

$$\overline{\omega} = \frac{\kappa}{T}\,\omega , \qquad \overline{k} = \left(\frac{\kappa}{T}\right)^{\frac{1}{z}} k_3 , \qquad z = \frac{r}{r_h} , \tag{3.120}$$

where we recall that $r_h = (T/\kappa)^{\frac{1}{z}}$. The above choice implies

$$V = \sqrt{1 - \left(\frac{z_h}{z}\right)^{d+z-1}} , \qquad z_h = 1 , \tag{3.121}$$

and the differential equations become

$$z^2 V \partial_z \xi_\pm + 2Mz\xi_\pm = \frac{\overline{\omega}}{r^{z-1}V} \mp \overline{k} + \left(\frac{\overline{\omega}}{r^{z-1}V} \pm \overline{k}\right) \xi_\pm^2 , \qquad \xi_\pm(z_h) = i . \tag{3.122}$$

We then have

$$\xi_\pm\big(\overline{z}_0, \overline{\omega}, \overline{k}\big) = \left(\frac{T}{\kappa}\right)^{-\frac{2M}{z}} \xi_\pm\big(r_0, \omega, k_3, T\big) . \tag{3.123}$$

3.C.2 Chirality

From equation (3.111) we observe that the spin-up and spin-down components ξ_+ and ξ_- are related by a reflection of the momentum

$$\xi_\pm(r, k_3, \omega) = \xi_\mp(r, -k_3, \omega) . \tag{3.124}$$

Furthermore, equations (3.14) and (3.13) which relate ξ to the selfenergy $\Sigma(p)$ and to the Green's function Σ to G_R do not spoil this symmetry. We thus obtain the following relation for the components of the full Green's function

$$G_R^{\pm}(\vec{k},\omega) = G_R^{\mp}(-\vec{k},\omega) \ . \tag{3.125}$$

This symmetry can easily be understood in the relativistic case of $z = 1$: since $\psi_\pm$ correspond to left and right-handed spinors in the boundary theory, the helicity h given by $h = \vec{\sigma}\cdot\vec{k}/|\vec{\sigma}\cdot\vec{k}|$ is conserved. In the nonrelativistic case $z \neq 1$, this may be viewed as a generalization of chirality.

3.C.3 Particle-hole symmetry

From equation (3.111) we also observe that the components ξ_+ and ξ_- enjoy the additional symmetry

$$\xi_\pm(r,k_3,\omega) = -\xi_\pm^*(r,-k_3,-\omega) \ , \tag{3.126}$$

where ξ^* denotes the complex conjugate of ξ. Noting then again that (3.14) and (3.13) preserve this property as well, we see that also the full Green's function satisfies

$$G_R^{\pm}(\vec{k},\omega) = -\left(G_R^{\pm}(-\vec{k},-\omega)\right)^* = -\left(G_R^{\mp}(\vec{k},-\omega)\right)^* \ , \tag{3.127}$$

where we used the chirality symmetry in the last equality. This symmetry can be seen as a *particle-hole* symmetry since it relates components with frequency ω to components with frequency $-\omega$.

3.C.4 A symmetry relating M to $-M$

In the case when the operator under consideration is right-handed, that is, $\mathcal{O}_+$, the source is identified with the boundary value of ψ_- instead. Hence, the transfer matrix $\xi(r,p)$ defined in (3.9) is replaced with

$$\zeta_+ = i\,\frac{\psi_{+,1}}{\psi_{-,1}} \ , \qquad\qquad \zeta_- = i\,\frac{\psi_{+,2}}{\psi_{-,2}} \ , \tag{3.128}$$

where $\psi_{1,2}$ are the up and down components of the spinors defined in (3.7) and (3.8). Let us now consider ζ_+ for definiteness, the discussion for ζ_- is analogous. First, we see that $\zeta_+ = -1/\xi_+$, and we easily verify that the equation for ζ_+ is exactly the same equation (3.17) that ξ_+ satisfies, but with the replacement $k_3 \to -k_3$ and $M \to -M$. In addition, the boundary conditions (3.18) for ζ_+ and ξ_+ are the same, and therefore we have the following symmetry property:

$$\zeta_+(r,M,\omega,k_3) = -\xi_+^{-1}(r,M,\omega,k_3) = \xi_+(r,-M,\omega,-k_3) \ . \tag{3.129}$$

On the other hand, equation (3.14) is now replaced with

$$\Sigma(p) = -g \lim_{r_0 \to \infty} r_0^{-2M} \zeta(r_0, p) \,, \tag{3.130}$$

and so we arrive at

$$\Sigma(-M, -\vec{k}, \omega) = -g^2 \, \Sigma^{-1}(+M, +\vec{k}, \omega) \,. \tag{3.131}$$

However, note that strictly speaking this derivation is valid only within the range $-z/2 < M < z/2$ for $\vec{k} = 0$ and within $-1/2 < M < 1/2$ for $\vec{k} \neq 0$. Outside this region one needs to subtract divergent terms to obtain the Green's functions from ξ and ζ, which can be shown by observing that the counterterms that are needed in order to renormalize G_R also respect this symmetry.

As a consequence of this symmetry, conditions on the functions $s_{1,M}$ and $s_{2,M}$ from (3.35) can be obtained as

$$\begin{aligned} s_{1,-M}(u)\, s_{2,+M}(u) &= s_{1,+M}(u)\, s_{2,-M}(u) \,, \\ s_{1,+M}(u)\, s_{1,-M}(u) - s_{2,+M}(u)\, s_{2,-M}(u) &= -1 \,. \end{aligned} \tag{3.132}$$

Solving (3.132) in favor of $s_{2,M}(u)$, we find for nondegenerate values of $s_{1,M}$ and $s_{2,M}$ that

$$s_{2,M}(u) = s_{1,M}(u) \sqrt{1 + \frac{1}{s_{1,M}(u)\, s_{1,-M}(u)}} \,, \tag{3.133}$$

and by using (3.133) in (3.35) we arrive at

$$G_R(\vec{k}, \omega) = -\frac{1}{\omega - \frac{1}{\lambda}\, \vec{\sigma} \cdot \vec{k}\, k^{z-1} - g\, k^{2M} s_{1,M}(u) \left(1 + \frac{\vec{\sigma} \cdot \vec{k}}{k} \sqrt{1 + \frac{1}{s_{1,M}(u)\, s_{1,-M}(u)}}\right)} \,. \tag{3.134}$$

Thus, we have reduced the problem to the determination of a single function $s_{1,M}(u)$ of a single variable $u = \omega/k^z$ for two values of M.

3.C.5 A symmetry of the momentum distribution

Using the above symmetries of the Green's function in combination with the sum rule, we can easily derive a convenient identity for the momentum distribution (3.45). Namely, we have

$$\begin{aligned} N^{\pm}_{\vec{k}} + N^{\pm}_{-\vec{k}} &= \frac{1}{\pi} \int_{-\infty}^{+\infty} \mathrm{d}\omega \, \left[\mathrm{Im}\, G^{\pm}_R(\vec{k}, \omega) n_F(\omega) + \mathrm{Im}\, G^{\pm}_R(-\vec{k}, \omega) n_F(\omega) \right] \\ &= \frac{1}{\pi} \int_{-\infty}^{+\infty} \mathrm{d}\omega \, \mathrm{Im}\, G^{\pm}_R(\vec{k}, \omega) \left[n_F(\omega) + n_F(-\omega) \right] \\ &= 1 \,, \end{aligned} \tag{3.135}$$

where we used (3.127) in the second line, and the sum rule (3.20) and $n_F(\omega) + n_F(-\omega) = 1$ in the third line.

3.D Pole structure and sum rules

In this appendix, we analyse the pole structure of the Green's function, and we show analytically for the case of vanishing temperature that the sum rule is satisfied. The situation of vanishing momenta can be analysed for all values of z, however, analytic expressions for the Green's function for $k \neq 0$ are only available for $z = 1$. We therefore restrict the latter computations to the relativistic case.

3.D.1 Pole structure

We now consider the pole structure of the Green's function in the case of vanishing momentum and zero temperature. Employing (3.33), we see that there is a trivial pole at $\omega = 0$ which corresponds to the free particle. A nontrivial pole is determined by the equation

$$0 = 1 - g\, c_z\, \omega^{\frac{2M}{z}-1} e^{-i\pi(\frac{M}{z}+\frac{1}{2})} \,. \tag{3.136}$$

Using then polar coordinates $\omega = |\omega| e^{i\theta}$, we find for the imaginary part of (3.136) the equation

$$0 = \sin\left[\frac{2M-z}{z}\,\theta - \frac{2M+z}{z}\,\frac{\pi}{2}\right] \,, \tag{3.137}$$

with solutions

$$\theta_n = \frac{\pi}{2} - \frac{n+1}{z-2M}\,\pi\, z \,, \qquad\qquad n \in \mathbb{Z} \,. \tag{3.138}$$

If we want to satisfy the Kramers-Kronig relations, that is, the requirement of no poles in the upper half-plane, we have to make sure that there is no solution to (3.138) in the range $(0, +\pi)$ for all values of n, that is

$$\theta_n \notin (0, +\pi) \qquad\qquad \forall n \,. \tag{3.139}$$

By noting that $0 < z - 2M < 2z$ for $|M| < \frac{z}{2}$, we see that the only possible solution in the forbidden range is given by $n = -1$ with $\theta_{-1} = \frac{\pi}{2}$. All the other solutions are already out of the forbidden range, but yield poles on the nonprincipal sheets of the complex plane. For example, for $n = -2$ the pole resides in $\theta_{-2} \in (\pi, +\infty)$ depending on the value of M, while for $n = 0$ it is in the range $\theta_0 \in (0, -\infty)$.

Let us now turn to the real part of (3.136). Employing again polar coordinates and using (3.138), we arrive at the equation

$$0 = 1 - g\, c_z\, |\omega|^{\frac{2M}{z}-1} (-1)^n \,, \tag{3.140}$$

which is solved by

$$|\omega| = |g\,c_z|^{\frac{z}{z-2M}} \;, \qquad\qquad \mathrm{sign}\,(g\,c_z) = (-1)^n \;. \tag{3.141}$$

It is now clear that in order to avoid the pole $\theta_{-1} = \frac{\pi}{2}$ on the principal sheet, we have to require

$$g\,c_z > 0 \;. \tag{3.142}$$

Furthermore, all other possible poles of the Green's function (specified by (3.138) and (3.141)) with even n are either on the lower-half of the principal sheet or on nonprincipal sheets of the complex plane. Therefore, for the choice of sign (3.142) the Kramers-Kronig relations are satisfied.

For the case of vanishing temperature and $z = 1$, analytic results also for $\vec{k} \neq 0$ are available. As it has been explained in [71], the analytic continuation of the Green's function for nonvanishing momenta is given by replacing $\omega \to \sqrt{\omega^2 - k^2}$. This implies that there are poles at $\omega = \pm|\vec{k}|$, with the pole in the lower half-plane corresponding to the retarded Green's function. Furthermore, for the choice of sign (3.142), there are no additional poles in the upper half-plane of the principal sheet. Therefore, we have shown that in the relativistic case the Kramers-Kronig relations are satisfied also for nonvanishing momenta.

3.D.2 Sum rule for $\vec{k} = 0$

The Green's function in the case of vanishing temperature and momenta can be found in equation (3.33). The spectral density (3.19) then reads

$$\rho(\vec{k}=0,\omega) = \frac{1}{2\pi}\,\mathrm{Im}\,\mathrm{Tr}\big[G_R(\vec{k}=0,\omega)\big] = -\frac{1}{\pi}\,\mathrm{Im}\,\left[\frac{1}{\omega - g\,c_z\,\omega^{\frac{2M}{z}}\,e^{-i\pi(\frac{M}{z}+\frac{1}{2})}}\right] \;. \tag{3.143}$$

Introducing the following constants

$$\mathcal{B} = g\,c_z \cos\left[\pi\left(\frac{M}{z}+\frac{1}{2}\right)\right] \;, \qquad\qquad \mathcal{C} = g\,c_z \sin\left[\pi\left(\frac{M}{z}+\frac{1}{2}\right)\right] \;, \tag{3.144}$$

we express the spectral density as

$$\rho(\vec{k}=0,\omega) = +\frac{1}{\pi}\,\frac{\mathcal{C}\,\omega^{\frac{2M}{z}}}{\left(\omega - \mathcal{B}\,\omega^{\frac{2M}{z}}\right)^2 + \left(\mathcal{C}\,\omega^{\frac{2M}{z}}\right)^2} \;. \tag{3.145}$$

Next, to compute the sum rule we recall the symmetry $\rho(\vec{k},-\omega) = \rho(\vec{k},+\omega)$. We then have

$$\begin{aligned}\int_{-\infty}^{+\infty} \mathrm{d}\omega\, \rho(\vec{k}=0,\omega) &= 2\int_{0}^{+\infty} \mathrm{d}\omega\, \rho(\vec{k}=0,\omega) \\ &= \frac{2}{\pi}\,\frac{z}{2M-z}\,\arctan\left[-\frac{\mathcal{B}}{\mathcal{C}}+\omega^{\frac{2M}{z}}\,\frac{\mathcal{B}^2+\mathcal{C}^2}{\mathcal{C}}\right]_{\omega=0}^{\omega=\infty} \\ &= \frac{2M}{2M-z}-\frac{z}{2M-z}\,\mathrm{sign}\,(g\,c_z)\ .\end{aligned} \tag{3.146}$$

Therefore, for the choice of sign (3.23) we indeed find that the sum rule (3.20) for vanishing momenta and vanishing temperature is satisfied

$$\int_{-\infty}^{+\infty} \mathrm{d}\omega\, \rho(\vec{k}=0,\omega) = 1\ . \tag{3.147}$$

3.D.3 Sum rule for $\vec{k} \neq 0$

In the case of $z = 1$ and vanishing temperature, the expression for the Green's function was given in equation (3.21) together with (3.24). To compute the sum rule in this situation, we write

$$\int_{-\infty}^{+\infty} \mathrm{d}\omega\, \rho(\vec{k},\omega) = \frac{2}{2\pi}\int_{0}^{+\infty} \mathrm{d}\omega\ \mathrm{Im}\,\frac{-2\omega}{p^2\left(1-g\,c_1\,e^{-i\pi(M+\frac{1}{2})}p^{2M-1}\right)}\ , \tag{3.148}$$

with p as in (3.24). Next, we take (3.24) into account to obtain

$$\begin{aligned}\int_{-\infty}^{+\infty} \mathrm{d}\omega\, \rho(\vec{k},\omega) =& +\frac{1}{\pi}\int_{0}^{+|\vec{k}|} \mathrm{d}\omega\ \mathrm{Im}\,\frac{-2\omega}{(\omega^2-k^2)\,(1+g\,c_1\,(k^2-\omega^2)^{2M-1})} \\ &+\frac{1}{\pi}\int_{+|\vec{k}|}^{+\infty} \mathrm{d}\omega\ \mathrm{Im}\,\frac{-2\omega}{(\omega^2-k^2)^2\left(1-g\,c_1\,e^{-i\pi(M+\frac{1}{2})}(\omega^2-k^2)^{2M-1}\right)}\ ,\end{aligned} \tag{3.149}$$

where we note that the first term on the right-hand side vanishes due to taking the imaginary part. Performing then the change of variables $x = \omega^2 - k^2$, we find

$$\int_{-\infty}^{+\infty} \mathrm{d}\omega\, \rho(\vec{k},\omega) = -\frac{1}{\pi}\int_{0}^{\infty} \mathrm{d}x\ \mathrm{Im}\,\left[\frac{1}{x^2-g\,c_1\,x^{2M+1}e^{-i\pi(M+\frac{1}{2})}}\right]\ . \tag{3.150}$$

After a further change of variables $y = x^2$, we arrive at

$$\int_{-\infty}^{+\infty} \mathrm{d}\omega\, \rho(\vec{k},\omega) = -\frac{2}{\pi}\int_{0}^{\infty} \mathrm{d}y\ \mathrm{Im}\,\left[\frac{1}{y-g\,c_1\,y^{2M}e^{-i\pi(M+\frac{1}{2})}}\right]\ , \tag{3.151}$$

which is a special case of the computation in appendix 3.D.2. We therefore find

$$\int_{-\infty}^{+\infty} \mathrm{d}\omega\, \rho(\vec{k},\omega) = 1\ . \tag{3.152}$$

3.E WKB calculation

In this appendix, we present details of the calculation leading to equation (3.66). We consider the case $M > 0$, $T = 0$ and without loss of generality make the assumptions $\omega > 0$, $\vec{k} = (0, 0, k_3)$ and $k_3 > 0$. Furthermore, we consider the spin-up component of the Green's function, the other cases can be worked out using the symmetries outlined in appendix 3.C.

The parameter which we take large in the WKB approximation is $\bar{k} \equiv k/\sqrt{\omega}$, and the fluctuation equations of $u_\pm$ are given by (3.95) which yield

$$\begin{aligned} 0 &= \partial_r^2 u_\pm + \left[\frac{2}{r} + \frac{\omega}{r^2\tilde{k}^2}\left(-\frac{\omega}{r} \pm k\right)\right]\partial_r u_\pm + \left[-\frac{\tilde{k}^2}{r^4} - \frac{M\omega}{r^3\tilde{k}^2}\left(\mp\frac{\omega}{r} + k\right) - \frac{M(M\pm 1)}{r^2}\right]u_\pm \\ &\equiv \partial_r^2 u_\pm + f_1^\pm(r)\partial_r u_\pm + f_2^\pm(r) u_\pm\ , \end{aligned} \tag{3.153}$$

where $\tilde{k}$ had been defined in (3.91). This expression can be put in the Schrödinger form by the transformation

$$u_\pm = h_\pm(r) y_\pm\ , \qquad\qquad h_\pm(r) = \exp\left(-\frac{1}{2}\int^r \mathrm{d}t\, f_1^\pm(t)\right)\ . \tag{3.154}$$

A suitable parametrization of the extra spatial coordinate in the limit $\bar{k} \gg 1$ is given in terms of $x = r/\sqrt{\omega}$. In this variable, the transformation (3.154) reads as follows

$$h_\pm(x) = \frac{\sqrt{x\bar{k} \pm 1}}{x^{3/2}}\ . \tag{3.155}$$

Then, the Schrödinger equations become

$$\frac{1}{\bar{k}^2}\frac{\mathrm{d}^2}{\mathrm{d}x^2} y_\pm(x) - V_\pm(x)\, y_\pm(x) = 0\ , \tag{3.156}$$

with the effective Schrödinger potentials

$$V_\pm(x) = \frac{1}{x^4} - \frac{1}{\bar{k}^2 x^6} + \frac{(\frac{1}{2}\pm M)(\frac{3}{2}\pm M)}{\bar{k}^2 x^2} + \frac{3}{4(x\bar{k}\pm 1)^2} - \frac{\frac{3}{2}\pm M}{x\bar{k}(x\bar{k}\pm 1)}\ . \tag{3.157}$$

In addition to solving the above Schrödinger equation for y_+ analytically using the WKB approximation as described below, we have also solved it numerically. The

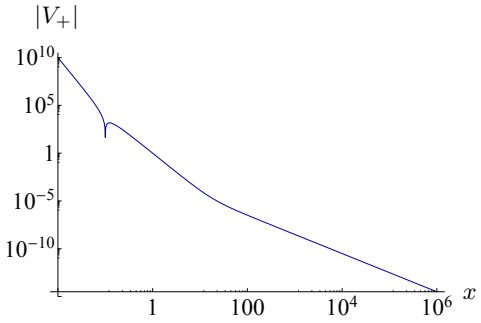

(a) Double-logarithmic plot of $|V_+|$. The turning point is approximately $x_{\mathrm{tp}} = 1/10$.

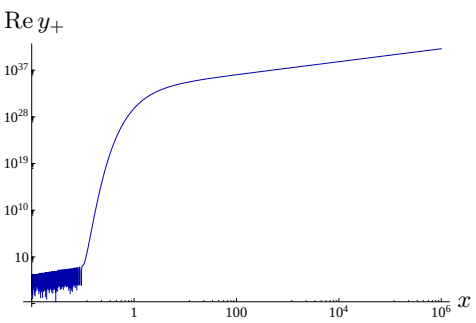

(b) Double-logarithmic plot of $\mathrm{Re}\, y_+$. The imaginary part is similar but with a minus sign. Left of the turning point there is oscillatory behaviour, the other regions exhibit exponential behaviour.

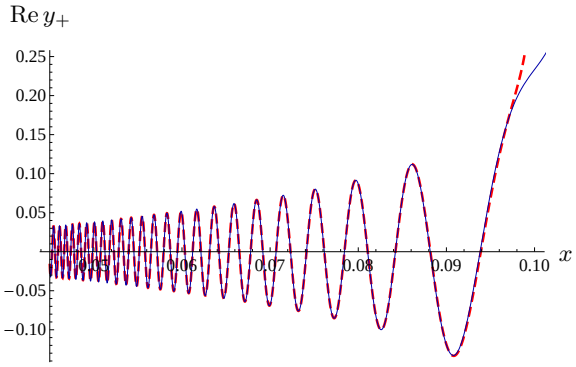

(c) Near-horizon oscillatory behaviour. Until the turning point, there is good agreement between the numerical (blue) and WKB (red) result. After that, the WKB solution is no longer valid.

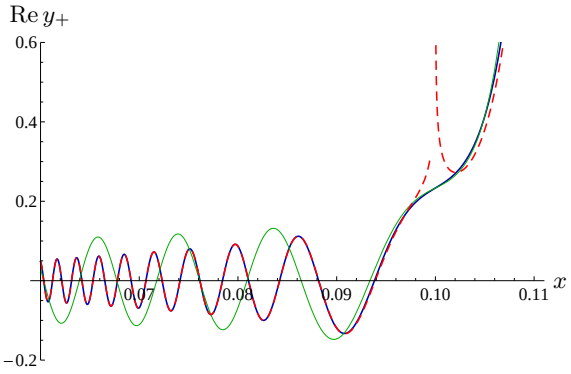

(d) Matching procedure near the classical turning point. The dashed red curves are the WKB results, the solid blue curve is the numerical solution, and the solid green curve is the Airy function solution needed in the matching formulae which agrees with the numerics around the turning point.

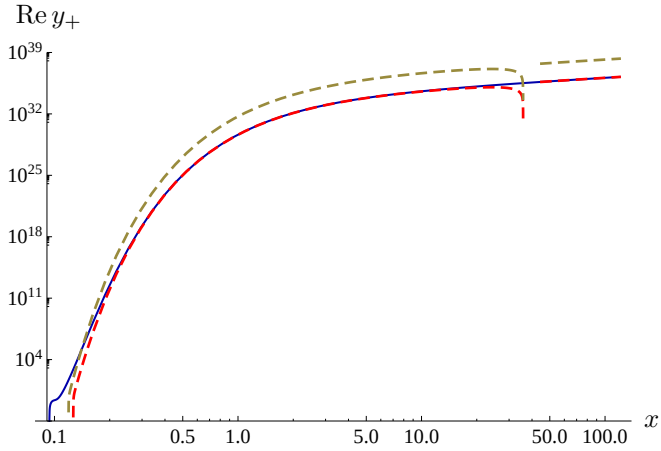

(e) Double-logarithmic plot of $\mathrm{Re}\, y_+$ in the classically disallowed region. The solid blue curve is the numerical solution, the dashed lines are the analytic solution (3.164) for exponents $\alpha = \pi/2$ (red) and $\alpha = 5/3$ (yellow). The former agrees with the numerical result, the latter deviates from it. For large x, the WKB results are not valid anymore but are taken over by the Bessel-function solutions plotted on the far right, which overlap with the WKB solution for smaller x.

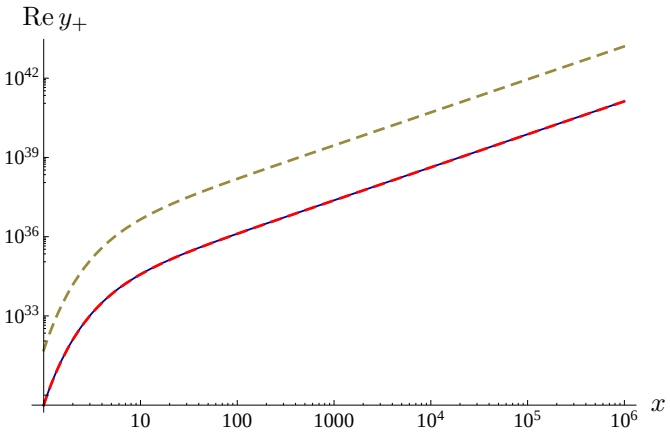

(f) Double-logarithmic plot of the near-boundary region, where the Bessel-function solution is valid. The blue curve is the numerical result, the dashed curves are the analytic result (3.168) for exponents $\alpha = \pi/2$ (red) $\alpha = 5/3$ (yellow).

Figure 3.18: Illustration of the numerical WKB calculation for $\bar{k} = 10$ and $M = 1/4$.

numerical results are presented in Fig. 3.18, which we discuss as we proceed in our computation.

We now focus on the plus component of the fluctuations. In the region close to the horizon at $x \ll 1$, and in the limit $\bar{k} \gg 1$, the relevant piece of the potential for y_+ reduces to

$$V_+ \approx \frac{1}{x^4} - \frac{1}{\bar{k}^2 x^6} \,, \tag{3.158}$$

from which we see that there is a turning point located at approximately $x_{\rm tp} = 1/\bar{k}$. In the region $x < x_{\rm tp}$ the WKB wavefunction is given by

$$y_+(x) = \frac{A_1}{(-V_+)^{1/4}}\, e^{+i\bar{k}\int_x^{x_{\rm tp}} {\rm d}t \sqrt{-V_+(t)}} + \frac{A_2}{(-V_+)^{1/4}}\, e^{-i\bar{k}\int_x^{x_{\rm tp}} {\rm d}t \sqrt{-V_+(t)}} \,, \tag{3.159}$$

with V_+ obtained from (3.158). The solution for $x < x_{\rm tp}$ is compared with the numerics in Fig. 3.18(c). This solution should be connected to the solution near the horizon at $x \to 0$, which yields the condition that $A_2 = 0$. We will not need to fix the coefficient A_1 because, as shown below, it will cancel out in the final answer. The next step is to continue the solution from the region $x < x_{\rm tp}$ to the region $x > x_{\rm tp}$ by using the well-known WKB connection formula, see for example [104, 134]. This procedure is illustrated in Fig. 3.18(d). One important subtlety here is that in the final answer we will need second-order corrections to the WKB formula as well. Noting that the parameter that plays the role of $\hbar$ here is $1/\bar{k}$, we find,

$$y_+(x) = \frac{A_1 e^{-i\frac{\pi}{4}}}{V_+(x)^{\frac{1}{4}}} \left[e^{\bar{k}\int_{x_{\rm tp}}^{x} {\rm d}t \sqrt{V_+(t)}} \left(1 + \frac{\sigma_+(x)}{\bar{k}}\right) + \frac{i}{2} e^{-\bar{k}\int_{x_{\rm tp}}^{x} {\rm d}t \sqrt{V_+(t)}} \left(1 + \frac{\sigma_-(x)}{\bar{k}}\right) \right], \tag{3.160}$$

where the second-order WKB coefficients can be found as (see for example [142])

$$\sigma_\pm = \pm \int_{x_{\rm tp}}^{x} {\rm d}t \left(\frac{1}{8} \frac{V_+''(t)}{V_+(t)^{\frac{3}{2}}} - \frac{5}{32} \frac{V_+'(t)^2}{V_+(t)^{\frac{5}{2}}} \right) \,. \tag{3.161}$$

This is our WKB solution in the classically disallowed region $x_{\rm tp} \ll x < \infty$, where we can now approximate the potential by[12]

$$V_+ \to \frac{1}{x^4} + \frac{M(M+1)}{\bar{k}^2 x^2} + \frac{M}{x^3 \bar{k}^3} - \frac{1}{x^6 \bar{k}^2} \,. \tag{3.162}$$

To the desired order in $\bar{k}$, (3.161) then yields

$$\pm\, \sigma_\pm = \frac{1}{4\bar{k}^2 x} + \frac{M(M+1)x^3}{4\bar{k}^2} + \frac{Mx^2}{8\bar{k}^3} - \frac{1}{4\bar{k}} + \dots \,, \tag{3.163}$$

[12]Note that we keep the leading $1/\bar{k}^2$ corrections in order to be consistent with keeping the $\sigma_\pm$ corrections in (3.160).

and with this approximation we find from (3.160) the following solution, which is illustrated in Fig. 3.18(e),

$$y_+(x) = A_1\, x\, e^{-i\frac{\pi}{4}} \left(e^{-\frac{\bar{k}}{x}} e^{\bar{k}^2} \kappa_+(x) + \frac{i}{2} e^{+\frac{\bar{k}}{x}} e^{-\bar{k}^2} \kappa_-(x) \right), \tag{3.164}$$

where we employed

$$x_{\rm tp} = \frac{1}{\bar{k}} - \frac{M(M+1)}{\bar{k}^5} + \dots\ , \tag{3.165}$$

and have defined the functions

$$\kappa_\pm \approx \left[1 \pm \frac{M(M+1)x}{2\bar{k}} \pm \frac{M}{2\bar{k}^2}\log(\bar{k}x)\right]\left[1 - \frac{M(M+1)x^2}{4\bar{k}^2} + \frac{1}{4x^2\bar{k}^2}\right]\left[1 \mp \frac{1}{4\bar{k}^2} \pm \frac{1}{4\bar{k}^3 x}\right]. \tag{3.166}$$

Note that here we only show terms up to the desired $1/\bar{k}^2$ order. The terms in the first brackets come from the corrections to the exponential term in (3.160), the second terms come from the expansion of the $V_+^{-1/4}$ and the last ones from the $\sigma_\pm$ corrections in (3.160).

The next step is to connect this solution to the region near the boundary at $x \to \infty$ and read off the Green's function from the coefficients of the near-boundary expansion. Note that the WKB approximation in the near-boundary limit $x \to \infty$ fails, because in this region we have an inverse-square potential which does not satisfy the WKB condition $|V_+'(x)/V^{\frac{3}{2}}(x)| \ll 1$. Thus, one has to solve the Schrödinger equation with the potential (3.162) exactly and connect it to the solution (3.164) in the overlapping region $\bar{k}/x \gg 1$. In the latter, we can approximate the potential as

$$V_+(x) \approx \frac{1}{x^4} + \frac{M(M+1)}{x^2\bar{k}^2}\ , \tag{3.167}$$

and the exact solution to the Schrödinger equation with this potential is found in terms of the Bessel functions as

$$y_+(x) = \sqrt{x}\left[B_1\, I_{-\frac{1}{2}-M}\left(\frac{\bar{k}}{x}\right) + B_2\, I_{\frac{1}{2}+M}\left(\frac{\bar{k}}{x}\right)\right], \tag{3.168}$$

where $B_{1,2}$ are coefficients so far undetermined. This solution is also shown in Fig. 3.18(e). In order to connect it to (3.164), we use the well-known asymptotic formula for the Bessel functions for large values of the variable $\bar{k}/x$ and we find

$$y_+(\bar{k}/x) \to \frac{x}{\sqrt{2\pi\bar{k}}}\left[B_1\left(e^{\frac{\bar{k}}{x}} + e^{-i\pi M} e^{-\frac{\bar{k}}{x}}\right) + B_2\left(e^{\frac{\bar{k}}{x}} - e^{i\pi M} e^{-\frac{\bar{k}}{x}}\right)\right] + \dots\ , \tag{3.169}$$

from which we obtain

$$B_1 = \frac{A_1 e^{-i\frac{\pi}{4}}\sqrt{2\pi\bar{k}}}{2\cos(\pi M)}\left(\frac{i}{2} e^{i\pi M} e^{-\bar{k}^2}\epsilon_- + e^{\bar{k}^2}\epsilon_+\right). \tag{3.170}$$

We shall not need the expression for B_2, and the constants $\epsilon_\pm$ are defined as follows

$$\epsilon_\pm = 1 \pm \frac{M}{2\bar{k}^2}\log\bar{k} \mp \frac{1}{4\bar{k}^2}\,. \tag{3.171}$$

On the other hand, using equation (3.155) together with the series expansion of the Bessel functions near $x \to \infty$ given in (3.168), we find that

$$u_+(x) \approx \bar{A}_+^u x^M + \dots\,, \tag{3.172}$$

where the superscript u denotes that we consider the spin-up component of the spinor $\bar{A}_+$. This is in accord with the asymptotic solution given in appendix 3.B.2 with

$$\bar{A}_+^u = B_1 \frac{\bar{k}^{-M} 2^{M+\frac{1}{2}}}{\Gamma(\frac{1}{2}-M)}\,, \tag{3.173}$$

where B_1 is determined by (3.170).

The next step in the calculation of the Green's function is to obtain the WKB solution for the u_- component in (3.153). One way would be to apply the same steps as above in the WKB calculation, however this process is more difficult than the u_+ case, since the potential for u_- shown in (3.157) has extra poles at $x = 1/\bar{k}$. Fortunately, u_- is related to u_+ by the first-order differential equation (3.94), and so we can use the result for u_+ to obtain u_- directly. Equation (3.94), specified to the spin-up component and in the rescaled variables x and $\bar{k}$, reads

$$u_- = \frac{i}{\bar{k}+\frac{1}{x}}\left(x^2\partial_x - Mx\right)u_+\,, \tag{3.174}$$

which for the solution (3.160) becomes

$$u_- = \frac{i}{\bar{k}+\frac{1}{x}}\left[x^2\left(\frac{h_+'(x)}{h_+(x)} - \frac{1}{4}\frac{V'(x)}{V(x)}\right) - Mx\right]u_+ + A(x)\,, \tag{3.175}$$

where the function $A(x)$ is given by

$$A(x) = \frac{ix^2 h_+}{\bar{k}+\frac{1}{x}}\,\frac{A_1 e^{-i\pi/4}}{V_+^{1/4}(x)}\left[e^{\bar{k}\int_{x_{\rm tp}}^x \mathrm{d}t\sqrt{V_+(t)}}\left(\bar{k}V_+^{\frac{1}{2}}(x)\left(1+\frac{\sigma_+(x)}{\bar{k}}\right)+\frac{\sigma_+'(x)}{\bar{k}}\right)\right.$$
$$\left. -\frac{i}{2}\,e^{-\bar{k}\int_{x_{\rm tp}}^x \mathrm{d}t\sqrt{V_+(t)}}\left(\bar{k}V_+^{\frac{1}{2}}(x)\left(1+\frac{\sigma_-(x)}{\bar{k}}\right)-\frac{\sigma_-'(x)}{\bar{k}}\right)\right]. \tag{3.176}$$

On the other hand, very close to the boundary, we can approximate the Schrödinger potential as

$$V_-(x) \approx \frac{1}{x^4} + \frac{M(M-1)}{x^2\bar{k}^2}, \tag{3.177}$$

and again, using this potential in the Schrödinger-like equation for y_-, the exact solution reads

$$y_-(x) = \sqrt{x}\left[C_1\, I_{-\frac{1}{2}+M}\left(\frac{\bar{k}}{x}\right) + C_2\, I_{\frac{1}{2}-M}\left(\frac{\bar{k}}{x}\right)\right] , \tag{3.178}$$

with $C_{1,2}$ some coefficients to be determined. Similarly as above, expanding the Bessel functions in this solution for large $x/\bar{k}$, and using $u_- = h_-(x)y_-(x)$ with (3.155), we find

$$u_-(x) \approx \bar{A}^u_- x^{-M} + \dots , \tag{3.179}$$

with

$$\bar{A}^u_- = C_1 \frac{\bar{k}^M\, 2^{-M+\frac{1}{2}}}{\Gamma(\frac{1}{2}+M)} . \tag{3.180}$$

Next, we employ the asymptotic formula for the Bessel functions in (3.178) for large $\bar{k}/x$ to match to the WKB result (3.175). In this matching, we also need to use (3.176), (3.164) and the relation $u_\pm(x) = h_\pm(x)y_\pm(x)$ with (3.155). The result is

$$C_1 = \frac{A_1 e^{-i\frac{\pi}{4}}\sqrt{2\pi\bar{k}}}{2\cos(\pi M)}\left(\frac{1}{2}e^{-i\pi M}e^{-\bar{k}^2}\gamma_- + ie^{\bar{k}^2}\gamma_+\right) , \tag{3.181}$$

and we shall not need the expression for C_2. The constants $\gamma_\pm$ read

$$\gamma_\pm = 1 \pm \frac{M}{2\bar{k}^2}\log\bar{k} \mp \frac{3}{4\bar{k}^2} . \tag{3.182}$$

Finally, as can be inferred for instance from (3.9), the spin-up eigenvalue of the matrix ξ is proportional to the ratio of u_- and u_+. Thus, using its definition from (3.14), the spin-up component of the selfenergy is proportional to the ratio of the constants $\bar{A}^u_-$ and $\bar{A}^u_+$. To be more precise,

$$\Sigma^+ = -i\, g\, \omega^M \frac{\bar{A}^u_-}{\bar{A}^u_+} = -i\, g\, 2^{-2M} k^{2M} \frac{\Gamma\left(\frac{1}{2}-M\right)}{\Gamma\left(\frac{1}{2}+M\right)}\frac{C_1}{B_1} . \tag{3.183}$$

If we then use (3.170), (3.173), (3.180) and (3.181), we obtain the final result for the spin-up component of the selfenergy as it was given in (3.65).

Before closing this appendix, let us remark the following. As explained at the beginning of section 3.4.3, the numerical prefactors both of the terms in $\epsilon_\pm$ and $\gamma_\pm$ and the one in the exponent, i.e., the number α in the end result $\operatorname{Im}\Sigma \sim \exp(-\alpha k^2/\omega)$, are difficult to determine analytically. This is because the integral in(3.160) leading to $\kappa_\pm$ cannot be done analytically. In the calculation presented here, we have approximated the potential V_+ by taking into account only the three most relevant terms in the region $x > x_{\text{tp}}$, which leads to $\alpha = 2$ as in (3.164). This is reasonable away

from the turning point, but close to the lower integration limit x_{tp} the x^{-6} term has a considerable contribution not taken into account. Furthermore, the turning point itself is determined by setting to zero an approximation to the effective potential. To do better, we should use the full potential everywhere, and expand the integrand as a series in $1/\bar{k}$. However, this series is not uniformly convergent because the integration limit x_{tp} depends on $1/\bar{k}$. In practice we can terminate the series at some point, which leads to a different approximation of the numerical prefactors. For example, if the full effective potential is taken into account and the integrand $\sqrt{V_+}$ is expanded in $1/\bar{k}$, the next contribution of order $\bar{k}^2$ is $-\bar{k}^2/6$, which results in $\alpha = 5/3$, and thus in a decay rate of $\Gamma \sim \exp(-5k^2/3\omega)$. Furthermore, we can do the same for the integral in the $\sigma_\pm$ from (3.161). Also, in the prefactor $V_+^{-1/4}$ the full potential can be taken into account. Then, the $\mathcal{O}(1/\bar{k}^2)$ terms in $\gamma_\pm$ and $\epsilon_\pm$ also receive extra corrections. Still, we are left with an approximation of the exact numbers, and it is not clear whether there occur cancellations between terms later on in the $1/\bar{k}$ expansion.

The integral over $\sqrt{V_+}$ can however be performed numerically. Figure 3.19 compares the numerical and analytic values of the number $\alpha/2$ that appears in the exponent. The numerical result is approximately $\pi/4$, whereas our improved approximated analytic calculation yields $5/6$. When we use $\alpha = \pi/2$ in the exponent, the resulting selfenergy agrees more accurately with the numerical results, as is shown in figures 3.15 and 3.18.

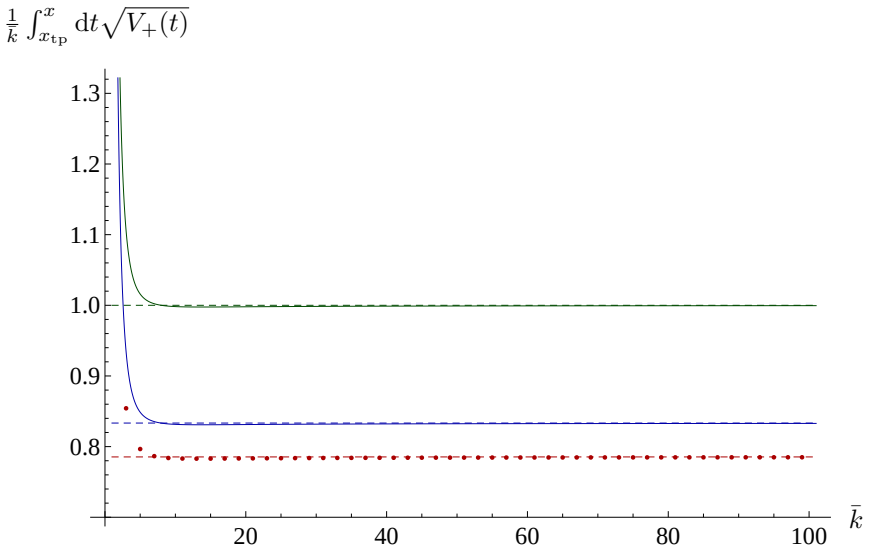

Figure 3.19: Plot of $\frac{1}{\bar{k}}\int_{x_{\rm tp}}^{x} {\rm d}t\sqrt{V_+(t)}$ as a function of $\bar{k}$, which appears in the exponents of (3.160) that determine the quasiparticle decay rate. For large $\bar{k}$, the $\bar{k}^2$ term in the exponent is dominant and therefore the curves converge to the numerical prefactor of this term. In this way, the correct factor can be determined numerically. Here, we have taken $M = +1/4$ and $x = 20$ as the upper integration limit, which is an intermediate value of x. The value of the integral is independent of M for $\bar{k} \to \infty$.
The solid green curve is the result when the two most relevant terms in the potential are taken into account, leading to $\alpha = 2$ (dashed green line). The solid blue curve is the resulting expression when the integration over the full potential is done analytically before terminating the series in $\bar{k}$, leading to the $\alpha = 5/3$ prefactor of the $\bar{k}^2$ term (the dashed blue line is the number $5/6$). The red dots show the value of the integral when it is performed numerically, and the dashed red line is the number $\pi/4$. The former converge to the latter curve, which is evidence that the value of the integral is approximately $\pi/4\bar{k}^2 + \ldots$. Thus, the exponent that determines the quasiparticle decay rate in the final WKB result will be $\exp(-\pi k^2/2\omega)$.

Chapter 4

Holographic interaction effects on transport in Dirac semimetals

Abstract — Strongly interacting Dirac semimetals are investigated using a holographic model especially geared to compute the single-particle correlation function for this case, including both interaction effects and nonzero temperature. We calculate the (homogeneous) electrical conductivity at zero chemical potential, and show that it consists of two contributions. The interband contribution scales as a power law either in frequency or in temperature for low frequency. The precise power is related to a critical exponent of the dual holographic theory, which is a parameter in the model. On top of that we find for nonzero temperatures a Drude peak corresponding to intraband transitions. A behaviour similar to Coulomb interactions is recovered as a special limiting case.

4.1 Introduction

Dirac semimetals are a state of matter that can be seen as the three-dimensional version of graphene. Indeed, Dirac semimetals are zero-gap semiconductors, and without interactions their conduction and valence band touch each other at isolated points in momentum space, the so-called Dirac points [144]. As a result these semimetals have a low-energy description in terms of massless (3+1)-dimensional Dirac fermions with a linear dispersion. Such a Dirac fermion consists of two Weyl fermions of opposite chirality. Breaking time-reversal or spatial inversion symmetry, the associated degeneracy of the Dirac point is lifted and the two Weyl nodes become separated in momentum space, forming a Weyl semimetal [112, 129, 145]. This hypothetical

This chapter is published as *Holographic interaction effects on transport in Dirac semimetals*, V.P.J. Jacobs, S.J.G. Vandoren, H.T.C. Stoof, Phys. Rev. B **90**, 045108 (2014) [143].

phase of matter exhibits unusual transport properties such as an anomalous Hall effect [146] and also gapless surface states forming a Fermi arc instead of the usual closed Fermi surface.

Dirac semimetals have been predicted theoretically [33] and are known to occur on the phase boundary between a topological and a trivial insulator [30]. However, to realize the Dirac semimetal in this manner turned out to be experimentally challenging [32]. Nevertheless, recent theoretical [28, 35] and experimental progress has ultimately resulted in the realization of Dirac semimetals in the crystals Na_3Bi [37] and Cd_3As_2 [38–40]. Their crystal symmetry prevents the Dirac points from becoming gapped, making these systems a more robust testing ground for relativistic physics in a tabletop experiment. On the theoretical side, most of the work on Dirac and Weyl semimetals has been on noninteracting systems [22, 112, 129, 145, 146], although in a number of cases, also Coulomb interactions [26, 47, 147] and short-ranged interactions [46] have been considered. In this work, however, we focus on a more strongly interacting Dirac semimetal that is coupled to a critical order-parameter field near a quantum critical point. If this critical point is nontrivial, the order-parameter fluctuations may induce strong interactions between the Dirac fermions that are not necessarily of a Coulombic nature and whose treatment goes beyond perturbation theory. In particular, we want to address what the effective low-energy theory is for Dirac fermions in the presence of such generic critical order-parameter fluctuations. Since the behaviour of fermions coupled to a critical collective mode is a long-standing problem in the context of non-Fermi liquids [148, 149], this motivates the search for a description of the strongly interacting Dirac semimetal using the recently developed techniques from the so-called anti-de Sitter/conformal field theory (AdS/CFT) correspondence.[14] In this work, we indeed present such a holographic model for a Dirac semimetal, where the interactions between the Dirac fermions are mediated by the critical fluctuations modeled in holography by a strongly coupled conformal field theory. The model describes a class of gapless and particle-hole symmetric systems, that behave as Dirac semimetals with strong interactions in the infrared and which are free in the ultraviolet.

To achieve this, we generalize previous work [71, 115] to formulate a holographic model that allows us to obtain the single-particle Green's function of the strongly interacting Dirac semimetal. Most importantly for our purposes, this correlation function satisfies the desired (zeroth-order) frequency sum rule, which makes it a feasible candidate for applications in realistic solid-state materials, e.g., by a direct comparison to angle-resolved photoemission spectroscopy (ARPES) experiments. Next, using this single-particle Green's function, we determine also the electrical conduc-

[14] For an introduction to applications of the AdS/CFT correspondence to condensed matter, see e.g. the following lecture notes, and references therein: [65, 66, 116].

tivity including the effects of the holographic interactions and nonzero temperature. It is very important to realize that because of particle-hole symmetry, the fermionic contribution to the electrical conductivity remains finite even in the absence of disorder. This is a result of the fact that in the particle-hole symmetric case the electric field cannot affect the centre-of-mass motion of the system and that the interactions cause a drag between the electrons and holes that lead to a finite relaxation time for the charge current.

Our main result, the optical conductivity, is plotted in Fig. 4.1. It consists of two contributions, which can be understood as coming from interband and intraband transitions. In particular, for very high frequencies, we obtain the free result [26, 112] where the conductivity scales linearly with frequency. As the frequency is lowered, a cross-over takes place as the holographic interaction effects dominate the conductivity. An example of other work in which there is a cross-over behaviour from infrared to ultraviolet in the context of holography is Ref. [150]. For zero temperature and in the infrared, the interband conductivity scales as $|\omega|^{3-4M}$, where $-1/2 < M < 1/2$ is the (dimensionless) fermion mass in the Anti-de Sitter background and physically represents a parameter related to the anomalous dimension of the order-parameter fluctuations in the conformal field theory. For $k_B T \gg \hbar\omega$, the interaction effects are temperature dominated and the interband conductivity scales as T^{3-4M}. On top of this, we have a Drude-like peak coming from the intraband contribution.

Interestingly, in the case $M = 1/2$, which requires a separate computation, the selfenergy scales linearly with logarithmic corrections.[115] These two features are also present in the conductivity, resulting in a Coulomb-like behaviour. Indeed, a linear scaling with logarithmic corrections is precisely the behaviour found in Ref. [26] for the dc conductivity in the case of Coulomb interactions. Note that the Fermi velocity is equal to the speed of light in our relativistic model so it is not renormalized.

4.2 Holography

The AdS/CFT correspondence generally provides correlation functions of operators in a strongly coupled conformal field theory, which can be computed by solving classical equations of motion in the dual curved spacetime of one dimension higher [65, 66, 116]. In particular, in the spirit of the semiholographic approach [68], the holographic prescription that starts from a free Dirac fermion in a curved (4+1)-dimensional bulk spacetime was shown in Refs. [71, 115] to lead on the flat (3+1)-dimensional boundary of the bulk spacetime to a model that corresponds to an elementary Weyl fermion coupled to a conformal field theory. This is in agreement with the general observation that holographic techniques are particularly appealing for the description of chiral boundary fermions [141]. To generalize this prescription

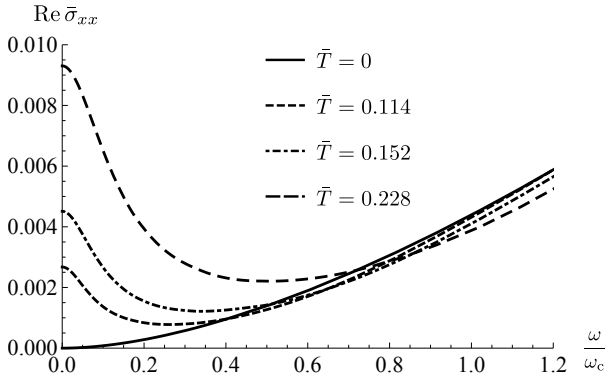

Figure 4.1: Real part of the dimensionless fermionic conductivity $\mathrm{Re}\,\bar{\sigma}_{xx} = \mathrm{Re}\,\sigma_{xx}\hbar c/e^2\omega_c$ as a function of the rescaled frequency ω/ω_c defined in the text. The curves are for the holographic parameter $M = 1/4$ and for different values of the dimensionless temperature $\bar{T} = k_B T/\hbar\omega_c$. For $\omega/\omega_c \gg 1$, the Dirac semimetal is free and $\sigma \propto |\omega|$ (not visible here). For $T = 0$ (solid curve) and as $\omega \simeq \omega_c$, a crossover occurs to a regime where selfenergy effects are dominant. Here, the conductivity scales as $\sigma \propto |\omega|^{3-4M}$. For lower frequencies and $T > 0$, on top of this power law, a Drude peak appears, corresponding to intraband transitions. For $T > 0$ and in the far infrared, i.e., $\hbar\omega \ll k_B T \ll \hbar\omega_c$, the interactions are temperature-dominated and the dc conductivity scales as $\sigma \propto T^{3-4M}$.

to a Dirac fermion, we essentially need two copies of this model, with the two Weyl fermions having opposite chirality. This can be illustrated by the free Dirac Hamiltonian, of which a particular representation in the Weyl basis is $H = \tau_3 \otimes \boldsymbol{\sigma} \cdot c\hbar\mathbf{k}$ with c the speed of light. The last factor is the Weyl Hamiltonian for a single Weyl cone, where $\hbar\boldsymbol{\sigma}/2$ denotes the electron spin, and the Pauli matrix τ_3 introduces the second Weyl cone with opposite chirality. We start by considering a (4+1)-dimensional asymptotically Anti-de Sitter background with radius ℓ, with the line element

$$\mathrm{d}s^2 = -\frac{V^2(r)r^2}{\ell^2}c^2\mathrm{d}t^2 + \frac{\ell^2}{r^2V^2(r)}\mathrm{d}r^2 + \frac{r^2}{\ell^2}\mathrm{d}\vec{x}^2. \tag{4.1}$$

Here, r is the extra spatial holographic dimension and the system is in thermal equilibrium at a temperature $T = 1/k_B\beta$ due to the presence of the planar black hole in the bulk described by the blackening function $V(r) = \sqrt{1 - (\pi\ell^2/\hbar\beta cr)^4}$. We now consider two uncoupled species of free probe Dirac fermions in 4+1 dimensions with masses $M_i\hbar/c\ell$, where $i = 1, 2$ and M_i are dimensionless numbers. They are described by the spinor fields $\Psi^{(i)}$ that propagate in the curved background of Eq. (4.1). The Dirac masses are subject to the restriction $-1/2 \leq M_i \leq 1/2$ where the cases $M_i = \pm 1/2$ need to be treated separately [115]. With respect to the boundary

chirality operator, both bulk Dirac fields can be conveniently expressed in terms of two chiral spinors $\Psi^{(i)}_{R(L)}$. Using the Dirac equation, the chiral components of each species are expressed in terms of the other as

$$\Psi^{(i)}_L = \begin{pmatrix} 0 & 0 \\ -i\xi^{(i)} & 0 \end{pmatrix} \Psi^{(i)}_R, \tag{4.2}$$

which is the defining equation for the diagonal 2×2 matrices $\xi^{(i)}$. Choosing the masses such that $M_1 = -M_2 \equiv M$, the complex eigenvalues of $\xi^{(1)}$ and $\xi^{(2)}$ are ξ_+ and ξ_-, and $-1/\xi_-$ and $-1/\xi_+$, respectively. A different choice for the masses M_i would not lead to this inverse relationship between the eigenvalues and ultimately break the desired spatial inversion symmetry on the boundary. As in Ref. [141], the bulk equations of motion for $\xi_\pm$ are given by[15]

$$\begin{aligned} \left(\frac{r}{\ell}\right)^2 V(r)\partial_r \xi_\pm + \frac{2Mr}{\ell^2}\xi_\pm & \\ = \frac{\omega}{cV(r)} \mp |\mathbf{k}| + \left(\frac{\omega}{cV(r)} \pm |\mathbf{k}|\right)\xi_\pm^2, & \end{aligned} \tag{4.3}$$

with the infalling boundary condition at the horizon $\xi_\pm(\pi\ell^2/\hbar\beta c) = i$. The variation of the action leading to Eq. (4.3) is well-defined only if we specify the action at the boundary. Therefore, Dirichlet conditions [141] are imposed on half of the chiral components of each bulk Dirac field. Most conveniently for our purposes we fix $\Psi^{(1)}_R$ and $\Psi^{(2)}_L$ at a slice $r = r_0$ close to the boundary, specifying the boundary terms as

$$S_\partial = i g_f \int_{r=r_0} \mathrm{d}^4x \sqrt{-g}\sqrt{g^{rr}} \left(\bar\Psi^{(1)}_R \Psi^{(1)}_L - \bar\Psi^{(2)}_L \Psi^{(2)}_R\right),$$

where g and $g_{\mu\nu}$ are respectively the determinant and the $\mu\nu$-component of the metric corresponding to Eq. (4.1) and g_f is a dimensionless normalization constant. Besides this, following the procedure in Refs. [68, 71, 115], we add kinetic terms for both $\Psi^{(1)}_R$ and $\Psi^{(2)}_L$ on the same slice which do not obstruct the variational principle. These additional terms describe elementary fermionic excitations in the boundary theory,

$$S_{\mathrm{kin}} = Z \int_{r=r_0} \mathrm{d}^4x \sqrt{-g} \left(\bar\Psi^{(1)}_R \not{\partial} \Psi^{(1)}_R + \bar\Psi^{(2)}_L \not{\partial} \Psi^{(2)}_L\right). \tag{4.4}$$

Here, Z is a dimensionful constant, $\not{\partial} = \Gamma^a e_a{}^\mu i\partial_\mu$, where $e_a{}^\mu$ are the vielbeins corresponding to the metric in Eq. (4.1), and Γ^a are the Dirac matrices in the (4+1)-dimensional bulk. The holographic prescription instructs that the generating functional for correlation functions in the boundary field theory is equal to the limit

[15] In Refs. [71, 115] rotational invariance was used to write $\vec{k} = (0, 0, k_3)$. Here, we consider the case $k_3 > 0$ without loss of generality.

$r \to \infty$ of the on-shell bulk action. Fourier transforming and putting the action on shell using Eq. (4.2), the bulk Dirac action vanishes, but the boundary terms do not. Performing the Gaussian integration over half of the chiral components of each species boils down to eliminating $\Psi_L^{(1)}$ and $\Psi_R^{(2)}$ using Eq. (4.2). After this, we carry out a field rescaling so that both $\Psi_R^{(1)}$ and $\Psi_L^{(2)}$ acquire the canonical dimensions of a (3+1)-dimensional spinor, and subsequently take a specific double-scaling limit to bring $r_0 \to \infty$, namely [71, 115],

$$\frac{r_0}{\ell} \to \infty, \qquad g_f \to 0, \qquad \frac{g_f}{Z}\left(\frac{r_0}{\ell}\right)^{2-2M} \to \frac{\lambda}{c\ell^{2M}}.$$

This results in an effective boundary action from which the corresponding retarded Green's function for the (3+1)-dimensional boundary Dirac fermion $\Psi = \Psi_R^{(1)} + \Psi_L^{(2)}$ can be obtained. So each of the chiral components of this Dirac fermion is supplied by one of the bulk fermion species. In four-vector notation, using the Minkowski metric with signature $(-1, 1, 1, 1)$, the retarded single-particle correlation function is given by

$$G_R(k) = \frac{ck_\mu + \Sigma_\mu(k)}{\big(ck + \Sigma(k)\big)^2}\gamma^\mu\gamma^0, \tag{4.5}$$

where $ck^0 = \omega + i0 \equiv \omega^+$, γ^μ are the (boundary) Dirac matrices, and $\Sigma_\mu(k)$ are the components of the effective selfenergy of the strongly interacting Dirac semimetal obeying

$$\Sigma_\mu(k) = -\frac{\lambda}{2}\lim_{r_0\to\infty}\left(\frac{r_0}{\ell^2}\right)^{2M}\left[(\xi_+ + \xi_-)\,\delta_\mu^0 + (\xi_+ - \xi_-)\,\frac{k_i}{|\vec{k}|}\delta_\mu^i\right]. \tag{4.6}$$

Here, the index i runs over the spatial directions, and $\lambda \geq 0$ is the square of the coupling constant between the Dirac fermion and the dual conformal field theory containing critical order-parameter fluctuations with an anomalous dimension related to M. Notice that for zero temperature, $V(r) = 1$, and Eq. (4.3) can be solved analytically [115], resulting in $\Sigma_\mu(k, T = 0) = (ck/\omega_c)^{2M-1}\, ck_\mu$, where $\omega_c = \big[\lambda\Gamma(1/2 - M)/(2c)^{2M}\Gamma(1/2 + M)\big]^{1/(1-2M)}$. Finally, the spectral-weight function is the 4×4 matrix $A(\mathbf{k}, \omega) = \mathrm{Im}\,[G_R(k)]/\pi$. After diagonalization, its components are given by

$$\mathcal{A}_\pm(\mathbf{k}, \omega) = \frac{1}{\pi}\mathrm{Im}\left[\frac{-1}{\omega^+ \mp c|\mathbf{k}| + \lambda \lim_{r_0\to\infty}(r_0/\ell^2)^{2M}\xi_\pm}\right], \tag{4.7}$$

where the $+(-)$ component denotes the conduction (valence) band of the Dirac semimetal. The components of the spectral-weight function $\mathcal{A}_\pm$ are normalized such that $\int_{-\infty}^{\infty}\mathcal{A}_\pm(\mathbf{k}, \omega)\mathrm{d}\omega = 1$, so the desired frequency sum rule is obeyed. This is in contrast to earlier holographic computations in the literature which yield correlation functions of composite operators [64, 121, 141].

4.3 Electrical conductivity

The fermionic contribution to the electrical conductivity $\sigma^{\mu\nu}$ is computed in linear-response theory. The (3+1)-dimensional Dirac fermions are thus minimally coupled to a sufficiently small background electric field. The Kubo formula relates the conductivity to the retarded current-current correlation function $\Pi^{\mu\nu}(\mathbf{q}, \omega^+)$ in the Dirac semimetal as $\sigma^{\mu\nu}(\mathbf{q}, \omega) = i\Pi^{\mu\nu}(\mathbf{q}, \omega^+)/\omega$. The retarded current-current correlation function can be expressed in terms of the fermionic Green's function from Eq. (4.5) using the particle-hole bubble diagram. To compute it, we start off in the Matsubara formalism, and afterwards make an analytic continuation to real frequency to obtain the retarded correlation function. Several cases can now be distinguished.

In the noninteracting case, i.e., $\lambda = 0$, the Matsubara Green's function is given by $G_M(k) = k_\mu \gamma^\mu \gamma^0 / ck^2$ with $k^0 = i\omega_m/c$ and ω_m the fermionic Matsubara frequencies. After regularization and analytic continuation, the free current-current correlation function at zero temperature is a manifestly transversal tensor, i.e., $\Pi_0^{\mu\nu}(q) = (q^2\eta^{\mu\nu} - q^\mu q^\nu)\Pi_0(q^2)$. Considering the homogeneous response, we obtain then at zero temperature $\sigma_{0,xx}(\mathbf{0}, \omega) = ie^2|\omega| \log[-(\omega^+/\omega_{\mathrm{exp}})^2]/12\pi^2\hbar c$. The real part of the free conductivity is universal and coincides with the result known from the literature [26, 112], $\mathrm{Re}\,[\sigma_{0,xx}(\mathbf{0}, \omega)] = e^2|\omega|/12\pi\hbar c$, i.e., the free conductivity of two coincident Weyl cones of opposite chirality at zero temperature and Fermi velocity c. The imaginary part of the conductivity, however, is nonuniversal and depends on a single frequency parameter ω_{exp} that should be determined by experiment from the vanishing of the imaginary part of the conductivity at that particular frequency in the Dirac semimetal of interest.

The zero temperature result just discussed originates from particle-hole excitations, i.e., transitions between the valence and conduction band. Additionally, at nonzero temperature, the noninteracting conductivity contains a Drude peak of weight T^2, which comes from the transport of thermally excited particles and holes within the same band. These two contributions are referred to as the inter- and intraband contribution, respectively. At nonzero temperature, the real part of the total noninteracting conductivity can be computed analytically, the result is

$$\mathrm{Re}\,\sigma_{0,xx}(\mathbf{0}, \omega) = \frac{e^2}{3\hbar c}\left(\frac{\pi}{3}\left[\frac{k_B T}{\hbar}\right]^2 \delta(\omega) + \frac{|\omega|}{4\pi}\tanh\left[\frac{\hbar|\omega|}{4k_B T}\right]\right). \tag{4.8}$$

In the interacting case, computing the current-current correlation function from the bubble diagram with dressed propagators and including the vertex corrections is an exact approach within linear-response theory. The interacting Green's function is given by Eq. (4.5). As an approximation we ignore the vertex corrections, but do take into account the selfenergy corrections to the propagator. This approximation is justified and consistent in the particle-hole symmetric case at zero chemical potential

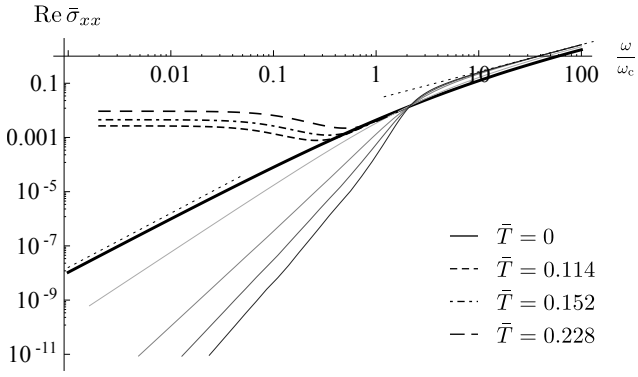

Figure 4.2: Logarithmic plot of the real part of the dimensionless fermionic conductivity $\mathrm{Re}\,\bar{\sigma}_{xx}$ as a function of the rescaled frequency ω/ω_c defined in the text. The black curves are for $M = 1/4$ and for different values of the dimensionless temperature $\bar{T}$. The grayscale curves are for $T = 0$ and for various values of M, respectively from top to bottom $M = 1/8$, $M = -1/8$, $M = -1/4$ and $M = -1/3$. The dotted lines denote the asymptotics for $M = 1/4$, respectively the free result for $\omega/\omega_c \gg 1$, and the zero-temperature infrared result for $\omega/\omega_c \ll 1$. Both results are mentioned explicitly in the text.

that is of interest to us here. This is because in this specific case the conductivity is finite even without impurity scattering, and the vertex corrections do not lead to a qualitatively different behaviour of the conductivity. In this so-called GG approximation, the current-current correlation tensor is not manifestly transversal anymore, but it is in fact almost transversal at zero temperature, with a 5% error. In the GG approximation, the conductivity consists again of two contributions, an interband and intraband part. Due to rotational invariance, all three spatial components of the conductivity tensor are equal. The total contribution to the interacting conductivity is in the GG approximation given by

$$\mathrm{Re}\,\sigma_{xx}(\mathbf{0},\omega) = \sigma^{\mathrm{inter}}(\mathbf{0},\omega) + \sigma^{\mathrm{intra}}(\mathbf{0},\omega).$$

We discuss the two contributions separately, which makes it easier to quantify the distinct behaviour they lead to. The results are also plotted separately in Figs. 4.3 and 4.4.

4.3.1 Interband contribution

The interband contribution to the interacting conductivity is in the GG approximation given by

$$\sigma^{\text{inter}}(\mathbf{0},\omega) = \frac{2e^2c^2}{3\pi}\int_0^\infty \mathrm{d}\rho\,\rho^2 \int_{-\infty}^{\infty}\mathrm{d}\omega' \frac{N_f(\hbar\omega') - N_f(\hbar\omega'+\hbar\omega)}{\hbar\omega} \times \Big(\mathcal{A}_+(\rho,\omega')\mathcal{A}_-(\rho,\omega'+\omega) + \mathcal{A}_-(\rho,\omega')\mathcal{A}_+(\rho,\omega'+\omega)\Big), \tag{4.9}$$

with $N_f(\epsilon) = (1+e^{\beta\epsilon})^{-1}$. It is shown in Fig. 4.3.

For zero temperature, two regimes can be discerned, which are reflected in the logarithmic plot of Fig. 4.2 as curves with a different slope.[16] For large external frequency, the interband conductivity approaches the ultraviolet behaviour, which is the interband part of the free result, i.e., the second term in Eq. (4.8). Here σ scales linearly in ω. As the external frequency is decreased, a cross-over occurs to the infrared behaviour. Here, the interband conductivity is dominated by the fermionic selfenergy and scales as a different power law in frequency. Indeed, from dimensional arguments, we can infer that the zero-temperature interband conductivity in the infrared vanishes as $\sigma(\omega) \propto e^2\omega_{\mathrm{c}}(|\omega|/\omega_{\mathrm{c}})^{3-4M}/12\pi\hbar c$. This scaling behaviour is confirmed by the numerical results shown in Fig. 4.2. The cross-over to the infrared behaviour occurs as the selfenergy term in the Green's function becomes dominant over the kinetic term, which is precisely at ω_{c}. This low-frequency behaviour reflects the fact that the order-parameter field has an anomalous dimension related to M in the infrared. An alternative way to understand the behaviour of the interband contribution can be accomplished using Fermi's golden rule. The effect of interactions is to smear out the delta peaks in the spectral function. At zero temperature, Lorentz invariance ensures that the delta peaks are broadened only inside the light-cone. As a consequence, an on average slightly higher photon energy is needed to acquire the same scattering rate as in the noninteracting case, so effectively the conductivity is lowered. For nonzero temperatures, the interband conductivity does not vanish but instead goes to a constant as $\omega \to 0$, as shown in Fig. 4.3. A nonzero temperature breaks Lorentz invariance and has an additional smearing-out effect on the peaks in the spectral-weight function, this time also outside of the light cone. Now there is residual spectral weight at the Dirac point, so even at zero photon frequency interband transitions can be made, resulting in a nonvanishing interband contribution to the dc conductivity. This effect dominates in the far infrared where $\hbar\omega \ll k_BT$. Depending on the value of temperature compared to the cross-over frequency ω_{c}, there are two or three regimes upon increasing the photon frequency. For $k_BT < \hbar\omega_{\mathrm{c}}$, the

[16] In Fig. 4.2 the total conductivity is shown, but at zero temperature it is dominated by the interband contribution for all frequencies.

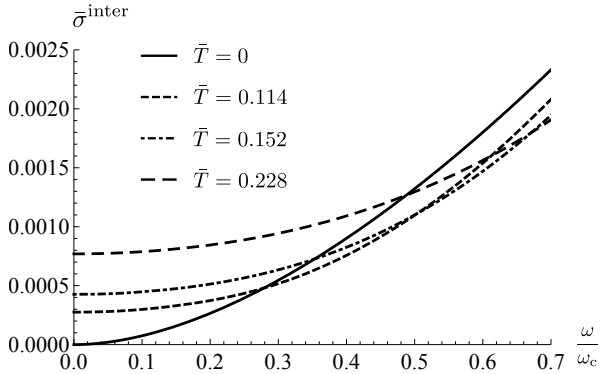

Figure 4.3: The dimensionless purely interband contribution $\bar{\sigma}^{\text{inter}} = \sigma^{\text{inter}} \hbar c / e^2 \omega_c$ as a function of the rescaled frequency ω/ω_c for $M = 1/4$ and for different values of the dimensionless temperature $\bar{T}$. For $T > 0$, this contribution goes to a constant as $\omega \to 0$.

zero-temperature interaction effects start to dominate, and the interband conductivity approaches the zero-temperature result from below, compensating for the extra smearing out and the spectral weight now available at zero frequency. This explains the intersection with the zero temperature curve in Figs. 4.1 and 4.3. As the frequency is increased beyond ω_c, the curve will approach the free result as explained above. If $k_B T > \hbar\omega_c$ a cross-over immediately to the free ultraviolet regime takes place around $k_B T = \hbar\omega$, and no intermediate regime can be discerned.

4.3.2 Intraband contribution

The intraband contribution is in the GG approximation given by

$$\sigma^{\text{intra}}(\mathbf{0},\omega) = \frac{e^2 c^2}{3\pi} \int_0^\infty \mathrm{d}\rho\, \rho^2 \int_{-\infty}^\infty \mathrm{d}\omega' \frac{N_f(\hbar\omega') - N_f(\hbar\omega' + \hbar\omega)}{\hbar\omega} \times \Big(\mathcal{A}_+(\rho,\omega')\mathcal{A}_+(\rho,\omega'+\omega) + \mathcal{A}_-(\rho,\omega')\mathcal{A}_-(\rho,\omega'+\omega) \Big). \tag{4.10}$$

This contribution is shown in Fig. 4.4.

In the noninteracting case, only zero frequency transitions contribute to σ^{intra}, leading to the first term in Eq. (4.8). If there are interactions, the bands become smeared out and less well-defined. In particular, some spectral weight is moved to the location of the other band. Therefore, even at zero temperature, there is a small contribution from high frequency transitions in σ^{intra}, and this leads to a similar power-law behaviour in the IR as in the interband part. Namely, σ^{intra} scales as ω^{3-4M} for small frequency. In the UV, the interactions have a perturbative effect, so that the intraband contribution scales as ω^{2M}. Because this power is less

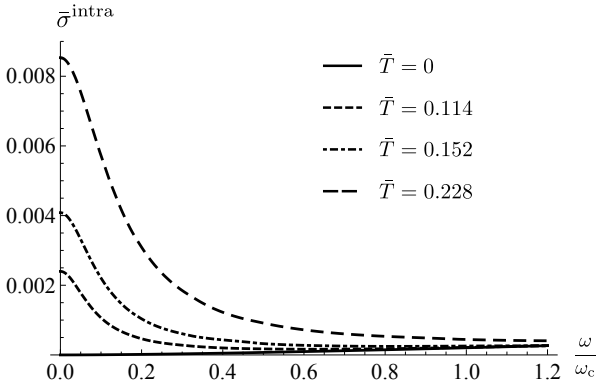

Figure 4.4: The dimensionless purely intraband contribution $\bar{\sigma}^{\text{intra}} = \sigma^{\text{intra}}\hbar c/e^2\omega_c$ as a function of the rescaled frequency ω/ω_c for $M = 1/4$ and for different values of the dimensionless temperature $\bar{T}$. For nonzero temperature the Drude peak is visible.

than one, it is subdominant to the interband part for high frequency. Indeed, the total conductivity asymptotes to the noninteracting case where it scales linearly with frequency, as can be seen in Fig. 4.2. The zero temperature intraband contribution vanishes at zero frequency just like the interband contribution.

At nonzero temperature, a Drude peak appears in the IR on top of the power law behaviour just discussed. It is the interaction analog of the delta peak that is the first term of Eq. (4.8) in the noninteracting case.

4.3.3 Infra-red approximation

In order to scrutinize the value of the conductivity in the dc limit $\hbar\omega/k_BT \ll 1$, we firstly introduce dimensionless variables $x = \hbar\omega\beta$ and $y = c\hbar|\mathbf{k}|\beta$. As can be inferred from Eq. (4.3), the eigenvalues $\xi_\pm$ scale as $\lim_{r\to\infty}(r/\ell^2)^{2M}\xi_\pm(\omega, |\mathbf{k}|) = (\hbar c\beta)^{-2M}s_M(x, \pm y)$, with s_M an M-dependent dimensionless function. Next, we observe that in the far infrared, the Green's function is dominated by the selfenergy term. We can approximate it by neglecting the kinetic part, so that the Green's function inherits the $1/T^{2M}$ temperature scaling from the selfenergy. This approximation is valid for $\hbar\omega \ll k_BT \ll \hbar\omega_c$. Proceeding to compute the conductivity as before, we now obtain in this limit the following expression for the total dc conductivity:

$$\sigma^{\text{IR}} = \lim_{\hbar\omega\beta\to 0} \text{Re}\,\sigma_{xx}(\mathbf{0}, \omega) \simeq \frac{e^2\omega_c}{12\pi\hbar c}\left(\frac{k_BT}{\hbar\omega_c}\right)^{3-4M} S_M^{\text{IR}},$$

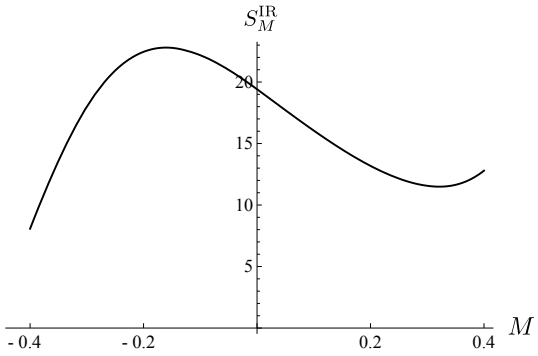

Figure 4.5: The numerical value of the dimensionless integral S_M^{IR} defined in the text as a function of M.

where S_M^{IR} is a dimensionless integral that in the limit $\hbar\omega\beta \to 0$ is given by

$$S_M^{\mathrm{IR}} = \left[\frac{\Gamma(\frac{1}{2}-M)}{4^M\Gamma(\frac{1}{2}+M)}\right]^2 \int_0^\infty \mathrm{d}y \int_{-\infty}^\infty \mathrm{d}x \frac{y^2}{\cosh^2(x/2)} \times \left(4\mathcal{A}_+^{\mathrm{IR}}(x,y)\mathcal{A}_-^{\mathrm{IR}}(x,y) + \left[\mathcal{A}_+^{\mathrm{IR}}(x,y)\right]^2 + \left[\mathcal{A}_-^{\mathrm{IR}}(x,y)\right]^2\right).$$

Here the components of the spectral-weight function in the far infrared are given in terms of the functions s_M by $\mathcal{A}_\pm^{\mathrm{IR}}(x,y) = \mathrm{Im}\,[-1/\pi s_M(x+i0,\pm y)]$. The numerical value of this integral is shown in Fig. 4.5 for various M. The conductivity thus indeed tends to a constant in the far infrared, and scales as $\sigma^{\mathrm{IR}} \propto T^{3-4M}$. This is true for both contributions, i.e., both the dc value of the interband part and the height of the Drude peak scale as T^{3-4M}. The above scaling argument also suggests that the width Γ of the Drude peak scales with temperature in the same way as the selfenergy, i.e., $\Gamma(T) \propto T^{2M}$, so that the Drude peak behaves as $T^{3-2M}\Gamma/(\Gamma^2+\omega^2)$. Our numerics are indeed consistent with this scaling.

4.4 Discussion

In this work, we have obtained a model for strongly coupled Dirac semimetals with holographic interaction effects. Using this model, we have computed the fermionic contribution to the electrical conductivity. We have shown that for small frequency, it inherits the scaling of the critical order-parameter field responsible for the interactions between the Dirac fermions. The reason that the electrical conductivity is finite at the charge neutrality point, is that an external electric field couples to particle and hole currents with opposite sign. This fact, combined with particle-hole symmetry,

makes sure that an electric field does not couple to the centre-of-mass motion of the system. In addition, the interactions lead to a drag force that relaxes the charge current in finite time, making the conductivity finite. This is in contrast to the thermal conductivity. Indeed, because of the linear dispersion, the heat current is directly proportional to the centre-of-mass momentum. Therefore interactions do not relax the heat current driven by a thermal gradient, i.e., the thermal conductivity of a Dirac semimetal is infinite [151].

A closely related consequence of particle-hole symmetry is the fact that vertex corrections are not crucial for obtaining the qualitative behaviour of the conductivity. The charge transport relaxation time is finite, and in the absence of vertex corrections, it is approximated by the single-particle lifetime. This decreases the final result for the conductivity by a multiplicative numerical factor. The latter represents an angular effect, taking into account that not all scattering events contributing to a finite lifetime, contribute to current relaxation equally effectively [152]. In fact, we expect this angular correction to be small in the strongly coupled case, where there is no preference for forward scattering, as opposed to weakly coupled systems where small-angle scattering is dominant. Therefore, our results in the GG approximation can be interpreted as a lower bound on the exact result, possibly with different numerical coefficients in the scaling laws, but with the same universal features. In particular, the facts that the UV limit yields the free result, that the IR limit is a scaling law with power $3 - 4M$, that there is a Drude peak, and that one or two crossovers are present in between these regimes, are all universal features that are not sensitive to vertex corrections. Computation of the vertex corrections requires further study. In particular, we need information on the dependence of the selfenergy on the dressed Green's function, which is difficult to obtain in the present model and this is beyond the scope of this work.

Holographic methods are usually entirely universal, in the sense that they can be used to describe classes of possible condensed-matter systems. The advantage is that our model is very general. However, it remains a challenge to predict the behaviour of specific realistic systems. We expect the obtained power-law behaviour of the conductivity to be applicable to a wide range of condensed-matter systems in a universality class determined by M, but its coefficient to depend on material specifics. For instance, in our model, the latter depends on the Fermi velocity c, which must be replaced by its appropriate experimental value. The Fermi velocities are of the order 10^5 and 10^6 m/s in Na_3Bi and Cd_3As_2, respectively [37, 39].

Hopefully, also future experiments will reveal the behaviour of Dirac semimetals coupled to fluctuating collective modes. Comparing holographic models with experimental data will then lead to a better understanding of the relation between string-theoretic methods and realistic condensed-matter systems.

Chapter 5

Towards a field-theory interpretation of bottom-up holography

Abstract — We investigate recent results for the electrical conductivity and the fermionic selfenergy, obtained in a holographic bottom-up model for a relativistic charge-neutral conformal field theory. We present two possible field-theoretic derivations of these results, using either a semiholographic or a holographic point of view. In the semiholographic interpretation, we also show how, in general, the conductivity should be calculated in agreement with Ward identities. The resulting field-theory interpretation may lead to a better understanding of the holographic dictionary in applied AdS/CMT.

5.1 Introduction

A phase transition takes place when the free energy of a system has a nonanalyticity as a function of another thermodynamic variable of the system, such as the temperature or the pressure. Phase transitions can be classified by the way the free energy changes at the transition, distinguishing discontinuous (first-order) and continuous (second or higher-order) phase transitions. During a first-order phase transition, the derivative of the free energy is discontinuous, and the variable describing the amount of order in the system, the order parameter, jumps from a zero to a nonzero value. In contrast, during a continuous phase transition the order parameter becomes nonzero in a continuous manner. In the latter case, precisely at this so-called critical point

This chapter is published as *Towards a field-theory interpretation of bottom-up holography*, V.P.J. Jacobs, S. Grubinskas, H.T.C. Stoof, J. High Energy Phys. **04** (2015) 033 [153].

the system has a diverging correlation length. This implies that the correlations in the system look the same at all scales.

Consider, for instance, a system of fermions and bosons in the vicinity of such a continuous phase transition. This is a generic situation in experimental and theoretical condensed-matter physics, see for example Ref. [149] and references therein. The bosons represent fluctuations in a collective field, the expectation value of which is the order parameter introduced above. As mentioned previously, there exists a control parameter p which can be tuned to a critical value p_c, at which the phase transition occurs. There, the correlation length of the bosonic fluctuations becomes infinite and the bosonic degree of freedom obtains a nonzero expectation value at one side of the transition. Then the system is said to be in the ordered phase. Examples of such an ordered phase are a superfluid, an (anti)ferromagnet or a charge-density wave. When the system is still in the disordered phase, but close to the critical point, the expectation value of the order parameter is zero but there are critical bosonic fluctuations which have an increasing importance as $p \to p_c$.

A phase transition occurring at zero temperature is known as a quantum phase transition [154–156], since the nature of the fluctuations of the order parameter is purely quantum. As suggested above, in the absence of a temperature scale and in the case of an infinite correlation length, the behaviour of the order parameter fluctuations can become fully scale invariant precisely at the transition. This can be the case both for weakly and strongly coupled systems. A typical phase diagram containing a quantum critical point is shown in the left panel of Fig. 5.1. In this figure, the quantum critical point is the end point at $T = 0$ of a line of nonzero-temperature phase transitions to an ordered phase. Interestingly, due to the absence of other scales, the quantum critical point dominates the behaviour of the system at p_c even for temperatures $T > 0$, which is therefore called the quantum critical region.

We can ask what the consequences of this criticality are for the fermions that are also present in the system. In many cases, this can be studied using a field-theoretic description where the order-parameter fluctuations give rise to an effective interaction for the fermions. In the simplest approach, the bosonic system becomes scale invariant and can be modeled by a conformal field theory.[18] This conformal field theory is coupled to fermions described by the spinor field χ and its conjugate

[18] Conformal invariance is more restrictive than scale invariance as it also includes symmetry under special conformal transformations. What is most relevant for our purposes, is that the theory is scale invariant so that a simple dimensional analysis can be applied. Throughout the paper we refer to some theories as a "conformal field theory", although we just need the property that it is scale invariant. While we are aware of the fact that this name is not always entirely appropriate, we do so in order to keep the analogy with the dual field theory in the AdS/CFT correspondence.

$\bar{\chi}$. In this case, the total system is modeled by the following action[19]

$$S = S_{\text{cft}}[\Phi^*, \Phi] + S_0[\bar{\chi}, \chi] + ig \int \mathrm{d}^4x \, \bar{\chi}\chi \, (\Phi + \Phi^*) \, . \tag{5.1}$$

The bosonic fluctuations are described by Φ, an operator in the conformal field theory described by the action S_{cft}, whose expectation value is proportional to the order parameter. The noninteracting fermionic action is denoted by S_0 and g is the coupling constant between the fermion and the conformal field theory.

When the bosonic excitations are free or weakly coupled, the full theory can be described elegantly using perturbation theory. However, it is more challenging to study S_{cft} in the case of a strongly coupled system. An example of a strongly coupled system with a continuous phase transition is a system of cold fermionic atoms at unitarity [79, 157]. At unitarity the scattering length parameterizing the interaction strength between the atoms becomes infinite, and there is no small parameter in which a perturbation expansion can be made.[20] For a positive chemical potential μ, this system exhibits a continuous phase transition from a normal to a superfluid state at a nonzero temperature. The critical temperature can be represented as a line in the (T, μ)-plane, which is suppressed as μ decreases and ends in a quantum critical point at zero temperature [86], see the right panel of Fig. 5.1.

A possible approach to obtain properties of a conformal field theory in the strongly coupled regime is derived from the holographic duality. Application of holographic methods to condensed-matter physics has been dubbed Anti-de Sitter/Condensed-Matter Theory (AdS/CMT) correspondence [65, 66, 116]. Essentially, it boils down to the fact that correlation functions of operators in strongly coupled conformal field theories are provided by classical computations in a gravity dual of one dimension higher. According to the discussion above, these correlation functions can then be used to study the effective behaviour of fermions in the vicinity of a quantum critical point.

With this application in mind, we recently described a model for interacting Dirac semimetals in the AdS/CMT set-up [71, 115]. This so-called dynamical-source model is constructed analogously to the theory in Eq. (5.1) and is similar to the semiholographic approach introduced in Ref. [68]. It contains elementary Dirac fermions living in (3+1)-dimensional Minkowski space that are coupled to a conformal field theory playing the role of the critical system. Here, elementary means that the fermionic creation- and annihilation operators satisfy the canonical equal-time anticommuta-

[19] In our notation, the spacetime arguments of the fields in the (3+1)-dimensional Lagrangian density are always suppressed if the fields are evaluated at the same spacetime point x^μ. Spinor indices are also suppressed and a sum over them is always implied.

[20] This regime can however be accessed with renormalization-group techniques [158].

tion relations given by

$$\left\{\hat{\chi}(\vec{x}, x^0), \hat{\chi}^\dagger(\vec{x}', x^0)\right\} = \delta^3\big(\vec{x} - \vec{x}'\big).$$

The conformal field theory they are coupled to, is in fact the dual ("boundary") field theory of classical Einstein gravity in a ("bulk") (4+1)-dimensional asymptotically Anti-de Sitter background with a planar Schwarzschild black hole. The main result is the retarded propagator of elementary Dirac fermions which contains a free part and a nontrivial selfenergy. This selfenergy comes about from adding probe Dirac fermions to the theory and integrating out the holographic dual conformal field theory part of the theory. This is why a boundary interpretation of the dynamical-source model is closely related to the system described in Eq. (5.1). The boundary Dirac fermions are made dynamical by an additional boundary term added to the fermionic action, which is an irrelevant perturbation to the conformal field theory, and its role is to provide the correct UV dynamics. As a consequence, the resulting retarded Green's function of the elementary fermionic operators defined by

$$G_R(x - x') = -i\theta\left(x^0 - x'^0\right)\left\langle\left\{\hat{\chi}(x), \hat{\chi}^\dagger(x')\right\}\right\rangle,$$

satisfies the zeroth-order frequency sum rule, i.e.,

$$\int_{-\infty}^{\infty} \frac{\mathrm{d}\omega}{c}\ \mathrm{Im}\ G_R(\vec{k}, \omega^+) = -\pi. \tag{5.2}$$

This is important in the light of condensed-matter applications, where this sum rule is required for the determination of experimentally accessible correlators. So these holographic correlation functions can be directly compared to experimental data, e.g. from photoemission experiments or from radio-frequency spectroscopy for fermionic atoms at unitarity.

The dynamical-source model is an example from a bigger class of models called holographic bottom-up models. This is a phenomenological approach to the holographic duality, which is an alternative to the so-called top-down approach. In top-down holography, the starting point is string theory in ten dimensions with a set of D-branes. The benchmark example is the duality between Type-IIB string theory in $\mathrm{AdS}_5 \times \mathrm{S}_5$, and $\mathcal{N} = 4$ Super-Yang-Mills theory in (3+1)-dimensional Minkowski space. By taking certain limits, consistent truncations to a lower-dimensional gravity theory can be made. If the string theory has a dual conformal field theory, the truncated field theory on the boundary is guaranteed to exist. However, the dimensional reduction usually leads to many technical difficulties, for instance, a large amount of degrees of freedom that have to be kept track of. It is usually not clear which of these degrees of freedom are important for the behaviour of the boundary field theory. Therefore, practical computations are often not feasible in such a set-up.

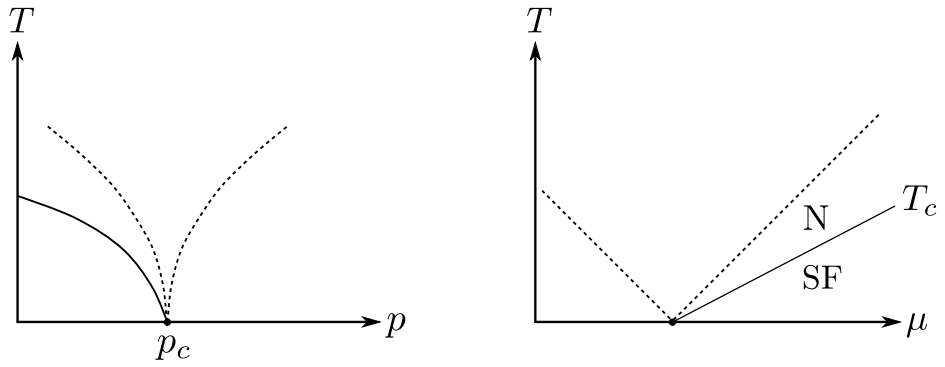

Figure 5.1: Left panel: Phase diagram containing a quantum critical point at the $T = 0$ end point of a line of phase transitions to an ordered phase. The dotted lines represent a cross-over to the quantum critical region which is directly above the quantum critical point. Right panel: Phase diagram of ultracold fermionic atoms at unitarity. Above the critical temperature T_c, the system is in the disordered or normal state, denoted by "N". For positive values of the chemical potential μ there is a line of second-order phase transitions to the ordered superfluid phase ("SF"). These phase transitions can for $T > 0$ be described using classical physics, but the line terminates in a quantum critical point at zero temperature and zero chemical potential. The dotted lines indicate the crossover from the classical regime to the quantum critical region, where the behaviour is dominated by the physics of the quantum critical point.

See, however, Ref. [159] for a recent example of a top-down approach to a condensed-matter problem.

In contrast, in bottom-up models, we start off on the gravity side with classical Einstein gravity, such as an (asymptotically) Anti-de Sitter spacetime. A few degrees of freedom are then put in by hand, for instance, a scalar field, the aforementioned Dirac field, or a Maxwell field. These represent the desired features of the strongly coupled field theory of interest, and it is a working assumption that this field theory exists. It is an effective low-energy theory, and there is no guarantee that these gravity theories can be embedded in a higher-dimensional string theory, where the duality was originally conjectured. It is for instance not clear that the Dirac fermions come from a certain limit of a string theory. Bottom-up holography is therefore a phenomenological approach, usually the subject of trial and error until successful, plausible or consistent results justify this approach. The upshot is that computations are relatively simple, without the necessity to deal with the many technicalities coming from string theory, but still manage to capture the universal and effective properties of many systems. In fact, this simplicity is particularly appealing for condensed-matter physics, where a description in terms of complicated supersym-

metric non-Abelian gauge theories seems a bit of an overkill. The relevance of this phenomenological approach for the study of the low-energy physics of condensed-matter systems, was first stressed by the authors of Ref. [160].

Most AdS/CMT models are bottom-up models. So for applications in condensed matter, bottom-up holography in the form of the AdS/CMT approach may be the preferred way to go, compared to the top-down approach. Nevertheless, even in the bottom-up case, the question remains whether the dual boundary theory in fact provides an adequate description of a specific condensed-matter system. The hope is that the dual strongly coupled quantum field theory bears sufficient resemblance to realistic quantum critical points, such as the ones in the examples above, and understanding this point is an ongoing challenge. An important approach to comprehend bottom-up holography from the field-theory side, is to investigate what are the minimal requirements for conformal field theories to have a gravity dual. Examples are Refs. [161–163], and more recently, Refs. [164–166], and references therein. These works are aimed at a better understanding of the so-called conformal bootstrap constraints in general conformal field theories that have a large number of degrees of freedom. This information can be used to analyse the bulk effective action, by comparing the structure of correlation functions computed directly in the conformal field theory and in bottom-up holography using Witten diagrams. Nevertheless, the difficulty remains, that in the bottom-up approach, the AdS/CMT correspondence just provides the correlation functions of the effective excitations in the boundary, without providing information about their microscopic nature. So the microscopic Hamiltonian of the actual boundary system remains hidden. That problem is the topic of this work. We investigate possible microscopic mechanisms in which AdS/CMT results at zero charge density, such as the fermionic selfenergy in the dynamical-source model can come about. To this end, we construct field theories of fermions coupled to a (strongly interacting) conformal field theory which mimic the bottom-up dynamical-source model mentioned above, as well as the theory in Eq. (5.1). The precise form of these simple field theories is motivated by making analogies to known holographic dualities. By making certain choices, it is possible to reproduce the result for the fermionic selfenergy and electrical conductivity obtained in the dynamical-source model and elsewhere in the literature. In this manner we aim at a better understanding of how holographic bottom-up results can originate from condensed-matter field theories. Our approach is different from that in Refs. [161–166] in the sense that we have in mind to find a possible microscopic theory of elementary fields of the conformal field theory, and only indirectly consider the structure of the conformal field theory operators and their correlators. Hopefully this paves the way for a more established bottom-up holographic dictionary, where the relation between microscopic field theories suitable for condensed-matter, and

holographic bottom-up model building becomes more precise. This might enhance the potential applicability of holographic results e.g. in condensed-matter theory and experiment.

The content of this paper is as follows. In section 5.2, we first review the results of a different bottom-up computation, namely of the electrical conductivity of a strongly coupled conformal field theory [167]. Next, we review the dynamical-source model for the electrical conductivity of Dirac fermions coupled to a strongly interacting conformal field theory. In section 5.3 we depart from holography and construct a purely field-theoretic model. This is referred to as the probe-fermion model, because it contains a conformal field theory coupled to a fermion in the spirit of Eq. (5.1). In addition, it contains a certain large-N limit and a suitably defined strong-coupling limit analogous to what happens on the field-theory side of the holographic duality. For both literature results in section 5.2, we show that this purely field-theoretic model reproduces the holographic results, thus providing a possible microscopic interpretation. Finally, in section 5.4 we realise that this possible interpretation has some disadvantages, and construct an alternative model that reproduces the AdS/CMT results. This last, so-called Fock, model then offers the interpretation of the dynamical-source model as a phenomenological way to incorporate finite-coupling corrections in the bulk setup. We end with a conclusion in section 5.5. There are also a number of appendices which contain more explanation and details of the calculations. In particular, our notation and conventions can be found in appendix 5.A.

5.2 Previous results

We start by briefly reviewing two literature results from the AdS/CMT correspondence. Firstly, the authors of Ref. [167] computed the electrical conductivity of the strongly coupled boundary conformal field theory with a gravity dual. Secondly, in Ref. [71] results were presented for the selfenergy of Dirac fermions coupled to a conformal field theory with the same gravity dual, in the dynamical-source model. With this fermionic selfenergy, the contribution to the electrical conductivity of the dynamical-source fermions was also computed [143]. In all three cases, the bottom-up gravity dual is classical Einstein gravity with a negative cosmological constant, that has as a solution an asymptotically Anti-de Sitter spacetime with a planar Schwarzschild black hole. The corresponding line element is in $4+1$ dimensions given by

$$\mathrm{d}s^2 = -\frac{V^2(r)r^2}{\ell^2}c^2\mathrm{d}t^2 + \frac{\ell^2}{r^2V^2(r)}\mathrm{d}r^2 + \frac{r^2}{\ell^2}\mathrm{d}\vec{x}^2, \tag{5.3}$$

where ℓ is the characteristic length scale of the asymptotically AdS spacetime. On top of this fixed background, extra fields are added, which are specified below.

5.2.1 Electrical conductivity of the boundary field theory

For the electrical conductivity of the boundary field theory, a Maxwell field is added to the bulk system. Its action is in 4+1 dimensions and in natural units given by

$$S_{\mathrm{em}} = -\frac{1}{4g_5^2\ell}\int \mathrm{d}^5x\sqrt{-g}F_{\mu\nu}F^{\mu\nu},$$

where g_5^2 is the 5-dimensional gauge coupling constant, g is the determinant of the metric corresponding to the line element in Eq. (5.3), and F is the electromagnetic field or Faraday tensor. Compared to Ref. [167] there is an additional factor ℓ so that g_5^2 is dimensionless here. The spatial components of the gauge field are fluctuating on top of the background in Eq. (5.3), and the linearized equation of motion for the gauge field in the curved background is considered. According to the holographic dictionary, the local U(1) symmetry becomes a global U(1) symmetry in the boundary field theory. The boundary value of the gauge field couples to the boundary U(1) symmetry current, and from the bulk gauge-field fluctuations the retarded two-point function of the boundary current is derived.

The boundary field is effectively charged by a rescaling of the global boundary current $J_\mu \to eg_5J_\mu$ so that it becomes the canonically normalized charge current. The conductivity is subsequently obtained via the Kubo formula and this results in 3+1 boundary dimensions in

$$\sigma = \frac{e^2k_BT}{\pi\hbar^2c}, \tag{5.4}$$

where T is the temperature. In Eq. (5.4) we have reexpressed the result from Ref. [167] in SI units. For our purposes the most important feature of this result is that the conductivity is linear in temperature. This is to be expected from dimensional analysis in the boundary conformal field theory. Note that the conductivity in Eq. (5.4) does not depend on ℓ, which is a consequence of the scale invariance of the system.

5.2.2 Semiholographic fermionic selfenergy and fermionic conductivity

In the computation of the selfenergy of Dirac fermions coupled to the boundary field theory in the dynamical-source model [71, 115, 143], two species of uncoupled probe Dirac fields $\Psi^{(i)}$ with $i = 1, 2$ are added to the bulk instead of a Maxwell field. Special boundary conditions are used, in particular, next to the usual Dirichlet

boundary conditions, an IR irrelevant kinetic boundary term for the Dirac fermions is taken into account. These boundary terms are imposed at a UV slice $r = r_0$, which is taken to the boundary at the end of the computation. The total action is

$$S = -ig_f \sum_{i=1}^{2} \int \mathrm{d}^5x\sqrt{-g}\bar{\Psi}^{(i)} \left(\frac{1}{2}\Gamma^a e_a{}^\mu \overleftrightarrow{D}_\mu - M_i\right) \Psi^{(i)} \\ - \int \mathrm{d}^4x\sqrt{-g}\left[ig_f\sqrt{g^{rr}}\left(\bar{\Psi}_R^{(1)}\Psi_L^{(1)} - \bar{\Psi}_L^{(2)}\Psi_R^{(2)}\right) + Z\bar{\Psi}\not{D}_4\Psi\right]\Bigg|_{r=r_0}.$$

Here, $\Psi_{R,L}^{(i)}$ are the chiral components of $\Psi^{(i)}$ with respect to the chiral Dirac matrix of the boundary, and $\Psi = \Psi_R^{(1)} + \Psi_L^{(2)}$ is the boundary Dirac spinor. Furthermore, $g^{\mu\nu}$ and $e_a{}^\mu$ are respectively the components of the asymptotically Anti-de Sitter metric introduced in Eq. (5.3) and the corresponding vielbeins, D_μ is the usual covariant derivative containing the spin connection, $\not{D}_4 = \sum_{a\neq r}\Gamma^a e_a{}^\mu i\partial_\mu$ is the boundary kinetic operator where Γ^a are the bulk Dirac matrices, g_f is a dimensionless coupling constant, and Z is a dimensionful wavefunction-renormalization constant. Finally, $M_1 = -M_2 = M$, are the dimensionless bulk Dirac masses, which are in the interval $-1/2 < M < 1/2$. This number M becomes a model parameter in the boundary field theory.

Again, the equation of motion is solved in the curved background and the action is evaluated on shell. This implies that the boundary conformal field theory is integrated out, and it takes on the role of an effective selfenergy for the boundary Dirac spinor Ψ. This selfenergy can be written as the solution of the Dirac equation in the curved background. As a result of the Gaussian integration, half of the chiral components of both $\Psi^{(i)}$ are eliminated, namely $\Psi_L^{(1)}$ and $\Psi_R^{(2)}$. So the chiral component of each bulk fermion species that is left, provides one of the chiral components of Ψ. Next, a field rescaling and the limit $r_0 \to \infty$ are carried out in a specific manner that keeps the boundary action finite. Together with the kinetic boundary term, the result is the retarded Green's function of Dirac fermions in 3+1 dimensions, with the retarded selfenergy coming from the interactions with the strongly coupled conformal field theory. For zero temperature, the result is[21]

$$G^{-1}(k) = \not{k} - \Sigma(k), \tag{5.5}$$

with the selfenergy

$$\Sigma(k) = -\frac{\lambda}{2^{2M}c}\frac{\Gamma(\frac{1}{2}-M)}{\Gamma(\frac{1}{2}+M)}\not{k}k^{2M-1}, \tag{5.6}$$

[21] Note that in order to make the selfenergy agree with our present conventions, we have, compared to Ref. [143], placed an additional minus sign in front of the action, and removed a factor $c\gamma^0$ from the inverse Green's function to arrive at Eqs. (5.5) and (5.6). See also appendix 5.A. Furthermore, the dimensionless number C_M in Eq. (5.7) is equal to $\left[2^{2M}\Gamma(\frac{1}{2}+M)/\Gamma(\frac{1}{2}-M)\right]^2 S_M^{\mathrm{IR}}$ in the notation of Ref. [143].

where $ck^0 = \omega + i0$ and the dimensionful quantity $\lambda = c\ell^{2M}(r_0/\ell)^{2-2M}g_f/Z \geq 0$ is the square of the coupling between the conformal field theory and the fermion. The anomalous dimension of the selfenergy quantifies the difference from the linear relativistic scaling. So we see that $2M-1$ is related to the anomalous dimension of the selfenergy.

Next, the dynamical-source fermion can be minimally coupled to a background electric field, and thus the contribution of the dynamical-source fermion to the electrical conductivity can be computed. In Ref. [143] this computation was carried out and for ω much smaller than both frequency scales present, namely, $\omega \ll k_B T/\hbar$ and $\omega \ll (\lambda/c^{2M})^{1/(1-2M)}$, the result was

$$\sigma_\chi = \frac{e^2c^2}{12\pi\hbar\lambda^2}\left(\frac{k_BT}{\hbar c}\right)^{3-4M} C_M. \tag{5.7}$$

Here, C_M is a dimensionless function of M. In contrast to the pure conformal field theory contribution from Eq. (5.4), this contribution scales as temperature to the power $3-4M$. So, the conductivity obtains a linear scaling in temperature only in the limit $M \to 1/2$. The point $M = 1/2$ thus corresponds to a case with no anomalous dimension, as is also visible in Eq. (5.6). In fact, a different calculation has to be carried out in this case, which results in logarithmic corrections to a linear power-law scaling.

5.3 Probe-fermion model

In an attempt to interpret the above results, we now construct a simple field theory, the probe-fermion model. The total action of this model is[22]

$$S_{\text{tot}}[\varphi,\bar\psi,\psi;A,\bar\chi,\chi] = S_0[\varphi]+S_0[\bar\psi,\psi;A]+S_{g_2}[\varphi,\bar\psi,\psi]+S_0[\bar\chi,\chi;A]+S_{g_1}[\varphi,\bar\psi,\psi;\bar\chi,\chi]. \tag{5.8}$$

The notation indicates that the action is a functional of the sets of fields φ_i, and ψ_i and $\bar\psi_i$, and of the sources A, and χ and $\bar\chi$. These ingredients are specified in the following.

Firstly, the fields ψ_i, $\bar\psi_i$ and φ_i together are referred to as the "conformal field theory". As discussed in the introduction, this name is not completely appropriate. It refers here to the scale-invariant theory that takes over the role of the field theory dual in the actual holographic model. The theory has a number of copies of fields $i = 1, ..., N$. Furthermore, the coupling constants g_2 and g_1 introduced below are

[22] For us, the inspiration to write down an action of this specific form came from the structure of supersymmetric Yang-Mills theory. For the readers without a background in supersymmetry, we have included appendix 5.B, in which we review some properties of supersymmetric Yang-Mills theory that may motivate the action in Eq. (5.8).

normalized in a certain way, by appropriate factors of $1/\sqrt{N}$. This normalization makes sure that a certain class of diagrams dominates in the large-N limit. The φ_i are real scalars whose contribution is given by the action

$$S_0[\varphi] = -\frac{\hbar}{2}\sum_{i=1}^{N}\int \mathrm{d}^4x\,\varphi_i\,(-i\partial)^{2-\eta}\,\varphi_i.$$

The propagator of the φ_i has an anomalous dimension η. Next, we have Dirac fermions ψ_i and their conjugates $\bar\psi_i = \psi_i^\dagger\gamma^0$. Writing $\not\partial = \gamma^\mu\partial_\mu$ and $\not A = \gamma^\mu A_\mu$, they are described by the action

$$S_0[\bar\psi,\psi;A] = -i\hbar\sum_{i=1}^{N}\int \mathrm{d}^4x\,\bar\psi_i\Big(\not\partial - \frac{ie}{\hbar}\not A\Big)\psi_i. \tag{5.9}$$

The components of the spinors ψ_i and $\bar\psi_i$ are Grassmann fields. The Dirac fermions are coupled to the real scalars through a local four-point interaction with coupling constant $g_2/2N$, described by the term

$$S_{g_2}[\varphi,\bar\psi,\psi] = \frac{i\hbar g_2}{2N}\sum_{i=1}^{N}\sum_{i'=1}^{N}\int \mathrm{d}^4x\,\varphi_i\,\bar\psi_i\,\psi_{i'}\,\varphi_{i'}. \tag{5.10}$$

There are also two "external" fields, i.e., not in the conformal field theory, which we motivate now. Firstly, in section 5.3.2, we compute the electrical conductivity of the field theory. To this end, the Dirac fermions ψ_i in Eq. (5.9) are minimally coupled with coupling e to a nondynamical U(1) gauge field A_μ. The scalar field φ is real and is not minimally coupled. Secondly, in section 5.3.1, the fermionic selfenergy is computed. To calculate it in the probe-fermion model, we add a single Dirac fermionic source χ to the theory with noninteracting action

$$S_0[\bar\chi,\chi;A] = -i\hbar\int \mathrm{d}^4x\,\bar\chi\Big(\not\partial - \frac{ie}{\hbar}\not A\Big)\chi. \tag{5.11}$$

Analogously to the computation in the dynamical-source model discussed in section 5.2 this is the external Dirac fermion that is coupled to a conformal field theory and obtains a nontrivial selfenergy when the field theory is integrated out. In other words, this χ fermion is the probe fermion that mimics the dynamical source. For generality, it is also minimally coupled to the U(1) gauge field. There is only a single species of this fermion because it is not part of the conformal field theory in which there is a large-N limit. Instead, the external source χ is coupled to the field theory through a local three-point interaction with coupling $g_1/\sqrt{N}$, described by the term

$$S_{g_1}[\varphi,\bar\psi,\psi;\bar\chi,\chi] = \frac{i\hbar g_1}{\sqrt{N}}\sum_{i=1}^{N}\int \mathrm{d}^4x\Big(\varphi_i\,\bar\chi\,\psi_i + \bar\psi_i\,\chi\,\varphi_i\Big).$$

Thus, we aim at an interpretation of the dynamical-source model, in which the dynamical-source fermion is a probe fermion coupled to a conformal field theory.

The real-time partition function is now

$$Z[A,\bar{\chi},\chi]=\int \mathrm{d}[\bar{\psi}]\mathrm{d}[\psi]\int \mathrm{d}[\varphi]\,\exp\left(\frac{i}{\hbar}S_{\mathrm{tot}}[\varphi,\bar{\psi},\psi;A,\bar{\chi},\chi]\right).$$

Our notation for the path-integral measure is $\mathrm{d}[\mathrm{field}]=\prod_{i=1}^{N}\mathrm{d}[\mathrm{field}_i]$. To perform the large-$N$ limit we perform a Hubbard-Stratonovich transformation to a collective spinor field π that decouples both interactions. To this end, the partition function is multiplied by

$$\begin{aligned}1=\int \mathrm{d}[\bar{\pi}]\mathrm{d}[\pi]\exp\Bigg[\frac{i}{\hbar}\int \mathrm{d}^4x\Big(\bar{\pi}-\frac{\hbar g_2}{2N}\sum_i\bar{\psi}_i\varphi_i-\frac{\hbar g_1}{\sqrt{N}}\bar{\chi}\Big)\Big(\frac{2N}{i\hbar g_2}\Big)\\ \times\Big(\pi-\frac{\hbar g_2}{2N}\sum_{i'}\psi_{i'}\varphi_{i'}-\frac{\hbar g_1}{\sqrt{N}}\chi\Big)\Bigg].\end{aligned}\tag{5.12}$$

Then, the partition function becomes

$$Z[A,\bar{\chi},\chi]=\int \mathrm{d}[\bar{\psi}]\mathrm{d}[\psi]\int \mathrm{d}[\varphi]\int \mathrm{d}[\bar{\pi}]\mathrm{d}[\pi]\,\exp\left(\frac{i}{\hbar}S^{\mathrm{HS}}_{\mathrm{tot}}[\varphi,\bar{\psi},\psi,\bar{\pi},\pi;A,\bar{\chi},\chi]\right),\tag{5.13}$$

with

$$\begin{aligned}S^{\mathrm{HS}}_{\mathrm{tot}}[\varphi,\bar{\psi},\psi,\bar{\pi},\pi;A,\bar{\chi},\chi]=S_0[\varphi]+S_0[\bar{\psi},\psi;A]+\int \mathrm{d}^4x\Big[\bar{\pi}\Big(\frac{2N}{i\hbar g_2}\Big)\pi\\ +\bar{\chi}\left[-i\hbar\Big(\not{\partial}-\frac{ie}{\hbar}\not{A}\Big)-\frac{2i\hbar g_1^2}{g_2}\right]\chi+\frac{2i\sqrt{N}g_1}{g_2}\big(\bar{\chi}\pi+\bar{\pi}\chi\big)+i\sum_i\Big(\bar{\pi}\varphi_i\psi_i+\bar{\psi}_i\varphi_i\pi\Big)\Big].\end{aligned}\tag{5.14}$$

Starting from Eq. (5.14) our approach is the following. Now that the interactions are decoupled, the only N dependence of the effective actions of the φ_i and ψ_i fields is an overall species sum. This just leads to N copies of the corresponding single-species partition functions. Furthermore, these actions are Gaussian, so we can integrate out the φ_i and ψ_i fields exactly. This mimics the integrating out of the conformal field theory in the semiholographic dynamical-source model. After this, we work in the random-phase approximation, which becomes exact when the large-N limit is taken. Then the collective field can be integrated out. The result is the generating functional in Eq. (5.20) below, from which the conductivity and the selfenergy of the probe fermion can be obtained. We will now derive Eq. (5.20) in several steps.

Before we integrate out anything, it is convenient to introduce some new notation. We first define the inverse noninteracting Green's function corresponding to a single

species of the scalar fields φ_i as

$$G_\varphi^{-1}(x,x') = -\big(-i\partial\big)^{2-\eta}\delta^4(x-x'). \tag{5.15}$$

The inverse noninteracting Green's function for a single species of the fermion fields ψ_i is a functional of A_μ, since

$$G_\psi^{-1}[A](x,x') = -i\left(\not\partial - \frac{ie}{\hbar}\not A\right)\delta^4(x-x'). \tag{5.16}$$

It is also possible to write the Green's function in their corresponding momentum-space representation. However, it is more elegant to go to a basis-independent description, where the Green's functions matrices are written without indices. We also introduce a matrix inner product, which is in the coordinate representation defined as:

$$\big(\phi\big|G_\phi^{-1}\big|\phi\big) \equiv \int \mathrm{d}^4x \int \mathrm{d}^4x'\ \bar\phi(x)\, G_\phi^{-1}(x,x')\,\phi(x'),$$

where ϕ denotes any of the fields with a suitably defined conjugate $\bar\phi$, which should be clear from the context. As before, a sum over spinor indices is always assumed if appropriate. Furthermore, all Green's functions are diagonal in species indices. With this definition, the quadratic part of the actions can be written as a basis-independent inner product. For example, the noninteracting fermion action from Eq. (5.9) becomes

$$S_0[\bar\psi,\psi;A] = \hbar\sum_{i=1}^{N}\big(\psi_i\big|G_\psi^{-1}[A]\big|\psi_i\big).$$

Now we integrate out the ψ_i fermions from Eq. (5.14), after which the effective action for the scalar fields is written in basis-independent notation as

$$S^{\mathrm{eff}}[\varphi,\bar\pi,\pi;A] = \frac{\hbar}{2}\sum_{i=1}^{N}\big(\varphi_i\big|G_\varphi^{-1} - \Sigma_\varphi[\bar\pi,\pi,A]\big|\varphi_i\big),$$

The scalars have an effective selfenergy, which is in the coordinate representation given by

$$\Sigma_\varphi[\bar\pi,\pi,A](x,x') = -\frac{2}{\hbar^2}\bar\pi(x)\,G_\psi[A](x,x')\,\pi(x').$$

Now it is straightforward to integrate out the scalar fields, which yields

$$\begin{aligned}&\int \mathrm{d}[\varphi]\exp\left[i\sum_{i=1}^{N}\big(\varphi_i\big|\frac{1}{2}G_\varphi^{-1} - \Sigma_\varphi[\bar\pi,\pi,A]\big|\varphi_i\big)\right]\\ &= \exp\left[-\frac{N}{2}\mathrm{Tr}\ln\Big(-G_\varphi^{-1} + \Sigma_\varphi[\bar\pi,\pi,A]\Big)\right].\end{aligned} \tag{5.17}$$

At this point we perform a fluctuation expansion of π around its expectation value $\langle\pi\rangle$. Here we expand around $\langle\pi\rangle = 0$ which is always a solution of the saddle-point equation. To obtain a nonzero result we thus have to go one order beyond the mean-field approximation, which is the random-phase approximation mentioned earlier. Because of the overall factor N in the exponent above, the random-phase approximation becomes exact in the large-N limit. Taking the large-N limit, we can therefore work up to first order in the scalar selfenergy and still obtain an exact result. Expanding the logarithm in Eq. (5.17) to this order yields

$$\mathrm{Tr}\ln\Big(-G_\varphi^{-1}+\Sigma_\varphi\Big) = \mathrm{Tr}\ln\Big(-G_\varphi^{-1}\Big)+\mathrm{Tr}\ln\Big(1-G_\varphi\Sigma_\varphi\Big) \simeq \mathrm{Tr}\ln\Big(-G_\varphi^{-1}\Big)-\mathrm{Tr}\,G_\varphi\Sigma_\varphi.$$

Here, Σ_φ is still a functional of π and $\bar\pi$, and this is used to obtain a selfenergy term for the π fluctuations. After these manipulations, the total partition function from Eq. (5.13) becomes

$$\begin{aligned} Z[A,\bar\chi,\chi] &= \exp\left[N\mathrm{Tr}\ln\Big(-G_\psi^{-1}[A]\Big)-\frac{N}{2}\mathrm{Tr}\ln\Big(-G_\varphi^{-1}\Big)\right] \\ &\times\int \mathrm{d}[\bar\pi]\mathrm{d}[\pi]\,\exp\left[iN\big(\pi\big|G_\pi^{-1}[A]\big|\pi\big)+i\big(\chi\big|\mathcal{G}_\chi^{-1}[A]\big|\chi\big)+\frac{i}{\hbar}\frac{2g_1\sqrt{N}}{g_2}\Big[i\big(\chi\big|\pi\big)+i\big(\pi\big|\chi\big)\Big]\right]. \end{aligned} \tag{5.18}$$

Here, we have used the notation

$$\big(\chi\big|\pi\big) = \int \mathrm{d}^4x\,\bar\chi(x)\pi(x),$$

and the noninteracting Green's function of the probe fermion is given in coordinate space by[23]

$$\mathcal{G}_\chi^{-1}[A](x,x') = \left[-i\Big(\partial\!\!\!/ - \frac{ie}{\hbar}A\!\!\!/\Big) - \frac{2ig_1^2}{g_2}\right]\delta^4(x-x'). \tag{5.19}$$

We have also defined the inverse collective-field propagator G_π^{-1}, which is a functional of A_μ through G_ψ and is given in momentum space by

$$G_\pi^{-1}[A](k) = \frac{2}{i\hbar^2 g_2} + \frac{i}{\hbar^2}\int\frac{\mathrm{d}^4q}{(2\pi)^4}\,G_\psi[A](k+q)\,G_\varphi(q).$$

Finally, we integrate out the collective-field fluctuations π, which reduces Eq. (5.18) to the generating functional

$$\begin{aligned} Z[A,\bar\chi,\chi] &= \exp\left[N\mathrm{Tr}\ln\Big(-G_\psi^{-1}[A]\Big)-\frac{N}{2}\mathrm{Tr}\ln\Big(-G_\varphi^{-1}\Big)+\mathrm{Tr}\ln\Big(-NG_\pi^{-1}[A]\Big)\right] \\ &\times\exp\left[i\big(\chi\big|\,\mathcal{G}_\chi^{-1}[A]+\left(\frac{2g_1}{\hbar g_2}\right)^2 G_\pi[A]\,\big|\chi\big)\right]. \end{aligned} \tag{5.20}$$

[23]The symbol G_χ is reserved for the fully dressed probe-fermion Green's function.

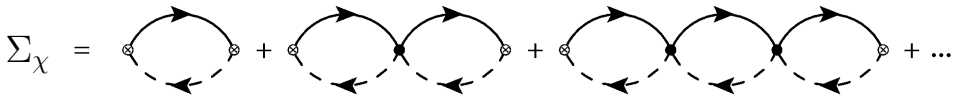

Figure 5.2: Probe-fermion selfenergy from Eq. (5.24) in a perturbation series in powers of g_2, denoted by the filled cicles. Empty circles represent the three-point vertex g_1, where χ can attach. The solid line is the noninteracting Green's function of a single species of ψ_i fermions, while the dashed line denotes the noninteracting scalar Green's function. Together, they form the bubble corresponding to the expression for $I(k)$ from Eq. (5.22).

This generating functional is the starting point for computing the selfenergy of the probe fermion and the electrical conductivity of the probe-fermion model.

5.3.1 Self-energy of the probe fermion

For the selfenergy of the probe fermion we consider Eq. (5.20) and set the field A_μ to zero. Going to momentum space, the effective action for the probe fermion is identified as

$$S^{\text{eff}}[\bar{\chi},\chi] = \hbar \int \frac{\mathrm{d}^4k}{(2\pi)^4}\, \bar{\chi}(k)\left[\not{k} - \frac{2ig_1^2}{g_2} + \frac{2ig_1^2}{g_2}\frac{1}{1-\frac{g_2}{2}I(k)}\right]\chi(k), \tag{5.21}$$

where

$$I(k) = \int \frac{\mathrm{d}^4q}{(2\pi)^4}\, G_\psi(k+q)\, G_\varphi(q). \tag{5.22}$$

From Eq. (5.21) we can read off the selfenergy of χ, which is

$$\Sigma_\chi(k) = \frac{2ig_1^2}{g_2}\left(1 - \frac{1}{1-\frac{g_2}{2}I(k)}\right) = \frac{-ig_1^2 I(k)}{1-\frac{g_2}{2}I(k)}. \tag{5.23}$$

Note in particular that all factors of N have dropped out from the selfenergy. The result in Eq. (5.23) can be seen as a resummation of the bubble sum, where the bubble diagram corresponds to $I(k)$, the internal vertices come with a factor g_2 and the exterior vertices with g_1. Namely, when we expand in powers of g_2 it becomes a geometric series,

$$\Sigma_\chi(k) \simeq -ig_1^2 I(k)\left(1 + \frac{g_2}{2}I(k) + \frac{g_2^2}{4}I^2(k) + ...\right). \tag{5.24}$$

This series is depicted in Fig. 5.2.

The loop integral I from Eq. (5.22) is computed in appendix 5.C. At zero temperature, the result is given by

$$I(k) = \frac{i\not{k}\left(k^2\right)^{\frac{\eta}{2}}}{(4\pi)^2}\, \frac{1}{\frac{\eta}{2}\left(1+\frac{\eta}{2}\right)\left(2+\frac{\eta}{2}\right)} \equiv i\not{k}\left(k^2\right)^{\frac{\eta}{2}} f(\eta),$$

where we defined the function f as

$$f(\eta) = \left[(4\pi)^2 \frac{\eta}{2}\left(1+\frac{\eta}{2}\right)\left(2+\frac{\eta}{2}\right)\right]^{-1}.$$

Inverting the matrix structure in Eq. (5.23) leads to two contributions to the self-energy,

$$\Sigma_\chi(k) = -\frac{ig_1^2}{1+\left(\frac{g_2}{2}\right)^2 (k^2)^{1+\eta} f^2(\eta)}\left[i\not{k}(k^2)^{\frac{\eta}{2}} f(\eta) - \frac{g_2}{2}(k^2)^{1+\eta} f(\eta)\mathbb{1}\right]. \tag{5.25}$$

We now define a strong-coupling limit as follows. The couplings g_1 and g_2 become infinite, but the ratio $g = g_1^2/g_2^2$ remains finite. Writing $g_1^2 = g g_2^2$, we see that this particular limit amounts to ignoring the 1 in the denominators of Eq. (5.25). Then, the probe-fermion selfenergy becomes

$$\Sigma_\chi(k) = \frac{4g}{f(\eta)}\not{k}\left(k^2\right)^{-\frac{\eta}{2}-1} + 2igg_2\mathbb{1}.$$

The second term is independent of momentum and is a formally infinite mass term, generated in the Hubbard-Stratonovich transformation. We can get rid of this term by adding a bare mass term for χ from the start, which precisely cancels this term in the strong-coupling limit. Then, the renormalized selfenergy is just given by the first term, i.e.,

$$\Sigma_\chi(k) = \frac{4g}{f(\eta)}\not{k}\left(k^2\right)^{-\frac{\eta}{2}-1}. \tag{5.26}$$

It is proportional to the product of $\not{k}$ and a power of k^2 related to the anomalous dimensions of the scalar fields. This is precisely the form of the selfenergy from Eq. (5.6) found in Ref. [71], if we make the identifications

$$\begin{aligned} \eta &= -2M-1, \\ g &= -\frac{\lambda\,\Gamma\left(\frac{1}{2}-M\right) f(-2M-1)}{c\,4^{M+1}\Gamma\left(\frac{1}{2}+M\right)}. \end{aligned} \tag{5.27}$$

The desired range $-1/2 < M < 1/2$ coincides with the interval $-2 < \eta < 0$.

We end with the remark that the case with no anomalous dimension, $\eta = 0$, corresponds to $M = -1/2$, and not to $M = 1/2$ as anticipated. Instead, the value $M = 1/2$ corresponds to $\eta = -2$. Note that the holographic result from Eq. (5.6) is obtained in the alternative quantization. In the regular quantization, the selfenergy from Eq. (5.6) would be replaced by its inverse. This is equivalent to Eq. (5.6) with the replacement of M by $-M$. So in the regular quantization, $\eta = 0$ indeed corresponds to $M = 1/2$. Nonetheless, in the probe-fermion model result from Eq. (5.26), setting $\eta = 0$ still does not make the selfenergy proportional to $\not{k}$, which is the expected form without an anomalous dimension.

5.3.2 Electrical conductivity

In this section we consider the total conductivity in the probe-fermion model in linear-response theory. This is formally achieved by making use of the fact that the total electric current J^μ in the Lagrangian of the probe-fermion model couples to a nondynamical U(1) gauge field A_μ. In practice, the total current consists of several contributions, which are defined through minimal coupling of the various charged fields to A_μ, for instance as in Eqs. (5.9) and (5.11).

In linear response, the conductivity tensor σ^{ij} is defined as

$$\Big\langle J^i(\vec{k},\omega)\Big\rangle = \sum_{j=1}^{3} \sigma^{ij}(\vec{k},\omega) E^j(\vec{k},\omega), \tag{5.28}$$

where $i,j = 1,2,3$, and we choose the temporal gauge where $A_0 = 0$. Furthermore, $E^j = i\omega A^j$ is a sufficiently small electric field. Because J^μ couples to A_μ in the functional integral, we have from Eq. (5.28) that

$$\sigma^{\mu\nu} \propto \left.\frac{\delta^2 \ln Z[A]}{\delta A_\nu \delta A_\mu}\right|_{A=0} \propto \Big\langle J^\mu J^\nu \Big\rangle.$$

So the generating functional Eq. (5.20) is only needed up to second order in A_μ. For the discussion in this section and in section 5.4.2 it is sufficient to consider only $\delta^2 \ln Z/\delta A_\mu \delta A_\nu$. Obtaining the conductivity from this is straightforward and will not be discussed in detail here. To consider the total contribution we start with the generating functional $Z[A,\bar\chi,\chi]$ from Eq. (5.20), and integrate out the fields $\bar\chi$ and χ. The result is $Z[A]$ where all matter fields are integrated out. The A-dependent part is thus given by

$$\ln Z[A] = N\mathrm{Tr}\ln\Big(-G_\psi^{-1}[A]\Big) + \mathrm{Tr}\ln\Big(-NG_\pi^{-1}[A]\Big) + \mathrm{Tr}\ln\Big(-G_\chi^{-1}[A]\Big), \tag{5.29}$$

where G_χ^{-1} is the full Green's function of the probe fermion, given by the quadratic part in χ and $\bar\chi$ in Eq. (5.20),

$$G_\chi^{-1}[A](x,x') = \mathcal{G}_\chi^{-1}[A](x,x') - \left(\frac{2g_1}{\hbar g_2}\right)^2 G_\pi[A](x,x').$$

Next, every term in Eq. (5.29) is expanded up to second order in A_μ to obtain the total conductivity. This is described in more detail in appendix 5.D and ultimately results in Eq. (5.61), a long expression for $\delta^2 \ln Z[A]/\delta A^\mu \delta A^\nu$. This expression contains all contributions to the total current-current correlation function, and is shown diagrammatically in Fig. 5.3. We classify the various contributions to the conductivity by the types of currents appearing inside the current-current correlation function.

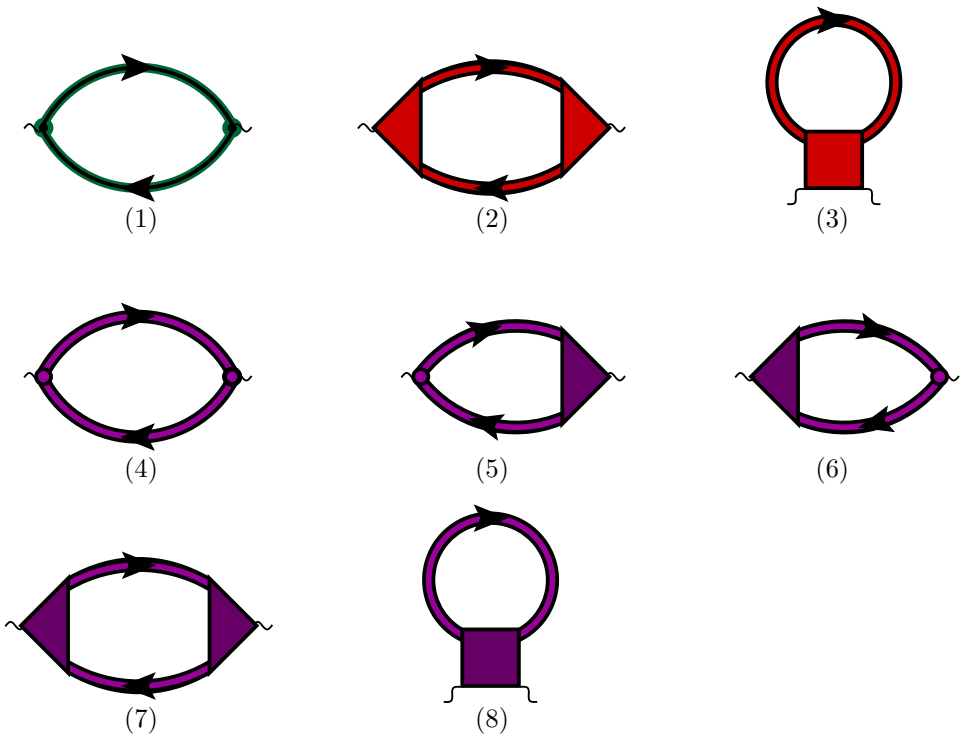

Figure 5.3: All diagrams corresponding to Eq. (5.61) in appendix 5.D contributing to the total current-current correlation function in the probe-fermion model. The Feynman rules are as follows. Small wiggly lines denote the locations where external photons with vector indices μ and ν attach. The single solid (green) line is $G_\psi[0]$. The green vertex is $e\gamma^\mu/\hbar$. The double (red) line is $G_\pi[0]$. The red three-point vertex is $\delta\Sigma_\pi/\delta A_\mu$. The red four-point vertex is $\delta^2\Sigma_\pi/\delta A_\mu\delta A_\nu$. The double purple line is $G_\chi[0]$. The purple circle is $e\gamma^\mu/\hbar$. The purple three-point vertex is $\delta\Sigma_\chi/\delta A_\mu$, and finally the purple four-point vertex is $\delta^2\Sigma_\chi/\delta A_\mu\delta A_\nu$.

In the probe-fermion model, there are three contributions to the total conductivity. To see this, we recall that both the fermions in the conformal field theory, and the external probe fermion χ are coupled to a U(1) gauge field, in Eqs. (5.9) and (5.11), respectively. So the total charge current is the sum of these two contributions,

$$J^\mu = J^\mu_{\text{cft}} + J^\mu_\chi,$$

where $J^\mu_\chi = -ec\bar{\chi}\gamma^\mu\chi$ as can be seen from the free probe-fermion action in Eq. (5.11).

The total current-current correlation function is in this case given by[24]

$$\begin{aligned}\left\langle J^\mu J^\nu \right\rangle &= \left\langle \left(J^\mu_{\text{cft}} + J^\mu_\chi\right)\left(J^\nu_{\text{cft}} + J^\nu_\chi\right) \right\rangle \\ &= \left\langle J^\mu_{\text{cft}} J^\nu_{\text{cft}} \right\rangle + \left\langle J^\mu_\chi J^\nu_\chi \right\rangle + 2\left\langle J^{(\mu}_\chi J^{\nu)}_{\text{cft}} \right\rangle.\end{aligned} \tag{5.30}$$

The expectation values in Eq. (5.30) are taken with respect to the full theory in Eq. (5.29), i.e., including χ, but with A_μ set to zero. Because χ is dynamical, it gives a correction proportional to $\mathcal{G}_\chi$ to the propagator of π in the conformal field theory. Therefore, the conformal field theory contribution $\left\langle J^\mu_{\text{cft}} J^\nu_{\text{cft}} \right\rangle$ can be further split up into a contribution where χ is set to zero, denoted with a subscript "cft" as $\left\langle J^\mu_{\text{cft}} J^\nu_{\text{cft}} \right\rangle_{\text{cft}}$ plus an additional piece that incorporates just the coupling of π to χ. This last piece is denoted by

$$\left\langle J^\mu_{\text{cft}} J^\nu_{\text{cft}} \right\rangle_{\text{cft,}} - \left\langle J^\mu_{\text{cft}} J^\nu_{\text{cft}} \right\rangle_{\text{cft}} .$$

Here, the expectation value cft' is taken with respect to the partition function $Z_{\text{cft'}}$ given by

$$Z_{\text{cft'}} = \int \mathrm{d}[\bar\pi]\mathrm{d}[\pi] \exp\left[\frac{i}{\hbar} S_{\text{cft}}[\bar\pi,\pi] - iN\left(\frac{2g_1}{\hbar g_2}\right)^2 \left(\pi\middle|\mathcal{G}_\chi[0]\middle|\pi\right)\right].$$

The second term in the exponent is a selfenergy correction for π, which arises if we first integrate out the probe fermion χ and its conjugate $\bar\chi$. The conformal field theory action is given by

$$S_{\text{cft}}[\bar\pi,\pi] = \hbar N\left(\pi\middle|G_\pi^{-1}[0]\middle|\pi\right) - i\hbar N \operatorname{Tr}\ln\left(-G_\psi^{-1}[0]\right) + i\hbar\frac{N}{2}\operatorname{Tr}\ln\left(-G_\varphi^{-1}\right).$$

We will interpret the separate contributions from Eq. (5.30) in the following, starting with the pure conformal field theory contribution in section 5.3.2.1 and considering the additional effect of the probe fermion in section 5.3.2.2. As it turns out, the various contributions in Eq. (5.30) may be distinguished physically by their different dependence on temperature in the dc limit. Finally, in section 5.3.2.3 we turn to semiholography, by means of which our model calculation of the current-current correlation function can be generalized to a probe fermion coupled to any conformal field theory.

5.3.2.1 Conductivity of the conformal field theory

The conductivity of the conformal field theory is proportional to $\left\langle J^\mu_{\text{cft}} J^\nu_{\text{cft}} \right\rangle_{\text{cft}}$ due to charging the ψ_i fermions. The real scalar fields φ_i are neutral. This corresponds to taking into account diagrams (1)-(3) of Fig. 5.3.

[24] The notation in the last term means we take the symmetric part of these cross terms, $A^{(\mu}B^{\nu)} = \frac{1}{2}\left(A^\mu B^\nu + A^\nu B^\mu\right)$.

Ignoring the χ-dependent contributions and the A_μ-independent determinant of the scalar Green's function, Eq. (5.29) becomes

$$\ln Z[A] = N\mathrm{Tr}\ln\Big(-G_\psi^{-1}[A]\Big) + \mathrm{Tr}\ln\Big(-NG_\pi^{-1}[A]\Big). \tag{5.31}$$

The relative factor of N in front of the terms in Eq. (5.31) is important. It indicates that up to leading order in N, the conductivity is given by the free fermion conductivity. This is represented by diagram (1) in Fig. 5.3. Interaction corrections, which correspond to diagrams (2) and (3), appear as $\mathcal{O}(1)$ corrections through G_π. The fermion selfenergy contributes only at $\mathcal{O}(1/N)$ so it does not appear here. This means that, to leading order, the fermionic conductivity of the probe-fermion model is the conductivity of N species of free Dirac fermions, which is at zero chemical potential and zero temperature given by [143]

$$\sigma_\psi(\omega) = \frac{Ne^2|\omega|}{12\pi\hbar c} + \mathcal{O}(1).$$

This is the leading fermionic contribution to the conductivity of the conformal field theory at zero temperature.

In the nonzero-temperature case, the electrical conductivity is given by the $T > 0$ conductivity of the free ψ_i fermions [143]. It is given by

$$\sigma_\psi(\omega) = \frac{Ne^2}{3\hbar c}\left[\frac{\pi k_B T}{3\hbar}\,\delta\left(\frac{\hbar\omega}{k_B T}\right) + \frac{\omega}{4\pi}\tanh\left(\frac{\hbar\omega}{4k_B T}\right)\right], \tag{5.32}$$

The factor $\tanh(\hbar\omega/4k_BT)$ comes from the difference of two Fermi distributions. This term is called the interband contribution and describes the contribution of particle-antiparticle excitations to transport. The conductivity also has a delta-function peak with a weight proportional to $k_BT/\hbar$ at the point $\hbar\omega/k_BT = 0$, which corresponds to intraband transport of thermally excited degrees of freedom. This delta-function peak is a consequence of the fact that in the probe-fermion model the conformal field theory is free at leading order in N. It comes from the imaginary part of a pole at zero frequency.

However, for a conformal field theory such as the theory in Ref. [167] that is strongly interacting in the large-N limit, we expect a finite result for the dc conductivity. In general, if the free result contains such a delta-function peak, interactions have the effect of smearing it out, forming a Drude-like peak in terms of a more general dimensionless function f of $\hbar\omega/k_BT$, which goes to a constant in the limit $\hbar\omega/k_BT \to 0$. Schematically,

$$\frac{k_BT}{\hbar}\delta\left(\frac{\hbar\omega}{k_BT}\right) \xrightarrow{\text{interactions}} \frac{k_BT}{\hbar}f\left(\frac{\hbar\omega}{k_BT}\right).$$

So in the strongly coupled case, we expect such an intraband term to contribute a term $Ne^2 k_B T\, f(0)/3\hbar^2 c$ in the dc limit, where $f(0)$ is a finite and nonzero universal constant. See Ref. [168] for an example of work where the universal coefficients of current-current correlation functions of a certain conformal field theory are computed in a $1/N$ expansion.

In this way, the probe-fermion model reproduces the result in Ref. [167], namely that the dc conductivity of a conformal field theory in a thermal state is linear in temperature, in the (3+1)-dimensional case. This is to be expected from dimensional analysis, as temperature is the only scale present. Depending on whether the theory is interacting or free, the prefactor can be finite, as in Ref. [167], or infinite, when the linear scaling in temperature comes from a delta-function peak.

5.3.2.2 Additional effects of the probe fermion

When the probe fermion is added to the conformal field theory, this gives rise to the rest of the terms in Eq. (5.30), namely,

$$\begin{aligned}\left\langle J^\mu J^\nu \right\rangle - \left\langle J^\mu_{\text{cft}} J^\nu_{\text{cft}} \right\rangle_{\text{cft}} = \left\langle J^\mu_\chi J^\nu_\chi \right\rangle + 2\left\langle J^{(\mu}_\chi J^{\nu)}_{\text{cft}} \right\rangle \\ + \left\langle J^\mu_{\text{cft}} J^\nu_{\text{cft}} \right\rangle_{\text{cft,}} - \left\langle J^\mu_{\text{cft}} J^\nu_{\text{cft}} \right\rangle_{\text{cft}} .\end{aligned} \tag{5.33}$$

All these terms contribute at $\mathcal{O}(1)$ to the total conductivity.

The first term on the right-hand side of Eq. (5.33), i.e., $\langle J^\mu_\chi J^\nu_\chi \rangle$, is the current-current correlation function of the probe fermion, and it is represented by diagram (4) of Fig. 5.3. Its contribution to the electrical conductivity is analogous to the conductivity of the interacting Dirac fermion in semiholography, computed in Ref. [143]. So as in Eq. (5.7), the dc conductivity of the probe fermion is proportional to T^{3-4M}, with $-1/2 < M < 1/2$. This can be understood by dimensional analysis. In the strong-coupling limit of the conformal field theory, the only dimensionful quantities present are the temperature and the coupling between probe fermion and conformal field theory, called g in the probe-fermion model. For fixed and finite g, every occurrence of the selfenergy provides a power $2M$ of temperature, while every propagator of χ contributes the inverse power. This is because in the dc limit, the selfenergy dominates over the free part of the χ propagator. So by counting propagators and comparing it to the dimension of conductivity in 3+1 dimensions, we can determine the scaling behaviour of these diagrams in the dc limit.

The second term on the right-hand side of Eq. (5.33), i.e., $\langle J^{(\mu}_\chi J^{\nu)}_{\text{cft}} \rangle$, is an interference term between the probe-fermion current and the current of the conformal field theory. This term gives rise to diagrams (5) and (6) of Fig. 5.3. Because the vertex function contains a factor of Σ_χ, the above counting suggests that this term scales with temperature as T^{2-2M}.

Thirdly, the combination $\left\langle J^{\mu}_{\text{cft}} J^{\nu}_{\text{cft}} \right\rangle_{\text{cft}}, - \left\langle J^{\mu}_{\text{cft}} J^{\nu}_{\text{cft}} \right\rangle_{\text{cft}}$ represents the effect that the addition of the probe fermion has on the current-current correlation function of the conformal field theory. This contribution is represented by diagrams (7) and (8). In this case, dimensional analysis suggests that these terms scale again linearly with temperature.

Summarizing, based on the discussions above and in section 5.3.2.1, we conclude that including all contributions in Fig. 5.3, i.e., up to subleading order in N, the total electrical conductivity in the dc limit is of the form

$$\sigma_{\text{dc}} \sim \underbrace{\Big(\mathcal{O}(N) + \mathcal{O}(1)\Big) T}_{\text{conformal field theory}} + \underbrace{\mathcal{O}(1)\, T^{2-2M}}_{\text{interference}} + \underbrace{\mathcal{O}(1)\, T^{3-4M}}_{\text{probe fermion}} + \mathcal{O}\left(\frac{1}{N}\right). \tag{5.34}$$

It is interesting to note that in the probe-fermion model, the probe-fermion conductivity and interference contribution can be identified from their anomalous scaling with temperature, despite the fact that they are subleading in N.

We note one more thing on this classification of diagrams. The total action in Eq. (5.8) has a local U(1) symmetry associated with conservation of the total charge current J^{μ}. The procedure to compute the current-current correlation function from appendix 5.D leading to the diagrams in Fig. 5.3 does not violate this gauge invariance. As a consequence, the Ward identity for current conservation is satisfied and $\left\langle J^{\mu} J^{\nu} \right\rangle$ is automatically transversal, i.e.,[25]

$$\partial_{\mu} \Big\langle J^{\mu} J^{\nu} \Big\rangle = 0.$$

It is interesting to consider how precisely the various contributions cancel when taking the divergence of $\left\langle J^{\mu} J^{\nu} \right\rangle$. For instance, the divergence of diagram (1) vanishes by itself because it contains only bare propagators and bare vertices. However, the probe-fermion contribution, diagram (4), contains dressed propagators but bare vertices, and therefore we need additional contributions to satisfy the Ward identity. These additional contributions are supplied by diagrams (5), (6) and (7). The divergence of diagrams (2), (3) and (8) vanishes because of the conformal field theory Ward identity in the absence of χ.

In Ref. [143], diagram (4) was computed numerically and its physical properties discussed in details. According to the classification in section 5.3.2, diagram (4) is the only contribution to the fermionic conductivity. The conductivity contributions due to the dependence of the selfenergy on the gauge field can be interpreted as interference with the conformal field theory, and a correction to the conductivity of the conformal field theory.

[25] To be precise, the finite part of $\left\langle J^{\mu} J^{\nu} \right\rangle$ is transversal. There may be longitudinal divergent parts that drop out after regularization.

5.3.2.3 Conductivity in semiholography

It is enlightening to reconsider the electrical conductivity of the boundary theory in the context of semiholography. The boundary action of the dual conformal field theory coupled to a fermionic dynamical source χ resembles the action in Eq. (5.1), namely, it is given by

$$S = S_{\text{cft}}[\bar{O}, O] + S_0[\bar{\chi}, \chi] + ig \int \mathrm{d}^4x \, \left(\bar{\chi} O + \bar{O}\chi\right). \tag{5.35}$$

Here, O is a fermionic composite operator in the conformal field theory S_{cft}. In general, in the presence of a boundary gauge field A_μ which couples to both the conformal field theory and to the dynamical source χ, this is modified to

$$S = S_{\text{cft}}[\bar{O}, O; A] + \big(\chi\big|\hbar G_0^{-1} - e\not{A}\big|\chi\big) + ig\big(\chi\big|O\big) + ig\big(O\big|\chi\big),$$

where

$$S_{\text{cft}}[\bar{O}, O; A] = S_{\text{cft}}[\bar{O}, O] + \frac{1}{c}\int \mathrm{d}^4x \, J^\mu_{\text{cft}} \, A_\mu,$$

and J^μ_{cft} is again the current of the conformal field theory. The conformal field theory can be integrated out, and for the dynamical source χ, this gives rise to an effective selfenergy,

$$\Sigma_\chi[A](x, x') = -i\left(\frac{g}{\hbar}\right)^2 \Big\langle \bar{O}(x')O(x)\Big\rangle_{\text{cft}+A},$$

and the subscript cft+A indicates that this is the expectation value with respect to the conformal field theory action in the presence of a current J^μ_{cft} sourced by the boundary gauge field.

As before, the total electrical conductivity of the boundary theory is proportional to the total current-current correlation function, which is in turn proportional to the expression $\delta^2 \ln Z[A]/\delta A_\mu \delta A_\nu$. It is convenient to integrate out the $\bar{\chi}$ and χ fields as well and, for taking these functional derivatives, to expand the generating functional $\ln Z[A]$ up to second order in the gauge field. The same procedure was carried out for the probe-fermion model in appendix 5.D. Besides the pure conformal field theory contribution, the resulting expression contains the various purple diagrams in Fig. 5.3 built from the χ propagators and vertices present in the theory. In particular, there will be vertices of the form $\delta\Sigma_\chi/\delta A_\mu$ and $\delta^2\Sigma_\chi/\delta A_\mu \delta A_\nu$. To investigate these, the selfenergy of the dynamical source is expanded in powers of the gauge field. We have

$$\begin{aligned}\Big\langle \bar{O}(x)O(x')\Big\rangle_{\text{cft}+A} \simeq \Big\langle \bar{O}(x)O(x')\Big\rangle_{\text{cft}} + \frac{i}{\hbar c}\int \mathrm{d}^4y \Big\langle \bar{O}(x)O(x')J^\mu_{\text{cft}}(y)\Big\rangle_{\text{cft}} A_\mu(y) \\ + \left(\frac{i}{\hbar c}\right)^2 \int \mathrm{d}^4y \int \mathrm{d}^4y' \Big\langle \bar{O}(x)O(x')J^\mu_{\text{cft}}(y)J^\nu_{\text{cft}}(y')\Big\rangle_{\text{cft}} A_\mu(y)A_\nu(y').\end{aligned}$$

This leads to the following expression for the three-point and four-point vertices

$$\begin{aligned}\frac{\delta\Sigma_\chi}{\delta A_\mu} &= \frac{1}{\hbar c}\left(\frac{g}{\hbar}\right)^2 \left\langle \bar{O}OJ^\mu_{\rm cft}\right\rangle_{\rm cft}, \\ \frac{\delta^2\Sigma_\chi}{\delta A_\mu \delta A_\nu} &= i\left(\frac{g}{\hbar^2 c}\right)^2 \left\langle \bar{O}OJ^\mu_{\rm cft}J^\nu_{\rm cft}\right\rangle_{\rm cft},\end{aligned} \tag{5.36}$$

respectively. Up to here this was just a field-theory calculation, but now we connect this result to holography. The vertices on the left-hand side of Eq. (5.36) contribute i.a. to the interference terms needed to satisfy the Ward identity.[26] On the right-hand side we find precisely the correlators of operators in a conformal field theory with a holographic dual. So in a semiholographic theory, the full conductivity satisfying the Ward identity can be computed with holography. This amounts to computing, besides the selfenergy that is proportional to $\langle \bar{O}O\rangle_{\rm cft}$, the correlators $\langle \bar{O}OJ^\mu_{\rm cft}\rangle_{\rm cft}$ and $\langle \bar{O}OJ^\mu_{\rm cft}J^\nu_{\rm cft}\rangle_{\rm cft}$ using the holographic prescription [73]. These correlators can be represented by the Witten diagrams in Fig 5.4.

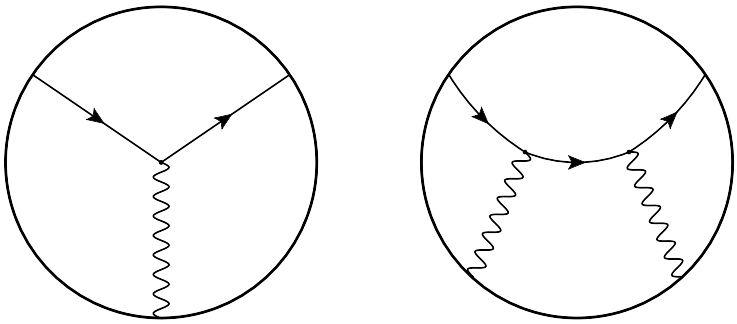

Figure 5.4: Witten diagrams for the correlators $\langle \bar{O}OJ^\mu_{\rm cft}\rangle_{\rm cft}$ and $\langle \bar{O}OJ^\mu_{\rm cft}J^\nu_{\rm cft}\rangle_{\rm cft}$.

As a final remark, we note that the coupling in the action in Eq. (5.1) is a special case of the coupling in the semiholographic action in Eq. (5.35), namely, in Eq. (5.1), the operator O is given by the product of the elementary fermion and a critical boson, $O = \chi\Phi$. Because the coupling in Eq. (5.35) contains only one power of χ, integrating out the critical theory leads to an effective selfenergy for χ, i.e., a term in the action proportional to $g^2\bar{\chi}\chi\langle\bar{O}O\rangle_{\rm cft}$. In contrast, integrating out the critical boson Φ in Eq. (5.1) yields a nonlocal effective interaction for χ of the form $g^2\left(\bar{\chi}\chi\right)^2\langle\Phi^*\Phi\rangle_{\rm cft}$.[27] This effective interaction can lead, for instance in the Hartree-Fock approximation,

[26] We have shown this in the probe-fermion model in section 5.3.2.2, but it is not hard to see that this is a general result.

[27] Such an effective four-point interaction is the starting point of the Fock model introduced in the next section.

to an effective selfenergy for χ. In a semiholographic setting, we need a bulk scalar field dual to the order parameter Φ that is sourced by the fermion bilinear $\bar{\chi}\chi$ on the boundary. This results in the required interaction term for χ where $\langle\Phi^*\Phi\rangle_{\mathrm{cft}}$ is related to the bulk-to-boundary propagator of the dual scalar field. As Eq. (5.1) just serves as a motivation for the problem discussed in this paper, a detailed treatment of this case in semiholography is beyond the scope of this paper.

5.4 Fock model

In section 5.3 we have seen that the probe-fermion model offers an interpretation of the dynamical-source model. Here the dynamical source is analogous to a probe fermion coupled to a conformal field theory. A disadvantage of the probe-fermion model is the fact that for $\eta = 0$, we do not recover the $M = 1/2$ behaviour with logarithmic corrections seen in the dynamical-source model. Furthermore, the conformal field theory of the probe-fermion model is free in the large-N limit. As a consequence the dominant contribution to the electrical conductivity comes from free ψ_i fermions, and it thus diverges in the dc limit.

These problems are addressed in the second field-theory model that we consider, the Fock model. Here, there is no separate probe fermion. Instead, we consider fermions with an effective interaction due to a propagator containing an anomalous dimension. This effective interaction reduces to a Coulomb-like potential for $\eta = 0$, which is the desired behaviour in the $M = 1/2$ case of the dynamical-source model. A nontrivial selfenergy, given by the selfconsistent Fock diagram, comes about by introducing a bosonic and nonlocal auxiliary field. In the strong-coupling limit, the fermionic propagator reduces to the inverse of the selfenergy, and this suggests that the kinetic term G_0^{-1} in the propagator arises due to finite-coupling corrections. Thus, we have a second interpretation of the dynamical-source model, where the source fermion lives in the dual conformal field theory, and the dynamical part of its propagator is an effective way to incorporate finite-coupling corrections.

In the Fock model, we have again N species of Dirac fermions. They are minimally coupled to a gauge field A_μ and interact via a nonlocal, real interaction potential Δ. The partition function is

$$Z[A] = \int \mathrm{d}[\bar{\psi}]\mathrm{d}[\psi] \exp\left[\frac{i}{\hbar}\Big(S_0[\bar{\psi},\psi;A] + S_\Delta[\bar{\psi},\psi]\Big)\right], \tag{5.37}$$

where the actions are given by

$$S_0[\bar{\psi},\psi;A] = -i\hbar\sum_{i=1}^{N}\int \mathrm{d}^4x\, \bar{\psi}_i\Big(\not{\partial} - \frac{ie}{\hbar}\not{A}\Big)\psi_i, \tag{5.38}$$

and

$$S_\Delta[\bar\psi,\psi] = \frac{\hbar g}{2N}\sum_{i,i'=1}^{N}\int \mathrm{d}^4x \int \mathrm{d}^4x' \Delta(x-x')\,\bar\psi_i(x)\,\psi_{i'}(x)\,\bar\psi_{i'}(x')\,\psi_i(x').$$

As discussed before, the motivation for this form of S_Δ is that a nonlocal interaction for the fermions is required to make their selfenergy nontrivial in the large-N limit. For a microscopic origin of this form of the interaction $\Delta(x-x')$, we imagine that integrating out other fields in a more complicated theory could lead to such a nonlocal effective interaction term, as was already discussed at the end of section 5.3.2.3. Because of the nonlocality, this interaction can carry momentum, and we choose it to have the momentum dependence of a relativistic scalar with an anomalous dimension η,

$$\Delta(x-x') = \int \frac{\mathrm{d}^4k}{(2\pi)^4}\frac{1}{-k^{2-\eta}}e^{ik\cdot(x-x')}. \tag{5.39}$$

We proceed by performing a Hubbard-Stratonovich transformation that decouples the interaction, by multiplying the partition function by

$$\begin{aligned}1 = \int \mathrm{d}[\rho]\exp\Bigg[\frac{i}{\hbar}\int \mathrm{d}^4x\int \mathrm{d}^4x'\sum_{\alpha,\beta}\Big(\rho_{\beta\alpha}(x',x) - \sum_{i=1}^{N}\frac{\hbar g}{N}\bar\psi_{i,\alpha}(x)\psi_{i,\beta}(x')\Big)\\ \times\frac{N\Delta(x-x')}{2\hbar g}\Big(\rho_{\alpha\beta}(x,x') - \sum_{i'=1}^{N}\frac{\hbar g}{N}\bar\psi_{i',\beta}(x')\psi_{i',\alpha}(x)\Big)\Bigg].\end{aligned} \tag{5.40}$$

We have written down the spin indices α,β explicitly. The auxiliary field ρ is a matrix in these indices, is nonlocal, and its expectation value is proportional to the fermionic density matrix. Defining the collective field ρ in this way is indicative of Fock theory, which explains the name of this model. As in the probe-fermion model, the factors of N are chosen such that certain diagrams survive in the large-N limit. We introduce new shorthand notation, by means of which the expression in Eq. (5.40) is written as

$$1 = \int \mathrm{d}[\rho]\exp\Bigg[\frac{i}{\hbar}\sum_{i,i'=1}^{N}\Big(\rho + \frac{\hbar g}{N}\psi_i\bar\psi_i\Big|\Big|\frac{N\Delta}{2\hbar g}\Big|\Big|\rho + \frac{\hbar g}{N}\psi_{i'}\bar\psi_{i'}\Big)\Bigg].$$

Compared to the notation in section 5.3, the double lines now express the dependence on two spacetime points of the field ρ and the product $\bar\psi\psi$. After this transformation, the action for the fermions is quadratic, and we can read off the inverse Green's function for a single fermion species. It is a functional of ρ and A_μ, and its matrix elements are in the coordinate representation given by

$$G^{-1}_{\psi,\alpha\beta}[A,\rho](x,x') = -i\left(\not\partial_{\alpha\beta} - \frac{ie}{\hbar}\not A_{\alpha\beta}(x)\right)\delta^4(x-x') - \frac{1}{\hbar}\rho_{\alpha\beta}(x,x')\Delta(x-x').$$

From now on, the spinor indices are again suppressed in our notation. We can integrate out the fermions, which results in the partition function

$$Z[A] = \int \mathrm{d}[\rho] \exp\left[N \mathrm{Tr} \ln\Big(- G_\psi^{-1}[A,\rho]\Big) + N\big(\rho\big|\big|\frac{i}{\hbar}\frac{\Delta}{2\hbar g}\big|\big|\rho\big)\right]. \tag{5.41}$$

We do a fluctuation expansion of ρ around its expectation value by writing $\rho = \langle\rho\rangle + \delta\rho$. In the large-$N$ limit, the approximation where we take only the leading term into account, becomes exact, because the path integral is dominated by this value. In this case, it is the mean-field approximation where we replace ρ by $\langle\rho\rangle$. The field ρ is bosonic so its expectation value can be nonzero. Setting the first-order terms in $\delta\rho$ to zero leads to an equation for $\langle\rho\rangle$. First, we expand the fermionic propagator to first order in $\delta\rho$,

$$G_\psi^{-1}[A,\rho](x,x') = G_\psi^{-1}[A,\langle\rho\rangle](x,x') - \frac{1}{\hbar}\Delta(x-x')\delta\rho(x,x'),$$

where we have defined the inverse fermion propagator in the mean-field approximation as

$$G_\psi^{-1}[A,\langle\rho\rangle](x,x') = -i\left(\not{\partial} - \frac{ie}{\hbar}\not{A}(x)\right)\delta^4(x-x') - \frac{1}{\hbar}\big\langle\rho(x,x')\big\rangle\Delta(x-x'). \tag{5.42}$$

This is the Dyson equation for the dressed fermion propagator. The second term on the right-hand side of Eq. (5.42) is the selfenergy of the fermions, which is proportional to $\langle\rho\rangle\Delta$. Thus, the mean-field approximation to ρ leads to the Fock approximation to the fermion selfenergy, which becomes exact for large N. This is in contrast to the probe-fermion model, which can be seen as a Hartree-like theory, in which the auxiliary field is local and the selfenergy of the ψ_i fields is $1/N$ suppressed.

To find the fermion selfenergy in the Fock model, we first set $A_\mu = 0$ so that $\langle\rho\rangle$ depends only on the difference in coordinates. Then we expand the logarithm in Eq. (5.41) in fluctuations, and demanding the first-order terms in $\delta\rho$ in the partition function to vanish, leads to the following equation for $\langle\rho\rangle$,

$$\big\langle\rho(x-x')\big\rangle = \frac{g\hbar}{i}G_\psi[0,\langle\rho\rangle](x-x'). \tag{5.43}$$

Together, Eq. (5.42) and Eq. (5.43) form a recursive equation for the dressed fermion propagator, and thus for the fermionic selfenergy. This recursive equation is elegantly expressed in momentum space as

$$G_\psi^{-1}(k) = \not{k} - \Sigma_\psi(k), \tag{5.44}$$

with the selfenergy

$$\Sigma_\psi(k) = -ig\int \frac{\mathrm{d}^4q}{(2\pi)^4}\Delta(k-q)G_\psi(q).$$

Note that we have also suppressed the functional dependence on A, ρ and $\langle\rho\rangle$, so that the dressed Green's function is denoted just by G_ψ. This Dyson equation for the fermion propagator is shown diagrammatically in Fig. 5.5.

Figure 5.5: Graphical representation of the Dyson equation from Eq. (5.44). Double lines denote the full Green's function G_ψ, while single lines denote the free propagator $1/\not{k}$. The wiggly line is the interaction Δ. The Fock bubble comes with a factor g, or equivalently, two factors $\sqrt{g}$. The latter can be associated with the solid dots.

5.4.1 Fermionic Fock selfenergy

Finding the fermionic selfenergy requires solving the recursive equation Eq. (5.44), which cannot be solved analytically. However, we can solve it both in the free case and the very strong-coupling limit. In the first, we just set $g = 0$ so that the selfenergy piece drops out, and obtain the trivial result $G_\psi(k) = 1/\not{k}$. We can depart from this trivial value of the coupling by means of perturbation theory in g.

The strong-coupling limit is the opposite limit, with the effect that the selfenergy term dominates over the $\not{k}$ term in Eq. (5.44), so that we can ignore it, and Eq. (5.44) becomes

$$\frac{1}{ig}G_\psi^{-1}(k) = \int \frac{\mathrm{d}^4q}{(2\pi)^4}\Delta(k-q)G_\psi(q). \tag{5.45}$$

In this limit, the fermion propagator must depend on g, otherwise Eq. (5.45) is inconsistent. It has dimensions of length in our conventions. Furthermore, in the absence of scales such as temperature, it must be a single power of k, it is fermionic so there is also a $\not{k}$ involved, and of course there can be a numerical prefactor. So we plug in the following Ansatz,

$$G_\psi(k) = g^y k^{x-1}\not{k}h(\eta),$$

where the function $h(\eta)$ is dimensionless. Plugging this Ansatz into Eq. (5.45) and equating the powers of g on both sides of the equality, leads to $y = -1/2$, and consequently, $x = -1 - \eta/2$. Then, the Green's function in the strong-coupling limit is given by

$$G_\psi(k) = -\frac{1}{\Sigma_\psi(k)} = \frac{\not{k}\,h(\eta)}{\sqrt{g}k^{2+\frac{\eta}{2}}}. \tag{5.46}$$

We can solve $h(\eta)$ from Eq. (5.45) by doing the momentum integral on the right-hand side, which is described in more detail in appendix 5.E, and results in

$$\frac{1}{h^2(\eta)} = \frac{\Gamma(1-\frac{\eta}{4})}{(4\pi)^2\Gamma(1+\frac{\eta}{4})}\left[\frac{\Gamma(1+\frac{\eta}{2})\Gamma(-\frac{\eta}{4})}{\Gamma(1-\frac{\eta}{2})\Gamma(2+\frac{\eta}{4})} - \frac{4+\eta}{2\eta}\,\frac{\Gamma(-1-\frac{\eta}{4})\Gamma(2+\frac{\eta}{2})}{\Gamma(3+\frac{\eta}{4})\Gamma(-\frac{\eta}{2})}\right]. \quad (5.47)$$

In the strong-coupling limit the Green's function is minus the inverse of the selfenergy. The selfenergy of the fermions is thus given by

$$\Sigma_\psi(k) = -\frac{\sqrt{g}}{h(\eta)}\not{k}k^{\frac{\eta}{2}}. \quad (5.48)$$

Note that this result is proportional to $\sqrt{g}$, which expresses the nonperturbative nature of the calculation. Switching to the retarded prescription amounts to setting $ck^0 = \omega + i0$. Thus, in the strong-coupling limit G_ψ coincides with the result from Eq. (5.6) in the dynamical-source model, if we make the following identifications,

$$\eta = 4M - 2,$$
$$\sqrt{g} = \frac{\lambda\,\Gamma(\frac{1}{2}-M)}{c\,4^M\Gamma(\frac{1}{2}+M)}h\,(4M-2)\,.$$

We see that the range $-2 < \eta < 0$, where $h(\eta)$ is real, covers only the positive-M part of the selfenergy in the dynamical-source model, as it corresponds to $0 < M < 1/2$. However, in this case the value $\eta = 0$ does correspond to $M = 1/2$.

5.4.2 Electrical conductivity

To compute the electrical conductivity of the fermions in the Fock model, we can start from the generating functional $\ln Z[A]$, which is, after making use of Eq. (5.43) in the presence of A_μ, given by

$$\ln Z[A] = N\mathrm{Tr}\ln\Big(-G_\psi^{-1}[A]\Big) - iN\,\big(G_\psi[A]\,\big|\big|\,\frac{g\Delta}{2}\,\big|\big|\,G_\psi[A]\,\big).$$

In principle, the procedure is the same as for the probe-fermion model, i.e., taking two functional derivatives of $\ln Z[A]$ with respect to the gauge field. However, less work is required if we make use of the fact that, in the Fock model, the total current density operator is exactly known in terms of the fermionic fields. It is given by

$$J^\mu(x) = -ec\sum_{j=1}^{N}\bar{\psi}_j(x)\gamma^\mu\psi_j(x).$$

The current-current correlation function is therefore proportional to

$$\left.\frac{\delta\langle J^\mu(x)\rangle}{\delta A_\nu(y)}\right|_{A=0} = Nice\lim_{x'\to x}\mathrm{tr}\left[\gamma^\mu\left.\frac{\delta G_\psi[A](x,x')}{\delta A_\nu(y)}\right|_{A=0}\right], \quad (5.49)$$

where the expectation value is taken with respect to the interacting action in the presence of A_μ, and the lowercase trace is just over spinor indices. Evaluation of Eq. (5.49) requires knowing G_ψ up to first order in A_μ. This information is obtained from the mean-field Dyson equation for G_ψ which we found in section 5.4.1, and which we recall here,

$$G_\psi^{-1}[A](x,x') = G_0^{-1}(x,x') - \frac{e}{\hbar}\delta^4(x-x')\not{A}(x) - \Sigma_\psi[A](x,x'), \tag{5.50}$$

with the inverse noninteracting fermion Green's function $G_0^{-1}(x,x') = -i\not{\partial}\delta^4(x-x')$ and with the selfenergy

$$\Sigma_\psi[A](x,x') = \frac{g}{i}G_\psi[A](x,x')\Delta(x-x'),$$

which depends on A_μ through G_ψ. It is not necessary to invert this Dyson equation. Namely, using the definition of the matrix inverse in the coordinate representation, it is easy to show that

$$\left.\frac{\delta G_\psi[A](x,x')}{\delta A_\nu(y)}\right|_{A=0} = -\int \mathrm{d}^4y' \int \mathrm{d}^4y''\, G_\psi[0](x,y')\,\Gamma^\nu(y',y'';y)\,G_\psi[0](y'',x').$$

We have introduced the three-point function Γ^ν, which is just the functional derivative with respect to A_ν of the inverse Green's function, i.e.,

$$\Gamma^\nu(y',y'';y) = \left.\frac{\delta G_\psi^{-1}[A](y',y'')}{\delta A_\nu(y)}\right|_{A=0}.$$

Then, the current-current correlation function obtained from Eq. (5.49) can be written as

$$\begin{aligned}\left\langle J^\mu(x)J^\nu(y)\right\rangle_{A=0} &= \frac{\hbar c}{i}\left.\frac{\delta\left\langle J^\mu(x)\right\rangle}{\delta A_\nu(y)}\right|_{A=0} \\ &= -Ne\hbar c^2\int \mathrm{d}^4y' \int \mathrm{d}^4y''\mathrm{tr}\Big[\gamma^\mu\, G_\psi[0](x,y')\,\Gamma^\nu(y',y'';y)\,G_\psi[0](y'',x)\Big].\end{aligned} \tag{5.51}$$

The current-current correlation function is thus given by the fermion bubble diagram with dressed propagators $G_\psi[0]$, one bare vertex proportional to $e\gamma^\mu$, and one dressed vertex Γ^ν, as is also shown in Fig. 5.6. We can rewrite the Dyson equation as a recursive equation for Γ^ν, by taking the derivative $\delta/\delta A_\nu$ of Eq. (5.50) and using the chain rule for functional derivatives. This yields

$$\begin{aligned}\Gamma^\nu(x,x';y) &= -\frac{e}{\hbar}\gamma^\nu\delta^4(x-x')\delta^4(x-y) \\ &+ \int \mathrm{d}^4z \int \mathrm{d}^4z' \frac{\delta\Sigma_\psi(x,x')}{\delta G_\psi(z,z')}\int \mathrm{d}^4y' \int \mathrm{d}^4y''\, G_\psi[0](z,y')\,\Gamma^\nu(y',y'';y)\,G_\psi[0](y'',z').\end{aligned} \tag{5.52}$$

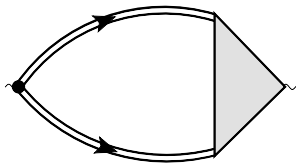

Figure 5.6: Diagram of the current-current correlation function from Eq. (5.51) containing the three-point vertex. The filled triangle is Γ^μ, the solid circle denotes the bare vertex proportional to $e\gamma^\mu$ and the double lines represent the dressed fermion propagator $G_\psi[0]$.

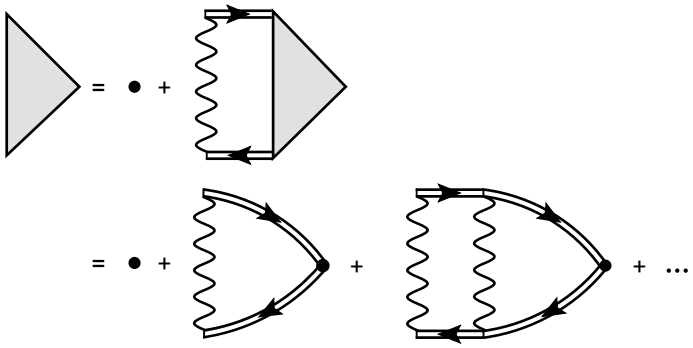

Figure 5.7: The recursive relation for the three-point vertex Γ^μ from Eq. (5.52), where we also made use of Eq. (5.53). The notation is the same as in Fig. 5.6, and each wiggly line is an interaction $g\Delta$.

The recursive equation for Γ^ν represents an infinite bubble sum, which is diagrammatically depicted in Fig. 5.7. The zeroth-order term in Eq. (5.52) is proportional to the bare vertex, and the rest is interpreted as interaction corrections to this vertex. It is more elegant to make the current-current correlation function explicitly symmetric in the indices μ and ν, by means of a four-point vertex, as is shown diagrammatically in Fig. 5.8. This requires knowledge of the dependence of the selfenergy on the Green's function, i.e., the object $\delta\Sigma_\psi(x,x')/\delta G_\psi(z,z')$. This four-point function is known in the Fock model, it is simply given by

$$\frac{\delta\Sigma_\psi(x,x')}{\delta G_\psi(z,z')} = \frac{g}{i}\Delta(x-x')\delta^4(x-z)\delta^4(x'-z'). \tag{5.53}$$

The required recursive equation for this four-point function is given diagrammatically in Fig. 5.9.

We can compute the conductivity in the Fock model again in the GG approximation where vertex corrections are ignored. Since the fermion propagator and

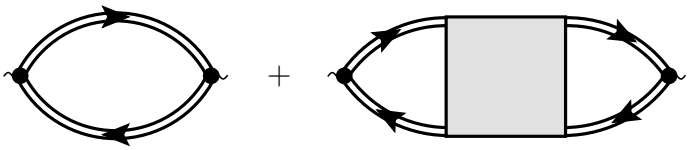

Figure 5.8: Diagrams for the current-current correlation function in terms of the four-point vertex in Fig. 5.9.

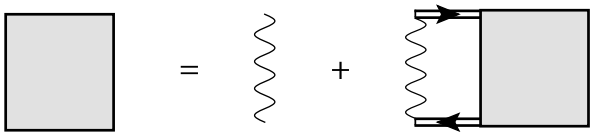

Figure 5.9: Recursive expression, corresponding to the Bethe-Salpeter equation for the four-point vertex.

selfenergy are the same as the propagator in the dynamical-source model, the result is also the same, i.e., the dc conductivity scales with T^{3-4M}. The scaling becomes linear in the limit $M \to 1/2$. Moreover, in the Fock model vertex corrections can in principle be included because the dependence of Σ_ψ on A_μ is exactly known as we have seen.

5.4.3 Finite-coupling corrections

In section 5.4.1 the Dyson equation from Eq. (5.44) was solved exactly in the strong-coupling limit and at zero temperature, which lead to the result in Eq. (5.48). Taking $A_\mu = 0$, $\vec{k} = 0$ and $\omega > 0$ for simplicity, the fermion Green's function in the strong-coupling limit can thus be written as $G_\psi(\omega) = -1/\Sigma_\psi(\omega) = c/\gamma^0 \tilde{g}\omega^{2M}$. Here, $\tilde{g}$ has the dimensions of frequency to the power $1 - 2M$, and contains the numerical prefactor of the selfenergy. We would like to generalize this result to also reproduce the correct weak-coupling behaviour by means of a $1/\tilde{g}$ expansion. In the absence of other scales like temperature, the exact result for $G_\psi(\omega)$ can only depend on the ratio $\omega/\tilde{g}\omega^{2M}$. So for general values of $\tilde{g}$, the solution to the selfconsistent Dyson equation for the Green's function can be written as

$$G_\psi^{-1}(\omega) = \frac{1}{c}\gamma^0 \tilde{g}\omega^{2M} f\left(\frac{\omega}{\tilde{g}\omega^{2M}}\right). \tag{5.54}$$

Here, f is a dimensionless function, which reduces to the correct asymptotic behaviour for very small and very large $\tilde{g}$ if we write a linear Ansatz for f of the

form

$$f(x) = 1 + xf'(\infty) + d(x),$$

where $d(x)$ is another dimensionless function that describes by construction the deviation from the linear behaviour at intermediate values of x. To recover the strong coupling result at $x = 0$, we have $f(0) = 1$ and $d(0) = 0$. The free result is obtained if $f(x)$ asymptotes to $-x$ for $x \gg 1$. So $d(\infty) = d'(\infty) = 0$ and $f'(\infty) = -1$. With this behaviour of f, Eq. (5.54) becomes

$$G_\psi^{-1} = \frac{1}{c}\gamma^0 \left(-\omega + \tilde{g}\omega^{2M} + \tilde{g}\omega^{2M} d\left(\frac{\omega}{\tilde{g}\omega^{2M}} \right) \right).$$

In the approximation where the intermediate function d is ignored, we obtain

$$G_\psi^{-1}(\omega) = -\frac{1}{c}\gamma^0 \left(\omega - \tilde{g}\omega^{2M} \right).$$

This Green's function is exactly a solution to the Dyson equation for very large and very small $\tilde{g}$. The kinetic term linear in ω comes about from a $1/\tilde{g}$ expansion of the strong-coupling result. The approximation here is that this $1/\tilde{g}$ term, which is exact for vanishing $\tilde{g}$, is generalized to intermediate values of the coupling, by ignoring the deviation function d. It is therefore an asystematic approximation to a systematic $1/\tilde{g}$ expansion, that nevertheless recovers the exact ultraviolet and infrared behaviour of the propagator.

This form of the propagator coincides with the Green's function of the dynamical-source model from Eq. (5.5). The $\tilde{g}$ denotes the prefactor of the selfenergy in Eq. (5.6). This leads to a second interpretation of the dynamical-source model. The kinetic term that makes the χ fermion dynamical, can be seen as a phenomenological correction from the infinite coupling limit.

5.5 Conclusion

The main motivation of this work is to obtain a more intuitive understanding of the results of bottom-up holography and in particular the dynamical-source model. In this work we have investigated two ways to interpret the holographic results, by means of the probe-fermion model and of the Fock model. Both reproduce the fermionic selfenergy in the large-N limit. Firstly, the probe-fermion model gives a semiholographic interpretation of the dynamical-source model, where a dynamical probe fermion is coupled to a "conformal field theory", i.e., for our purposes, a theory that is scale invariant in the large-N limit. The conductivity then consists of three contributions, i.e., contributions of the probe fermion, the conformal field theory and an interference term. The conformal field theory contribution consists of an $\mathcal{O}(N)$

and an $\mathcal{O}(1)$ part, the other two contributions are $\mathcal{O}(1)$. These contributions scale all three with a different power in temperature in the dc limit, which in particular makes the probe-fermion contribution experimentally distinguishable, even though it is subleading with respect to the conformal field theory. Unfavorable properties of the probe-fermion model are that the conformal field theory becomes free in the large-N limit, and that removing the anomalous dimension does not reproduce the $M = 1/2$ result as anticipated. In contrast, in the Fock model, the fermionic field is itself part of the conformal field theory, and the noninteracting part of its propagator can be understood to be a phenomenological way to incorporate finite-coupling corrections. This latter interpretation also suggests that the dynamical-source model can be effectively understood in a bottom-up holographic sense. The conductivity corresponds to the result in the dynamical-source model if vertex corrections are ignored. The latter can in principle be taken into account in the Fock model.

This work can be extended in various ways. A simple generalization would be to turn on temperature and chemical potential in the field theory, and to look at nonrelativistic cases, e.g. by considering Galilean invariance or a dynamical exponent z unequal to 1. These would be the first steps towards describing the system of cold atoms at unitarity mentioned in the introduction. There are a myriad occurrences of bottom-up models with nonzero temperature and chemical potential to compare with in the literature, see e.g. [64, 98, 101, 103, 119, 160] for an incomplete list. The nonrelativistic case $z \neq 1$ can be studied by using a Lifshitz geometry [135, 169]. It is possible to consider these cases also in semiholography, and compare them to the field-theory model. The thought behind these generalizations is to see if a simple field-theory analogy continues to hold in a more general case. The choices that we have to make in order to retrieve the holographic or semiholographic results, provide a means to interpret the latter in a more conventional, field-theoretic sense. Then, we can have some confidence that such a field-theory construction also works the other way around, by suggesting the appropriate way to construct a (semi)holographic bottom-up model in cases where it is not immediately known or obvious. Eventually, we hope to achieve a phenomenological bottom-up dictionary, in particular one which also works for semiholography.

5.A Notation and conventions

We work in SI units, unless stated otherwise. The metric tensor is given by

$$\eta_{\mu\nu} \;=\; \mathrm{diag}(-1, 1, 1, 1),$$

where Greek indices run over $0, 1, 2, 3$. Latin indices run over spatial directions $1, 2, 3$. The spacetime position vector and four-derivative operator are respectively given by

$x^\mu = (ct, \vec{x})$ and $\partial_\mu = (1/c\ \partial_t, \vec{\nabla})$. The wave-four-vector is given by $k^\mu = (\omega/c, \vec{k})$. Fourier transformations to momentum space, and inverse Fourier transformations, are respectively performed as follows,

$$f(x) = \int \frac{\mathrm{d}^4 k}{(2\pi)^4} f(k) e^{ik\cdot x}, \qquad f(k) = \int \mathrm{d}^4 x f(x) e^{-ik\cdot x},$$

where $k \cdot x = k_\mu x^\mu$. The Dirac matrices obey the Clifford algebra

$$\{\gamma^\mu, \gamma^\nu\} = 2\eta^{\mu\nu}\mathbb{1},$$

where $\mathbb{1}$ denotes the 4×4 identity matrix, and we note explicitly that $(\gamma^0)^2 = -\mathbb{1}$.

The notation for fermionic Green's functions is as follows. The noninteracting Green's functions of the ψ_i and χ fermions at $A_\mu = 0$, appearing in sections 5.3 and 5.4 are time-ordered connected Green's functions associated with the differential operator $-i\partial\!\!\!/$. This is done in order to keep the notation concise and Lorentz invariance manifest during the manipulations in section 5.3 and 5.4. In contrast to this, in Ref. [143], the noninteracting Green's function of the dynamical-source fermion at $A_\mu = 0$ is the retarded Green's function corresponding to the differential operator $-i\gamma^0\partial\!\!\!/$, so it includes the factor γ^0, peeled off from $\bar{\Psi}$. The reason for this definition in Ref. [143] was that this gives immediately the correct retarded Green's function that satisfies the sum rule from Eq. (5.2).

5.B Supersymmetric Yang-Mills theory

For the readers without a background in supersymmetry, we briefly review the basic properties of (supersymmetric) Yang-Mills theory [170]. Ordinary Yang-Mills theory is a non-Abelian gauge theory with gauge group SU(N_c), which contains vector bosons A^a_μ called gluons and transforming in the adjoint representation of this gauge group. In supersymmetric Yang-Mills theory, the symmetry is extended by adding $\mathcal{N}$ extra fermionic supersymmetry generators. These act as ladder operators on the gluon states, each time changing the spin by $\pm 1/2$, thus creating a supermultiplet of particle states. For example, in the case of global $\mathcal{N} = 4$ supersymmetry, the supermultiplet consists of a single vector boson (gluon), two Dirac fermions (gluinos) and three complex scalars, denoted by X, which all transform in the adjoint representation of SU(N_c). Note that the number of bosonic and fermionic degrees of freedom are both equal to 8, as required by supersymmetry. Supersymmetric Yang-Mills theory is a conformal field theory in $d = 3 + 1$ dimensions, the symmetry being the conformal group SO(4,2).

There is an additional global symmetry called R-symmetry, which says that the $\mathcal{N}$ supersymmetry generators can be interchanged without affecting the supersymmetry

algebra. In 3+1 dimensions and for $\mathcal{N} = 4$, the R-symmetry group is U(4). This corresponds to global U(4) transformations in the supermultiplet that conserve helicity, i.e., the gluinos or X scalars are interchanged among themselves. This is important for our discussion of the electrical conductivity of supersymmetric Yang-Mills theory. When we speak about the electrical conductivity of the dual field theory, we imagine to take a global U(1) subgroup of this R-symmetry, which defines a charge e just like in Ref. [167]. Unlike the gluinos and X scalars, the gluon is a singlet under R-symmetry, so the gluon is electrically neutral according to this definition.

Bottom-up models containing for instance the Maxwell or Dirac field in an asymptotically Anti-de Sitter background, are usually by construction very similar to the theory that is obtained from the benchmark duality between Type IIB string theory in $\mathrm{AdS}_5 \times \mathrm{S}_5$ and four-dimensional $\mathcal{N} = 4$ supersymmetric Yang-Mills theory in certain limits. Our working assumption is that the boundary conformal field theory dual to an asymptotically Anti-de Sitter background has similar field content and interaction structure as $\mathcal{N} = 4$ supersymmetric Yang-Mills theory. Moreover, the boundary conformal field theory is supposed to be in the large-N_c limit, where N_c is the number of colours. Secondly, it is supposedly in the large 't Hooft coupling limit, where the 't Hooft coupling $\lambda_H = g_{YM}^2 N_c$ and g_{YM} is the Yang-Mills coupling. It is also important to mention that supersymmetric Yang-Mills theory is a conformal field theory without an anomalous dimension of its fundamental fields, since the beta function of g_{YM} is exactly zero. However, composite operators consisting of traces over multiple fundamental fields can obtain an anomalous dimension. If these operators are sourced, the theory is deformed away from supersymmetric Yang-Mills theory. In the bottom-up models considered here, the boundary field theory can obtain anomalous dimensions by adding extra bulk degrees of freedom that provide a source for these composite operators. For example, as in Ref. [71], a bulk Dirac field with mass M can be added and it sources a composite chiral operator in the boundary with an anomalous dimension depending on M. In addition, temperature introduces a scale to the boundary field theory. In holographic models, the presence of a black brane in the bulk spacetime breaks conformal invariance of the boundary by putting it in a thermal state with temperature T, coinciding with the Hawking temperature. At nonzero temperature, supersymmetry is broken in the boundary, but the superpartners of the gluons are still present in the theory. Moreover, temperature does not cause anomalous dimensions. As is clear from Fig. 5.1, raising the temperature of a conformal field theory will bring the system into the quantum critical region. This does not affect the scaling dimensions of the operators in the critical theory.

The field content and properties of supersymmetric Yang-Mills theory were for us the inspiration to write down the ingredients of the probe-fermion model correspond-

ing to the contributions in Eq. (5.8). Firstly, to us, the fields ψ_i, $\bar{\psi}_i$ and φ_i together resemble the field content of the fermionic sector of the conformal supersymmetric Yang-Mills theory. We refer to this part of the model as the "conformal field theory", despite the fact that it is not conformal, but only scale invariant, for some values of the coupling g_2. It has a number of copies of fields $i = 1, ..., N$ that roughly mimics the large number of colours of the SU(N_c) gauge theory. The real scalars φ_i are inspired by the gluons of supersymmetric Yang-Mills theory. They are obviously not the actual gluons of a non-Abelian gauge theory. Supersymmetric Yang-Mills theory has no anomalous dimension, but it is possible that self-interactions of the gluons in a more general non-Abelian gauge theory, caused by loop corrections, can effectively lead to an anomalous dimension. Motivated by this possibility, we give the scalar propagator an anomalous dimension parameterized by η. The gluinos of supersymmetric Yang-Mills theory were our inspiration for the Dirac fermions ψ_i. We consider for now only the fermionic sector, so there are no counterparts of the X scalars of supersymmetric Yang-Mills theory. The scalar field φ_i remains neutral in the probe-fermion model. Our thought behind this is the fact that in supersymmetric Yang-Mills theory, the gluon is a singlet under R-symmetry as discussed above.

In the probe-fermion action, the coupling between the probe fermion and the conformal field theory is in the large-N limit given by a term of the form $\bar{\chi}\pi$ and its conjugate, where $\pi \propto \sum_{i=1}^{N} \psi_i \varphi_i / N$. This turns out to be similar to a composite operator of the form $O = \mathrm{Tr}\,[\Psi\Phi]$ in a typical boundary gauge theory, where the fields Ψ and Φ are respectively an elementary fermionic and bosonic field in the adjoint representation of the gauge group SU(N_c). This means they can be written as $\Phi = \sum_a t^a \Phi^a(x)$, where a indexes the adjoint representation of SU(N_c), and t^a denotes its generators. Working this out using the usual normalization $\mathrm{Tr}[t^a t^b] = -\delta_{ab}/2$, we obtain $O \propto \sum_a \Psi^a \Phi^a$, where a takes $N_c^2 - 1$ values. In the large-N_c limit the 1 is negligible, so this suggests that N in the probe-fermion model corresponds to N_c^2, and that π may be related to a composite operator of the single-trace form $\mathrm{Tr}\,[\Psi\Phi]$, to which the dynamical source couples.

5.C Loop integral for the probe-fermion selfenergy

In this section the loop integral in Eq. (5.22) for the fermionic selfenergy in the probe-fermion model is computed at zero temperature. It is repeated here for clarity,

$$I(k) = \int \frac{\mathrm{d}^4 q}{(2\pi)^4} G_\psi(k+q)\, G_\varphi(q).$$

The inverse propagators of the φ_i and ψ_i fields are given in Eqs. (5.15) and (5.16), respectively. In momentum space, they are given by

$$G_\varphi(k) = \frac{1}{-k^{2-\eta}},$$

and

$$G_\psi(k) = \frac{1}{\not{k}}.$$

Then the integral $I(k)$ becomes $I(k) = -\gamma^\mu \mathcal{I}_\mu(k)$, with

$$\mathcal{I}_\mu(k) = \int \frac{\mathrm{d}^4 q}{(2\pi)^4} \frac{k_\mu + q_\mu}{q^{2-\eta}(k+q)^2}.$$

We first compute the integral $\mathcal{I}_\mu$ for $\eta \neq 0$. After subtraction of ultraviolet divergences for the real part, the integral is finite for $\eta > 0$. The result for η in the desired interval $-2 < \eta < 0$ is obtained by analytic continuation [171]. After shifting the integration variable q to $q - k$, to handle the tensor structure, we write the integrand as a derivative with respect to k_μ. This yields

$$\begin{aligned}\mathcal{I}_\mu(k) &= -\frac{1}{\eta}\frac{\partial}{\partial k^\mu}\int \frac{\mathrm{d}^4 q}{(2\pi)^4}\frac{1}{q^2\left[(q-k)^2\right]^{-\frac{\eta}{2}}} + k_\mu \int \frac{\mathrm{d}^4 q}{(2\pi)^4}\frac{1}{q^2\left[(q-k)^2\right]^{1-\frac{\eta}{2}}} \\ &\equiv \mathcal{I}_\mu^{(1)}(k) + \mathcal{I}_\mu^{(2)}(k).\end{aligned} \tag{5.55}$$

We compute both terms separately, starting with the first term. We use the generalized Feynman trick,

$$\frac{1}{A^\alpha B^\beta} = \frac{\Gamma(\alpha+\beta)}{\Gamma(\alpha)\Gamma(\beta)}\int_0^1 \mathrm{d}u \frac{u^{\alpha-1}(1-u)^{\beta-1}}{\left[uA + (1-u)B\right]^{\alpha+\beta}},$$

which allows us to rewrite the angular integrations in terms of an Euler integral. Another appropriate shift in the integration variable removes the $k \cdot q$ terms, after which we obtain

$$\begin{aligned}\mathcal{I}_\mu^{(1)}(k) &= \frac{1}{2}\frac{\partial}{\partial k^\mu}\int_0^1 \mathrm{d}u\, u^{-1-\frac{\eta}{2}} \int \frac{\mathrm{d}^4 q}{(2\pi)^4}\frac{1}{\left[q^2 + u(1-u)k^2\right]^{1-\frac{\eta}{2}}} \\ &= -\left(1-\frac{\eta}{2}\right)k_\mu \int_0^1 \mathrm{d}u\, u^{-1-\frac{\eta}{2}} u(1-u) \int \frac{\mathrm{d}^4 q}{(2\pi)^4}\frac{1}{\left[q^2 + u(1-u)k^2\right]^{2-\frac{\eta}{2}}}.\end{aligned}$$

The momentum integral results in

$$\int \frac{\mathrm{d}^4 q}{(2\pi)^4}\frac{1}{\left[q^2 + u(1-u)k^2\right]^{2-\frac{\eta}{2}}} = \frac{i}{(4\pi)^2}\frac{1}{-\frac{\eta}{2}\left(1-\frac{\eta}{2}\right)}\left[u(1-u)k^2\right]^{\frac{\eta}{2}}. \tag{5.56}$$

With this result we can perform the u integral, which is finite for $\eta > -4$, leading to

$$\int_0^1 \mathrm{d}u\ (1-u)^{1+\frac{\eta}{2}} = \frac{1}{2+\frac{\eta}{2}}.$$

Finally, the first term of the integral $\mathcal{I}_\mu$ is obtained as

$$\mathcal{I}_\mu^{(1)}(k) = \frac{ik_\mu \left(k^2\right)^{\frac{\eta}{2}}}{(4\pi)^2} \frac{1}{\frac{\eta}{2}\left(2+\frac{\eta}{2}\right)}.$$

For the second term $\mathcal{I}_\mu^{(2)}$ we apply the same steps. After Feynman's trick combined with appropriate shifts of the integration variable,

$$\begin{aligned}\mathcal{I}_\mu^{(2)}(k) &= k_\mu \int \frac{\mathrm{d}^4 q}{(2\pi)^4} \frac{1}{q^2\left[(q-k)^2\right]^{1-\frac{\eta}{2}}} \\ &= k_\mu \left(1-\frac{\eta}{2}\right) \int_0^1 \mathrm{d}u u^{-\frac{\eta}{2}} \int \frac{\mathrm{d}^4 q}{(2\pi)^4} \frac{1}{\left[q^2+u(1-u)k^2\right]^{2-\frac{\eta}{2}}}.\end{aligned}$$

The momentum integral is again given by Eq. (5.56). The u integral is finite for $\eta > -2$ and results in a factor $1/(1+\eta/2)$. Finally, $\mathcal{I}_\mu^{(2)}$ becomes

$$\mathcal{I}_\mu^{(2)}(k) = \frac{ik_\mu \left(k^2\right)^{\frac{\eta}{2}}}{(4\pi)^2} \frac{1}{-\frac{\eta}{2}\left(1+\frac{\eta}{2}\right)}.$$

Then, the total integral I is obtained by adding both terms, which gives

$$I(k) = -\gamma^\mu \left(\mathcal{I}_\mu^{(1)}(k) + \mathcal{I}_\mu^{(2)}(k)\right) = \frac{i\not{k} \left(k^2\right)^{\frac{\eta}{2}}}{(4\pi)^2} \frac{1}{\frac{\eta}{2}\left(1+\frac{\eta}{2}\right)\left(2+\frac{\eta}{2}\right)},$$

for $-2 < \eta < 0$. This result was used to compute the selfenergy of the probe fermion in section 5.3.1.

For completeness, we also compute the integral I at $\eta = 0$. It has a logarithmic divergence for $\eta = 0$. We show below how it can be regularized. We now have to deal with

$$\mathcal{I}_\mu(k) = \int \frac{\mathrm{d}^4 q}{(2\pi)^4} \frac{q_\mu}{q^2(q-k)^2}.$$

To get rid of the tensor structure, a derivative is inconvenient because this leads to a logarithm in the integrand. Instead, we shift $q \to q + k/2$ so that the denominator becomes even under $q \to -q$. Then, we can drop the odd term in the numerator. This is allowed as long as we regularize the integral, so that the contributions at infinity drop out. Using Feynman's trick once more, this leads to

$$\mathcal{I}_\mu(k) = \frac{k_\mu}{2} \int_0^1 \mathrm{d}u \frac{\mathrm{d}^4 q}{(2\pi)^4} \frac{1}{\left[q^2+u(1-u)k^2\right]^2}.$$

The loop integral is logarithmically divergent in 3+1 dimensions, but can be computed by analytical continuation to d dimensions by means of dimensional regularization,

$$\int \frac{\mathrm{d}^d q}{(2\pi)^d} \frac{1}{\left[q^2 + u(1-u)k^2\right]^2} = \frac{i}{(4\pi)^{\frac{d}{2}}} \Gamma\left(2 - \frac{d}{2}\right) \left[u\,(1-u)\,k^2\right]^{\frac{d}{2}-2}.$$

Subsequently, the u integral yields for $d > 2$

$$\int_0^1 \mathrm{d}u\, u^{\frac{d}{2}-2} (1-u)^{\frac{d}{2}-2} = \frac{2^{3-d}\sqrt{\pi}\,\Gamma\left(\frac{d}{2}-1\right)}{\Gamma\left(\frac{d-1}{2}\right)}.$$

Plugging this into $\mathcal{I}_\mu(k)$ and expanding around $d = 4 - \epsilon$, we obtain for the integral I,

$$\begin{aligned} I(k) &= -\frac{i\not{k}\left(k^2\right)^{\frac{d}{2}-2}}{(4\pi)^{\frac{d}{2}}} 2^{2-d}\sqrt{\pi}\frac{\Gamma\left(2-\frac{d}{2}\right)\Gamma\left(\frac{d}{2}-1\right)}{\Gamma\left(\frac{d-1}{2}\right)} \\ &\simeq -\frac{i\not{k}}{2(4\pi)^2}\left[\frac{2}{\epsilon} + \ln\left(\frac{1}{k^2}\right) + \ln(16\pi) + \psi^{(0)}\left(\frac{3}{2}\right)\right], \end{aligned} \tag{5.57}$$

where $\psi^{(0)}(z)$ is the digamma function, defined as $\psi^{(0)}(z) = \Gamma'(z)/\Gamma(z)$. Our choice for the renormalization condition for Eq. (5.57) that introduces a scale into the logarithm is the following. We subtract from Eq. (5.57) $I(k_{(0)})$, that is, $I(k)$ evaluated at a constant and nonzero reference momentum scale $k_{(0)}$. Thus we obtain the renormalized loop integral at $\eta = 0$,

$$I(k) = \frac{i\not{k}}{2(4\pi)^2} \ln\left(\frac{k^2}{k_{(0)}^2}\right).$$

So $k_{(0)}^2$ is the value of k^2 at which the loop integral vanishes, which remains undetermined here and should ultimately be determined from experiment.

5.D Generating functional for current-current correlation function in the probe-fermion model

Here we give in more detail the derivation of Eq. (5.61), which was diagrammatically represented in Fig. 5.3. We start from the generating functional given in Eq. (5.29), repeated here for clarity,

$$\ln Z[A] = N\mathrm{Tr}\ln\Big(-G_\psi^{-1}[A]\Big) + \mathrm{Tr}\ln\Big(-NG_\pi^{-1}[A]\Big) + \mathrm{Tr}\ln\Big(-G_\chi^{-1}[A]\Big). \tag{5.58}$$

In what follows, we first rearrange the terms inside the logarithms on the right-hand side so that A-dependent terms are separated from A-independent terms. This

includes explicitly expanding all functionals of A up to second order. Next, we expand the logarithms up to second order in A. Finally, we differentiate twice with respect to the gauge field, and write the result in the coordinate basis, which gives us the desired Eq. (5.61).

It is convenient to write the propagators in representation-independent notation. The inverse ψ_i propagator is given in Eq. (5.16), and we write it as

$$\begin{aligned} G_\psi^{-1}[A] &= G_0^{-1} - \frac{e}{\hbar}\not{A}, \\ G_0^{-1}(x,x') &= -i\not{\partial}\delta^4(x-x'). \end{aligned}$$

The inverse of the full Green's function G_χ^{-1} is given by the quadratic part in Eq. (5.20), in basis-independent notation,

$$\begin{aligned} G_\chi^{-1}[A] &= G_0^{-1} - \frac{e}{\hbar}\not{A} - \Sigma_\chi[A] \\ \Sigma_\chi[A] &= \frac{2ig_1^2}{g_2} + \left(\frac{2g_1}{\hbar g_2}\right)^2 G_\pi[A]. \end{aligned}$$

We split the inverse π propagator in an A-dependent and A-independent part,

$$\begin{aligned} G_\pi^{-1}[A] &= \mathcal{G}_\pi^{-1} - \Sigma_\pi[A], \\ \mathcal{G}_\pi^{-1} &= \frac{2}{i\hbar^2 g_2}, \\ \Sigma_\pi[A] &= -\frac{i}{\hbar^2} G_\varphi^T G_\psi[A], \end{aligned}$$

where $G_\varphi^T = G_\varphi(x',x)$ in the coordinate representation. At this point we can reexpress Eq. (5.58) as

$$\begin{aligned} \ln Z[A] = N\mathrm{Tr}\ln\Big(-G_0^{-1} + \frac{e}{\hbar}\not{A}\Big) \\ + \mathrm{Tr}\ln\Big(-N\mathcal{G}_\pi^{-1} + N\Sigma_\pi[A]\Big) + \mathrm{Tr}\ln\Big(-G_0^{-1} + \frac{e}{\hbar}\not{A} + \Sigma_\chi[A]\Big). \end{aligned} \tag{5.59}$$

In the above expression, the capital trace Tr sums over both the spinor indices and the infinite matrix (coordinate or momentum) indices of the propagators. We are going to expand this expression up to second order in the vector potential. As an intermediate step, we expand the selfenergy terms which are functionals of A_μ as

$$\Sigma_\pi[A] = \Sigma_\pi[0] + A_\lambda \frac{\delta\Sigma_\pi}{\delta A_\lambda}[0] + \frac{1}{2}A_\lambda A_\rho \frac{\delta^2\Sigma_\pi}{\delta A_\lambda \delta A_\rho}[0], \tag{5.60}$$

and similar for $\Sigma_\chi[A]$.[28] From now on, we suppress the notation [0] indicating the absence of functional dependence on the gauge field. So it is implicit here that all propagators and vertices are evaluated with A_μ set to zero. With this, the generating functional Eq. (5.59) becomes

$$\begin{aligned}
\ln Z[A] &= N\mathrm{Tr}\ln\left[-G_0^{-1}\left(\mathbb{1}-\frac{e}{\hbar}G_0\not{A}\right)\right] \\
&+\mathrm{Tr}\ln\left[-N\left(\mathcal{G}_\pi^{-1}-\Sigma_\pi\right)\left\{\mathbb{1}-\left[\mathcal{G}_\pi^{-1}-\Sigma_\pi\right]^{-1}\left(A_\lambda\frac{\delta\Sigma_\pi}{\delta A_\lambda}+\frac{1}{2}A_\lambda A_\rho\frac{\delta^2\Sigma_\pi}{\delta A_\lambda\delta A_\rho}\right)\right\}\right] \\
&+\mathrm{Tr}\ln\left[\left(-G_0^{-1}+\Sigma_\chi\right)\left\{\mathbb{1}-\left[G_0^{-1}-\Sigma_\chi\right]^{-1}\left(\frac{e}{\hbar}\not{A}+A_\lambda\frac{\delta\Sigma_\chi}{\delta A_\lambda}+\frac{1}{2}A_\lambda A_\rho\frac{\delta^2\Sigma_\chi}{\delta A_\lambda\delta A_\rho}\right)\right\}\right].
\end{aligned}$$

We can simplify this even further by rewriting $G_0^{-1}-\Sigma_\chi = G_\chi^{-1}$, the inverse χ propagator evaluated at $A_\mu = 0$, and similarly for π we write $\mathcal{G}_\pi^{-1} - \Sigma_\pi = G_\pi^{-1}$. Then it is easy to expand $\ln Z$ up to second order in the gauge field. Using $\mathrm{Tr}\ln(AB) = \mathrm{Tr}\ln A + \mathrm{Tr}\ln B$ we can separate the gauge-field-dependent parts in the logarithms above. The factors N drop out everywhere, except in the first term, to which just the free ψ_i fields contribute. Performing the two derivatives explicitly, finally yields

[28] Note that upon reinstating all coordinate dependence, expression Eq. (5.60) is given by

$$\begin{aligned}
&\Sigma_\pi[A](x,x') \\
&= \Sigma_\pi[0](x,x') + \int \mathrm{d}^4y A_\lambda(y)\frac{\delta\Sigma_\pi(x,x')}{\delta A_\lambda(y)}[0] + \frac{1}{2}\int\mathrm{d}^4y\int\mathrm{d}^4y' A_\lambda(y)A_\rho(y')\frac{\delta^2\Sigma_\pi(x,x')}{\delta A_\lambda(y)\delta A_\rho(y')}[0].
\end{aligned}$$

$$
\begin{aligned}
&- \frac{\delta^2 \ln Z[A]}{\delta A_\mu(z)\delta A_\nu(z')}\bigg|_{A=0} = \\
&\quad N\left(\frac{e}{\hbar}\right)^2 \mathrm{tr}\Big[G_0(z,z')\gamma^\nu G_0(z',z)\gamma^\mu\Big] \\
&\quad + \int \mathrm{d}^4x \int \mathrm{d}^4x' \int \mathrm{d}^4x'' \int \mathrm{d}^4x''' \mathrm{tr}\Big[G_\pi(x,x')\frac{\delta\Sigma_\pi(x',x'')}{\delta A_\mu(z)}G_\pi(x'',x''')\frac{\delta\Sigma_\pi(x''',x)}{\delta A_\nu(z')}\Big] \\
&\quad + \int \mathrm{d}^4x \int \mathrm{d}^4x' \mathrm{tr}\Big[G_\pi(x,x')\frac{\delta^2\Sigma_\pi(x',x)}{\delta A_\mu(z)\delta A_\nu(z')}\Big] \\
&\quad + \left(\frac{e}{\hbar}\right)^2 \mathrm{tr}\Big[G_\chi(z,z')\gamma^\nu G_\chi(z',z)\gamma^\mu\Big] \\
&\quad + \frac{e}{\hbar}\int \mathrm{d}^4x \int \mathrm{d}^4x' \mathrm{tr}\Big[G_\chi(x,z')\gamma^\nu G_\chi(z',x')\frac{\delta\Sigma_\chi(x',x)}{\delta A_\mu(z)}\Big] \\
&\quad + \frac{e}{\hbar}\int \mathrm{d}^4x \int \mathrm{d}^4x' \mathrm{tr}\Big[G_\chi(x,z)\gamma^\mu G_\chi(z,x')\frac{\delta\Sigma_\chi(x',x)}{\delta A_\nu(z')}\Big] \\
&\quad + \int \mathrm{d}^4x \int \mathrm{d}^4x' \int \mathrm{d}^4x'' \int \mathrm{d}^4x''' \mathrm{tr}\Big[G_\chi(x,x')\frac{\delta\Sigma_\chi(x',x'')}{\delta A_\mu(z)}G_\chi(x'',x''')\frac{\delta\Sigma_\chi(x''',x)}{\delta A_\nu(z')}\Big] \\
&\quad + \int \mathrm{d}^4x \int \mathrm{d}^4x' \mathrm{tr}\Big[G_\chi(x,x')\frac{\delta^2\Sigma_\chi(x',x)}{\delta A_\mu(z)\delta A_\nu(z')}\Big].
\end{aligned}
\tag{5.61}
$$

The lowercase trace tr sums only over the spinor indices. All contributions to the right-hand side of Eq. (5.61) are of order $\mathcal{O}(1)$, except the first which is of $\mathcal{O}(N)$. The terms in Eq. (5.61) appear in the same order as the numbered diagrams in Fig. 5.3.

5.E Loop integral for the Fock selfenergy

This section provides some details for the computation of the loop integral in the expression for the Fock model selfenergy, in the strong-coupling limit and at zero temperature. Plugging in the result for G_ψ from Eq. (5.46), we write Eq. (5.45) as

$$
\frac{i}{h^2(\eta)}\not{k}k^{\frac{\eta}{2}} = \gamma^\mu \mathcal{K}_\mu(k), \tag{5.62}
$$

where $\mathcal{K}_\mu$ is the loop integral that is the focus of this appendix, given by

$$
\mathcal{K}_\mu(k) = \int \frac{\mathrm{d}^4q}{(2\pi)^4} \frac{q_\mu}{\big[(q-k)^2\big]^{1-\frac{\eta}{2}} q^{2+\frac{\eta}{2}}}.
$$

The power of q^2 in the denominator is the only difference with the momentum integral $\mathcal{I}_\mu$ of the probe-fermion model, computed in appendix 5.C. The integral $\mathcal{K}_\mu$ can be

computed in the same manner as $\mathcal{I}_\mu$, and as before we obtain the result for $\eta < 0$ by analytic continuation. As in Eq. (5.55), the numerator q_μ can be written as a $\partial/\partial k^\mu$ and a k_μ term, respectively,

$$\mathcal{K}_\mu(k) = \mathcal{K}_\mu^{(1)}(k) + \mathcal{K}_\mu^{(2)}(k).$$

As an intermediate result, performing the same steps as for $\mathcal{I}_\mu^{(1)}$ in appendix 5.C yields for the first term

$$\begin{aligned}\mathcal{K}_\mu^{(1)}(k) &= -\frac{1}{\eta}\frac{\partial}{\partial k^\mu}\int \frac{\mathrm{d}^4 q}{(2\pi)^4}\frac{1}{\left(q^2\right)^{1+\frac{\eta}{4}}\left[(q-k)^2\right]^{-\frac{\eta}{2}}} \\ &= -\frac{ik_\mu k^{\frac{\eta}{2}}}{(4\pi)^2}\frac{4+\eta}{2\eta}\frac{\Gamma(-1-\frac{\eta}{4})\Gamma(1-\frac{\eta}{4})\Gamma(2+\frac{\eta}{2})}{\Gamma(1+\frac{\eta}{4})\Gamma(3+\frac{\eta}{4})\Gamma(-\frac{\eta}{2})}.\end{aligned}$$

For the second term we find

$$\mathcal{K}_\mu^{(2)}(k) = k_\mu \int \frac{\mathrm{d}^4 q}{(2\pi)^4}\frac{1}{q^{2+\frac{\eta}{2}}\left[(q-k)^2\right]^{1-\frac{\eta}{2}}} = \frac{ik_\mu k^{\frac{\eta}{2}}}{(4\pi)^2}\frac{\Gamma(1-\frac{\eta}{4})\Gamma(1+\frac{\eta}{2})\Gamma(-\frac{\eta}{4})}{\Gamma(1+\frac{\eta}{4})\Gamma(1-\frac{\eta}{2})\Gamma(2+\frac{\eta}{4})}.$$

Adding these two results and solving Eq. (5.62) for $h(\eta)$ yields the required expression in Eq. (5.47). Again, the integral has a logarithmic divergence for $\eta = 0$. For a sensible result with $h(\eta)$ real, we must be certain that the result for $1/h^2(\eta)$ is positive. This is the case for $-2 < \eta < 0$.

Chapter 6

Towards semiholographic ultracold Fermi gases

One of the steps towards a more realistic model of semiholographic ultracold atoms is to break particle-hole symmetry and incorporate a nonzero fermion density. A nonzero equilibrium density means there is an associated nonzero chemical potential. In this chapter we describe how to do semiholography at nonzero chemical potential. This chapter is based on joint work and therefore has some overlap with Ref. [3].

The inverse Green's function for free relativistic Dirac fermions at a nonzero mass m and chemical potential μ is given by

$$G_0^{-1}(\omega, \vec{k}) = \left(\omega + \frac{\mu}{\hbar}\right) \mathbb{1}_4 + \gamma^0 \vec{\gamma} \cdot c\vec{k} + \gamma^0 \frac{imc^2}{\hbar}. \tag{6.1}$$

This can be obtained by minimally coupling the fermions to a nondynamical vector field whose temporal component is μ/ec and whose spatial components are zero.

In the interacting theory, the selfenergy also depends on the chemical potential in a nontrivial manner. How should we modify the bulk theory to include the effect of the chemical potential into the selfenergy? As it turns out, similarly to Eq. (6.1), we have to add a global U(1) symmetry to the quantum field theory that governs the interactions between the Dirac fermions. Its gravity dual then has to have a local U(1) symmetry [120, 121, 167]. For this reason, we add a U(1) gauge field A_μ in the bulk. This changes the background and as we will see in section 6.1.1, solving the Einstein equations in the presence of the gauge field leads for dynamical exponent $z = 1$ to a Reissner-Nordström black-brane metric.

The second step is to additionally incorporate a nonrelativistic scaling. It was proposed in Ref. [172–174] that the conformal symmetry of the boundary theory should be reduced to the Schrödinger symmetry group, or more generally, Galilean invariance. This reduced symmetry on the boundary is realized by a gravity dual with a metric having the required isometries. However, it turns out the gravity dual

has two extra dimensions instead of one, therefore leading to the wrong scaling of thermodynamic variables such as the entropy. Another way to realize a nonrelativistic scaling of the quantum critical point is by incorporating Lifshitz symmetry. Of course this anisotropic scaling was already present in chapter 3 at charge neutrality. In the charged case the background with dynamical exponent $z > 1$ is a bit more complicated. There are various geometric realizations of Lifshitz scaling exhibiting the correct thermodynamics, including Refs. [123, 124, 135, 169, 175].

In both cases $z = 1$ and $z > 1$, the bulk field A_0 acquires a nontrivial radial profile, and the boundary value of the temporal component of the bulk gauge field corresponds to the chemical potential in the dual quantum field theory. Again, to compute the fermionic selfenergy we also add probe fermions to the bulk theory, but this time they are charged under the U(1) gauge field. The equation of motion for the probe fermions in the new background thus also contains the minimal coupling to the A_0 component. As a result, the fermionic operators in the dual quantum field theory responsible for the interactions are at nonzero μ. Finally, in semiholography, we add a chemical potential term in the boundary action, so that the free part of the Green's function has the form of Eq. (6.1). So the free fermionic part of the theory is at the same chemical potential as the quantum field theory. In section 6.1.3 we also describe the effect of a boundary mass term on the spectral-weight function.

6.1 Charged Lifshitz semiholography

It is possible to obtain a charged black-brane background that is asymptotically Lifshitz and thus corresponds to a boundary theory at nonzero density with dynamical exponent different from one [135]. The gravity theory contains a U(1) gauge field under which the black brane is charged, and the boundary value of its temporal component corresponds to a chemical potential on the boundary. However, to realize the asymptotically Lifshitz background we require additional fields, namely a second Maxwell field and a scalar field. The charge corresponding to the second gauge field is completely determined in terms of the scalar by the equations of motion and ensures the asymptotically Lifshitz scaling.

This setup is presented in Ref. [135] in natural units, so all quantities have the dimensions of a power of length. We need many of the results of Ref. [135] for the computation of the fermionic spectrum, and therefore we discuss this setup in detail. As was also done in Refs. [1, 3], we reformulate these results in SI units, which is more convenient for our purposes. The SI units of the gravitational constant and vacuum permeability can be determined from the (d+1)-dimensional Poisson equation. The Poisson equation for gravity is given by

$$\nabla^2 \varphi_{\text{grav}} = 4\pi G_{d+1} \rho_{\text{mass}}, \tag{6.2}$$

where φ_{grav} is the gravitational scalar potential having dimensions of energy/mass, and ρ_{mass} is the mass density, which has dimensions of mass/length^d. So the (d+1)-dimensional gravitational constant G_{d+1} has SI units of $\text{m}^{d+2}\ \text{J}^{-1}\ \text{s}^{-4}$. For electromagnetism, the Poisson equation is

$$\nabla^2\varphi_{\text{EM}} = -\frac{\rho}{\varepsilon_0}, \tag{6.3}$$

where φ_{EM} is the electromagnetic scalar potential with dimensions of energy/charge, and ρ is the charge density, so it has dimensions charge/length^d. Thus, the (d+1)-dimensional vacuum permittivity ε_0 has SI units of $\text{C}^2\ \text{m}^{2-d}\ \text{J}^{-1}$. Using the definition $1/c^2 = \varepsilon_0\mu_0$, it is easy to see that the (d+1)-dimensional vacuum permeability μ_0 has SI units of $\text{J}\ \text{s}^2\ \text{C}^{-2}\ \text{m}^{d-4}$.

6.1.1 Charged black-brane background

The bulk theory is described in SI units by the Einstein-Maxwell-dilaton action,[29]

$$\begin{aligned} S = {} & \frac{c^3}{16\pi G_{d+1}}\int \mathrm{d}^{d+1}x\sqrt{-g}\left(R - 2\Lambda - \frac{1}{2}\partial_\mu\varphi\partial^\mu\varphi\right) \\ & - \frac{1}{4\mu_0 c}\int \mathrm{d}^{d+1}x\sqrt{-g}\sum_{i=1}^{2} e^{\lambda_i\varphi}F_{i,\mu\nu}F_i^{\mu\nu}, \end{aligned} \tag{6.4}$$

where d is the number of boundary spacetime dimensions. Furthermore, R is the Ricci scalar, φ is the dilaton field,[30] $F_{i,\mu\nu} = \partial_\mu A_{i,\nu} - \partial_\nu A_{i,\mu}$, λ_i are coupling constants, and Λ is the cosmological constant. The equations of motion for φ, $A_{i,\mu}$, and $g_{\mu\nu}$ are

$$\begin{aligned} & \nabla^\mu\nabla_\mu\varphi - \frac{8\pi G_{d+1}}{\mu_0 c^4}\sum_{i=1}^{2}\lambda_i e^{\lambda_i\varphi}F_i^2 = 0, \\ & \nabla_\nu\left(F_i^{\mu\nu}e^{\lambda_i\varphi}\right) = 0, \\ & R_{\mu\nu} - \frac{2\Lambda}{d-1}g_{\mu\nu} - \frac{1}{2}\partial_\mu\varphi\partial_\nu\varphi - \frac{8\pi G_{d+1}}{\mu_0 c^4}\sum_{i=1}^{2}e^{\lambda_i\varphi}\left(F_{i,\mu}^{\rho}F_{i,\nu\rho} - \frac{F_i^2}{2(d-1)}g_{\mu\nu}\right) = 0, \end{aligned} \tag{6.5}$$

where ∇_μ is the covariant derivative. Just like in chapter 3, it is convenient to use a metric Ansatz consistent with a static asymptotically Lifshitz spacetime, corresponding to the line element

$$\mathrm{d}s^2 = -V^2(r)\frac{r^{2z}}{\ell^{2z}}c^2\mathrm{d}t^2 + \frac{\ell^2}{r^2V^2(r)}\mathrm{d}r^2 + \frac{r^2}{\ell^2}\mathrm{d}\vec{x}^2, \tag{6.6}$$

[29] Despite the unconventional placement of G_{d+1}, both terms in the action are still of the same (leading) order in the $1/N$-expansion.

[30] Note that φ has been rescaled with a factor $\sqrt{16\pi\hbar G_{d+1}/c^3}$ with respect to a relativistic scalar field with canonical dimensions, making it dimensionless.

where $z \geq 1$ is the dynamical exponent and $V(r)$ is the blackness factor that is required to go to 1 near the boundary for the correct asymptotics. The solutions are reported in Ref. [135] and the discussion below is based on that paper. The dilaton field has a radial profile given by

$$\varphi(r) = \sqrt{2(d-1)(z-1)}\,\ln r + \ln\hat{\varphi}, \tag{6.7}$$

where $\hat{\varphi}$ is an integration constant that makes the right-hand side dimensionless. For simplicity, we restrict ourselves to the case where the only nonzero components of the gauge fields are the temporal components $A_{i,0}$, and they only depend on r. Then, the only independent nonzero components of both field-strength tensors are $F_{i,r0}$, for which the solutions are given by

$$F_{i,r0} = \rho_i e^{-\lambda_i\varphi(r)} r^{z-d}. \tag{6.8}$$

Here, ρ_i are integration constants with SI units J s C^{-1} m^{d-z-2}. Because of the antisymmetry of $F_{i,\mu\nu}$, the conjugate momenta of $A_{i,0}$ are zero, so there are two constants of motion. These can be interpreted as charges, and are given by the "Gauss' laws" of this theory, the temporal components of the Maxwell equation in Eq. (6.5). The total charge can then be computed using Stokes' theorem, and is given by

$$Q_i = \frac{\ell^{z-d}}{\mu_0 c}\rho_i V_{d-1}, \tag{6.9}$$

where $V_{d-1} = \int \mathrm{d}^{d-1}x$ denotes the volume of a (d-1)-dimensional surface. Next, the blackness factor can be determined from the Einstein equations, resulting in

$$\begin{aligned} V^2(r) = &-\frac{2\Lambda\ell^2}{(d-1)(d+z-1)} - \left(\frac{r_m}{r}\right)^{d+z-1} \\ &+ \frac{8\pi G_{d+1}\ell^{2z}r^{2-2d}}{\mu_0 c^4(d-1)}\sum_{i=1}^{2}\frac{e^{-\lambda_i\varphi}\rho_i^2}{d-z-1+\lambda_i\sqrt{2(d-1)(z-1)}}. \end{aligned} \tag{6.10}$$

Here, r_m is another integration constant. At this point not all independent equations are used yet. It turns out that a solution of the remaining equations is given by fixing λ_1, λ_2 and either ρ_2 or $\hat{\varphi}$ as follows,

$$\begin{aligned} &\lambda_1 = \sqrt{\frac{2(z-1)}{d-1}}, \qquad \lambda_2 = -\sqrt{\frac{2(d-1)}{z-1}}, \\ &\rho_2^2 = -\frac{(z-1)\hat{\varphi}^{\lambda_2}\Lambda\ell^{2(1-z)}\mu_0 c^4}{4\pi G_{d+1}(d+z-2)}. \end{aligned} \tag{6.11}$$

With these expressions plugged in into Eq. (6.10), the term with ρ_2 becomes independent of r and contributes to the cosmological constant term. The interpretation is

that the charge of the second gauge field supports the asymptotically Lifshitz spacetime. To make the blackness factor asymptote to 1 near the boundary as desired, the cosmological constant is set to

$$\Lambda = -\frac{(d+z-1)\,(d+z-2)}{2\ell^2}. \tag{6.12}$$

This leaves ρ_1 as a free parameter. Indeed, the first gauge field $A_{1,\mu}$ corresponds to an electromagnetic potential sourced by a nonzero charge density proportional to ρ_1. Because ρ_1 appears in the blackness factor $V(r)$ that resembles that of the Reissner-Nordström black brane for $z = 1$, we interpret ρ_1 as a charge density that is present on the black-brane horizon. In contrast, the constant of motion associated to the second gauge field is not a free parameter. Instead, together with the coupling constant λ_2, it is fixed by the equations of motion in terms of the strength of the scalar field $\hat{\varphi}$, and thus ensures the asymptotically Lifshitz scaling of this background. At this point, it is convenient to use instead of the combination $\rho_1^2\hat{\varphi}^{-\lambda_1}$ the following dimensionless quantity

$$Q^2 = \frac{8\pi G_{d+1}\rho_1^2\hat{\varphi}^{-\lambda_1}\ell^{2(2-d)}}{(d-1)(d+z-3)\mu_0 c^4}. \tag{6.13}$$

With this, the blackness factor becomes

$$V^2(r) = 1 - \left(\frac{r_m}{r}\right)^{d+z-1} + Q^2\left(\frac{r}{\ell}\right)^{-2(d+z-2)}. \tag{6.14}$$

The black-brane horizon is defined as the value of r where the blackness factor has a zero,

$$V(r)\Big|_{r=r_h} \equiv 0. \tag{6.15}$$

In general there is more than one solution, and r_h is taken to be the largest of those, i.e., it is the outermost horizon. A consideration of the thermodynamics of the black brane results in expressions for the integration constant r_m and the black-brane temperature T in terms of the horizon radius [135],

$$r_m^{d+z-1} = r_h^{d+z-1}\left(1 + Q^2\left(\frac{r_h}{\ell}\right)^{-2(d+z-2)}\right), \tag{6.16}$$

and

$$T = \frac{\hbar c r_h^z}{4\pi k_B \ell^{z+1}}\left(d+z-1-(d+z-3)\,Q^2\left(\frac{r_h}{\ell}\right)^{-2(d+z-2)}\right). \tag{6.17}$$

The asymptotically Lifshitz black-brane geometry is now specified by Eqs. (6.6), (6.14), (6.16), and (6.17). There are two free parameters, Q (or the combination $\rho_1^2\hat{\varphi}^{-\lambda_1}$) and T (or r_h, as it is not possible to invert Eq. (6.17) analytically).

Next, we consider the solution for the A_0 field that ultimately becomes the chemical potential of the dual field theory. From the on-shell solution for the field-strength tensor in Eq. (6.8) we obtain

$$A_0(r) = -\frac{\rho_1 \hat{\varphi}^{-\lambda_1}}{d+z-3}\left(r^{3-d-z} - r_h^{3-d-z}\right). \tag{6.18}$$

The integration constant was fixed by requiring the electromagnetic scalar potential to vanish on the black-brane horizon. For large values of r, that is, near the boundary, the second term dominates and A_0 becomes constant. The quantity $\mu = qcA_0(\infty)$ is interpreted as the chemical potential of the dual field theory, where q is the charge of excitations on the boundary coupled to $A_0(\infty)$. Thus, we obtain

$$A_0(r) = \frac{\mu}{cq}\left(1 - \left(\frac{r}{r_h}\right)^{3-d-z}\right). \tag{6.19}$$

So there is a third free parameter in the theory, and we have the freedom to choose μ as the free parameter, or equivalently, the combination $q\rho_1\hat{\varphi}^{-\lambda_1}$. In the latter case, μ can be written as a function of T, Q^2 and a new dimensionless parameter $\hat{q}$ in the following way,

$$\mu = \frac{\hbar c}{\ell}\left(\frac{r_h}{\ell}\right)^{3-d-z} Q^2\,\frac{\hat{q}}{Q}. \tag{6.20}$$

The parameter $\hat{q}$ is defined so that it is proportional to $q\rho_1\hat{\varphi}^{-\lambda_1}/Q$, namely,

$$\frac{\hat{q}}{Q} = \frac{q\rho_1\hat{\varphi}^{-\lambda_1}\ell^{4-d-z}}{\hbar Q^2(d+z-3)}. \tag{6.21}$$

This construction may seem awkward at first. However, the motivation for organizing the free parameters of the theory in this manner, is that it allows for a more physical interpretation of the parameters. Namely, Q^2, $\hat{q}/Q$ and T represent roughly the square of total black-brane charge, the ratio of the charges of the field-theory excitations and the black brane, and temperature both on the boundary and in the bulk theory. It is remarkable that adding one new parameter to the boundary theory, the chemical potential, results in a bulk theory that has two extra parameters. In other words, the Einstein-Maxwell-dilaton theory provides a nonunique bulk generalization of boundary theories with $z \geq 1$ and $\mu \neq 0$ that fall in the same universality class. Later on, we will compute μ numerically using the following algorithm.

- Choose a value for the dimensionless parameter Q, this determines Q^2.
- Choose a temperature T and numerically solve for the corresponding horizon radius using Eq. (6.17). Once Q^2 and r_h are fixed, r_m and $V(r)$ are also known through Eqs. (6.16) and (6.14) respectively, which is useful for computing the fermionic spectrum later on.

- Write $Q\hat{q}$ in Eq. (6.20) as $Q^2\hat{q}/Q$. Choose a value for the dimensionless ratio $\hat{q}/Q$ and compute the chemical potential from Eq. (6.20).

We do not consider the solutions for the other gauge field and the dilaton. These do not couple to the probe fermions and therefore play no role in the computation of the fermionic spectrum.

So, we have seen that adding a chemical potential on the boundary, leads us to a gravity dual that contains two extra parameters, basically the chemical potential itself and the ratio of charge of the boundary excitations and on the black-brane horizon. This section is concluded with two remarks about this background. Firstly, for dynamical exponent $z = 1$, the second gauge field vanishes and the solution becomes the charged Reissner-Nordström metric, which is asymptotically Anti-de Sitter.

Secondly, as opposed to the uncharged black-brane solution used in chapters 3 and 4, the charged black brane solutions have a nonzero horizon radius at zero temperature. The entropy of a black brane is proportional to the area of the horizon as given by the Bekenstein-Hawking formula. So this means the Reissner-Nordström black brane and its $z > 1$ cousin have a large ground-state degeneracy, and they do not seem to correspond to the ground state [176]. The results of this background may not be applicable at zero temperature, but above a critical temperature, at which a phase transition to the true ground state occurs. An example is the electron star background mentioned in section 1.6. In this background there is no horizon, but the charge is carried by a charged, gravitating perfect fluid. However, connections have been made to condensed-matter systems such as spin liquids which exhibit frustration and also have a nonvanishing entropy at zero temperature [177].

6.1.2 Fermions

Now that the background setup is satisfactorily discussed, we add two species of probe Dirac fermions on top in the usual manner, see for example section 5.2.2 of chapter 5. The bulk fermions are minimally coupled only to the physical gauge field $A_{1,\mu}$. To the action of Eq. (6.4) we add the fermion action

$$\begin{aligned} S = &-i\hbar g_f \sum_{j=1}^{2} \int \mathrm{d}^{d+1}x\sqrt{-g}\bar{\Psi}^{(j)} \left(\frac{1}{2}\overleftrightarrow{\not{D}} - \frac{iq}{\hbar}\not{A}_1 - \frac{M_j}{\ell}\right)\Psi^{(j)} \\ &- i\hbar g_f \int_{r=r_0} \mathrm{d}^d x\sqrt{-g}\sqrt{g^{rr}}\left(\bar{\Psi}_R^{(1)}\Psi_L^{(1)} - \bar{\Psi}_L^{(2)}\Psi_R^{(2)}\right) \\ &- i\hbar Z \int_{r=r_0} \mathrm{d}^d x\sqrt{-g}\bar{\Psi}\not{D}_z\Psi\,. \end{aligned} \tag{6.22}$$

Here, $\overleftrightarrow{\not{D}} = \overrightarrow{\not{D}} - \overleftarrow{\not{D}}$, where $\overrightarrow{\not{D}} = \Gamma^{\underline{a}} e_{\underline{a}}{}^{\mu}(\partial_\mu + \frac{1}{4}(\Omega_\mu)_{\underline{bc}})\Gamma^{\underline{bc}}$ as before (see e.g. Eq. (3.82)) and where $\overleftarrow{\not{D}} = \Gamma^{\underline{a}} e_{\underline{a}}{}^{\mu}(\overleftarrow{\partial}_\mu - \frac{1}{4}(\Omega_\mu)_{\underline{bc}})\Gamma^{\underline{bc}}$. Note that the covariant derivative of Γ^μ vanishes. Furthermore, the boundary kinetic operator for $z = 1$ is $\not{D}_z = \sum_{a \neq r} \Gamma^{\underline{a}} e_{\underline{a}}{}^{\mu}(\partial_\mu - iqA_{\mu,1}(r))$. For $z > 1$ it is the proper kinetic operator for a fermion with Lifshitz scaling, as was also discussed in section 3.2 for the undoped case.

The procedure is now analogous to what was described in section 4.2. We choose $M_1 = -M_2 = M$. The boundary term in Eq. (6.22) does not affect the bulk equation of motion for both the fermions. The bulk Dirac equations of both fermion species can be written as in Eq. (4.2), the equation for this case is written explicitly below in Eq. (6.25). Following the procedure in 4.2, we integrate out the components $\Psi_L^{(1)}$ and $\Psi_R^{(2)}$, effectively replacing them by the other two components, and perform the double-scaling limit to keep the boundary action finite, which is for the Lifshitz case given by Eq. (3.12). The inverse retarded Green's function of the boundary Dirac fermion $\Psi = \Psi_R^{(1)} + \Psi_L^{(2)}$ is then in its momentum-space representation given by

$$G_R^{-1}(\vec{k}, \omega) = \left(\omega + \frac{\mu}{\hbar}\right) \mathbb{1}_4 + \gamma^0 \vec{\gamma} \cdot c\vec{k} \frac{|c\vec{k}|^{z-1}}{\lambda} + \gamma^0 \gamma^\mu \Sigma_\mu(\vec{k}, \omega). \tag{6.23}$$

The selfenergy is given in terms of $\xi_\pm$ by Eq. (4.6), which we repeat here for clarity

$$\Sigma_\mu(\vec{k}, \omega) = -\frac{g}{2} \lim_{r_0 \to \infty} \left(\frac{r_0}{\ell^2}\right)^{2M} \left[(\xi_+ + \xi_-)\, \delta_\mu^0 + (\xi_+ - \xi_-)\, \frac{k_i}{|\vec{k}|} \delta_\mu^i\right]. \tag{6.24}$$

Note that the coupling constant called λ in chapter 4 has been renamed to g, in order to avoid confusion with the spin-orbit coupling strength $1/\lambda$ multiplying the renormalized kinetic term in Eq. (6.23).

For nonzero chemical potential and dynamical exponent $z \geq 1$, the differential equation for the complex functions $\xi_\pm$ is given by

$$\left(\frac{r}{\ell}\right)^2 V(r) \partial_r \xi_\pm + \frac{2rM}{\ell^2} \xi_\pm = \frac{\Omega}{c} \mp k_3 + \left(\frac{\Omega}{c} \pm k_3\right) \xi_\pm^2, \tag{6.25}$$

with the boundary condition $\xi_\pm(r_h) = i$, and where we again set $\vec{k} = (0, 0, k_3)$ with $k_3 > 0$. The blackness function $V(r)$ is given by Eq. (6.14) and

$$\Omega = \frac{1}{V(r)} \left(\frac{\ell}{r}\right)^{z-1} \left[\omega + \frac{\mu}{\hbar} \left(1 - \left(\frac{r}{r_h}\right)^{3-d-z}\right)\right], \tag{6.26}$$

due to minimal coupling of both bulk fermions to $A_{1,\mu}$. Note that M still determines the universality class of the boundary theory, as it dominates the asymptotic scaling behaviour of $\xi_\pm$ even in the presence of a chemical potential.

Everywhere in this thesis we chose to relate the masses of both bulk fermion species as $M_1 = -M_2$. This motivation for this is that the scaling dimensions of both chiral components on the boundary coincide. When the masses can vary independently, we essentially have another free parameter in the boundary theory. We investigate what type of boundary theory is obtained when $M_1 \neq -M_2$ in appendix 6.B.

6.1.3 Boundary Dirac mass

Analogously to Eq. (6.1), we can also add a mass term for the boundary Dirac fermion, by adding to the action of Eq. (6.22) the following term

$$S_m = iZ \int_{r=r_0} \mathrm{d}^d x \sqrt{-g} \bar{\Psi} \tilde{m} c \Psi. \tag{6.27}$$

This terms couples $\Psi_R^{(1)}$ and $\Psi_L^{(2)}$ on the r_0 brane. Adding this term is allowed, because the variation of S_m does not contribute once the chiral components of Ψ are fixed on the boundary by the Dirichlet conditions. The boundary mass term stays finite during the double-scaling limit if the mass $\tilde{m}$ is rescaled as well, as $\tilde{m} = m(r_0/\ell)^{-z}$. This results in an additional mass term in the inverse Green's function in Eq. (6.23),

$$G_R^{-1}(\vec{k},\omega) = \left(\omega + \frac{\mu}{\hbar}\right) \mathbb{1}_4 + \gamma^0 \vec{\gamma} \cdot c\vec{k} \frac{|c\vec{k}|^{z-1}}{\lambda} + \gamma^0 \gamma^\mu \Sigma_\mu(\vec{k},\omega) + \gamma^0 \frac{imc^2}{\hbar}. \tag{6.28}$$

The Green's function $G_R(\vec{k},\omega)$ has two distinct eigenvalues that are twofold degenerate and given by

$$\frac{1}{\omega + \mu/\hbar - \Sigma_0 \pm \sqrt{\left(c\vec{k}\left|c\vec{k}\right|^{z-1}/\lambda + \vec{\Sigma}\right)^2 + (mc^2/\hbar)^2}}. \tag{6.29}$$

6.2 Phenomenology of the spectral-weight function

The fermionic spectral-weight function is proportional to the trace of the imaginary part of the retarded Green's function corresponding to Eq. (6.28), i.e.,

$$\begin{aligned} A(\omega,\vec{k}) &= -\frac{1}{4\pi} \operatorname{Im} \operatorname{Tr} G_R(\omega,\vec{k}) \\ &= -\frac{1}{\pi} \operatorname{Im} \left[\frac{\omega + \mu/\hbar - \Sigma_0(\omega,\vec{k})}{\left(\omega + \mu/\hbar - \Sigma_0(\omega,\vec{k})\right)^2 - \left(c\vec{k}\left|c\vec{k}\right|^{z-1}/\lambda + \vec{\Sigma}(\omega,\vec{k})\right)^2 - (mc^2/\hbar)^2} \right]. \end{aligned} \tag{6.30}$$

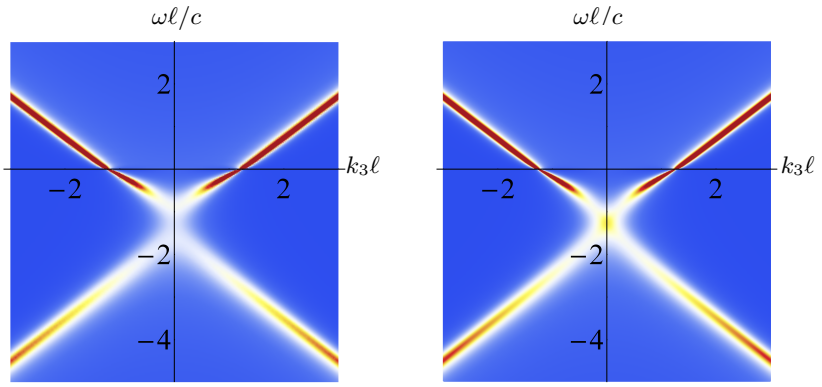

(a) $M = 1/4$, $\bar{m} = 1$ **(b)** $M = 1/4$, $\bar{m} = 0$

Figure 6.1: Trace of the components of the spectral-weight function for the extremal case with $T = 0$, $M = 1/4$, $r_h/\ell = z = g/\ell^{2M-1}c = \hat{q} = 1$, $\mu\ell/\hbar c = \sqrt{2}$, and $\bar{m} = mc\ell/\hbar = 1$ (left) and $\bar{m} = 0$ (right).

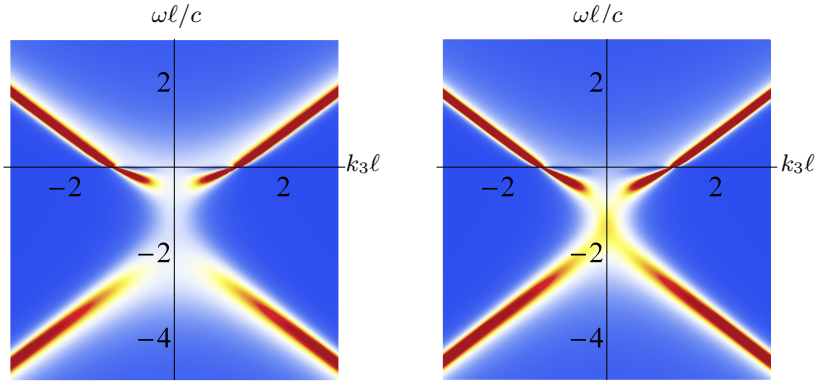

(a) $M = 0$, $\bar{m} = 1$ **(b)** $M = 0$, $\bar{m} = 0$

Figure 6.2: Trace of the components of the spectral-weight function for $M = 0$. The other parameters are the same as in Fig. 6.1. The left figure is adapted from Ref. [3].

This spectral-weight function is plotted in Figs. 6.1, 6.2, and 6.3.

As can be clearly seen in Figs. 6.1 and 6.2, there are features at zero energy that look like Fermi surfaces. To further analyse these features, we zoom in to small values of ω. Close examination of the differential equation in Eq. (6.25) reveals a numerical issue with the boundary condition. As before, the infalling boundary condition translates to $\xi_\pm(r_h) = i$, which we derive in appendix 6.A in more detail. However, at $r = r_h$, there is a singularity in the differential equation because $V(r_h) = 0$. In

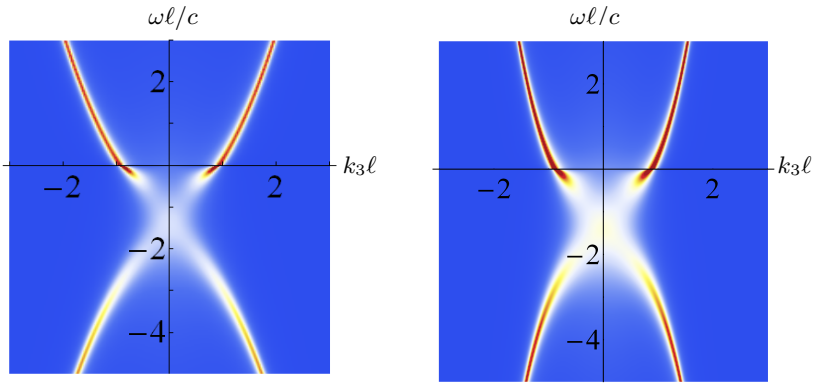

(a) $M = 0$, $z = 2$ **(b)** $M = 0$, $z = 3$

Figure 6.3: Trace of the components of the spectral-weight function for $M = 0$, $T = 0$, $r_h/\ell = g/\ell^{2M-1}c = \hat{q} = 1$, $\bar{m} = 0$, $\mu\ell/\hbar c = \sqrt{2}$, and $z = 2$ (left) and $z = 3$ (right).

the numerical computation this is avoided by imposing the boundary condition at $r = r_h + \epsilon$, where ϵ is a small enough positive number. Here, small enough means that we solve the differential equation for ever smaller values of ϵ and check which value is small enough so that the solution converges. In principle this has to be done for every value of the parameters, in practice we check the convergence in samples. For large ω the solution converges for relatively large values of ϵ. However, for small but nonzero ω and nonzero μ, very small values of ϵ are needed for convergence, making the numerical calculation slow. This problem is not present in the uncharged black-hole backgrounds. To remedy it [3], we expand the coefficients in the differential equation in powers of $r - r_h$, and solve this less complicated differential equation in a small region $\epsilon < r - r_h < \epsilon'$ close to the horizon. At $r - r_h = \epsilon'$ we match the two equations by using the solution of the expanded version as boundary condition for the exact differential equation. This method turns out to be faster. Finally, we check that the final result is independent of ϵ and ϵ'. Because we are analysing putative Fermi surfaces, we perform the expansion of Eq. (6.25) at zero temperature, for which

$$\frac{r_h}{\ell} = \left(\frac{d+z-1}{Q^2\,(d+z-3)}\right)^{\frac{-1}{2(d+z-2)}}. \tag{6.31}$$

For definiteness we also choose $d = 4$, $z = 1$, and $Q^2 = 2$, so that $\mu = \sqrt{2}\,\hbar c\hat{q}/\ell$, $r_h/\ell = 1$, and

$$V^2(r) = 1 - 3\left(\frac{\ell}{r}\right)^4 + 2\left(\frac{\ell}{r}\right)^6. \tag{6.32}$$

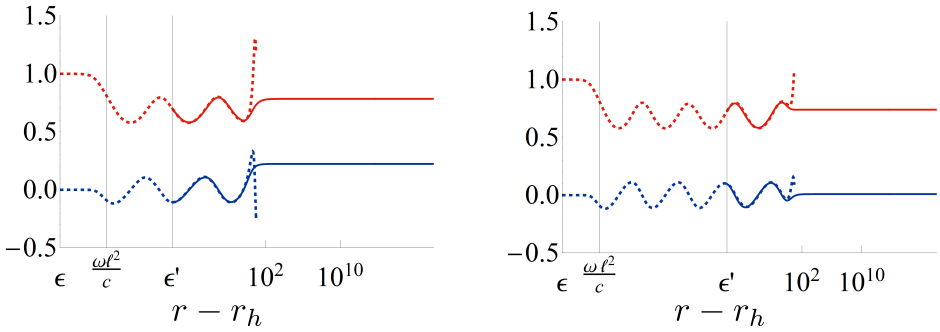

(a) $\epsilon/\ell = 10^{-20}$, $\omega\ell/c = 10^{-15}$ **(b)** $\epsilon/\ell = 10^{-30}$, $\omega\ell/c = 10^{-25}$

Figure 6.4: Log-linear plots of the behaviour of the bulk Dirac equation as a function of $r - r_h$. The dashed and solid curves are respectively the solution $\tilde{\xi}_+$ of the approximated differential equation in Eq. (6.34) and the solution ξ_+ of the exact equation. The blue and red colours indicate the real and imaginary parts, respectively. In both figures we have chosen $k_3\ell = 3/10$, $M = 0$, and $\epsilon'/\ell = 10^{-8}$, in addition to the parameter values mentioned just before Eq. (6.32) in the main text. Figures adapted from Ref. [3].

Introducing a new variable x as

$$x = \ln\left(\frac{r-\ell}{\ell}\right), \tag{6.33}$$

so that $r - \ell \to 0$ corresponds to $x \to -\infty$, the differential equation with expanded coefficients is

$$\begin{aligned} 0 = {} & \frac{\partial}{\partial x}\tilde{\xi}_\pm + \frac{M}{\sqrt{3}}\left(1+e^x\right)\tilde{\xi}_\pm \pm \frac{k_3\ell}{2\sqrt{3}}\left(1-\tilde{\xi}_\pm^2\right) \\ & - \frac{\ell}{c}\left[\frac{\omega}{12}e^{-x} + \frac{\mu}{6\hbar} + \frac{13\omega}{72} + \left(\frac{\mu}{9\hbar} + \frac{11\omega}{144}\right)e^x\right]\left(1+\tilde{\xi}_\pm^2\right) + \mathcal{O}\left(e^{2x}\right). \end{aligned} \tag{6.34}$$

We have renamed the solutions $\tilde{\xi}_\pm$, to avoid confusion with the solutions $\xi_\pm$ of the exact equation. The boundary conditions are $\tilde{\xi}_\pm = i$ at $x = \ln(\epsilon/\ell)$, where ϵ/ℓ should be of the order $\omega\ell/c \times 10^{-5}$. The solutions are matched at $r_h + \epsilon'$, i.e., $\tilde{\xi}_\pm = \xi_\pm$ at $r - \ell = \epsilon'$, and the rest of the solutions is then obtained from the exact differential equation. The behaviour of the solutions is shown in Fig. 6.4.

We investigate the different behaviour of the solution $\tilde{\xi}_\pm(x)$ in the regions $\ln(\omega\ell/c) \ll x \ll \ln(\epsilon'/\ell)$ and $\ln(\epsilon/\ell) \ll x \ll \ln(\omega\ell/c)$. For $\ln(\omega\ell/c) \ll x \ll \ln(\epsilon'/\ell)$, we can neglect the $\mathcal{O}(e^x)$ terms in Eq. (6.34), and assuming $\mu = \sqrt{2}\hat{q}\hbar c/\ell \gg \hbar\omega$, we also neglect the $13\omega/72$ and $\omega e^{-x}/12$ terms. Then, the x dependence of the solution

$\tilde{\xi}_\pm$ comes only from a term proportional to

$$\sim \tan\left(\sqrt{\left(\frac{\mu\ell}{\hbar c}\right)^2 - 3\left(\left(k_3\ell\right)^2 + M^2\right)}\left(\frac{x}{6} + C\right)\right), \tag{6.35}$$

where C is an integration constant. This explains the oscillatory behaviour in $x = \ln(r/\ell - 1)$ that is visible in Fig. 6.4. The solution is only oscillatory for $\mu > \sqrt{3(k_3^2\ell^2 + M^2)}\hbar c/\ell$. This log-periodic oscillatory behaviour of the selfenergy close to $\omega = 0$ and for μ greater than a value depending on $|\vec{k}|$, is very similar to the behaviour found in 2+1 boundary dimensions in Ref. [121] and further investigated in Ref. [120]. In those works, it is the spectral-weight function that behaves in this manner, and we point out that the authors employ the usual holographic prescription, so that the spectral-weight function in Refs. [120, 121] is proportional to our selfenergy. Finally, for $\ln(\epsilon/\ell) \ll x \ll \ln(\omega\ell/c)$ the solution converges because the $\omega e^{-x}/12$ cannot be neglected. This explains why ϵ should be modified for small ω, namely, to allow the solution to converge near the horizon.

6.2.1 Fermi surfaces

Now that the small-frequency behaviour of the selfenergy is under control, we can finally scrutinize the features in the spectral-weight function. The analysis is similar to the one in section 3.4.2 of chapter 3. As in Refs. [120, 121], for $d = 4$ we also find sharp peaks at $\omega = 0$ and at nonzero values of $|\vec{k}|$, which we denote by $\pm k_F$. As opposed to the analysis in chapter 3, k_F has to be determined by solving $\mathrm{Re}\, G_R^{-1}(k_F, 0) = 0$ numerically. Focusing on the imaginary part of the selfenergy at zero temperature, we find it vanishes as

$$\mathrm{Im}\,\Sigma(\pm k_F, \omega) \sim |\omega|^\nu, \tag{6.36}$$

where ν is a function of the parameters of the theory. For $M = 0$ and $mc\ell/\hbar = 1$ we find $k_F\ell \approx 1.14629$ and $\nu \approx 0.47$, and for $mc\ell/\hbar = 2$ we obtain $\nu \approx 0.38$. Because $\nu < 1$ there are no well-defined quasiparticles despite the presence of a sharp Fermi surface. Thus, the system is a non-Fermi liquid.

A similar result was found in Ref. [120], and also for a different gravitational background in Ref. [134]. The authors of Ref. [120] present a particularly detailed analysis of the dependence of the power ν on the parameters of their model. All of this is to be contrasted to a Landau Fermi liquid where $\nu = 2$ (i.e., the smallest integer > 1), and to the semiholographic Fermi liquid found in chapter 3 where the quasiparticle lifetime vanishes exponentially.

If the chemical potential is increased further, a splitting into multiple bands can be discerned. This results in the appearance multiple Fermi surfaces as is shown

in Fig. 6.5. It is tempting to interpret these multiple bands as multiple-particle bound states corresponding to molecule formation, which have a similar structure. However, this requires further study, as it is for example not clear that this bulk dual provides the correct holographic description or that this result does not break down when quantum corrections are taken into account. These features, too, were seen in Ref. [120]. The authors explain them to be a result of scaling behaviour with a complex scaling exponent, leading to discrete scale invariance, physically related to pair production of charged fermions near the horizon [178]. It is interesting that the presence of the kinetic term in the semiholographic result does not spoil these features.

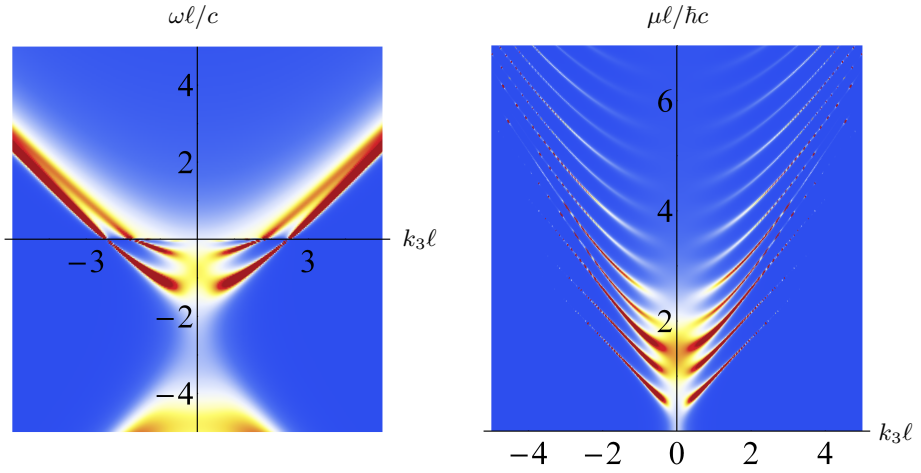

(a) Fixed μ **(b)** Fixed ω

Figure 6.5: Spectral-weight function for $M = 0$, $T = 0$, $\bar{m} = z = r_h/\ell = g/\ell^{2M-1}c = 1$, and for fixed $\mu\ell/\hbar c = 2\sqrt{2}$ (left) and fixed $\omega\ell/c = -1/100$ (right). On the left we see multiple features looking like bands appearing for a higher value of μ, as compared to Fig. 6.2(a). The figure on the right shows that more Fermi surfaces appear when the chemical potential is increased further. These figures are adapted from Ref. [3].

6.3 Discussion

In this chapter we have described an extension of semiholography which resulted in the spectral-weight functions of a semiholographic Dirac semimetal at nonzero chemical potential and $z \neq 1$. This was done with the application to ultracold atomic gases in mind, but in that context these results are still preliminary and more

research should be carried out. In particular, this includes a quantitative study of the effect of the new parameters introduced by the charged Lifshitz background, similar to the detailed analysis in Ref. [120].

In order to get from Dirac fermions to fermionic atoms which are nonrelativistic particles, in Ref. [3] it was attempted to take the nonrelativistic limit $mc^2 \gg \hbar c|\vec{k}|$. This leads to some issues which are connected to the fact that the boundary mass m does not appear as a parameter in the selfenergy. Perhaps a bulk origin of the boundary mass m could solve this problem. Furthermore, as in chapter 3, we can compute the momentum distribution by integrating the the spectral-weight function over frequency. Here it will depend on μ, i.e., $N_{\vec{k}}(\mu) = \int_{-\infty}^{\mu} \mathrm{d}\omega \rho(\vec{k}, \omega)$ at zero temperature. An additional momentum integration gives us the average total particle number as a function of μ. Inverting this relation gives us access to the renormalization of the chemical potential discussed in the introduction, a quantity of great importance for unitary Fermi gases.

6.A Infalling boundary conditions

In this appendix we explicitly derive the infalling boundary condition at the horizon of the quantity $\xi_\pm$ in Eqs. (3.17), (4.3), and (6.25). The physical interpretation is that the spinor components behave like plane waves that can only go into the black-hole horizon, and this corresponds to the retarded correlator on the boundary.

We first consider the case $\mu = 0$, $z \geq 1$, $T \neq 0$ and $\omega \neq 0$. Recall that $\xi_\pm$ are defined as

$$u_- = -i\xi_+ u_+, \qquad d_- = -i\xi_- d_+, \tag{6.37}$$

where $u_\pm$ and $d_\pm$ are complex numbers that are the components of the two-spinors $\psi_\pm$,

$$\psi_\pm = \begin{pmatrix} u_\pm \\ d_\pm \end{pmatrix}, \tag{6.38}$$

which are themselves the chiral components of the bulk Dirac 4-spinor. The bulk Dirac equation leads to the following four coupled first-order equations

$$\begin{aligned} \frac{r}{\ell}\left(\frac{r}{\ell}V\partial_r \pm \frac{M}{\ell}\right) u_\mp &= i\left(-\frac{\omega}{cV}\left(\frac{\ell}{r}\right)^{z-1} \pm k_3\right) u_\pm, \\ \frac{r}{\ell}\left(\frac{r}{\ell}V\partial_r \pm \frac{M}{\ell}\right) d_\mp &= i\left(-\frac{\omega}{cV}\left(\frac{\ell}{r}\right)^{z-1} \mp k_3\right) d_\pm, \end{aligned} \tag{6.39}$$

with $V(r)$ given by Eq. (3.3). The horizon is defined as the value of r where $V(r)$ vanishes, so $V(r)$ is small near the horizon. For the spinor components we perform

a power-law expansion in $r - r_h$, which is captured by the near-horizon Ansatz

$$u_\pm = v_\pm V^{\alpha_\pm}(r), \qquad d_\pm = w_\pm V^{\beta_\pm}(r), \tag{6.40}$$

where $v_\pm$ and $w_\pm$ are constants and the four powers $\alpha_\pm$ and $\beta_\pm$ are to be determined. For the first-order equations in Eq. (6.39) this means that $\partial_r u_\mp$ is replaced by $\alpha_\mp(d+z-1)(r_h/r)^{d+z}u_\mp/(2r_hV^2)$, and that $\partial_r d_\mp$ is replaced by $\beta_\mp(d+z-1)(r_h/r)^{d+z}$ $d_\mp/(2r_hV^2)$. Multiplying all equations by V, taking the limit $r \to r_h$, and using $V(r \to r_h) \to 0$, we identify the leading-order behaviour near the horizon for $\omega \neq 0$ as

$$\begin{aligned} \eta\, \alpha_\mp\, u_\mp &= -i\, \hat{\omega}\, u_\pm, \\ \eta\, \beta_\mp\, d_\mp &= -i\, \hat{\omega}\, d_\pm, \end{aligned} \tag{6.41}$$

where $\hat{\omega} = \omega\ell/c$ and

$$\eta = \frac{d+z-1}{2}\left(\frac{r_h}{\ell}\right)^z. \tag{6.42}$$

For a nontrivial solution, the powers of V on both sides of the equations must cancel each other out, so we find

$$\alpha_+ = \alpha_-, \qquad \beta_+ = \beta_-. \tag{6.43}$$

Plugging this in and solving for $\alpha_\pm$ and $\beta_\pm$, we obtain

$$\alpha_\pm = -\frac{i\hat{\omega}}{\eta}\frac{v_\mp}{v_\pm}, \qquad \beta_\pm = -\frac{i\hat{\omega}}{\eta}\frac{w_\mp}{w_\pm}. \tag{6.44}$$

Using Eq. (6.43) we write $(\alpha_\pm)^2 = \alpha_\pm\alpha_\mp$, which, combined with Eq. (6.44), leads us for real $v_\pm$ to

$$\left(\frac{v_\mp}{v_\pm}\right)^2 = 1 \quad \longrightarrow \quad \frac{v_\mp}{v_\pm} = \gamma, \tag{6.45}$$

with $\gamma = \pm 1$, and idem for $w_\pm$. Thus, Eq. (6.44) reduces to

$$\alpha_\pm = \beta_\pm = -\gamma\frac{i\hat{\omega}}{\eta} = -\gamma\frac{i\hbar\omega}{2\pi k_B T}. \tag{6.46}$$

Recalling the definition of the powers in Eq. (6.40), we see that infalling boundary conditions correspond to the choice $\gamma = 1$ [141]. Finally, for the ratios $\xi_\pm$ at the horizon this results in

$$\xi_\pm(r, \omega, \vec{k})\Big|_{r=r_h} = i. \tag{6.47}$$

For the case $\mu \neq 0$, the infalling boundary condition will be the same, because all modifications to the differential equation for $\xi_\pm$, i.e., minimal coupling to A_0 and a different expression for $V(r)$, drop out at leading order in $r - r_h$.

6.B The case $M_1 \neq -M_2$

In this appendix we investigate the boundary theory for $M_1 \neq -M_2$. For simplicity, we consider only the case of asymptotically Anti-de Sitter ($z = 1$) at zero chemical potential in $d = 4$ dimensions, it is straightforward to generalize this to the case of dynamical exponent greater than one and nonzero chemical potential.

We start with the bulk Dirac equations for both fermion species as written in Eq. (4.2). In chapter 4, setting $M_1 = -M_2$ and making use of the symmetry of the bulk Dirac equation in Eq. (3.129), the eigenvalues of both $\xi^{(i)}$ matrices could be related, resulting in a selfenergy with a matrix structure as in Eq. (4.5). When M_1 and M_2 remain independent, both species have a different asymptotic behaviour, and the double-scaling limit has to be modified to

$$\frac{r_0}{\ell} \to \infty, \qquad g_f \to 0, \tag{6.48}$$

in such a way that

$$\frac{g_f}{Z^{(1)}} \left(\frac{r_0}{\ell}\right)^{2-2M_1} \to \frac{g_1}{c\ell^{2M_1}}, \qquad \frac{g_f}{Z^{(2)}} \left(\frac{r_0}{\ell}\right)^{2+2M_2} \to \frac{g_2}{c\ell^{-2M_2}}, \tag{6.49}$$

Here g_1 and g_2 have different dimensions, and $Z^{(i)}$ replace Z as the dimensionful prefactors of the kinetic action in Eq. (4.4). Keeping the procedure unchanged otherwise, we obtain instead

$$G_R^{-1}(\vec{k},\omega) = \omega \mathbb{1}_4 + \gamma^0 \vec{\gamma}\cdot c\vec{k} + \begin{pmatrix} g_1 \left(r_0/\ell^2\right)^{2M_1} \xi^{(1)} & 0 \\ 0 & -g_2 \left(r_0/\ell^2\right)^{-2M_2} \left(\xi^{(2)}\right)^{-1} \end{pmatrix}, \tag{6.50}$$

where the limit $r_0 \to \infty$ is implied. As was done to obtain the final result in Eq. (4.5), the selfenergy matrix can be decomposed in terms of Dirac matrices. However, for $M_1 \neq -M_2$, in the decomposition not only $\gamma^0\gamma^\mu$, but also an extra term proportional to $\gamma^0\gamma^\mu\gamma^5$ appears. We obtain in four-vector notation

$$G_R^{-1}(k) = \left[ck_\mu + \frac{1}{2}\left(\Sigma_\mu^{(1)} + \Sigma_\mu^{(2)}\right)\right]\gamma^0\gamma^\mu + \frac{1}{2}\left(\Sigma_\mu^{(1)} - \Sigma_\mu^{(2)}\right)\gamma^0\gamma^\mu\gamma^5, \tag{6.51}$$

where

$$\Sigma_\mu^{(1)}(k) = -\frac{g_1}{2}\left(\frac{r_0}{\ell^2}\right)^{2M_1}\left[\left(\xi_+^{(1)} + \xi_-^{(1)}\right)\delta_\mu^0 + \left(\xi_+^{(1)} - \xi_-^{(1)}\right)\frac{k_i}{|\vec{k}|}\delta_\mu^i\right], \tag{6.52}$$

and

$$\Sigma_\mu^{(2)}(k) = -\frac{g_2}{2}\left(\frac{r_0}{\ell^2}\right)^{-2M_2}\left[\left(\xi_+^{(-2)} + \xi_-^{(-2)}\right)\delta_\mu^0 + \left(\xi_+^{(-2)} - \xi_-^{(-2)}\right)\frac{k_i}{|\vec{k}|}\delta_\mu^i\right]. \tag{6.53}$$

Here, we used rotational invariance to diagonalize the 2×2 matrices $\xi^{(i)}$. The eigenvalues of $\xi^{(1)}(k)$ and $\xi^{(2)}(k)$ are denoted by $\xi_{\pm}^{(1)}(k)$ and $\xi_{\pm}^{(2)}(k)$, respectively. Importantly, we used the symmetries in Eqs. (3.124) and (3.129). The superscript (-2) of the $\xi_{\pm}^{(-2)}$ in Eq. (6.53) indicates that they are the solutions of the differential equation (4.3) with M_2 replaced by $-M_2$, i.e., $\xi_{\pm}^{(-2)}(k, M_2) = \xi_{\pm}^{(2)}(k, -M_2)$. The $\xi_{\pm}^{(1)}$ in Eq. (6.52) are functions of M_1 as usual.

For $M_1 = -M_2$ and $g_1 = g_2$, the selfenergies of both species are equal, i.e., $\Sigma_{\mu}^{(1)} = \Sigma_{\mu}^{(2)}$, and the $\gamma^0\gamma^\mu\gamma^5$ term in the inverse Green's function of Eq. (6.51) drops out. However, for general M_1 and M_2 this term is present. The $\mu = 0$ component of $\gamma^0\gamma^\mu\gamma^5$ breaks spatial inversion symmetry in the boundary, and any of the vector components break time-reversal symmetry. This can be observed in components of the spectral-weight function.

A separation four-vector between the two chiral components such as in Eq. (6.51) is also present in the free Weyl semimetal described in section 2.2. However, in Eq. (6.51) the selfenergy has different scaling behaviour for each of the chiral components, whereas on physical grounds the interactions in a Weyl semimetal are expected to behave in a chirality-invariant way. Therefore, this is at the moment not a promising direction for us, but perhaps varying M_1 and M_2 independently can be of use for other purposes.

*****

Nederlandse samenvatting

Dirac- en Weyl-halfmetalen zijn nieuwe vormen van zogenaamde topologische materie waarin de elektronen zich gedragen volgens de wetten van de relativistische kwantummechanica. Dit leidt tot ongewone eigenschappen, die interessant zijn zowel vanuit een fundamenteel oogpunt als voor potentiële toepassingen in nieuwe elektronica. Dirac-halfmetalen worden vaak beschouwd als de driedimensionale vorm van het koolstofmembraan grafeen, en zijn het uitgangspunt voor de fabricatie van Weyl-halfmetalen. In die laatste materialen is verliesvrij transport mogelijk dat geen energie kost en beschermd is tegen onzuiverheden, wat dit materiaal een mogelijke kandidaat maakt voor toepassingen in kwantumcomputers en als platform voor valleytronica.

Voordat dit zover is, is er meer fundamenteel begrip nodig van het effect van elektronische wisselwerkingen op transport in deze materialen. In dit proefschrift wordt het effect van sterke wisselwerkingen in deze systemen onderzocht met behulp van een nieuwe techniek die ontwikkeld is in de snaartheorie. Deze zogenaamde holografische techniek maakt het mogelijk om complexe berekeningen in sterk gecorreleerde systemen te herformuleren in termen van de thermodynamica van zwarte gaten en de fysica in de bijkomende gekromde ruimte. Het onderzoek in dit proefschrift spitst zich toe op het berekenen van de spectrale dichtheidsfunctie en elektrische conductiviteit van sterk gekoppelde Dirac- en Weyl-halfmetalen. Deze grootheden zijn experimenteel meetbaar, respectievelijk via foto-emissie en optische experimenten. Dit onderzoek levert dus naast inzicht in de effecten van wisselwerkingen, mogelijk een belangrijke bijdrage om holografische technieken in contact te brengen met de experimentele wereld. We zullen nu in meer detail uitleggen wat de bovengenoemde begrippen betekenen en wat de belangrijkste resultaten en conclusies uit de verschillende hoofdstukken in dit proefschrift zijn.

Elektronische bandenstructuur

Dit proefschrift gaat over driedimensionale Dirac- en Weyl-halfmetalen. Beide zijn een vorm van materie met bijzondere eigenschappen, die al in de jaren dertig van de vorige eeuw theoretisch voorspeld zijn. Echter, pas in 2013 zijn driedimensionale Dirac-halfmetalen voor het eerst in een laboratorium waargenomen, in onder andere de kristallen Na_3Bi en Cd_3As_2. Weyl-halfmetalen zijn in januari 2015 experimenteel bevestigd. Om beter te begrijpen wat deze materialen bijzonder maakt en waarom dit belangrijk is, is het nuttig om eerst kort te bespreken hoe de theoretische natuurkunde, en in het bijzonder de vastestoffysica, materie beschrijft.

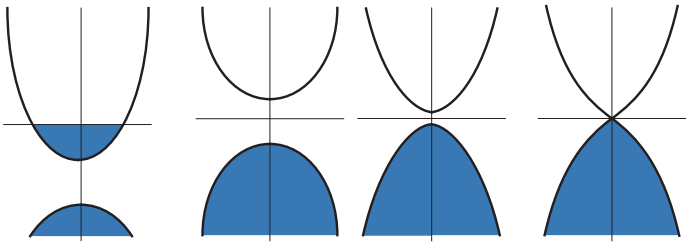

Figuur 1: Bandenstructuur van (van links naar rechts) een geleider, een isolator, een halfgeleider en een halfmetaal. De verticale as is de energie, de horizontale as is één van de componenten van de impulsvector, de andere twee componenten zijn hier niet weergegeven. Blauw staat voor opgevulde energietoestanden.

Materialen worden in de vastestoffysica vaak geclassificeerd naar de vorm van hun elektronische bandenstructuur [179]. Deze classificatie is schematisch weergegeven in figuur 1. De vorm van de bandenstructuur kan sterk verschillen tussen materialen, en heeft grote gevolgen voor de fysische eigenschappen van deze verschillende materialen.

Elektronen zijn fermionen, identieke deeltjes met een antisymmetrische golffunctie. Dit betekent dat een bepaalde energietoestand bezet kan zijn door slechts één elektron. Als dit de laagste energietoestand is, zullen de overige elektronen hogere energietoestand moeten innemen. De hoogste energie die elektronen bij een temperatuur van nul Kelvin kunnen bereiken, heet het Ferminiveau. Als er veel elektronen vanaf het Ferminiveau in een hogere energietoestand kunnen komen met zo goed als geen toegevoegde energie, zal het materiaal stroom- en/of warmtegeleidende eigenschappen hebben. In dit geval ligt het Ferminiveau in de geleidingsband en noemen we het materiaal een *geleider*. Metalen zoals koper zijn hiervan een voorbeeld. Is er echter geen mogelijkheid in de huidige band om de energie te verhogen, dan hebben de elektronen weinig bewegingsvrijheid en is dit materiaal een *isolator*. Het energieverschil tussen de huidige band, de zogenaamde valentieband, en de geleidingsband

wordt de bandkloof genoemd. Deze is bij een isolator groter dan de thermische energie van de elektronen en het Ferminiveau ligt in dit geval in de bandkloof. Als het Ferminiveau in de bandkloof ligt, maar de thermische energie van de elektronen groot genoeg is om de geleidingsband te bereiken, spreken we van een *halfgeleider*. Deze worden veel gebruikt in de elektronica omdat hun geleidingseigenschappen goed te beheersen zijn.

Een concreet voorbeeld van een bandenstructuur is te zien in figuur 2a. Dit is een theoretische berekening van de bandenstructuur van het materiaal Cd_3As_2. Het Ferminiveau, aangegeven met E_F, ligt niet in een bandkloof, desondanks is Cd_3As_2 geen geleider. De valentie- en geleidingsband raken elkaar slechts op één geïsoleerd punt in de impulsruimte. Daardoor kunnen er nog steeds weinig elektronen de geleidingsband bereiken, we spreken hier van een kleine toestandsdichtheid. Dit is in feite de situatie in een halfgeleider waarbij de bandkloof tot nul gekrompen is. De geleidingseigenschappen van materialen met een bandenstructuur als die van Cd_3As_2 verschillen van zowel metalen als halfgeleiders. Daarom worden deze materialen halfmetalen genoemd.

Dirac-halfmetalen

Een Dirac-halfmetaal is een halfmetaal waarbij de elektronen rond het Ferminiveau worden beschreven als massaloze oplossingen van de Diracvergelijking. Het punt in de impulsruimte waar de geleidings- en valentieband elkaar raken wordt dan ook een *Diracpunt* genoemd. De Diracvergelijking beschrijft relativistische fermionen. De energie van deze deeltjes is lineair in de impuls, in tegenstelling tot de kwadratische dispersierelatie van niet-relativistische deeltjes.

Het materiaal Cd_3As_2 is een Dirac-halfmetaal met twee Diracpunten, deze zijn schematisch weergegeven in figuur 2b. Deze materialen zijn erg interessant voor zowel thereotici als voor experimentatoren, omdat ze een nieuwe toepassing van de Diracvergelijking vormen in de vastestoffysica, naast de deeltjesfysica. Dirac-halfmetalen bieden de mogelijkheid om relativistische fysica te onderzoeken in verscheidene stoffen.

Vanwege de specifieke geleidingseigenschappen bieden deze materialen perspectief op nieuwe technologische toepassingen. Het meest bekende Dirac-halfmetaal is grafeen. De ontdekking en realisatie van grafeen in 2004 heeft Andre Geim en Konstantin Novoselov in 2010 de Nobelprijs opgeleverd. Inmiddels zijn er meer dan 100.000 onderzoeksartikelen en meer dan 5000 patenten over grafeen verschenen [180], en is het ook buiten de wetenschappelijke wereld regelmatig in het nieuws. Grafeen is een koolstofmembraan van één atoom dik en wordt daarom een tweedimensionaal materiaal genoemd. In dit proefschrift behandelen we uitsluitend Dirac-halfmetalen in drie ruimtelijke dimensies, waarvan Cd_3As_2 en Na_3Bi specifieke voorbeelden zijn.

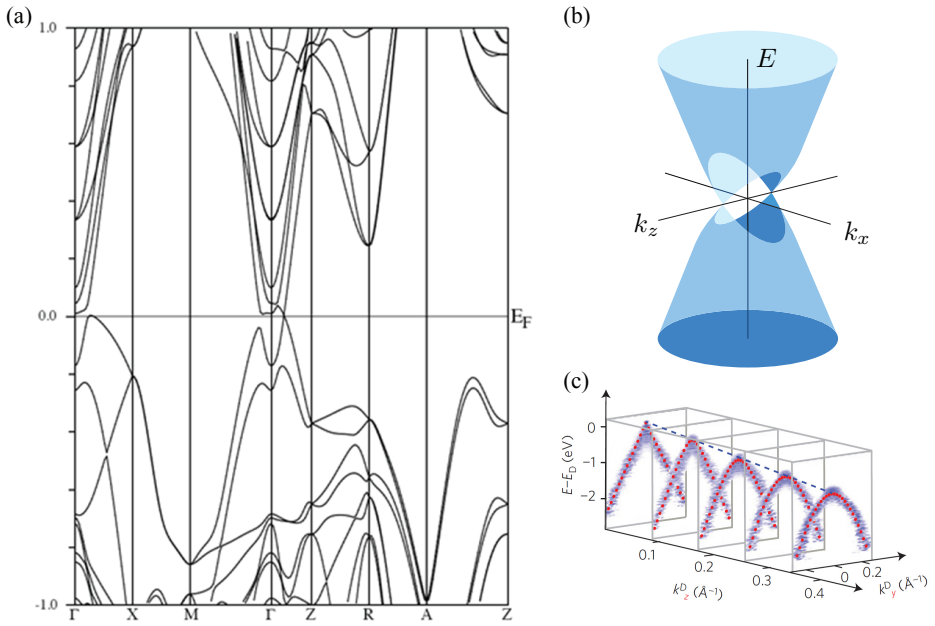

Figuur 2: (a): bandenstructuur van Cd_3As_2. De horizontale as geeft een bepaald pad door de impulsruimte weer, de verticale as is de energie en E_F geeft het Ferminiveau aan. Het Diracpunt bevindt zich op de ΓZ-lijn. Deel van figuur S2 uit Ref. [38]. (b): schematische weergave van de twee Diracpunten in Cd_3As_2. Figuur geïnspireerd door een figuur in Ref. [180]. (c): experimentele meting van de valentieband rond een Diracpunt in Cd_3As_2. De lineaire relatie tussen energie (verticaal) en impuls (horizontaal) is duidelijk te zien, evenals de afwijking hiervan als we van het Diracpunt weggaan. Deel van een figuur uit Ref. [37].

De rol van symmetrie

Hoe komen de Diracpunten precies tot stand? Losse elektronen zijn niet massaloos, en bovendien is de Diracvergelijking een relativistische vergelijking terwijl de snelheden van de elektronen in het materiaal zelf niet dicht in de buurt komen van de lichtsnelheid. Het bestaan van Diracpunten is bijzonder, want twee energiebanden die dicht bij elkaar liggen stoten elkaar meestal af als gevolg van kwantumfluctuaties.

Het blijkt dat de relativistische Dirac-fysica rond het Ferminiveau van Dirac-halfmetalen een emergente eigenschap is, die voortkomt uit het samenspel tussen de vele elektronen en atomen in het kristalrooster. Zoals vaak in de natuurkunde speelt de onderliggende *symmetrie* hierbij een grote rol, in dit geval de ruimtelijke symmetrie van het kristalrooster. In materialen zoals Cd_3As_2 blijkt de totstandkoming van Diracpunten het gevolg te zijn van de invariantie van de kristalstructuur onder

rotaties over een hoek van 90 graden. Deze invariantie van het rooster legt beperkingen op aan de bandenstructuur, waaronder de eis dat er banden zijn die elkaar bij het Ferminiveau moeten kruisen. Op het moment dat deze discrete rotatiesymmetrie gebroken wordt, vervalt deze eis en kan er een bandkloof ontstaan op het Diracpunt, waardoor het ophoudt te bestaan.

Topologische Weyl-halfmetalen

In een Diracpunt komen twee tweevoudig ontaarde energiebanden tegelijk bij elkaar, waardoor in dit punt een viervoudige ontaarding optreedt. Deze wordt gedeeltelijk opgeheven als we de symmetrie onder tijdsomkeringen of de puntsymmetrie rond het Diracpunt breken. Hierdoor splitst het Diracpunt zich op in twee zogenaamde Weylpunten die tweevoudig gedegenereerd zijn. Dit kan begrepen worden door een massaloos Dirac-fermion te zien als een superpositie van een linkshandig en een rechtshandig Weyl-fermion. Het gedrag rond een Weylpunt wordt vervolgens beschreven door de Weylvergelijking. Materialen die Weylpunten bevatten heten Weyl-halfmetalen, en ook deze materialen zijn zeer recentelijk experimenteel gevonden.

Het bijzondere van Weyl-halfmetalen is dat losse Weylpunten erg robuust zijn. Terwijl Diracpunten slechts beschermd zijn door symmetrie, is een Weylpunt beschermd tegen verstoringen en onzuiverheden, oftewel *topologisch beschermd*. Weylpunten kunnen alleen vernietigd worden als een linkshandig en een rechtshandig Weylpunt elkaar tegenkomen. Als gevolg van deze topologische bescherming hebben Weyl-halfmetalen exotische geleidingseigenschappen, zoals we aanstonds zullen zien.

Het effect van wisselwerkingen

Tot zover hebben we alleen vrije systemen besproken, maar het is plausibel dat in bepaalde situaties, zoals in de buurt van een fase-overgang, nietlokale wisselwerkingen een rol spelen in deze materialen. Deze worden theoretisch beschreven door de elektronen te koppelen aan andere vrijheidsgraden die hun eigen dynamica hebben.

In dit proefschrift kijken we naar wisselwerkingen in Dirac- en Weylpunten die worden beschreven door een sterk gecorreleerde kwantumveldentheorie, een complexe theorie waarmee het lastig rekenen is. Dit komt doordat we rekening moeten houden met veel ingrediënten tegelijk die allemaal alle de andere ingrediënten voelen. Toch is het mogelijk om dit systeem indirect te beschrijven, via de zogenaamde holografische techniek. Het gaat hier dus over *holografische wisselwerkingen*, en dit verklaart het tweede deel van de titel van dit proefschrift.

We zijn met name geïnteresseerd in de spectrale dichtheidsfunctie en de elektrische conductiviteit van de Dirac- en Weylfermionen, omdat deze experimenteel meetbaar

zijn. De spectrale dichtheisfunctie bijvoorbeeld kan gemeten worden via foto-emissie experimenten. De resultaten van een dergelijk experiment zonder sterke correlaties zijn te zien in figuur 2c. Deze grootheid geeft dus een indicatie van de effecten van wisselwerkingen op de bandenstructuur. Een voorproefje van onze resultaten voor de spectrale dichtheidsfunctie in de aanwezigheid van holografische wisselwerkingen uit hoofdstukken 3 en 6 zijn te zien in figuur 3. De holografische techniek wordt verderop in wat meer detail bespreken. Hiernaast hebben we ook onderzocht of een sterk versimpelde versie van de kwantumveldentheorie de holografische resultaten zou kunnen benaderen. Een daartoe geschikt model wordt geconstrueerd in hoofdstuk 5. De details van deze constructie geven ons meer inzicht in de onderliggende werking van de holografische techniek.

Ladingstransport

Zoals eerder gezegd zijn we naast het spectrum ook geïnteresseerd in de geleidingseigenschappen van Dirac- en Weyl-halfmetalen. In hoofdstuk 2 wordt de *elektrische conductiviteit* berekend van vrije Dirac- en Weylpunten. In deze berekening wordt een klein elektrisch veld aangelegd, waardoor er een elektrische stroom gaat lopen. De conductiviteit is de evenredigheidscoëfficiënt tussen de verwachtingswaarde van de stroomdichtheid en de elektrische veldsterkte, en geeft aan hoe goed de stroomgeleiding is. Hoofdstuk 4 is gewijd aan het bepalen van de elektrische conductiviteit in het interagerende geval. Een van de resultaten is te zien in figuur 3d.

In Weyl-halfmetalen met gebroken tijdsomkeringssymmetrie vindt nog een andere vorm van transport plaats via het zogenaamde anomale Hall-effect. Hierbij vindt ladingstransport zonder warmteontwikkeling plaats in de richting loodrecht op het aangelegde elektrische veld. Een Weyl-halfmetaal heeft een anomale Hall-conductiviteit ongelijk aan nul. De topologische aard van de bandenstructuur van Weylpunten is hiervoor verantwoordelijk. De anomale Hall-conductiviteit van twee vrije Weylpunten wordt berekend in hoofdstuk 2.

Het is deze eigenschap die Weyl-halfmetalen interessant maakt voor praktische toepassingen, zoals het zogenaamde valleytronics [181]. Daarbij wordt de bezetting van een rechts- of linkshandig Weylpunt gebruikt als informatiedrager in een computer, net zoals bij conventionele elektronica de aan- en afwezigheid van lading de enen en nullen zijn. Het transport van elektronen in conventionele materialen leidt tot opwarming en daardoor tot een grens aan de rekensnelheid. Het verliesloos transport in topologische systemen lost in principe dit probleem op en maakt dus in theorie snellere computers mogelijk.

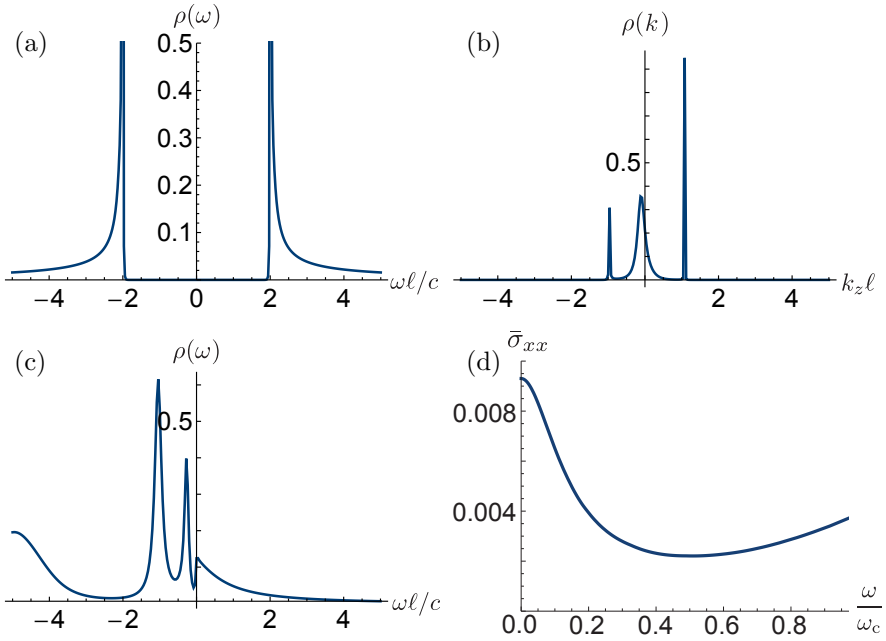

Figuur 3: Spectrale dichtheidsfunctie in verschillende situaties, en elektrische conductiviteit. (a): resultaat uit hoofdstuk 3. De effecten van holografische interacties leiden tot een verbreding van de spectrale dichtheidsfunctie die zich voor lage energie en temperatuur gedraagt als een machtswet. De macht is een parameter in de holografische theorie en hangt van het specifieke materiaal af. (b): bij nietrelativistische schalingssymmetrie vinden we een kwantumfaseovergang in de grondtoestand. Dit is een van de componenten van het spectrum uit hoofdstuk 3 als functie van de impuls in de Fermivloeistoffase bij kleine frequentie. Twee Ferminiveaus zijn zichtbaar als scherpe pieken. (c): spectrum van een gedoteerd Dirac-halfmetaal bij een bepaalde waarde van de chemische potentiaal. Dit is een niet-Fermivloeistof die wordt geanalyseerd in hoofdstuk 6. (d): elektrische conductiviteit als functie van de frequentie ω van het elektrische veld. Bij lage frequentie is het effect van de wisselwerkingen dominant, wat onder andere leidt tot een piek in de conductiviteit. De functionele vorm van deze piek wordt bepaald in hoofdstuk 4. Bij zeer hoge frequenties vinden we het vrije resultaat uit hoofdstuk 2 terug.

Holografie

Een hologram is een tweedimensionaal object waarmee men een driedimensionaal beeld kan vormen door er licht op te schijnen. Dit driedimensionale beeld ontstaat via interferentie tussen lichtgolven die via het hologram terugkaatsen en diegene die het hologram nog niet geraakt hebben. Met de term holografie in dit proefschrift bedoelen we net iets anders, namelijk het holografische principe. Dat zegt dat de

natuurkundige beschrijving van een volume in de ruimtetijd versleuteld is in het oppervlak, dus een gebied met een dimensie lager, dat dit volume omgeeft. Dit idee komt voort uit de zoektocht van vele wetenschappers naar de hereniging van de kwantummechanica met de algemene relativiteitstheorie van Einstein en is uiteindelijk door Gerard 't Hooft geformuleerd in 1993. Gecombineerd met oudere aanwijzingen over de overeenkomsten tussen een bepaalde theorie van kwantumzwaartekracht, de zogenaamde snaartheorie, en de kwantumchromodynamica, de theorie die quarks beschrijft, was dit de opmaat voor de vooruitgang die in 1998 geboekt werd door Juan Maldacena: de AdS/CFT correspondentie. Dit is een dualiteit, een exacte wiskundige overeenkomst tussen twee ogenschijnlijk verschillende theorieën. Deze twee theorieën zijn eigenlijk twee manieren om naar hetzelfde systeem te kijken. Net zoals bij een hologram gaat het om een natuurkundig systeem dat een zustertheorie heeft in één dimensie meer.

De sterk gecorreleerde kwantumveldentheorie die de interacties tussen Dirac- en Weyl-fermion beschrijft, heeft een zustertheorie waarin zwaartekracht een rol speelt. Het is een Anti-de Sitter universum in vier ruimtelijke dimensies, een oplossing van de Einsteinvergelijking in de algemene relativiteitstheorie, met negatieve kromming en een zwart gat in het midden. Het cruciale aan de Anti-de Sitter geometrie is dat dit universum een driedimensionale rand heeft, waarop de veldentheorie leeft. In de analogie met het hologram is de veldentheorie dus de holografische plaat, en het Anti-de Sitter universum het driedimensionale holografische beeld.

De *holografische techniek* is een toepassing van de AdS/CFT correspondentie die we in dit proefschrift verkennen. Het mooie hiervan is dat de thermodynamica van zwarte gaten en de fysica in de bijbehorende gekromde ruimtetijd een eenvoudiger beschrijving vormen van de kwantumveldensoep op de rand van het universum. Zoals uitgebeeld is in figuur 4, kan dit dus gebruikt worden als een werktuig om resultaten te krijgen in de complexe veldentheorie, door te rekenen aan de gravitationele kant.

Tot slot

De holografische techniek is sinds 1998 door veel wetenschappers gebruikt voor toepassingen in onder andere de gecondenseerde materie en de kwantumchromodynamica. In dit proefschrift laten we zien dat het mogelijk is om deze techniek ook in sterk gecorreleerde Dirac- en Weyl-halfmetalen toe te passen, door deze te koppelen aan een veldentheorie met een duale gravitationele beschrijving. De resultaten voor de spectrale dichtheidsfunctie en de conductiviteit in de hoofdstukken 3, 4 en 6 zijn theoretische voorspellingen die mogelijk in een experiment met Dirac- en/of Weyl-halfmetalen getest kunnen worden.

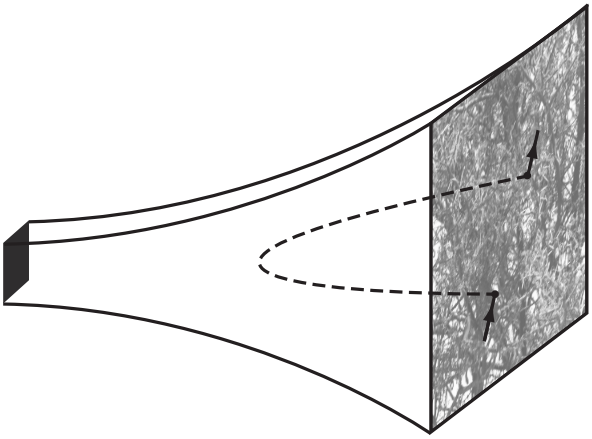

Figuur 4: Voorstelling van de holografische techniek. Het vierdimensionale Anti-de Sitter universum is schematisch afgebeeld, de gekromde lijnen geven de kromming van de ruimtetijd aan. Helemaal links, diep in het universum bevindt zich een zwart gat. Op de driedimensionale, vlakke rand van het universum, helemaal rechts in beeld, leeft de "kwantumsoep" van de sterk gecorreleerde kwantumveldentheorie. De berekening van een correlatiefunctie in dit systeem (zwarte pijlen) wordt vereenvoudigd door de vierde dimensie in te gaan (stippellijn), alwaar de effecten van zwaartekracht de gewenste beschrijving geven.

Ten eerste leiden onze resultaten tot beter inzicht in het gedrag van deze materialen wanneer ze sterk gecorreleerd zijn, zoals bij een fase-overgang het geval is. Met name begrip van de effecten op ladingstransport kan bijdragen aan de ontwikkeling van nieuwe technologie. Er is nog veel werk te doen voor we een complete theoretische beschrijving hebben. Daarom moeten de resultaten die hier gepresenteerd zijn, gezien worden als een eerste stap in een nieuwe onderzoeksrichting. We zijn in het bijzonder geïnteresseerd in het gedoteerde geval en in de effecten op het anomale transport in Weyl-halfmetalen. Deze thema's vallen buiten dit proefschrift, maar zijn het onderwerp van actueel onderzoek.

Ten tweede biedt dit onderzoek nieuwe mogelijkheden voor een experimentele test van de holografische techniek. Hieruit kunnen we leren of, en hoe, deze techniek nog beter geoptimaliseerd kan worden voor realistischer resultaten. Het is boeiend om te zien dat het fundamentele natuurkundige onderzoek naar de eenwording van kwantummechanica en zwaartekracht leidt tot onverwachte toepassingen zoals deze holografische techniek, die uiteindelijk zullen leiden tot een beter begrip van de complexe fysica van sterk gecorreleerde systemen.

*****

Acknowledgements

One does not simply write a thesis. Not without the support of many individuals, who have contributed greatly to this research and to my life in the past few years.

I'm very grateful to my supervisors Henk Stoof and Stefan Vandoren, who have given me the opportunity to do a PhD in Utrecht on an exciting and challenging topic. While having a different scientific background, they have established an inspiring and successful collaboration. We had many enjoyable physics discussions, from which I have learned very much. Thank you for sharing your knowledge with me. I'm grateful you for your enthusiasm, your untiring support and encouragement, your challenging questions, your open and positive attitude, and for debunking the occasional red herrings. Most importantly, thank you for your confidence in me. It has truly been a pleasure to work with you these four years.

Next, I have had the pleasure to join forces with five young people working on their Master's thesis projects. Part of this research has contributed directly to this thesis, all of it to my physics knowledge. Watse Sybesma, Pim Borman, Simonas Grubinskas, Yoran Tournois, and Vasilis Vlachodimitropoulos, thanks for your hard work, your difficult questions, your indispensable scientific contributions and your enthusiasm. I've had a lot of fun with you and have learned much from you. Good luck with your careers in the future.

I'm thankful to my reading committee for reviewing my many-paged thesis, Umut Gürsoy, Cristiane Morais Smith, Giuseppe Policastro, Koenraad Schalm, and Bernard de Wit. I'd like to thank Umut in particular for his scientific support in many forms, from which this thesis has greatly benefitted. Also thanks to my other past and present collaborators Erik Plauschinn and Panos Betzios, I very much enjoyed working with you. My research and physics knowledge have also benefitted from instructive questions and valuable comments from Rembert Duine, Lars Fritz, Sean Hartnoll, Gerard 't Hooft, Cristiane Morais Smith, Giuseppe Policastro, Koenraad

Schalm, Dirk Schuricht, and Jan Zaanen. Finally, I'd like to acknowledge the anonymous referees of our papers, who contributed considerably to the quality of the papers.

Furthermore, I have to acknowledge the Institute for Theoretical Physics of Utrecht University, which is a fantastic place to work. This is in part due to its strong researchers who have also been excellent colleagues. I hope this institute will prosper in the future and keeps producing outstanding science and researchers. Thanks to the following people among the PhDs and postdocs for the pleasant working atmosphere, the interesting talks, the scientific discussions next to the coffee machine, and the occasional soccer or canoeing tournament: Aaron, Alessandra, Alessandro, Andreas, Andrew, Anja, Anne, Arie-Willem, Aron, Benedetta, Bram, Carolin, Chiara, Christoph, Clement, Dražen, Drian, Erik[3], Flavio, Giuseppe, Guido, Hai-Qing, Hedwig, Jan, Jasper, Javier[2], Jeffrey, Jeroen, Jiansen, Jildou, Jogundas (thanks for teaching me Lithuanian, you rupūžė), Jorgos, Jules (also for the pleasant lunches), Kiril, Lei, Luís, Marco, Marcos, Martijn, Mathijs, Natália, Nava (also for teaching me how to recognize priviliges), Nick, Niklas, Olga, Panos, Phil, Philipp, Ralph, Riccardo, Rick, Roberto, Shaoyu, Shun-Pei, Simonas, Stefan, Stijn, Tara, Tatjana, Thomas, Ties, Tobias, Vladimir, Watse, Wellington, Wilke, Wouter, Yvette. Furthermore, I'm thankful to the people of the supporting staff, working hard dealing with the organization of the institute and other important matters, Els, Joost, Marion, Olga, Riny, Wanda. Also thanks to Jaap Dijkhuis for the support in the high ranks. For my pleasant teaching experiences I thank Gleb Arutyunov, Gerard Barkema, Rembert Duine, and René van Roij. Thanks to my officemates Javier, Kiril, Shun-Pei, Tobias, and Watse, for the enjoyable environment, the random conversations, research suggestions, and some much-needed humour. Special thanks to the BEC crew for the nice Friday afternoon seminars and the many pleasant beer/metal/barbecue events, in particular Rembert for the whisky. I'm thankful to you all, and also to the other staff members and the Master's students of the Institute whom I have met during my studies and PhD, and who have shown interest in my research and well-being.

Wilke, you have not only been my mentor on paper, but throughout the years you've become my scientific mentor, my personal smart ass, but moreover a very good friend. I'm truly thankful for your help and advice, and look back to our adventures with a smile hoping there are some nice trips to come. Thessa, we have been in the same boat for a long time. It has always been good to share with you the perks and pains of taking care of ourselves and becoming independent researchers. All the best in the future. Watse, I could not have been more lucky to share a research project and an office with such a cheerful and lively person as you are. Thanks for all the good vibrations (sorry if that's awkward, but I mean the black hole ones. Oh... never mind.). Much success with the challenges to come, learn as much as you can and

enjoy every minute of it.

During these year I have had the opportunity to travel to conferences around the world, during which I have spoken with many inspiring people, too many to mention here. Thanks to Johanna Erdmenger and David Vegh for their interest in our research. Migael Strydom, Ann-Kathrin Straub, Nele Callebaut, thank you for the enjoyable moments in Cambridge, Munich and on Crete.

There are a number of people outside of physics whom I could always count on to unwind. First of all, my chicas, Helen, Martje and Nienke, I love having you in my life. Thanks for your company, the memorable episodes, the wine and cheese and tuurlijk the sauna moments, our many trips to cities and the outdoors, in short, an enjoyable friendship which I value very much. Thanks to my homies Alje, Raja, Renee, and Thomas, who provided a relaxing, nerdy, and supergezellig place to come home to in my first year of the PhD. Cheers to the math, the parties, and to the unforgettable experience of living together. Thanks to the adventurers Wouter, Assia, Bas, Blanca, Jelmer, Martijn, Rob and Sylvia for their friendship, hospitality and awesome birding trips around the world. I enjoyed the wisdom of my friends Henk, Maartje and Peter, who have educated me beyond science. Also thanks to the wonderful people I met during activities of the Jeugdbond voor Natuur- en Milieustudie, and those of the birding crews of Deception Tours and the Strandpluvier, with whom I have enjoyed nature and birdwatching time and time again. In particular, my dear friends Ferry, Frank, Jan, Janne, Jip, Jojanneke, Jorrit, Judith, Lieke, Lodewijk, Marloes, Niels, Pieter, Rutger, Sander, Sjoerd, Teize, and Thomas, thank you all. Marjolein, despite not making the trip Utrecht-Nijmegen very often, I could truly appreciate your frequent messages, kind words and phone calls, thank you. I enjoyed the company of these biologists tolerating me at their Friday evening borrels, Alex, David, Harmjan, Hesther, Maria^2, Marieke, Lucas, Rene, Robert, Sasha, Tobias, Willem-Jan. Thanks to the Sinterklaas crew, Erik, Gerhard, Lydia, Pieter, and Wessel, for a bizarre, hilarious and slightly controversial distraction. Finally, special thanks to my paranymphs Marten and Martje for backing me during the endgame.

I am very grateful to my semifamily Alice, Ron, Josse, Jessica, Paul, and Lies for their inspiring company. Thanks to my family for providing a solid foundation and for the support during these years. In particular I'd like to thank my lovely parents Ank and Hans, my brother Frank, and Batsheva for their unconditional support and pertinacious encouragement.

Finally, there is one very important person to whom I am infinitely grateful.

Marten, thank you for always being there for me.

*****

Curriculum Vitae

Vivian Jacobs was born on June 21, 1988 in Enschede, the Netherlands. She attended the Utrechts Stedelijk Gymnasium in Utrecht from 1999 to 2005. She enrolled in the Bachelor's programme in physics and astronomy at Utrecht University, graduating *cum laude* in 2009. From 2008 to 2009, she also attended the first year of the Master's programme Astrophysics at Utrecht University. In 2009 she decided to switch to theoretical physics, and enrolled in the Master's programme in Theoretical Physics at Utrecht University, graduating in August 2011 with the Master's thesis "Kubo formalism for spin drag in an atomic Fermi gas" under supervision of dr. R. A. Duine and prof. H. T. C. Stoof.

Vivian started her PhD research in Utrecht in September 2011, working under the supervision of prof. S. J. G. Vandoren and prof. H. T. C. Stoof. The results of this PhD research can be read in this thesis. During this time, Vivian also had the opportunity to co-supervise the thesis research of five Master's students graduating under supervision of prof. Stoof, part of which also contributed to the research presented here.

*****

Bibliography

[1] Z. W. Sybesma, *Weyl Semimetals and Holography with a hint of Massive Spinors*, Master's thesis, Institute for Theoretical Physics, Utrecht University (2012).

[2] S. Grubinskas, *Towards a field-theoretic interpretation of bottom-up AdS/CMT*, Master's thesis, Institute for Theoretical Physics, Utrecht University (2014).

[3] P. Borman, *Holographic Fermions: From Black Branes Towards Cold Atoms*, Master's thesis, Institute for Theoretical Physics, Utrecht University (2014).

[4] J. G. Bednorz and K. A. Müller, Z. Phys. B **64**, 189 (1986).

[5] M. Troyer and U.-J. Wiese, Phys. Rev. Lett. **94**, 170201 (2005).

[6] A. Adams, L. D. Carr, T. Schäfer, P. Steinberg, and J. E. Thomas, New J. Phys. **14**, 115009 (2012).

[7] P. A. M. Dirac, Proc. R. Soc. A **117**, 610624 (1928).

[8] K. S. Novoselov, A. K. Geim, S. V. Morozov, D. Jiang, Y. Zhang, S. V. Dubonos, I. V. Grigorieva, and A. A. Firsov, Science **306**, 666 (2004).

[9] K. Novoselov, A. K. Geim, S. Morozov, D. Jiang, M. Katsnelson, I. Grigorieva, S. Dubonos, and A. Firsov, Nature **438**, 197 (2005).

[10] A. H. Castro Neto, F. Guinea, N. M. R. Peres, K. S. Novoselov, and A. K. Geim, Rev. Mod. Phys. **81**, 109 (2009).

[11] J. von Neumann and E. P. Wigner, Phys. Z. **30**, 467 (1929).

[12] B. A. Bernevig, *Topological Insulators and Topological Superconductors* (Princeton University Press, 2013).

[13] H. Weyl, Proc. Natl. Acad. Sci. U. S. A. **15**, 323 (1929).

[14] M. V. Berry, Proc. R. Soc. A **392**, 4557 (1984).

[15] H. B. Nielsen and M. Ninomiya, Phys. Lett. B **130**, 389 (1983).

[16] A. A. Zyuzin, S. Wu, and A. A. Burkov, Phys. Rev. B **85**, 165110 (2012).

[17] A. A. Zyuzin and A. A. Burkov, Phys. Rev. B **86**, 115133 (2012).

[18] D. T. Son and N. Yamamoto, Phys. Rev. Lett. **109**, 181602 (2012).

[19] A. G. Grushin, Phys. Rev. D **86**, 045001 (2012).

[20] V. Aji, Phys. Rev. B **85**, 241101 (2012).

[21] M. Vazifeh and M. Franz, Phys. Rev. Lett. **111**, 027201 (2013).

[22] P. Goswami and S. Tewari, Phys. Rev. B **88**, 245107 (2013).

[23] P. Goswami and S. Tewari, arXiv:1311.1506 (2013).

[24] Z. Wang and S.-C. Zhang, Phys. Rev. B **87**, 161107 (2013).

[25] H. Pan, M. Wu, Y. Liu, and S. A. Yang, arXiv:1503.08075 (2015).

[26] P. Hosur, S. A. Parameswaran, and A. Vishwanath, Phys. Rev. Lett. **108**, 046602 (2012).

[27] Á. Bácsi and A. Virosztek, Phys. Rev. B **87**, 125425 (2013).

[28] Z. Wang, H. Weng, Q. Wu, X. Dai, and Z. Fang, Phys. Rev. B **88**, 125427 (2013).

[29] B.-J. Yang and N. Nagaosa, Nature Commun. **5**, 4898 (2014).

[30] S. Murakami, New J. Phys. **9**, 356 (2007).

[31] S. Murakami, New J. Phys. **10**, 029802 (2008).

[32] S.-Y. Xu, Y. Xia, L. A. Wray, S. Jia, F. Meier, J. H. Dil, J. Osterwalder, B. Slomski, A. Bansil, H. Lin, R. J. Cava, and M. Z. Hasan, Science **332**, 560 (2011).

[33] S. M. Young, S. Zaheer, J. C. Y. Teo, C. L. Kane, E. J. Mele, and A. M. Rappe, Phys. Rev. Lett. **108**, 140405 (2012).

[34] C. Fang, M. J. Gilbert, X. Dai, and B. A. Bernevig, Phys. Rev. Lett. **108**, 266802 (2012).

[35] Z. Wang, Y. Sun, X.-Q. Chen, C. Franchini, G. Xu, H. Weng, X. Dai, and Z. Fang, Phys. Rev. B **85**, 195320 (2012).

[36] L. He, X. Hong, J. Dong, J. Pan, Z. Zhang, J. Zhang, and S. Li, Phys. Rev. Lett. **113**, 246402 (2014).

[37] Z. K. Liu, B. Zhou, Y. Zhang, Z. J. Wang, H. M. Weng, D. Prabhakaran, S.-K. Mo, Z. X. Shen, Z. Fang, X. Dai, Z. Hussain, and Y. L. Chen, Science **343**, 864 (2014).

[38] S. Borisenko, Q. Gibson, D. Evtushinsky, V. Zabolotnyy, B. Büchner, and R. J. Cava, Phys. Rev. Lett. **113**, 027603 (2013).

[39] M. Neupane, S.-Y. Xu, R. Sankar, N. Alidoust, G. Bian, C. Liu, I. Belopolski, T.-R. Chang, H.-T. Jeng, H. Lin, A. Bansil, F. Chou, and M. Z. Hasan, Nature

Commun. **5**, 3786 (2014).

[40] Z. K. Liu, J. Jiang, B. Zhou, Z. J. Wang, Y. Zhang, H. M. Weng, D. Prabhakaran, S.-K. Mo, H. Peng, P. Dudin, T. Kim, M. Hoesch, Z. Fang, X. Dai, Z. X. Shen, D. L. Feng, Z. Hussain, and Y. L. Chen, Nature Mater. **13**, 677 (2014).

[41] S.-Y. Xu, I. Belopolski, N. Alidoust, M. Neupane, C. Zhang, R. Sankar, S.-M. Huang, C.-C. Lee, G. Chang, B. Wang, G. Bian, H. Zheng, D. S. Sanchez, F. Chou, H. Lin, S. Jia, and M. Z. Hasan, arXiv:1502.03807 (2015).

[42] S.-Y. Xu, C. Liu, S. K. Kushwaha, R. Sankar, J. W. Krizan, I. Belopolski, M. Neupane, G. Bian, N. Alidoust, T.-R. Chang, H.-T. Jeng, C.-Y. Huang, W.-F. Tsai, H. Lin, P. P. Shibayev, F.-C. Chou, R. J. Cava, and M. Z. Hasan, Science **347**, 294 (2015).

[43] B.-J. Yang, E.-G. Moon, H. Isobe, and N. Nagaosa, Nature Phys. **10**, 774 (2014).

[44] S.-M. Huang, S.-Y. Xu, I. Belopolski, C.-C. Lee, G. Chang, B. Wang, N. Alidoust, M. Neupane, H. Zheng, D. Sanchez, A. Bansil, G. Bian, H. Lin, and M. Z. Hasan, arXiv:1503.05868 (2015).

[45] W.-Y. He, S. Zhang, and K. T. Law, arXiv:1501.02348 (2015).

[46] V. Mastropietro, J. Phys. A **47**, 465003 (2013).

[47] A. A. Burkov, M. D. Hook, and L. Balents, Phys. Rev. B **84**, 235126 (2011).

[48] H. Isobe and N. Nagaosa, Phys. Rev. B **87**, 205138 (2013).

[49] J. González, F. Guinea, and M. Vozmediano, Phys. Rev. B **59**, R2474 (1999).

[50] L. Fritz, J. Schmalian, M. Müller, and S. Sachdev, Phys. Rev. B **78**, 085416 (2008).

[51] W. Witczak-Krempa, M. Knap, and D. Abanin, Phys. Rev. Lett. **113**, 136402 (2014).

[52] J. Hofmann, E. Barnes, and S. Das Sarma, arXiv:1410.1547 (2014).

[53] S. Gupta, Z. Hadzibabic, M. W. Zwierlein, C. A. Stan, K. Dieckmann, C. H. Schunck, E. G. M. van Kempen, B. J. Verhaar, and W. Ketterle, Science **300**, 1723 (2003).

[54] A. Damascelli, Phys. Scr. **T109**, 61 (2004).

[55] Q. Chen, Y. He, C.-C. Chien, and K. Levin, Rep. Prog. Phys. **72**, 122501 (2009).

[56] A. Altland and B. D. Simons, *Condensed Matter Field Theory* (Cambridge University Press, 2010).

[57] H. Bruus and K. Flensberg, *Many-Body Quantum Theory in Condensed Matter Physics* (Oxford University Press, 2004).

[58] Y. A. Kharkov and O. P. Sushkov, arXiv:1503.01554 (2015).

[59] V. Riva and J. Cardy, Phys. Lett. B **622**, 339 (2005).

[60] J. M. Maldacena, Adv. Theor. Math. Phys. **2**, 231 (1998).

[61] E. Witten, Adv. Theor. Math. Phys. **2**, 253 (1998).

[62] S. S. Gubser, I. R. Klebanov, and A. M. Polyakov, Phys. Lett. B **428**, 105 (1998).

[63] S. A. Hartnoll, P. Kovtun, M. Müller, and S. Sachdev, Phys. Rev. B **76**, 144502 (2007).

[64] M. Čubrović, J. Zaanen, and K. Schalm, Science **325**, 439 (2009).

[65] S. A. Hartnoll, Class. Quantum Grav. **26**, 224002 (2009).

[66] J. McGreevy, Adv. High Energy Phys. **2010**, 723105 (2010).

[67] S. Sachdev, Annu. Rev. Condens. Matter Phys. **3**, 933 (2012).

[68] T. Faulkner and J. Polchinski, J. High Energy Phys. **06**, 012 (2011).

[69] A. Mukhopadhyay and G. Policastro, Phys. Rev. Lett. **111**, 221602 (2013).

[70] E. Iancu and A. Mukhopadhyay, arXiv:1410.6448 (2014).

[71] U. Gürsoy, E. Plauschinn, H. Stoof, and S. Vandoren, J. High Energy Phys. **05**, 018 (2012).

[72] R. Contino and A. Pomarol, J. High Energy Phys. **11**, 058 (2004).

[73] P. Betzios and U. Gürsoy, *Semi-Holography, Ward Identities and Conductivity*, work in progress (2015).

[74] P. W. Phillips, B. W. Langley, and J. A. Hutasoit, Phys. Rev. B **88** (2013).

[75] G. E. Volovik, Lect. Notes Phys. **870**, 343 (2013).

[76] A. G. Truscott, K. E. Strecker, W. I. McAlexander, G. B. Partridge, and R. G. Hulet, Science **291**, 2570 (2001).

[77] K. O'Hara, S. Hemmer, M. Gehm, S. Granade, and J. Thomas, Science **298**, 2179 (2002).

[78] M. J. Ku, A. T. Sommer, L. W. Cheuk, and M. W. Zwierlein, Science **335**, 563 (2012).

[79] K. B. Gubbels and H. T. C. Stoof, Phys. Rep. **525**, 255 (2013).

[80] Y. Nishida and D. T. Son, Phys. Rev. D **76** (2007).

[81] A. Bagrov, B. Meszena, and K. Schalm, J. High Energy Phys. **09**, 106 (2014).

[82] C. A. Regal, C. Ticknor, J. L. Bohn, and D. S. Jin, Nature **424**, 4750 (2003).

[83] C. Chin, M. Bartenstein, A. Altmeyer, S. Riedl, S. Jochim, J. H. Denschlag, and R. Grimm, Science **305**, 1128 (2004).

[84] I. D'Amico and G. Vignale, Phys. Rev. B **62**, 4853 (2000).

[85] A. Sommer, M. Ku, G. Roati, and M. W. Zwierlein, Nature **472**, 201 (2011).

[86] K. Damle and S. Sachdev, Phys. Rev. B **56**, 8714 (1997).

[87] M. Blake and A. Donos, Phys. Rev. Lett. **114** (2015).

[88] S. A. Hartnoll and C. P. Herzog, Phys. Rev. D **77**, 106009 (2008).

[89] R. A. Davison, Phys. Rev. D **88**, 086003 (2013).

[90] M. Blake and D. Tong, Phys. Rev. D **88**, 106004 (2013).

[91] B. Goutéraux, J. High Energy Phys. **04**, 181 (2014).

[92] A. Lucas, S. Sachdev, and K. Schalm, Phys. Rev. D **89**, 066018 (2014).

[93] R. A. Davison, K. Schalm, and J. Zaanen, Phys. Rev. B **89**, 245116 (2014).

[94] M. Blake, D. Tong, and D. Vegh, Phys. Rev. Lett. **112**, 071602 (2014).

[95] T. Andrade and B. Withers, J. High Energy Phys. **05**, 101 (2014).

[96] A. Lucas, J. High Energy Phys. **03**, 071 (2015).

[97] T. Faulkner, N. Iqbal, H. Liu, J. McGreevy, and D. Vegh, Science **329**, 1043 (2010).

[98] T. Faulkner, N. Iqbal, H. Liu, J. McGreevy, and D. Vegh, Phys. Rev. D **88**, 045016 (2013).

[99] W. Witczak-Krempa and S. Sachdev, Phys. Rev. B **86**, 235115 (2012).

[100] S. A. Hartnoll, Nature Phys. **11**, 54 (2015).

[101] S. A. Hartnoll and A. Tavanfar, Phys. Rev. D **83**, 046003 (2011).

[102] S. A. Hartnoll and L. Huijse, Class. Quantum Grav. **29**, 194001 (2012).

[103] V. G. M. Puletti, S. Nowling, L. Thorlacius, and T. Zingg, J. High Energy Phys. **01**, 117 (2011).

[104] S. A. Hartnoll, D. M. Hofman, and D. Vegh, J. High Energy Phys. **08**, 096 (2011).

[105] M. Čubrović, Y. Liu, K. Schalm, Y.-W. Sun, and J. Zaanen, Phys. Rev. D **84** (2011).

[106] M. V. Medvedyeva, E. Gubankova, M. Čubrović, K. Schalm, and J. Zaanen, J. High Energy Phys. **12**, 025 (2013).

[107] M. Kargarian, M. Randeria, and N. Trivedi, arXiv:1503.00012 (2015).

[108] M. E. Peskin and D. V. Schroeder, *An Introduction to Quantum Field Theory* (Westview Press, 1995).

[109] S.-M. Huang, S.-Y. Xu, I. Belopolski, C.-C. Lee, G. Chang, B. Wang, N. Alidoust, G. Bian, M. Neupane, A. Bansil, H. Lin, and M. Z. Hasan, arXiv:1501.00755 (2015).

[110] D. Thouless, M. Kohmoto, M. Nightingale, and M. den Nijs, Phys. Rev. Lett. **49**, 405 (1982).

[111] W.-K. Tse, Z. Qiao, Y. Yao, A. MacDonald, and Q. Niu, Phys. Rev. B **83**, 155447 (2011).

[112] X. Wan, A. M. Turner, A. Vishwanath, and S. Y. Savrasov, Phys. Rev. B **83**, 205101 (2011).

[113] M. A. Silaev and G. E. Volovik, Phys. Rev. B **86**, 214511 (2012).

[114] R. Okugawa and S. Murakami, Phys. Rev. B **89**, 235315 (2014).

[115] U. Gürsoy, V. Jacobs, E. Plauschinn, H. Stoof, and S. Vandoren, J. High Energy Phys. **04**, 127 (2013).

[116] C. Herzog, J. Phys. A **42**, 343001 (2009).

[117] S. Sachdev, arXiv:1002.2947 (2010).

[118] S. A. Hartnoll, in *Black Holes in Higher Dimensions*, edited by G. T. Horowitz (Cambridge University Press, 2012) p. 387.

[119] S.-S. Lee, Phys. Rev. D **79**, 086006 (2009).

[120] T. Faulkner, H. Liu, J. McGreevy, and D. Vegh, Phys. Rev. D **83**, 125002 (2011).

[121] H. Liu, J. McGreevy, and D. Vegh, Phys. Rev. D **83**, 065029 (2011).

[122] S. A. Hartnoll, J. Polchinski, E. Silverstein, and D. Tong, J. High Energy Phys. **04**, 120 (2010).

[123] S. Kachru, X. Liu, and M. Mulligan, Phys. Rev. D **78**, 106005 (2008).

[124] M. Taylor, arXiv:0812.0530 (2008).

[125] V. Keränen and L. Thorlacius, Class. Quantum Grav. **29**, 194009 (2012).

[126] G. T. Horowitz and B. Way, Phys. Rev. D **85**, 046008 (2012).

[127] S. Harrison, S. Kachru, and H. Wang, J. High Energy Phys. **02**, 085 (2014).

[128] N. Bao, X. Dong, S. Harrison, and E. Silverstein, Phys. Rev. D **86**, 106008 (2012).

[129] A. A. Burkov and L. Balents, Phys. Rev. Lett. **107**, 127205 (2011).

[130] Y. Korovin, arXiv:1107.0558 (2011).

[131] M. Alishahiha, M. R. M. Mozaffar, and A. Mollabashi, Phys. Rev. D **86**, 026002 (2012).

[132] L. Q. Fang, X.-H. Ge, and X.-M. Kuang, Phys. Rev. D **86**, 105037 (2012).

[133] N. Iqbal and H. Liu, Phys. Rev. D **79**, 025023 (2009).

[134] N. Iizuka, N. Kundu, P. Narayan, and S. P. Trivedi, J. High Energy Phys. **01**, 094 (2012).

[135] J. Tarrío and S. Vandoren, J. High Energy Phys. **09**, 017 (2011).

[136] T. Meng and L. Balents, Phys. Rev. B **86**, 054504 (2012).

[137] D. T. Son and B. Z. Spivak, Phys. Rev. B **88**, 104412 (2013).

[138] P. Hosur, Phys. Rev. B **86**, 195102 (2012).

[139] D. N. Voskresensky, arXiv:1208.5163 (2012).

[140] S. Sachdev, private communication (2012).

[141] N. Iqbal and H. Liu, Fortschr. Phys. **57**, 367 (2009).

[142] L. D. Landau and E. M. Lifshitz, *Course of Theoretical Physics: Vol. 3, Quantum Mechanics: Non-relativistic Theory* (Pergamon Press, 1977).

[143] V. P. J. Jacobs, S. J. G. Vandoren, and H. T. C. Stoof, Phys. Rev. B **90**, 045108 (2014).

[144] C. Herring, Phys. Rev. **52**, 365 (1937).

[145] G. B. Halász and L. Balents, Phys. Rev. B **85**, 035103 (2012).

[146] K.-Y. Yang, Y.-M. Lu, and Y. Ran, Phys. Rev. B **84**, 075129 (2011).

[147] A. Sekine and K. Nomura, J. Phys. Soc. Jpn. **83**, 094710 (2013).

[148] C. M. Varma, Z. Nussinov, and W. van Saarloos, Phys. Rep. **361**, 267 (2002).

[149] H. v. Löhneysen, A. Rosch, M. Vojta, and P. Wölfle, Rev. Mod. Phys. **79**, 1015 (2007).

[150] S. S. Gubser and F. D. Rocha, Phys. Rev. Lett. **102**, 061601 (2009).

[151] M. Müller, L. Fritz, S. Sachdev, and J. Schmalian, in *Proceedings of the XVIth Int. Congress on Math. Physics 09 Prague*, edited by P. Exner (World Scientific Publishing, 2010) p. 602.

[152] G. D. Mahan, *Many-Particle Physics* (Kluwer Academic / Plenum Publishers, New York, 2000).

[153] V. Jacobs, S. Grubinskas, and H. Stoof, J. High Energy Phys. **2015**, 033 (2015).

[154] S. L. Sondhi, S. M. Girvin, J. P. Carini, and D. Shahar, Rev. Mod. Phys. **69**, 315 (1997).

[155] S. Sachdev, *Quantum Phase Transitions* (Cambridge University Press, 1999).

[156] M. Vojta, Rep. Prog. Phys. **66**, 2069 (2003).

[157] W. Zwerger (Ed.), *The BCS-BEC Crossover and the Unitary Fermi Gas* (Springer-Verlag Berlin Heidelberg, 2012).

[158] K. B. Gubbels and H. T. C. Stoof, Phys. Rev. Lett. **100**, 140407 (2008).

[159] J. Erdmenger, C. Hoyos, A. O'Bannon, and J. Wu, J. High Energy Phys. **12**, 086 (2013).

[160] C. Charmousis, B. Goutéraux, B. S. Kim, E. Kiritsis, and R. Meyer, J. High Energy Phys. **11**, 151 (2010).

[161] H. Liu, Phys. Rev. D **60**, 106005 (1999).

[162] V. Balasubramanian, S. B. Giddings, and A. Lawrence, J. High Energy Phys. **03**, 001 (1999).

[163] E. D'Hoker, S. D. Mathur, A. Matusis, and L. Rastelli, Nucl. Phys. B **589**, 38 (2000).

[164] I. Heemskerk, J. Penedones, J. Polchinski, and J. Sully, J. High Energy Phys. **10**, 079 (2009).

[165] A. L. Fitzpatrick, E. Katz, D. Poland, and D. Simmons-Duffin, J. High Energy Phys. **07**, 023 (2011).

[166] S. El-Showk and K. Papadodimas, J. High Energy Phys. **10**, 106 (2012).

[167] P. Kovtun and A. Ritz, Phys. Rev. D **78**, 066009 (2008).

[168] Y. Huh, P. Strack, and S. Sachdev, Phys. Rev. B **88**, 155109 (2013).

[169] U. H. Danielsson and L. Thorlacius, J. High Energy Phys. **03**, 070 (2009).

[170] D. Z. Freedman and A. van Proeyen, *Supergravity* (Cambridge University Press, 2012).

[171] C. G. Bollini, J. J. Giambiagi, and A. G. Domínguez, Il Nuovo Cimento Series 10 **31**, 550 (1964).

[172] D. T. Son, Phys. Rev. D **78**, 046003 (2008).

[173] K. Balasubramanian and J. McGreevy, Phys. Rev. Lett. **101**, 061601 (2008).

[174] C. A. Fuertes and S. Moroz, Phys. Rev. D **79**, 106004 (2009).

[175] K. Balasubramanian and J. McGreevy, Phys. Rev. D **80**, 104039 (2009).

[176] A. Chamblin, R. Emparan, C. V. Johnson, and R. C. Myers, Phys. Rev. D **60**, 064018 (1999).

[177] S. Sachdev, Phys. Rev. Lett. **105** (2010).

[178] B. Pioline and J. Troost, J. High Energy Phys. **03**, 043 (2005).

[179] J. R. Hook and H. E. Hall, *Solid State Physics* (Wiley, 1995).

[180] Z. Zhu and J. E. Hoffman, Nature **513**, 319 (2014).

[181] S. A. Parameswaran, T. Grover, D. A. Abanin, D. A. Pesin, and A. Vishwanath, arXiv:1306.1234 (2013).